Experimental Investigation of Accelerator Beam Dynamics with a Linear Paul Trap



Lucy Martin
Trinity College, Oxford

Thesis submitted in fulfilment of the requirements for the degree of Doctor of Philosophy at the University of Oxford

Hilary term, 2020

Abstract

This thesis describes a range of experiments performed using a linear Paul trap to investigate the transverse beam dynamics of intense hadron accelerators. Due to the complexity of the dynamics in intense hadron accelerators, it is advantageous to use a scaled experiment to gain insight into these machines. A Paul trap is used to study accelerator dynamics, as the Hamiltonians of the two systems are equivalent.

The IBEX Paul trap at the Rutherford Appleton Laboratory, Oxfordshire, has been commissioned. The first trapping of argon ions is observed, and the system is characterised, developing an understanding of the ion creation process, ion lifetime, longitudinal temperature, transverse emittance, and the process of ion extraction from the trap. A Faraday cup and MCP are used as diagnostics for the trap and are calibrated carefully to detect accurately the number of ions confined.

Both the IBEX and S-POD (Hiroshima University, Japan) linear Paul traps are used to study space-charge-driven resonances quantitatively for the first time. The particle-in-cell code Warp is used to gain a deeper understanding of the experiment and to assist with the interpretation of results. Values are extracted describing the location of the greatest ion loss in tune space for a given intensity for equal transverse tunes. These values are compared to values predicted both analytically and through simulation.

In the second half of this thesis, a design for a novel particle accelerator is considered, using the theory of Nonlinear Integrable Optics (NIO). In NIO, a highly nonlinear magnet is inserted into a linear lattice (known as a T-insert), resulting in regular and bounded particle motion. Detailed studies are undertaken to ascertain whether a simpler version of this theory, Quasi-Integrable nonlinear Optics (QIO), can be tested in a Paul trap.

A T-insert lattice is designed to meet the constraints of QIO, as well as the constraints imposed by the IBEX hardware. A number of these lattices are tested on the IBEX trap, confirming that enough ions are confined to study QIO in the presence of space-charge forces and that it is possible to create a T-insert with sufficient precision. To verify that the T-insert lattice created within the Paul trap meets the conditions for QIO, a method to measure the beta function in a Paul trap has been designed and tested.

Finally, a series of simulations are presented, showing that with a simple upgrade to the IBEX trap it is possible to create an octupole potential of high-enough quality to test QIO, while also retaining the ability to create a high-quality quadrupole to make the T-insert lattice. The impact of misalignment and scraping within the trap on the dynamic aperture and tune spread is studied using Warp. The resistance of the lattice to resonant excitation is investigated.

The experimental and simulation studies described show that QIO can be tested in a Paul trap, and pave the way for a range of studies of this exciting concept.

For my parents.

Acknowledgements

Before anyone else, my thanks go to my supervisor, Suzie. Thank you for allowing me to work on such an interesting and challenging project, and for your support, guidance and constant belief in me. Knowing that your door was always open was a huge reassurance.

Thank you to the JAI and everyone I have worked with at Oxford, especially Armin for the challenging conversations and sound advice. Thanks also to the intense beams group at RAL, in particular to David Kelliher for his endless patience, Shinji Machida for sharing his expertise, and Chris Prior for the mathematical help and seasonal garden produce. I am indebted to all the members of the ISIS team who took the time to help with IBEX, most notably Emi Yamakawa, Peter Giffin-Hicks, Sunil Patel, and Alex Pertica.

I would also like to thank the Beam Physics group at Hiroshima University for allowing me to visit their lab and learn from their years of experience, the knowledge I gained over two months was invaluable. Furthermore, I am grateful to Kiersten Ruisard for sharing tips, tricks, and examples of code relating to quasi-integrable optics, it was immeasurably helpful.

Thanks to everyone who has rowed with, or coached me, over the last three years at City of Oxford, especially the "We are" four. You have reminded me daily of the value of hard work, dedication, and balance, and I owe you my sanity. A huge thank you also to my friends for making my time in Oxford so enjoyable. Thanks, Hazel and Olly, for being brilliant housemates, Robin, for the breakfasts and comments on my "wiggly green line", Alissa, for letting me be part of your life, Natalie, for the postcards and half marathons, and Caitlin, for being there, day in day out. Thank you Peter, for being the perfect antidote to stress.

Finally, thank you to my family. Thank you for believing that I could do this, for driving the length of the country to visit, and for the endless support. I couldn't have done this without you, and will never be able to thank you enough.

Contents

Introduction **1**

1 High-intensity hadron accelerators **3**
1.1 A brief history of circular accelerators . . . 4
1.2 Intense accelerators . . . 5
1.3 Hamiltonian formalism for transverse dynamics . . . 6
1.3.1 Frenet-Serret coordinates . . . 8
1.4 Transverse particle dynamics . . . 10
1.4.1 The linear focusing solution . . . 10
1.4.2 Courant-Snyder representation . . . 11
1.4.3 Transfer matrices . . . 14
1.4.4 Resonance . . . 17
1.5 Space-charge effects in high-intensity beams . . . 18
1.5.1 Space-charge forces . . . 18
1.5.2 Special 2D distributions . . . 21
1.5.3 Coherent and incoherent motion . . . 21
1.5.4 Images and impedance . . . 23
1.6 Mitigation of beam loss . . . 23
1.7 The motivation for Paul traps . . . 26
1.8 Thesis outline . . . 28

2 Paul trap dynamics and experimental setup **29**
2.1 Introduction to Paul traps for accelerator physics . . . 30
2.2 Transverse dynamics in a Paul trap . . . 33
2.2.1 Equivalence of the Paul trap Hamiltonian to the accelerator case . . . 34
2.2.2 Mathematical description of the ion distribution . . . 36
2.3 The Mathieu equations . . . 39
2.4 The IBEX experimental setup . . . 40
2.5 Previous Paul trap work . . . 48
2.6 Simulations with Warp . . . 50
2.7 Chapter summary . . . 52

3 IBEX characterisation **53**
3.1 The Faraday cup . . . 54
3.2 Ion accumulation and lifetime . . . 56
3.3 Temperature measurement . . . 60

3.4 MCP characterisation . . . 62
3.4.1 CCD camera . . . 62
3.4.2 Monte Carlo simulation of transverse distribution . . . 65
3.4.3 Relationship between ion number and luminosity . . . 67
3.4.4 Saturation of the MCP . . . 68
3.4.5 Calibration against Faraday cup . . . 70
3.5 Calibration of applied voltages . . . 73
3.5.1 Voltage correction . . . 75
3.6 Emittance estimate . . . 75
3.7 Chapter summary . . . 77

4 A study of coherent and incoherent resonances 78
4.1 Published works . . . 79
4.2 Coherent and incoherent resonances . . . 79
4.3 Experimental procedure using S-POD . . . 86
4.4 Simulation of the experiment . . . 90
4.5 Detailed simulation at a cell tune of 0.25 . . . 93
4.6 Analysis of S-POD data . . . 98
4.7 Discussion . . . 105
4.8 Tune splitting . . . 109
4.8.1 Simulation . . . 114
4.8.2 Discussion . . . 115
4.9 Chapter summary . . . 117

5 Future high-intensity accelerators 119
5.1 Introduction to novel high-intensity accelerators . . . 119
5.2 The theory of Nonlinear Integrable Optics . . . 120
5.2.1 What is an integrable lattice? . . . 120
5.2.2 Danilov and Nagaitsev's integrable solution . . . 122
5.2.3 Nonlinear decoherence and Landau damping . . . 125
5.3 An introduction to IOTA and UMER . . . 126
5.3.1 IOTA . . . 126
5.3.2 UMER . . . 128
5.4 Past simulation work . . . 130
5.5 Comparison between an octupole in an accelerator and in a Paul trap . . . 132
5.6 The benefits and drawbacks of using IBEX to test NIO . . . 133
5.7 Chapter summary . . . 135

6 Experimental creation of a T-insert with IBEX 137
6.1 T-insert design for IBEX . . . 137
6.1.1 A first attempt at T-insert design . . . 140
6.2 Experimentally creating the T-insert . . . 143
6.3 Testing the T-insert . . . 148
6.3.1 Quadrupole perturbation . . . 153
6.4 Beta-function measurement using dipole kicks . . . 156

6.4.1 Dipole oscillation . . . 157
6.4.2 Experimental limitations . . . 159
6.4.3 Measurement method . . . 161
6.4.4 Results . . . 162
6.4.5 Discussion . . . 163
6.4.6 Alternative methods . . . 165
6.5 Chapter summary . . . 167

7 Simulation of Nonlinear Integrable Optics in a Paul trap 169
7.1 Octupole trap . . . 170
7.1.1 Multipole components . . . 170
7.1.2 Octupole strengths . . . 173
7.2 Simulation of QIO . . . 174
7.3 A T-insert matrix kick and ideal octupole . . . 177
7.4 Using Warp to simulate a perfect T-insert and realistic octupole . . . 180
7.4.1 Introducing the octupole . . . 181
7.5 Introducing a perturbation . . . 182
7.6 Space charge . . . 187
7.7 Chapter summary . . . 189
7.8 Further work . . . 190

8 Conclusions 193
8.1 Further work . . . 197

A 199
A.1 IBEX tune scan data . . . 199
A.2 Ion distribution . . . 201
A.3 Fully integrable solutions . . . 204
A.4 T-insert error study . . . 206
A.5 Further simulations of QIO . . . 208
A.6 IBEX trap alignment . . . 211

Bibliography 213

List of Figures

1.1 The Frenet-Serret coordinate system. 8
1.2 Oscillations in a matched beam. 12
1.3 The phase space ellipse. 13
1.4 Diagram illustrating the effects of space-charge forces on particle tunes. . . . 22
1.5 Illustration of the decoherence of a transversely oscillating beam. 24
1.6 Illustration of the conditions for Landau damping. 25

2.1 A CAD representation of the IBEX ion trap, where the trapping region is in the centre of the four cylindrical rods. 32
2.2 Photograph of the IBEX ion trap. 32
2.3 Diagram (not to scale) of the IBEX trapping region. 33
2.4 Stability diagram for the Mathieu equations. 41
2.5 Photograph of the IBEX laboratory. 43
2.6 Diagram of the IBEX electron gun. 44
2.7 The IBEX MCP, phosphor screen and camera. 47
2.8 Typical timing structure of an IBEX experiment. 48

3.1 Noise reduction on the signals from the Faraday cup and MCP. 55
3.2 Ion number over a range of storage periods for four different argon pressures. 57
3.3 The number of ions created within the trap, varying electron-gun duration at two different argon pressures. 58
3.4 Ion number variation with ramping time between cell tune of 0.15 and 0.3. . 59
3.5 The number of ions extracted from the trap at different depths of the longitudinal potential well. 61
3.6 An example of ion arrival times at the MCP from a simple Monte Carlo model and analytical description. 63
3.7 Predicted time structure of the light signal from the phosphor screen. 64
3.8 Creation of the mask from the phosphor screen. 65
3.9 A comparison between the expected ion distribution on the phosphor screen based on a simple Monte Carlo Model, and the image taken experimentally by the CCD camera. 66
3.10 An example of the projection of the CCD image onto the x and y axis at a cell tune of 0.15, and the fitting process used to extract the luminosity. . . . 68
3.11 Comparison of the number of electrons collected by the phosphor screen to the integrated luminosity of the signal. 69
3.12 Comparison of the number of electrons collected by the phosphor screen with the number of ions collected by the Faraday cup. 71

3.13 Gain of the MCP for different values of U_{MCP}. 72
3.14 A calibration tune scan showing the number of ions extracted for cell tunes in the range 0.1 to 0.4, for small ion numbers and large confinement times. . 74
3.15 Simulated data showing the Full Width Half Maximum (FWHM) for a range of emittance values, at four different cell tunes. 76

4.1 Measured ion number extracted from the S-POD trap against cell tune. . . . 87
4.2 Tune shift against ion number for the four resonances at lowest tune in Fig. 4.1. 88
4.3 Variation of the beta function with cell tune. 90
4.4 Simulated RMS emittance growth at the cell tunes $\frac{1}{6}$, $\frac{1}{4}$ and $\frac{1}{3}$. 91
4.5 Diagram showing the shape of coherent resonance due to the finite width of the stopband. 93
4.6 A detailed study of the resonance at a tune of 0.25. 95
4.7 Emittance growth (RMS) in the horizontal direction at bare cell tunes (a) 0.253, (b) 0.255, (c) 0.258 and (d) 0.26. 96
4.8 Kurtosis in the horizontal direction at bare cell tunes of (a) 0.253, (b) 0.255, (c) 0.258 and (d) 0.26. 99
4.9 Tune footprints for bare cell tunes of (b) 0.253, (c) 0.255, (d) 0.258 and (e) 0.26. 100
4.10 Tune shift multiplied by the emittance, for the four resonances studied, against the ion number. 103
4.11 Values of A_m from the fitting process in Fig. 4.10, with error bars based on the fit in Fig. 4.10 and the calculation of the emittance at each ion number. 104
4.12 Diagram showing the voltages applied to the IBEX rods to create unequal transverse tunes. 110
4.13 A selection of experimental data showing ion loss against horizontal cell tune for the resonance at a cell tune of ~ 0.25, in the case of equal and unequal transverse tunes, where the vertical cell tune is fixed at 0.15. 111
4.14 Ion number against the tune corresponding to the greatest ion loss for the $Q = 0.25$ resonance, for equal and unequal tunes. 113
4.15 The emittance growth over time at a cell tune of Q_x =0.254, Q_y =0.15. . . . 114
4.16 Comparison of emittance growth in simulation for equal and unequal tunes. . 115

6.1 Flow diagram of the T-insert lattice design process. 141
6.2 Optics of the first T-insert design, where voltage pulses have an amplitude of 25 V. 142
6.3 Oscilloscope trace showing the noise, with no load, on the WMA300 amplifier and the custom built amplifiers. 144
6.4 Diagram showing the structure of the T-insert lattice and drift region, for a phase advance of $0.135\times 2\pi$ over the drift. 145
6.5 Optics of the lattice L_3. 147
6.6 Flow diagram of the matching process. 150
6.7 Oscilloscope trace showing the experimental setup for trapping with lattice L_3. 151

6.8 Oscilloscope trace showing the experimental setup for trapping with lattice L_3, with matching to a FODO lattice before extraction. 152
6.9 An example ion distribution on the phosphor screen, when the lattice L_3 is also applied to the end caps during ion extraction. 152
6.10 The number of ions extracted from lattice L_3, when a quadrupole perturbation of 0.1 V is applied at a range of frequencies. 154
6.11 The optics of lattice L_3, reconstructed from a recorded oscilloscope trace. . . 155
6.12 Experimentally applied voltages for lattice L_3, with the calibration factor applied. 156
6.13 An example of the tunes (Q_x) calculated from successive oscilloscope traces of lattice L_3. 157
6.14 Schematic end view of S-POD rods, showing the voltages applied in the beta function measurement. 160
6.15 An example fit to data showing ion loss for different strengths of dipole kick. 163
6.16 Comparison of reconstructed beta function for tunes $\frac{1}{5}$, $\frac{1}{7}$ and $\frac{1}{9}$ with the beta functions expected from the applied waveforms. 164
6.17 Simulations showing a comparison between the full extracted ion distribution on the MCP and a 40 ns snap shot. 166

7.1 A transverse slice of the octupole trap design. 171
7.2 The sum of higher-order ($m > 4$) strength harmonics of the field, as a function of radius in the multipole trap. 172
7.3 The beta function of the QIO lattice, the required octupole potential, and the voltages applied to the trap. 174
7.4 Diagram showing the methods of simulation used for QIO. 176
7.5 Dynamic aperture and tune spread, when an ideal octupole is used and the T-insert is implemented through matrix multiplication of the ions. 178
7.6 Dynamic aperture and tune spread, when an ideal octupole is used and the T-insert is implemented through matrix multiplication of the ions. Scraping is applied. 179
7.7 A Warp simulation of the QIO lattice, the T-insert is implemented through a matrix kick, the octupole is created by applying voltages to the plates and rods. 180
7.8 A Warp simulation of the QIO lattice, the T-insert is implemented through a matrix kick. The octupole is created by applying voltages to the plates and rods, error is included. 181
7.9 Particle loss and change in the standard deviation of the ion distribution in x, when the octupole potential is introduced to the linear lattice L_3. 183
7.10 Particle loss and change in the standard deviation of the ion distribution in x, when a quadrupole perturbation is applied to an approximate QIO lattice. 184
7.11 Poincaré plots showing the motion of a single particle through phase space, when a perturbation is applied, both with and without the octupole potential. 185
7.12 Phase space when a quadrupole perturbation is applied to a QIO lattice, with the octupole potential switched off. 186
7.13 Phase space when a quadrupole perturbation is applied to a QIO lattice, with the octupole potential switched on. 187

7.14 A projection of the phase space distributions shown in Fig. 7.13 onto the x axis. 188
7.15 Beta function of lattice L_3 with space charge. 190

A.1 Measured ion number extracted from the IBEX trap against cell tune. 200
A.2 Error study of lattice L_3. 207
A.3 A comparison of the dynamic aperture calculated by a python script and a Warp simulation using an ideal octupole potential. 209
A.4 Dynamic aperture and tune spread of the imperfect T-insert lattice to which a perturbation is applied in Section 7.5. 209
A.5 Dynamic aperture and tune spread from the initial T-insert lattice design . . 210
A.6 Phase space in coupled coordinates when a quadrupole perturbation is applied to a QIO lattice, with the octupole potential switched on. 210

List of Tables

4.1 Analytically calculated C_m values for a 2D KV beam. 83
4.2 The transverse temperature, RMS beam size and RMS emittance calculated for each ion number studied. 104
4.3 The values of C_m for beams of equal tunes extracted from simulation performed by the Beam Physics group at Hiroshima University. 107
4.4 The difference in C_2 for the cases of equal and unequal tunes. 110
4.5 Example voltages for unequal cell tunes, where the rf voltage is a sinusoid with a frequency of 1 MHz. 112

6.1 The constraints on a T-insert lattice for the IBEX trap. 140
6.2 The design parameters for the first T-insert design, where all voltage pulses have a constant amplitude. 143
6.3 The parameters of lattice L_1. 145
6.4 The design parameters common between lattices L_1, L_2 and L_3. 145
6.5 The scaling relation between lattice L_1, L_2 and L_3. 145
6.6 The maximum number of ions extracted from the three L_κ lattices at different trapping times. 148
6.7 The number of ions extracted from the lattice L_3 with and without matching. 149
6.8 The maximum beta function and emittance, compared to expected values, when dipole kicks are used to give ion loss. 162

7.1 Change in the dynamic aperture and tune spread with octupole strength over 1000 lattice periods 177

A.1 Alignment data at position 1. 212
A.2 Alignment data at position 2. 212

Glossary

Incoherent resonance: The resonant excitation of a single particle, or a subset of particles within the distribution, when the tune of these particles meets the resonant condition,

$$Q_0 + \Delta Q = \frac{n}{m},$$

where n and m are integers, and ΔQ is the incoherent tune shift. Incoherent resonances can be excited by magnetic multipoles created in error, or by a multipole term arising from space charge, which has a periodicity dependent on the lattice structure (also known as space-charge structure resonance). For example, for a Gaussian beam, a Taylor expansion of the beam core gives all multipole terms of even-order, which are then driven by the envelope oscillations of the beam.

Coherent resonance: The resonant excitation of the distribution as a whole, when the resonant condition

$$Q_0 + C_m \Delta Q = \frac{n}{m},$$

is met. C_m is a factor between 0 and 1, depending on the order of the resonance, and ΔQ is the RMS incoherent tune shift. The C_m factor is discussed in greater detail in Chapter 4. Coherent resonances can be excited by magnetic multipoles created in error, or by a multipole term arising from space charge. In beams of two or more dimensions, coherent resonances can also be driven by anisotropy, for example, due to different values of emittance of focusing strength in the transverse directions.

Coherent parametric instability: Coherent instabilities grow exponentially from small perturbations in the initial particle distribution. They are known as parametric, as the instability is driven by the modulation of the focusing force. The word instability is used as a periodic solution exists but is unstable.

Mismatch: Beam loss can also result from a difference between the Twiss parameters in two different lattice sections, for example, at the point of injection into a ring. Perfect matching occurs when the β and β' from both lattice sections are equal at the point where they meet, so the phase space ellipse of the injected particles matches that of the ring. If this is not true, the difference in the phase spaces results in oscillations about the equilibrium solution. Both space-charge and nonlinear fields lead to an amplitude dependence of oscillation frequencies and filamentation of the beam, leading to emittance growth.

Halo: A beam halo, where a relatively small number of particles are excited to regions beyond the tails of the distribution, can be excited by a mismatch or a resonance. The oscillation of the beam core drives particles to a large amplitude through parametric resonance.

Kapchinskij-Vladimirskij (KV) distribution: The KV distribution is often used in analytical descriptions of space charge, as it is the simplest model of a beam, with all particles oscillating with the same frequency. In a KV distribution, particles populate the surface of a 4D hyper-ellipsoid in phase space, defined by the values of beam size and emittance. When this ellipse is projected onto real space, it gives a uniform elliptical beam. The space-charge forces of a KV distribution are linear, so the particle distribution remains the same in a linear focusing lattice, and the distribution is referred to as stationary.

Waterbag distribution: Waterbag distributions are often used in space-charge simulations. Particles uniformly fill a 4D hyper-ellipsoid, resulting in nonlinear space-charge forces within the particle distribution. A waterbag distribution is therefore not stationary.

Gaussian distribution: A Gaussian distribution is Gaussian in the 4D phase space, and also in the real space projection. Space-charge forces are nonlinear, and so the distribution is not stationary. Gaussian distributions are often truncated at a number of standard deviations to avoid unrealistically long tails in the distribution.

Decoherence: In a distribution of particles which has a range of frequencies, the collective motion of the distribution is damped as the particles begin to oscillate out of time with one another.

Detuning: A subset of the particles in the distribution, whose incoherent frequency matches the frequency of an external driving force, are excited. However, strong nonlinear fields can create an amplitude-dependent tune spread large enough that the excited particles now oscillate at a slightly different frequency and are no longer driven by the resonance.

Landau damping: In a distribution where the frequency of coherent oscillation lies within the range of incoherent frequencies within the beam, energy is transferred from the coherent oscillation mode to the incoherent oscillation of particles so that coherent oscillations never form.

Dynamic aperture: The innermost radius of the region of stable motion in the phase space of a circular accelerator. Experimentally the dynamic aperture can be considered in the short term, over $10^3 - 10^4$ revolutions of the machine, or in the long term, which can be up to 10^9 turns.

Introduction

The development of particle accelerators has led to huge advances in our understanding of particle physics over the last century. Today, accelerators such as the Large Hadron Collider (LHC) represent the cutting edge of particle physics research, with particle collisions at high energy used to probe the standard model and to search for new physics [1].

However, accelerators are used in a wide range of applications, for example, the production of radioisotopes for cancer therapy and the creation of semiconductors through ion implantation [2]. There are potential applications for accelerators in nuclear power, including the transmutation of nuclear waste. Additionally, user facilities such as ISIS neutron and muon source [3] and Diamond Light Source [4] use accelerators to answer a wide range of scientific questions, studying subjects from drug delivery systems to ancient Egyptian vases [5].

Accelerators and beams are rich in interesting physics. Most modern accelerators are constructed using the principle of strong focusing, where a series of alternating focusing and defocusing quadrupole magnets are used to keep charged particles within a beam pipe. This underlying alternating-gradient structure leads to transverse particle motion that resembles harmonic oscillation, ensuring that particles can be confined and accelerated, but making such accelerators susceptible to the resonant excitation of particles.

In the case of intense beams, where many particles are confined, the electromagnetic forces of interaction between individual particles must be accounted for. These forces mean that fully self-consistent solutions are required to describe particle motion. Such solutions cannot be found analytically in most cases, so simulations are employed to solve the systems

numerically. However, these simulations are often computationally intensive and contain a number of assumptions or simplifications, making it difficult to study the dynamics of intense beams over longer timescales, for example, a full acceleration cycle.

This thesis describes a different approach to the study of intense beams, using a Paul trap, a scaled experiment capable of reproducing the transverse dynamics in an accelerator. A Paul trap confines a large number of very low energy ions using electric, rather than magnetic, fields. This thesis describes how a Paul trap has been used to understand high-intensity beams, and the progress made towards testing concepts for future, novel, accelerators.

Chapter 1

High-intensity hadron accelerators

This chapter gives an introduction to the theory of intense hadron accelerators, describing concepts that will be used throughout the rest of this thesis.

At the beginning of this chapter, a brief history of the development of high-intensity accelerators is given, and the terms used to describe intense accelerators are described. In Section 1.3, the Hamiltonian description of accelerator dynamics is introduced, as the Hamiltonian of an accelerator will later be compared to the Hamiltonian of a linear Paul trap, justifying the use of a Paul trap as a tool for accelerator physics. Throughout the rest of the chapter, this mathematical description of an accelerator is developed, resulting in the equations of motion for particles in a linear focusing channel.

In Section 1.5.1, space-charge forces are introduced, and their effect on the betatron tune is derived. The later sections of the chapter explain the difference between incoherent and coherent motion, introducing sources of beam loss in intense accelerators as well as ways to mitigate this beam loss. Section 1.7 explains how a Paul trap can be of use in the study of intense beams, outlining the advantages over simulation studies. Finally, the structure of this thesis is outlined in Section 1.8.

1.1 A brief history of circular accelerators

In 1932, following the development of electrostatic accelerators and the first linacs, the first cyclotron was constructed, using an iron magnet to produce a bending field between two circular poles. Injected particles spiralled out from the centre of the machine as they reached higher energies, accelerated by an alternating voltage applied to two D shaped electrodes within the magnetic field [6]. However, this form of acceleration only worked well for non-relativistic particles, where the revolution frequency remains the same as energy is increased.

In the first cyclotron, particles at large vertical amplitudes experienced a greater bending force from the edge of the electrodes, which was sufficient to confine particles vertically. Horizontal focusing was added through iron shims, creating a slightly stronger field in the centre of the cyclotron [7]. For higher-energy particles synchrocyclotrons were employed, decreasing the rf frequency with acceleration; however, this limited acceleration to small pulses of particles at a time, restricting the average beam current.

To keep up with demands from particle physics experiments the first synchrotrons were constructed. They used a number of separate dipole magnets to bend a beam around a ring, the strength of whose dipoles was increased throughout an acceleration cycle. Although at first weak transverse focusing was used, separate focusing magnets were found to be required to keep particles within a beam pipe for thousands of turns. Separate accelerating regions, such as RF cavities, were introduced to transfer energy to the particles [8].

This design is still the basic structure of modern synchrotrons. The beam is bent around the ring by several dipole magnets and so-called “strong focusing” is provided by quadrupole magnets. In an accelerator containing only dipole and quadrupole magnets, the focusing is described as linear, as the focusing force increases linearly with distance from the magnet centre. In modern accelerators, higher-order magnets, such as sextupoles, are included to provide greater control over the beam. Throughout the rest of this thesis “accelerator” refers to a modern, strong-focusing machine.

1.2 Intense accelerators

In this work, I focus on the dynamics of intense beams. An intense beam contains a large density of charged particles. A large number of particles is not sufficient to give an intense beam, they must also be confined within a small region of space. A high-intensity accelerator is a machine that accelerates and controls these intense beams. The beam current (usually given in Amps) refers to the rate of flow of units of charge past a fixed point in the accelerator. The power (given in Watts) of a beam is given by the beam current multiplied by the energy (in eV) of the accelerated particles.

The development of high-intensity accelerators has progressed rapidly since the 1970s with the construction of synchrotrons such as ISIS[3] and JPARC[9], as well as the SNS accumulator ring [10]. Many steps have been taken to understand intense beams and to mitigate effects that lead to beam loss, including the development of increasingly sophisticated particle-tracking codes. The insight gained from simulations is often credited with helping accelerators like ISIS operate above design intensity [11, 12].

Developments in accelerator hardware, such as the ability to inject H^- ions (allowing the stacking of a beam onto the same phase space through foil stripping, as Liouville's theorem will not apply [13]) and fast transition crossing, have allowed higher intensities to be reached [14]. However, even at modest particle energies, beam loss can lead to the activation of accelerator components, damaging the accelerator and increasing the radiation dose received by operators working on the machine. As a general rule, unplanned beam loss should be kept below an average of $1\,\mathrm{Wm}^{-1}$, which is an increasingly small fraction as beams become more intense [15]. The power deposited by lost particles can be reduced by ensuring that they are lost earlier in the acceleration cycle when they have lower energy. This is usually achieved using a collimator.

Multi-stage acceleration is commonly used to generate intense beams. For example, at the ISIS synchrotron at the Rutherford Appleton Laboratory, UK, the beam is first created by a H^- source, before acceleration through a Radio Frequency Quadrupole (RFQ) and 70 MeV,

4-tank, 202.5 MHz drift-tube linear accelerator. The H^- beam is then stripped using a thin foil as it enters the synchrotron, leaving a proton beam [16]. Pulses are produced at a rate of 50 Hz. The beam current is $\sim$225 μA and beam energy is 800 MeV, leading to a beam power of $\sim$180 kW [11].

1.3 Hamiltonian formalism for transverse dynamics

As this thesis relies on the equivalence between the transverse Hamiltonian of an accelerator and a Paul trap, in this section I include the derivation of the Hamiltonian of an accelerator.

Particles travelling through an accelerator are controlled and accelerated with electromagnetic fields. The Lorentz force, describing the interaction of a charged particle with an electromagnetic field, is given by

$$\vec{F} = e(\vec{E} + \vec{v} \times \vec{B}), \tag{1.1}$$

where $\vec{F}$ is the force experienced by a particle with charge e, travelling through a magnetic field $\vec{B}$ and electric field $\vec{E}$, at velocity $\vec{v}$.

The magnetic and electric fields can be related to the vector potential $\vec{A}$ and the scalar potential Φ, through

$$\vec{E} = -\nabla\Phi - \frac{\partial \vec{A}}{\partial t} \quad \text{and} \quad \vec{B} = \nabla \times \vec{A}. \tag{1.2}$$

The dynamics of a particle in an electromagnetic field are governed by the location and velocity of the particle as well as the properties of the field. The action S, of a particle with position q_i and velocity $\dot{q}_i$, is given by $S = \int_{t1}^{t2} L(q_i, \dot{q}_i, t)$, where L is the Lagrangian. From the principle of least action, which states that a particle moves along a path which S is stationary, and following the introduction in [17], the Lagrangian for a charged particle of mass m moving in an electromagnetic field is

$$L = -mc^2\sqrt{1 - \frac{v^2}{c^2}} - e\Phi + e\vec{v}\cdot\vec{A}. \tag{1.3}$$

Using the relationship

$$H(p_i, q_i, t) = \sum \dot{q}_i p_i - L(q_i, \dot{q}_i, t), \quad \text{where} \quad p_i = \frac{\partial L}{\partial \dot{q}_i}, \tag{1.4}$$

and p_i is the canonical momentum, the Hamiltonian of a charged particle in an electromagnetic field is given by

$$H = e\Phi + \sqrt{c^2(\vec{p} - e\vec{A})^2 + m^2c^4}. \tag{1.5}$$

In the non-relativistic case, this can be Taylor expanded to give

$$H = e\Phi + mc^2\left(1 + \frac{(\vec{p} - e\vec{A})^2}{2m^2c^2}\right), \tag{1.6}$$

and ultimately simplified to

$$H = e\Phi + \frac{(\vec{p} - e\vec{A})^2}{2m}. \tag{1.7}$$

Hamilton's equations, describing the particle motion associated with this Hamiltonian, are given by

$$x' = \frac{\partial H}{\partial p_x}, \qquad p_x' = -\frac{\partial H}{\partial x}, \qquad y' = \frac{\partial H}{\partial p_y}, \qquad p_y' = -\frac{\partial H}{\partial y}, \tag{1.8}$$

where the prime denotes the derivative with respect to s.

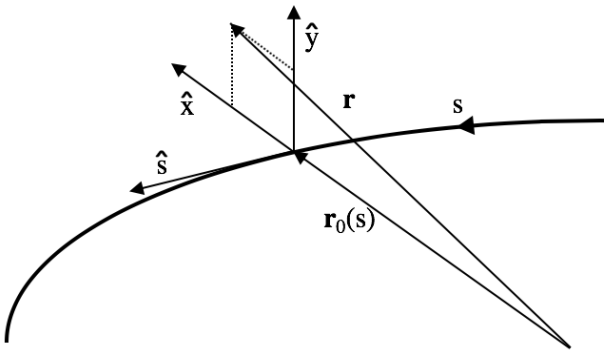


Figure 1.1: The Frenet-Serret coordinate system.

1.3.1 Frenet-Serret coordinates

Particle motion in a circular accelerator is often described with respect to a co-moving coordinate system, based on an ideal trajectory through an accelerator. This ideal trajectory is called the reference orbit. In the regions where the reference trajectory bends, the coordinate system bends accordingly. In Frenet-Serret coordinates ($\hat{s}$, $\hat{x}$ and $\hat{y}$), $\hat{s}$ is aligned with the ideal path a particle would take through the accelerator, $\hat{x}$ and $\hat{y}$ are then perpendicular to both each other and $\hat{s}$, creating an orthogonal coordinate system. The unit vector $\hat{x}$ is taken to be the horizontal direction with respect to the orbit, and $\hat{y}$ the vertical.

Following the diagram in Fig. 1.1, where ρ is the radius of curvature of the reference orbit,

$$\hat{s}(s) = \frac{d\vec{r_0}(s)}{ds}, \qquad \hat{x}(s) = -\rho(s)\frac{d\hat{s}(s)}{ds}, \qquad \hat{y}(s) = \hat{x}(s) \times \hat{s}(s). \tag{1.9}$$

In this new co-ordinate system, the Hamiltonian can be found through a canonical transformation. The independent variable is then changed from t to s. Following [18], the new Hamiltonian, expanded to second order in p_x and p_y, as $p_x, p_y << p$ (the paraxial approximation), where p is the total momentum, is found to be

$$H \approx -p(1 + \frac{x}{\rho}) + \frac{(1 + x/\rho)}{2p}\left[(p_x - eA_x)^2 + (p_y - eA_y)^2\right] - eA_s. \tag{1.10}$$

When describing a typical accelerator this can be simplified significantly. Only the case in which there is no electric potential is required ($\Phi = 0$), with transverse magnetic fields ($A_x = A_y = 0$), this gives,

$$H \approx -p(1 + \frac{x}{\rho}) + \frac{(1 + \frac{x}{\rho})}{2p}(p_x^2 + p_y^2) - eA_s. \tag{1.11}$$

The energy of a particle is $E = H - e\Phi$ and the momentum is $p = \sqrt{\frac{E^2}{c^2} - m^2c^2}$.

In the straight-line approximation $\rho = \infty$. Performing the change of scale

$$\tilde{p}_x = \frac{p_x}{p}, \qquad \tilde{p}_y = \frac{p_y}{p} \quad \text{and} \quad \tilde{H} = \frac{H}{p}, \tag{1.12}$$

the simplified Hamiltonian becomes

$$\tilde{H} = \frac{1}{2}(\tilde{p}_x^2 + \tilde{p}_y^2) - \frac{e}{p}A_s. \tag{1.13}$$

A detailed description of this process is given in reference [18].

Multipole expansion

The magnetic vector potential of a magnet with $2m$ poles is

$$A_s = \sum_m A_m f_m(x, y), \quad \text{where} \quad f_m(x, y) = (x + iy)^m. \tag{1.14}$$

The real terms are taken for normal magnetic multipoles and the imaginary terms for skew multipoles. For a long magnet, taking the paraxial approximation [8],

$$B_y(y = 0) = -\frac{\partial A_s}{\partial x} = -\sum_{m=1}^{\infty} m A_m x^{m-1}. \tag{1.15}$$

Taylor expanding the field $B_y(y = 0)$ gives

$$-\sum_{m=1}^{\infty} mA_m x^{m-1} = -\sum_{m=1}^{\infty} \frac{1}{(m-1)!}\Big(\frac{d^{m-1}B_y}{dx^{m-1}}\Big)_0 x^{m-1} \tag{1.16}$$

$$\text{and therefore} \quad A_m = \frac{1}{m!}\Big(\frac{d^{m-1}B_y}{dx^{m-1}}\Big)_0. \tag{1.17}$$

Here m refers to the order of the multipole, $m = 1$ corresponds to a dipole, $m = 2$ to a quadrupole, etc. The subscript $_0$ indicates that the differentiation is performed on the s axis of the magnet.

1.4 Transverse particle dynamics

1.4.1 The linear focusing solution

Taking only the quadrupole magnetic fields, Hamilton's equations (Eqn. 1.8) can be used to find the equations of motion for a particle moving through a quadrupole potential. From Eqn. 1.17, the vector potential of a normal quadrupole magnet ($m = 2$) is given by

$$\vec{A} = \begin{pmatrix} 0 \\ 0 \\ \frac{1}{2}\Big(\frac{\partial B_y}{\partial x}\Big)_0 (x^2 - y^2) \end{pmatrix}. \tag{1.18}$$

The Hamiltonian in Eqn. 1.13 can then be used to give the Hamiltonian describing motion in a single, normal, quadrupole as

$$\tilde{H} = \frac{1}{2}(\tilde{p}_x^2 + \tilde{p}_y^2) - \frac{1}{2}\frac{e}{p}\Big(\frac{\partial B_y}{\partial x}\Big)_0 (x^2 - y^2), \tag{1.19}$$

$$= \frac{1}{2}(\tilde{p}_x^2 + \tilde{p}_y^2) + \frac{K}{2}(x^2 - y^2), \tag{1.20}$$

where K is the normalised quadrupole strength, $K = -\frac{e}{p}\Big(\frac{\partial B_y}{\partial x}\Big)_0$. Strong focusing, however, depends upon a series of alternating gradient quadrupoles, meaning that K itself is location-

dependent and that the final form of the Hamiltonian becomes

$$\tilde{H} = \frac{1}{2}(\tilde{p}_x^2 + \tilde{p}_y^2) + \frac{K(s)}{2}(x^2 - y^2). \tag{1.21}$$

From Hamilton's equations, and in the absence of coupling, Hill's equations describing particle motion are found to be of the form

$$\begin{aligned} x'' + K(s)x = 0, \\ y'' - K(s)y = 0. \end{aligned} \tag{1.22}$$

From Hill's equations, it is easy to see that alternating gradient focusing is essential. If $K(s)$ was simply a positive constant, the particle would experience oscillation in the x direction but exponential growth in the y.

1.4.2 Courant-Snyder representation

As Hill's equation (1.22) is similar to a harmonic oscillator, the solution takes a similar form, with

$$x = \sqrt{2\beta_x(s)J_x}\cos\left(\phi_x(s) - \phi_0\right), \quad \text{and} \tag{1.23}$$

$$x' = \frac{1}{2}\sqrt{\frac{2J_x}{\beta_x(s)}}\beta_x'(s)\cos\left(\phi_x(s) - \phi_0\right) - \sqrt{2\beta_x(s)J_x}\phi_x'(s)\sin\left(\phi_x(s) - \phi_0\right), \tag{1.24}$$

where the oscillations are referred to as betatron oscillations. Here β_x (not the relativistic parameter) and ϕ_x (the angle) vary through the accelerator and are dependent on the accelerator structure. J_x is a constant, known as the action, and both J_x and ϕ_0 are determined

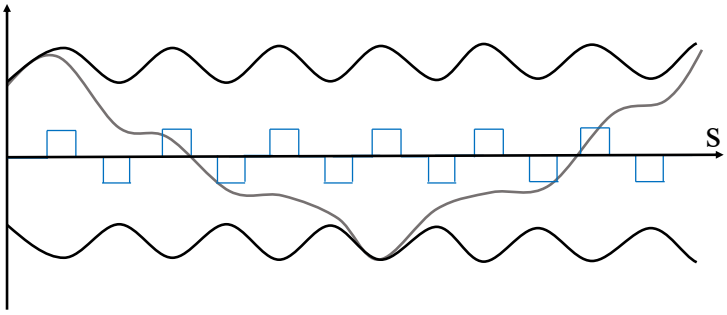


Figure 1.2: Oscillations in a matched beam. The blue rectangles represent focusing and defocusing quadrupole magnets, the black line the beam envelope and the grey line an example of a cosine-like single-particle motion.

by the initial conditions.

Substituting these solutions back into Hill's equations and equating coefficients [19], gives

$$\phi_x(s) = \int \frac{ds}{\beta_x(s)}, \tag{1.25}$$

$$\text{and} \quad \frac{1}{2}\beta_x\beta_x' - \frac{1}{4}\beta_x'^2 + K(s)\beta_x^2 = 1, \tag{1.26}$$

which is simplified by defining $\alpha_x = -\beta_x'/2$. From these equations, it is apparent that the angle ϕ gives the phase advance between two points on a beamline.

These equations of motion describe the sinusoidal oscillation about the beam axis of individual particles within an envelope of size $\sqrt{J_{\max}\beta_x(s)}$, which contains all particles as $J_{\max}$ is the maximum action of the distribution. To study the particle distribution as a whole, the statistical average of x^2 over all of the particles in the beam is taken [20], giving

$$\langle x^2 \rangle = 2\beta_x \langle J_x \cos^2 \phi_x \rangle. \tag{1.27}$$

Making the assumption that the angle variables are initially randomly distributed between 0 and 2π, and that there is no correlation between action and angle variables, $\langle x^2 \rangle = \beta_x \epsilon_x$, where ϵ_x is known as the Root Mean Square (RMS) emittance of the beam. In the

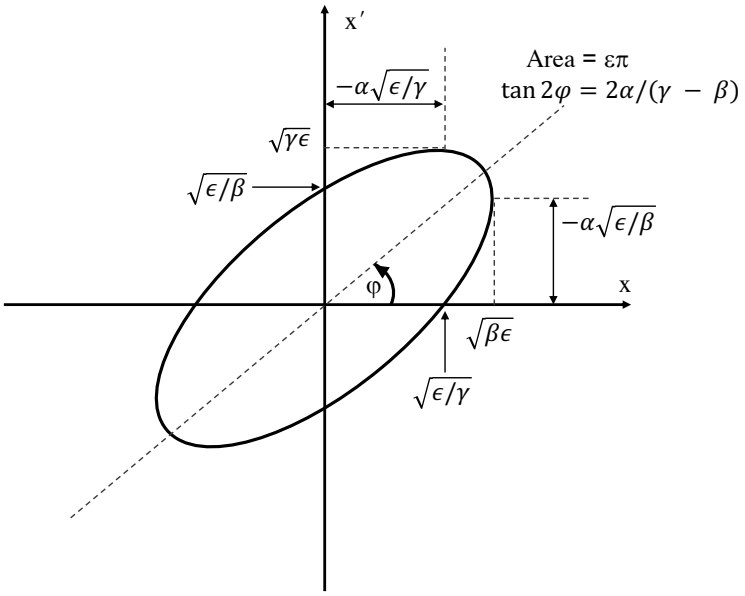


Figure 1.3: The phase space ellipse.

same way $\langle xp_x \rangle = -\alpha_x \epsilon_x$ and $\langle p_x^2 \rangle = \gamma_x \epsilon_x$, where $\gamma_x = (1 + \alpha_x^2)/\beta_x$.

The RMS emittance of a beam is defined as

$$\epsilon_x = \sqrt{\langle x^2 \rangle \langle p_x^2 \rangle - \langle x p_x \rangle^2}. \tag{1.28}$$

The emittance is also known as the Courant-Snyder invariant, as for the uncoupled Hill's equations

$$\beta_x x'^2 + 2\alpha_x x x' + \gamma_x^2 x^2 = \epsilon_x = \text{constant}. \tag{1.29}$$

This invariant describes an ellipse in phase space (x, x'), as shown in Fig. 1.3, which contains 68% of the particles within the beam. This ellipse has an area of $\pi\epsilon$ and its orientation is defined by β, α, and γ, together known as the Twiss parameters.

Liouville's theorem

Liouville's theorem states that under conservative forces the particle density in phase space remains the same throughout a beamline. Liouville's theorem does not only hold for the

two-dimensional phase space shown in Fig. 1.3, but also for the full six-dimensional phase space. Changes in the phase-space density, and therefore the emittance, arise only from non-conservative forces, for example when a beam is accelerated, damped, or loses energy to synchrotron radiation.

Mathematically, for a distribution described by $\Psi(\vec{q},\vec{p},t)$ (in an n-dimensional space), $\int \Psi(\vec{q},\vec{p},t)d^nqd^np = N$, where N is the total number of particles, the time evolution of the system is then described by Liouville's equation

$$\frac{d\Psi}{dt} = \frac{\partial\Psi}{\partial t} + \sum_{i=1}^{n}(\frac{\partial\Psi}{\partial q_i}\dot{q}_i + \frac{\partial\Psi}{\partial p_i}\dot{p}_i) = 0. \tag{1.30}$$

1.4.3 Transfer matrices

From the solution to Hill's equation given in Eqn. 1.23, it can be shown that the motion of a particle can be described by a matrix transformation acting on a vector containing the initial conditions of the particle.

There are two types of solution to Hill's equation, sine-like ($\phi_0 = \frac{\pi}{2}$) and cosine-like ($\phi_0 = 0$) solutions. Figure 1.2 shows an example of a cosine-like trajectory in grey [19].

Sine-like solutions meet the initial conditions

$$S(s_0) = 0 \quad \text{and} \quad S'(s_0) = 1, \tag{1.31}$$

whereas for the cosine-like solutions

$$C(s_0) = 1 \quad \text{and} \quad C'(s_0) = 0. \tag{1.32}$$

General solutions can then be expressed in terms of sine-like and cosine-like solutions,

$$x(s) = C(s)x_0 + S(s)x_0'. \tag{1.33}$$

Equating the generalised solutions expressed in Eqn. 1.33 to the solution to Hill's equations in Eqn. 1.23 and Eqn. 1.24 gives

$$C(s) = \sqrt{\frac{\beta(s)}{\beta_0}}(\cos\phi(s) + \alpha_0 \sin\phi(s)), \quad \text{and} \quad S(s) = \sqrt{\beta(s)\beta_0}\sin\phi(s). \tag{1.34}$$

Transforming Eqn. 1.33 and its derivative into a matrix equation gives

$$\begin{pmatrix} x(s) \\ x'(s) \end{pmatrix} = \begin{pmatrix} C(s) & S(s) \\ C'(s) & S'(s) \end{pmatrix} \begin{pmatrix} x_0 \\ x_0' \end{pmatrix}. \tag{1.35}$$

By considering a periodic system, for example one turn of a circular accelerator, $\beta(s) = \beta_0$ and

$$\begin{pmatrix} x(s) \\ x'(s) \end{pmatrix} = \begin{pmatrix} \cos\phi_0 + \alpha_0 \sin\phi_0 & \beta_0 \sin\phi_0 \\ \gamma_0 \sin\phi_0 & \cos\phi_0 - \alpha_0 \sin\phi_0 \end{pmatrix} \begin{pmatrix} x_0 \\ x_0' \end{pmatrix}. \tag{1.36}$$

Transfer matrices for individual accelerator components can also be found; the effect of many elements in an accelerator lattice on particle motion can be determined by multiplying together the matrices relating to each element. However, it is usually unnecessary to complete this process for an entire accelerator ring. Usually, accelerators are designed with some periodicity, repeating sections of the lattice. The number of repeating sections within a larger lattice is known as the superperiodicity.

The simplest transfer matrix is that of a drift region, where no external forces act upon the beam as it passes through the beam pipe. In this simple case

$$M_{\text{drift}} = \begin{pmatrix} 1 & l \\ 0 & 1 \end{pmatrix}, \tag{1.37}$$

where l is the length of the drift region. For quadrupole magnets, the transfer matrices are instead given by

$$M_{\text{focusing}} = \begin{pmatrix} \cos\sqrt{|K|}l & \frac{1}{\sqrt{|K|}}\sin\sqrt{|K|}l \\ -\sqrt{|K|}\sin\sqrt{|K|}l & \cos\sqrt{|K|}l \end{pmatrix}, \quad \text{where} \quad K > 0,$$

and

$$M_{\text{defocusing}} = \begin{pmatrix} \cosh\sqrt{|K|}l & \frac{1}{\sqrt{|K|}}\sinh\sqrt{|K|}l \\ \sqrt{|K|}\sinh\sqrt{|K|}l & \cosh\sqrt{|K|}l \end{pmatrix}, \quad \text{where} \quad K < 0. \tag{1.38}$$

For the quadrupole matrices, the thin-lens approximation can be taken, assuming an infinitesimally thin magnet. Then

$$M_{\text{thin}} = \begin{pmatrix} 1 & 0 \\ -Kl & 1 \end{pmatrix} = \begin{pmatrix} 1 & 0 \\ -\frac{1}{f} & 1 \end{pmatrix}, \tag{1.39}$$

where f is the focal length of the quadrupole. This highlights the similarity between a quadrupole in accelerator design and a lens in linear optics. However, unlike an optical lens, a quadrupole which focuses in one transverse plane defocuses in the other, as $K_x = -K_y$. Due to this, a system of quadrupoles is required, with alternating magnets focusing in alternating planes. Such a system is described as a FODO lattice, with the F denoting a focusing quadrupole, the D a defocusing quadrupole and O a drift region.

Stable solutions

The phase advance in a section of accelerator lattice can be obtained from the matrix in Eqn. 1.36. From Eqn. 1.36, $\mathrm{Tr}(M) = 2\cos\phi$, where Tr refers to the trace of the matrix and ϕ is the phase advance around the ring. If $\mathrm{Tr}(M) > 2$ then only complex solutions for ϕ exist, and the lattice is described as unstable; there is no closed orbit on which the beam can circulate. In accelerator physics, the phase advance is often discussed in terms of the tune, Q, where $Q = \frac{\phi}{2\pi}$ so that the tune describes the number of betatron oscillations per accelerator period. Usually, the fractional tune (the non-integer part of the tune) is of greatest interest.

The fractional tune can be used to describe the motion of a particle in phase space. If at a given point in the ring of a circular accelerator x and x' are plotted for a single particle, the resulting diagram (a Poincaré plot) traces out the motion of the particle in phase space. The Poincaré plot will show an ellipse similar to that in Fig. 1.3. The orientation of the ellipse is described by the Twiss parameters at that location, and the area is given by the initial conditions of the particle. The particle moves around the ellipse at a rate governed by the fractional tune of the accelerator. For a fractional tune of zero, the particle would return to the same point in phase space after each revolution in a circular accelerator.

1.4.4 Resonance

The term resonance refers to the amplification of oscillations in a system when the ratio of the driving frequency to the natural frequency of the system is an integer. In accelerators, particles matching this condition can be driven to larger amplitudes and ultimately lost.

Accelerators are designed to avoid integer tunes, as particles would then meet the resonant condition for transverse dipole oscillations. However, as higher-order magnetic multipoles are capable of driving resonances at the natural frequency divided by m, simple fractional tunes are also avoided.

This resonant condition can be expressed as

$$kQ_x + lQ_y = n, \tag{1.40}$$

where k, l and n are integers, the driving term of the resonance is proportional to $x^k y^l$, and $k + l = m$ is the order of the resonance. Here, n is the Fourier component of the error exciting the resonance.

By combining Eqn. 1.16 and Eqn. 1.13, the Hamiltonian for an accelerator with arbitrary multipoles, considering the x direction for simplicity, is given by

$$\tilde{H} = \frac{1}{2}\tilde{p}_x^2 - \frac{e}{p}\Big(\frac{1}{m!}\Big)\Big(\frac{d^{m-1}B_y}{dx^{m-1}}\Big)_0 x^m. \tag{1.41}$$

A canonical transform and perturbation theory can then be used to study the effects of nonlinear resonances [21].

1.5 Space-charge effects in high-intensity beams

The work in this thesis is centred around understanding and mitigating space-charge effects which lead to particle loss in intense beams. In this section, I describe the impact of space-charge forces within an accelerator, which will be compared to the Paul trap case in Chapter 2.

1.5.1 Space-charge forces

In [8], Wilson uses a uniform beam of cylindrical cross-section to give an example of transverse space-charge forces. Using Gauss' law, the electrostatic field experienced by a test particle in the distribution, in its rest frame, is

$$\vec{E_r} = \frac{\rho}{2\epsilon_0}\vec{r}, \tag{1.42}$$

where ρ is the charge density within the cylinder.

Transforming this into the laboratory frame shows both electric and magnetic contributions to the space-charge forces, as the particles behave as parallel line currents. The fields acting on the test particle are then given by

$$\vec{E_r} = \frac{\rho}{2\epsilon_0}\vec{r} \quad \text{and} \quad \vec{B_\psi} = \frac{\rho v}{2\epsilon_0 c^2}\vec{r}. \tag{1.43}$$

The force on the particle then becomes

$$\vec{F} = e(\vec{E} + \vec{v} \times \vec{B}) = \frac{e\rho}{2\epsilon_0}(1-\beta^2)\vec{r} = \frac{e\rho\vec{r}}{2\epsilon_0\gamma^2}, \tag{1.44}$$

where e is the particle charge, $\beta = \frac{v}{c}$ and γ is the relativistic factor $\gamma = \frac{1}{\sqrt{1-\beta^2}}$. The space-charge forces acting on a given particle are inversely proportional to γ^2, indicating that space-charge forces decrease as the particle-energy increases.

In the regime where space-charge forces cannot be neglected, for example in lower-energy accelerators where many particles are accelerated, space charge adds an extra defocusing element to the accelerator lattice, counteracting the focusing effect of the quadrupoles. This extra defocusing force shifts the frequency at which particles in the accelerator oscillate transversely (the tune) to a lower value.

This depression in tune for a uniform distribution can be estimated, following the analysis in [22]. Particle motion, including the space-charge defocusing term, can now be expressed as

$$x'' + (K(s) + K_{\mathrm{SC}}(s))x = 0, \tag{1.45}$$

Here K_{SC} can be calculated from the expression describing the space-charge forces (Eqn. 1.44), as

$$x'' = \frac{d^2x}{ds^2} = \frac{1}{\beta^2c^2}\frac{d^2x}{dt^2} = \frac{\ddot{x}}{\beta^2c^2} = \frac{1}{\beta^2c^2}\frac{F_x}{m_0\gamma}, \tag{1.46}$$

for constant particle velocity, in the simplest approximation F_x can be taken as the defocusing force from a uniform cylinder of charge, as above.

The matrix describing a single turn of an accelerator is given by

$$M_0(s) = \begin{pmatrix} \cos\phi_0 + \alpha_0 \sin\phi_0 & \beta_0 \sin\phi_0 \\ \gamma_0 \sin\phi_0 & \cos\phi_0 - \alpha_0 \sin\phi_0 \end{pmatrix}, \tag{1.47}$$

where α_0, β_0, and γ_0 are the Twiss parameters. The equivalent description, with the addition of a small quadrupole error, is given by

$$M(s) = \begin{pmatrix} 1 & 0 \\ -\Delta K ds & 1 \end{pmatrix} M_0(s). \tag{1.48}$$

The tune of the ideal accelerator, Q_0, is given by $\mathrm{Tr}(M_0) = 2\cos(2\pi Q_0)$. For the same lattice, with the space-charge term treated as an error to the quadrupole focusing, the tune becomes Q, where $Q = Q_0 + \Delta Q$ and

$$\mathrm{Tr(M)} = 2\cos(2\pi Q_0) - \Delta K ds \beta_0 \sin(2\pi Q_0) = 2\cos(2\pi(Q_0 + \Delta Q)). \tag{1.49}$$

This gives a change in tune of

$$\Delta Q = \frac{1}{4\pi}\Delta K \beta_0 ds. \tag{1.50}$$

Integrating this expression around the ring gives the change in ring tune for a single particle as

$$\Delta Q = \frac{1}{4\pi}\int_0^{2\pi R} \Delta K \beta_0 ds, \tag{1.51}$$

where R is the radius of the ring. If a cylindrical uniform distribution of charge is again assumed, this gives a tune shift of

$$\Delta Q_x = -\frac{r_p N}{2\pi\epsilon_x \beta^2\gamma^3}, \tag{1.52}$$

where r_p is the classical particle radius ($r_p = q^2/(4\pi\epsilon_0 m_0 c^2)$), N the number of particles within the beam and ϵ_x the emittance in the horizontal direction. As expected this tune shift is proportional to the intensity.

1.5.2 Special 2D distributions

The space-charge forces felt by a given particle depend on the transverse distribution of the entire beam. In both simulation and the analytical calculation of space-charge effects, it is usual to assume a specific type of particle distribution, which is matched to the lattice (the envelope follows the focusing periodicity [23]). Three commonly used particle distributions are Kapchinskij-Vladimirskij (KV), waterbag, and Gaussian. A detailed definition of these distributions is given in the glossary [24].

KV distributions are often used in analytical descriptions of space charge, as the space-charge forces of a KV distribution are linear. For nonlinear beams, the distribution is described through its moments, and RMS quantities are considered. Beams are considered equivalent if they have the same first and second moments.

1.5.3 Coherent and incoherent motion

Eqn. 1.52 gives the tune depression from a KV distribution. However, realistic particle distributions are not uniform, giving space-charge forces which are no longer linear with respect

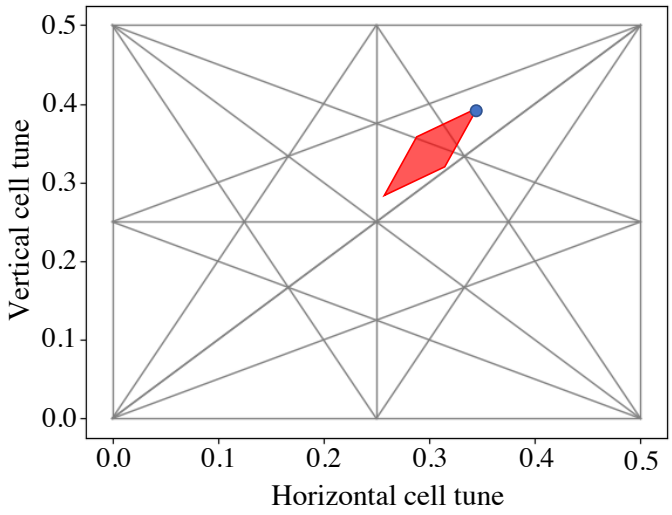


Figure 1.4: Diagram illustrating the effects of space-charge forces on particle tunes. Grey lines represent up to fourth-order resonances. The blue circle represents the tune footprint of beam without space charge and the red triangle is an example of the tune footprint with space-charge forces included.

to the radius of the distribution. This means that each particle experiences an amplitude-dependent tune shift. The distribution as a whole experiences both a tune depression and a tune spread. This is illustrated in Fig. 1.4 with a simple diagram.

In this case, it becomes important to distinguish between two different types of particle motion, the incoherent motion, which refers to the oscillation of a single particle within the distribution, and coherent oscillation, referring to the oscillation of the distribution as a whole. The frequency of coherent oscillation should not be confused with the RMS incoherent tune of a given beam.

Resonance and instability are the leading causes of beam loss in an intense beam. Following Hofmann, in [23], detailed definitions of the terms incoherent resonance, coherent resonance, coherent parametric instability, mismatch [25], and halo are given in the glossary. These terms are used to describe the mechanisms of particle loss throughout this thesis.

1.5.4 Images and impedance

The space-charge effects originating from the beam itself, as described so far, are referred to as self-field effects, resulting in "direct" space-charge effects. Direct space-charge effects will be the subject of the remainder of this thesis.

However, "indirect" space-charge effects are also possible; these result from the interaction of the beam with accelerator components, such as the beam pipe, magnets, and diagnostics. The beam pipe can lead to an incoherent tune spread through image charges, or indeed a coherent shift as a result of the betatron oscillations of the beam [22].

Longitudinal effects complicate the situation further. For a bunched beam, the charge density varies around the ring, which can lead to instability. As a particle performs longitudinal oscillations within a bunch it experiences a range of line densities, and therefore a range of tunes, which can result in repeated crossing of resonant stopbands.

Furthermore, any cavity-like object within the beam pipe can resonate if excited by a passing bunch. This results in EM wakefields created in the beampipe, which are in turn experienced by later bunches passing through the cavity. Such effects are characterised as impedance and are a source of longitudinal instability.

1.6 Mitigation of beam loss

A frequency spread can often be induced within an accelerator beam to help mitigate the effects of resonances. In this section, the mechanisms behind the stabilisation of the beam through a frequency spread are described. In Chapter 5, these terms are used to describe the effects of nonlinear integrable optics, a proposed new technique for the mitigation of beam loss due to resonances.

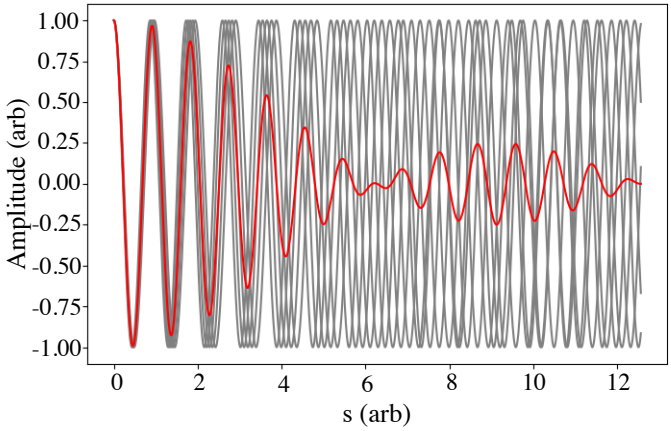


Figure 1.5: Illustration of the decoherence of a transversely oscillating beam. The grey curves show the motion of particles with an initial frequency spread, and the red curve shows the average motion of the beam.

Decoherence

Decoherence can be best understood by considering a distribution of particles, oscillating transversely, with a spread in their oscillating frequency and initial conditions $x(0) = 0$ and $\dot{x}(0) \neq 0$ [26]. As the particles oscillate at slightly different frequencies, the collective motion of the distribution is damped as the particles begin to oscillate out of time with one another. This is shown in Fig. 1.5, where five particles with a small frequency spread are allowed to oscillate after receiving a transverse kick.

Detuning

If the nonlinear fields are strong enough, the detuning of a subset of the particles is also achievable. In this situation, a subset of the particles in the distribution, whose incoherent frequency matches the frequency of an external driving force, are excited. However, the strong nonlinear fields create an amplitude-dependent tune spread large enough that the excited particles now oscillate at a slightly different frequency and are no longer driven by the resonance, increasing stability.

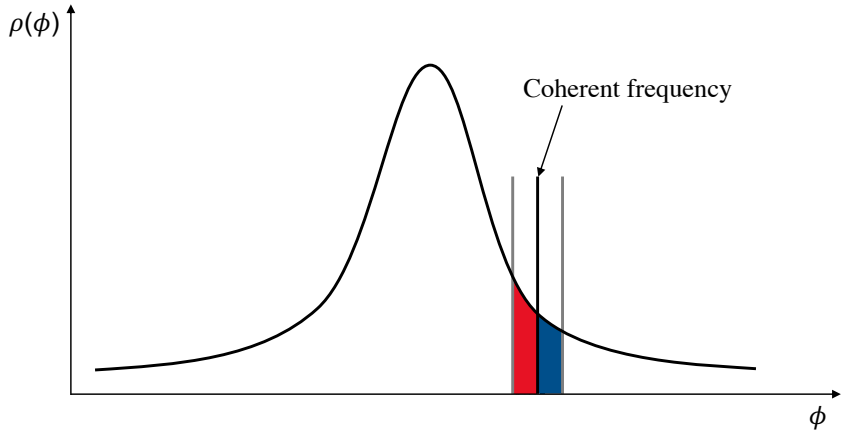


Figure 1.6: Illustration of the conditions for Landau damping. Red highlights the particles which will gain energy to match the coherent frequency and blue the particles which will lose energy.

Landau damping

Landau damping is defined as the transfer of energy from coherent to incoherent motion so that instabilities never form. However, describing Landau damping mathematically is a complex problem, and because of this, simulations are often used to verify predictions.

Following the introduction to Landau damping in [26], three conditions must be met for Landau damping to occur. Firstly, there must be an incoherent tune spread within the beam. Secondly, the frequency of the coherent mode of oscillation of the same particles must lie within this tune spread [27].

Finally, the coherent frequency of the distribution must lie on the downward slope of the spectral distribution of the particles, as shown in Fig. 1.6. In Fig. 1.6, particles highlighted in red have a frequency slightly lower than the coherent mode, so they gain energy to match the coherent frequency, moving to a larger amplitude where they oscillate at a higher frequency. For the particles in blue, the reverse process occurs. However, as there are more red particles than blue, energy is transferred from the coherent oscillation to the incoherent. For this mechanism to work, the particle distribution needs to have a greater density in the centre so that larger amplitudes correspond to greater frequencies.

A frequency spread is often created using octupole magnets. However, there are several

disadvantages to using external octupole fields to increase stability in this way. Firstly, there are often not many particles in the tails of the distribution, i.e. at large amplitude, which can mean that large octupole strengths are required. Strong octupoles introduce nonlinearities at large amplitudes, reducing the dynamic aperture and lifetime of the beam.

Furthermore, the octupoles can alter the chromaticity through feed-down effects to lower-order multipoles. In many accelerators, collimation is used to get rid of particles from the tails of the distribution. If the shape of the distribution is not well known, then a calculation of the impact of the octupole fields can be challenging.

1.7 The motivation for Paul traps

Particle accelerators are complex machines, designed to meet a large range of requirements for a broad range of applications. In the high-intensity regime, the dynamics of accelerators are complicated further by space-charge forces. Even for a linear lattice, realistic space-charge forces result in a coupling of the horizontal and vertical Hamiltonian, meaning that the equations describing the motion of particles in the system may no longer be solved analytically.

Most often, particle-tracking codes are employed to understand the dynamics of these accelerators. These simulations are often computationally intensive, making it difficult to study dynamics accurately over longer time scales. Furthermore, reference [28] shows that although benchmarked codes usually agree to within a few percent, discrepancies can be greater when considering detailed aspects of the beam behaviour. Additionally, there are known limitations associated with different methods of simulation. For example, in Particle-In-Cell (PIC) codes (see Section 2.6) many particles are required to provide good enough statistics to correctly represent phenomena such as halo formation and to reduce noise.

If the simulation involves tracking a beam over a short-enough distance ($\sim$ km), then fourth-order Runge-Kutta or similar high-accuracy integration methods can be used [28]. However, over larger distances the small errors present even in high-accuracy codes accumu-

late, leading to nonphysical results, and symplectic methods are required, which conserve the energy of the system[1] [30].

Intense beams can be studied experimentally, but the study of effects leading to particle loss can lead to activation and damage of the accelerator. Furthermore, accelerators have a fixed spatial structure; although the tune can be altered by changing magnet strengths, this is limited by the positioning of magnets and other components within the machine. Accelerators, therefore, have a limited operational range in both tune and intensity, meaning that only some of the parameter space can be studied using a single machine.

Instead, we use a linear Paul trap (LPT) to study accelerator physics. In an LPT, four cylindrical rods are used to create a time-varying electric quadrupole potential, which confines positively charged argon ions. The transverse dynamics in an LPT are equivalent to those within an accelerator with linear focusing.

An LPT is a compact experimental system, the size of a laboratory benchtop, with the addition of two racks of electronics. The trap is inexpensive compared to an accelerator and is relatively simple to use, requiring just a single operator. As ions are confined at an incredibly low energy ($\sim$0.1 eV), they can be lost from the trap without damaging the experiment and so no form of shielding is required. The system is incredibly flexible, different numbers of ions (corresponding to a range of intensities) can be stored, and any stable cell tune can be studied.

[1] A matrix is symplectic if $M^T J M = J = \begin{pmatrix} O & I \\ -I & O \end{pmatrix}$, where J is the Jacobian, O the zero matrix and I the identity matrix. A mapping from one point to another is symplectic if the Jacobian is everywhere symplectic [29].

1.8 Thesis outline

The structure of this thesis is as follows.

Chapter 2 introduces Paul traps as tools for accelerator physics, and the experimental setup of the IBEX Paul trap is outlined. In Chapter 3, the characterisation of the IBEX trap and experimental deduction of several key trap parameters are described. Chapter 4 presents a study of coherent resonances using the S-POD trap and Warp simulations.

In Chapter 5, the theory of nonlinear integrable optics (NIO) and quasi-integrable optics (QIO) is described, and the amplitude of the octupole voltage required to test quasi-integrable optics in IBEX calculated. Chapter 6 describes the design and experimental implementation of a T-insert lattice, a requirement for QIO. The nonlinear upgrade to the IBEX trap required to test QIO is described and Warp simulations of the IBEX QIO lattice are presented in Chapter 7. Conclusions and recommendations for further work are given in Chapter 8.

Chapter 2

Paul trap dynamics and experimental setup

In this chapter, I introduce linear Paul traps and explain how they can be used to answer a number of questions in accelerator physics. In Sections 2.2 and 2.3, a mathematical description of IBEX is given, explicitly showing the equivalence between transverse motion in a Paul trap and in an accelerator. In Section 2.4, I describe the experimental setup of the Intense Beam Experiment (IBEX), a linear Paul trap based at the Rutherford Appleton Laboratory (RAL), in Oxfordshire. The establishment of IBEX as a tool for accelerator physics forms the majority of the experimental work in this thesis. In Section 2.5, previous work in the field of accelerator physics using Paul traps is outlined, much of which this thesis builds upon. Finally, in Section 2.6, I describe the simulation tools that helped to both design experiments and interpret results.

This chapter provides the theoretical basis and detailed description of the experimental setup, but the detailed commissioning is reported in Chapter 3.

2.1 Introduction to Paul traps for accelerator physics

The parallel between alternating-gradient accelerators and ion traps extends back to the invention of the ion trap in the 1950s, and their inventor Wolfgang Paul [31]. After Paul started his career in molecular beam and particle accelerator physics in the 1950s, he later went on to win the Nobel prize in 1989 for "the development of the ion-trap technique"[32]. In his 1989 Nobel lecture, Paul compared the ion trap directly to a particle accelerator;

> "It employs not only the focusing and defocusing forces of a high-frequency electric quadrupole field acting on ions but also exploits the stability properties of their equations of motion in analogy to the principle of strong focusing for accelerators which had just been conceived. If one extends the rules of two-dimensional focusing to three dimensions one possesses all ingredients for particle traps."[33].

Since their invention, ion traps have been used in a wide range of applications, most notably in mass spectrometry, quantum computing, and for precision measurements. However, in most of these applications, only a small number of particles are trapped, extracted, and detected at any one time [34].

Linear Paul traps designed to confine large numbers of ions and to study accelerator physics questions were first proposed in 2001, by the Beam Physics group at Hiroshima University, Japan [35, 36], and at the Plasma Physics Laboratory, Princeton University, US [37]. Although the two groups went on to construct very different traps, the intention in both laboratories was to study the physics of beams dominated by space charge. The fundamental idea was to use a Paul trap to create an electrical quadrupole, confining a single species of low-energy ions (sometimes referred to as a non-neutral plasma). The transverse dynamics of ions in the Paul trap will then be equivalent to that of particles experiencing linear focusing in an accelerator, the trapped ions simulating particle motion in the accelerator rest frame. As the ions within the Paul trap move non-relativistically, the space-charge forces due to a number of particles in an accelerator can be replicated with a smaller number of ions.

The Princeton plasma physics laboratory designed and built a large Paul trap, creating

a column of caesium ions 2 m long and 0.01 m in radius, with the intention of moving to barium ions at a later date [38]. The inscribed radius of the trap was 0.1 m, and voltages of up to 400 V were applied to the rods of the trap, requiring a voltage oscillation frequency of ~ 60 kHz. The electrodes in the Princeton trap were four segments of a single cylinder, so the ion distribution was almost completely enclosed within the circular aperture.

The Beam Physics group at Hiroshima University instead proposed a much smaller trap, the Simulator for Particle Orbit Dynamics (S-POD) [39]. Ions were originally produced by ionising calcium atoms from an atomic oven, and later by ionising argon gas, introduced from a gas bottle into the vacuum vessel. When calcium ions are trapped, a laser system can be used to study the ions in real-time by exciting them into a higher-energy state and detecting the photons emitted as they decay. The Beam Physics group has used a number of Paul trap designs, tailored to study different aspects of beam physics. For example, calcium ions and a laser-cooling system are used to study very cold, crystalline beams [40]. There are currently three S-POD traps, each used in slightly different accelerator physics studies.

The latest version of the S-POD linear Paul trap used to study high-intensity beam physics is described in [41]. Argon ions are trapped by four cylindrical electrodes. The inscribed radius of the trap, r_0, is 5 mm and the radius of the rods, ρ, is 5.75 mm. These values are chosen to minimise higher-order components of the field, as $m = 6$ is minimised when $\rho/r_0 \approx 1.15$ [36]. Argon gas is chosen as it is inert, gaseous at room temperature, and has a charge-to-mass ratio which means it can be confined at a full range of cell tunes using radio frequency (rf) voltages of ~ 1 MHz and amplitudes smaller than 150 V.

The cylindrical rod structure is used as it makes it possible to ionise atoms in the region where they will be trapped, using an electron gun. The gun points vertically downwards into the trap so that electrons travel between the cylindrical electrodes. Cylindrical rods are also easy to manufacture with extreme precision ($\sim 10\,\mu$m), however, as they are not hyperbolic they will introduce some higher-order multipoles into the trap [42].

As a consequence of close collaboration between both the Hadron Beams group at the University of Oxford and the Intense Beams group at the Rutherford Appleton Laboratory

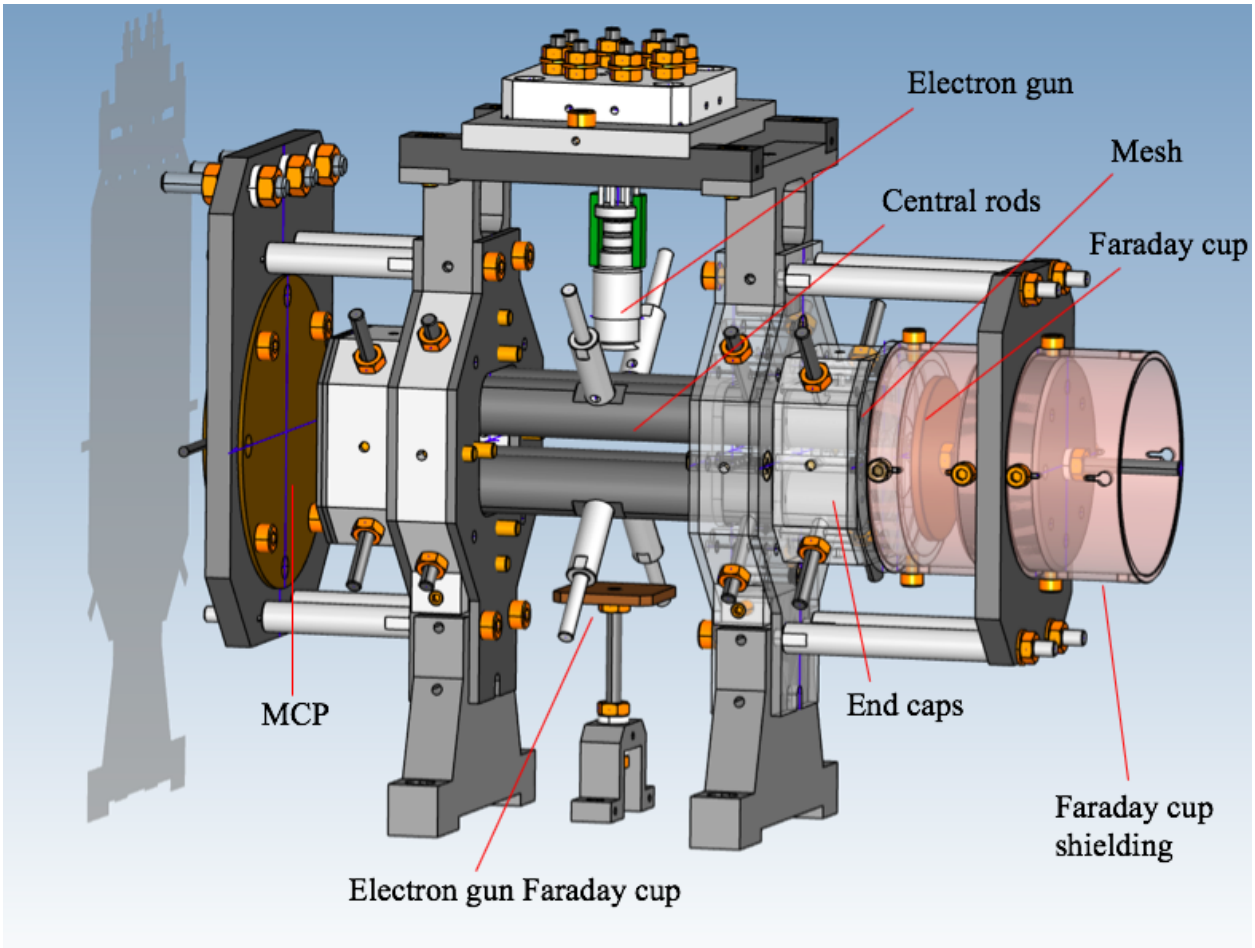


Figure 2.1: A CAD representation of the IBEX ion trap, where the trapping region is in the centre of the four cylindrical rods.

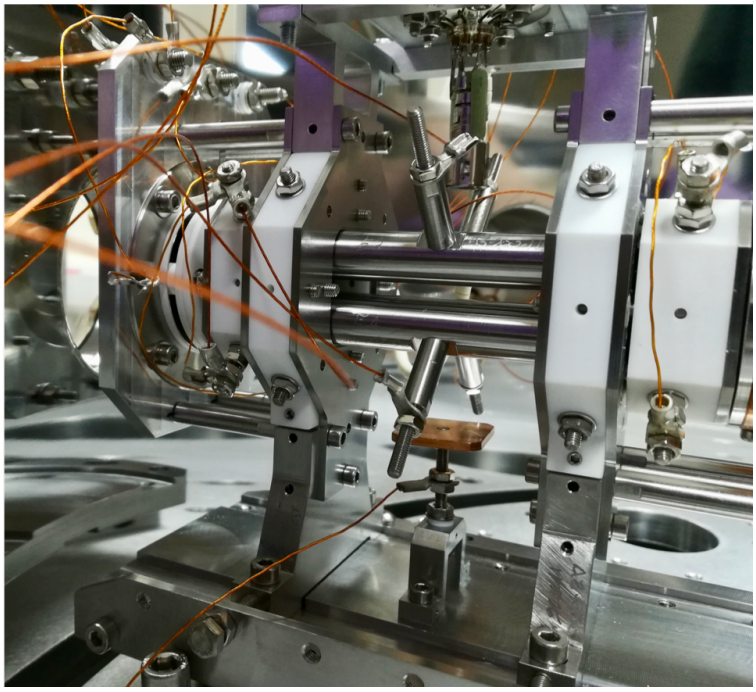


Figure 2.2: Photograph of the IBEX ion trap.

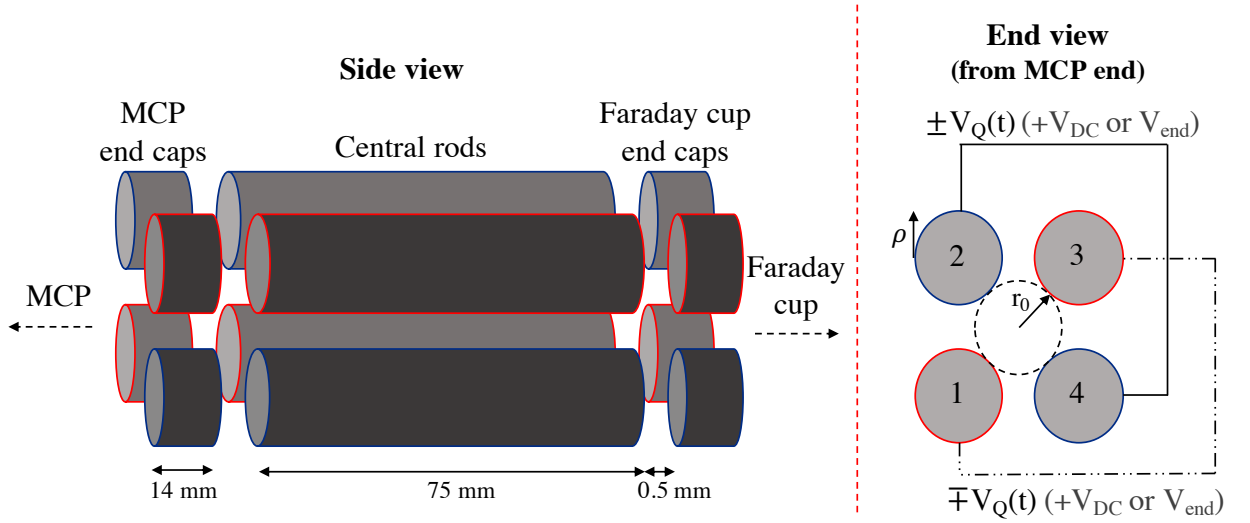


Figure 2.3: Diagram (not to scale) of the IBEX trapping region. In IBEX $r_0 = 5\,\text{mm}$ and $\rho = 5.75\,\text{mm}$. The IBEX trap must be rotated through 45 degrees to match the x and y axis in an accelerator.

(RAL), with the Beam Physics group at Hiroshima University, the Intense Beam Experiment (IBEX) linear Paul trap was constructed at RAL, beginning in 2015 [43]. IBEX has a very similar design to the S-POD traps, as described in Section 2.4, where the differences between IBEX and S-POD are also highlighted. A diagram and photograph of the IBEX trap are shown in Fig. 2.1 and Fig. 2.2 respectively.

2.2 Transverse dynamics in a Paul trap

Charged particles cannot be trapped with a static potential alone, as the potential must satisfy Laplace's equation, resulting in no minimum of the potential in which to confine particles [44]. A time-varying potential is therefore needed. To create linear focusing, a linear force in the transverse direction is required, such that $F = -kr$.

As $F = -\nabla U$, where U is the potential energy, an electric quadrupole field is required so that

$$U = \frac{V_{\text{rf}} q \cos(\omega_{\text{rf}} t)}{r_0^2}(\alpha x^2 + \beta y^2), \tag{2.1}$$

where r_0 is the radial distance from the axis to the rods, as shown in Fig. 2.3. To satisfy Laplace's equation, $\alpha + \beta = 0$.

The saddle potential, described in Eqn. 2.1, varies in time, creating a pseudopotential capable of confining ions. The motion of a particle within this potential is characterised by two frequencies. The first is the frequency of the micromotion of the particle, ω_{rf}, which is the same as the oscillation frequency of the voltage. However, the larger oscillations within the pseudopotential are characterised by a lower frequency, the tune.

This pseudopotential, created within a Paul trap, results in transverse ion motion which has the same characteristics as transverse motion in an accelerator, as the Hamiltonians of the two systems are equivalent.

2.2.1 Equivalence of the Paul trap Hamiltonian to the accelerator case

Following from Section 1.3, a non-relativistic charged particle moving in electromagnetic fields generated by the scalar potential ϕ and vector potential $\vec{A}$, obeys the Hamiltonian

$$H = \frac{(p - e\vec{A})^2}{2m} + e\phi. \tag{2.2}$$

In a Paul trap, only electric fields are used, so the $\vec{A}$ term can be dropped from the above expression. If only rf dipole and quadrupole fields are applied to the rods, the externally applied potential is expressed as

$$\phi(x, y; t) = V_D(t)\frac{x}{r_0} + V_Q(t)\frac{(x^2 - y^2)}{r_0^2}, \tag{2.3}$$

where V_D is the dipole potential and V_Q the quadrupole potential. For the case of a simple quadrupole trap, ignoring any axial motion, the Hamiltonian becomes

$$H_{\text{paul}} = \frac{(p_x^2 + p_y^2)}{2m} + qV_Q(t)\frac{(x^2 - y^2)}{r_0^2} + q\phi_{\text{sc}}, \tag{2.4}$$

where ϕ_{sc} is the potential due to space-charge forces and the charge on the ion is given by q, changed from e to agree with the literature.

Performing the change of scale:

$$\frac{H_{\text{paul}}}{mc^2} \rightarrow H_{\text{paul}}, \tag{2.5}$$

$$\frac{p_x}{mc} \rightarrow p_x, \tag{2.6}$$

$$\frac{p_y}{mc} \rightarrow p_y, \tag{2.7}$$

making the canonical momenta dimensionless, and changing the independent variable from time t, to length $\tau = ct$, gives the new Hamiltonian,

$$H_{\text{paul}} = \frac{(p_x^2 + p_y^2)}{2} + \frac{1}{2}K_{\text{p}}(\tau)(x^2 - y^2) + \frac{q}{mc^2}(\phi_{\text{sc}}). \tag{2.8}$$

Here,

$$K_{\text{p}}(\tau) = \frac{2qV_Q(\tau)}{mc^2 r_0^2}. \tag{2.9}$$

This can be compared to the Hamiltonian of an accelerated beam given in Eqn. 1.21, so that $K = K_{\text{p}}$ and

$$K = \frac{q}{p}\Big(\frac{\partial B_y}{\partial x}\Big)_0 = \frac{2qV_Q(\tau)}{mc^2 r_0^2}. \tag{2.10}$$

Throughout the rest of this thesis, the velocity, c, in the above scale change is taken to be the speed of light. In the standard operation of the LPT, the electrodes are excited sinusoidally, with $V_Q(\tau) = V_{\mathrm{rf}} \cos\left(\frac{2\pi\tau}{\lambda}\right)$. As a result of this, the wavelength of the rf voltage is much larger than the dimensions of the trap, on the order of hundreds of metres. Due to this scaling relation, traditional accelerator software, such as MAD-X [45], can also be used to design lattices for a Paul trap. However, the s length scale and beta-function size become on the order of hundreds of metres. This corresponds to an RMS beam size on the order of millimetres, where $\sigma = \sqrt{\beta\epsilon}$ can still be used to describe the size of the ion distribution.

2.2.2 Mathematical description of the ion distribution

Envelope equations for beams with a uniform charge density were first presented by Kapchinski and Vladimirsky [46]. This work was later extended by Sacherer, who showed that such equations are relevant for all distributions with elliptical symmetry, as RMS equivalent values can be used to describe the distribution [47]. Sacherer later derived the envelope equations for linear external focusing forces with the addition of space charge, showing that the envelope equation depends only on the linear part of the space-charge forces, provided the charge distribution has elliptical symmetry [48].

The envelope equations in a Paul trap can be derived from Hill's equations, which can be found from the Hamiltonian of a Paul trap in the same way as from the Hamiltonian of an accelerator, as the two are equivalent. As the focusing is linear, the transverse directions are not coupled, and the equation of motion in the x direction is,

$$\frac{d^2x}{d\tau^2} + K_{\mathrm{p}}(\tau)x + K_{\mathrm{sc}}x = 0, \tag{2.11}$$

where K_{sc} is the space-charge-dependent defocusing.

Following from the description in Section 1.4.2, the ansatz [47],

$$x = \omega_x(\tau)e^{i\phi_x(\tau)}, \tag{2.12}$$

is assumed, where $\omega_x(\tau)$ is a real function. The form of this solution can be interpreted physically, $e^{i\phi_x(\tau)}$ refers to the oscillation of a single ion and is dependent on the initial conditions of that ion [49]. The factor $\omega_x(\tau)$ describes the envelope in which these individual particles oscillate, which is independent of any particle initial conditions.

Writing $x = A\omega_x(\tau)\cos(\phi_x(\tau) + \phi_0)$, and substituting this solution back into Eqn. 2.11, gives

$$\begin{aligned} &A\left[\left(\frac{d^2\omega_x}{d\tau^2}\right) - \omega_x\left(\frac{d\phi_x}{d\tau}\right)^2 + K_{\mathrm{p}}\omega_x + K_{\mathrm{sc}}\omega_x\right]\cos(\phi_x(\tau) + \phi_0) \\ -&A\left[2\left(\frac{d\omega_x}{d\tau}\right)\left(\frac{d\phi_x}{d\tau}\right) + \omega_x\left(\frac{d^2\phi_x}{d\tau^2}\right)\right]\sin(\phi_x(\tau) + \phi_0) = 0. \end{aligned} \tag{2.13}$$

As sine and cosine are independent functions, for Eqn. 2.13 to be true for all τ, the terms in the square brackets in Eqn. 2.13 must separately equal zero.

The equation,

$$\frac{1}{\omega_x}\frac{d}{d\tau}(\omega_x^2\frac{d\phi_x}{d\tau}) = 2(\frac{d\omega_x}{d\tau})(\frac{d\phi_x}{d\tau}) + \omega_x(\frac{d^2\phi_x}{d\tau^2}) = 0, \tag{2.14}$$

gives the relationship $\frac{d\phi_x}{d\tau} = \frac{1}{\omega_x^2}$. Combining this with Eqn. 2.13 gives the envelope equation,

$$\frac{d^2\omega_x}{d\tau^2} - \frac{1}{\omega_x^3} + K_{\mathrm{p}}\omega_x + K_{\mathrm{sc}}\omega_x = 0. \tag{2.15}$$

Making the substitution $a = \omega_x\sqrt{\epsilon_x}$, where a is the RMS beam size, gives

$$\frac{d^2a}{d\tau^2} - \frac{\epsilon_x^2}{a^3} + K_{\mathrm{p}}a + K_{\mathrm{sc}}a = 0. \tag{2.16}$$

This derivation assumes that emittance is constant or that its time dependence is known.

Building on Section 1.5.1, K_{sc} is found by considering the ion distribution within the trap as a cylinder with Gaussian transverse distribution, with a standard deviation of a. Magnetic terms can be neglected as ions are travelling non-relativistically. Then the envelope is described by

$$\frac{d^2a}{d\tau^2} - \frac{\epsilon_x^2}{a^3} + K_{\mathrm{p}}a - \frac{N_L r_p}{(a+b)} = 0, \tag{2.17}$$

where N_L is the line density and b is the vertical beam size, $b = \omega_y\sqrt{\epsilon_y}$. A similar equation exists for the vertical direction.

Taking the smooth approximation (replacing the periodic focusing with continuous linear focusing with the same average focusing strength) and assuming $\epsilon_x = \epsilon_y$, so that $a = b$,

$$\frac{d^2a}{d\tau^2} - \frac{\epsilon_x^2}{a^3} + \kappa_{\mathrm{p}}^2 a - \frac{N_L r_p}{2a} = 0, \tag{2.18}$$

where κ_{p} is a constant which depends on the external focusing potential. Following the analysis in reference [36], and assuming that the ion distribution is stationary $(\frac{d^2a}{d\tau^2}) = 0$, Eqn. 2.18 can be rearranged to give

$$N_L = \frac{2a}{r_p}\left(\kappa_{\mathrm{p}}^2 a - \frac{\epsilon_x^2}{a^3}\right) = \frac{2}{r_p}\left(\left(\frac{\phi a}{\lambda_{\mathrm{rf}}}\right)^2 - \frac{\epsilon_x^2}{a^2}\right), \tag{2.19}$$

as κ_{p} is related through the phase advance, ϕ, to the wavelength of the rf voltage, λ_{rf} through $\phi = \kappa_{\mathrm{p}}\lambda_{\mathrm{rf}}$.

Again assuming a stationary plasma, the transverse temperature, T, is defined to be $K_B T = \langle p_x^2\rangle/m$, where K_B is the Boltzmann constant.

Finally, the plasma frequency is given by $\omega_p = \sqrt{n_I q^2/(m\epsilon_0)}$, where n_I is the number density of ions. The frequency is therefore location-dependent for non-uniform distributions.

References [50], [51], and [52] all explain how these parameters must be considered in the design of a Paul trap so that voltage waveforms that can easily be created using standard amplifiers can be used to confine enough ions to study space-charge physics. This mathematical description of the trapped ions will later be used in Chapter 4.

2.3 The Mathieu equations

In the ion-trap community, the Mathieu equations are used to describe the stability of a trap, or, to show which particles or molecules can be stored at a certain voltage and frequency [33, 53]. The mathematics is the same as previously described, but the terminology is slightly different.

The potential energy in the trapping region can be expressed as

$$U_{\mathrm{Tot}} = U_{\mathrm{end}} + U_{\mathrm{rf}} = -\frac{kqV_{\mathrm{end}}}{2z_0^2}(x^2 + y^2) + \frac{qV_Q(t)}{r_0^2}(x^2 - y^2), \tag{2.20}$$

where V_{end} is a DC voltage applied to the endcaps[1].

Choosing to work in the x direction, and using $F = -\nabla U_{\mathrm{Tot}}$, gives an equation of motion of

$$\ddot{x} = \frac{q}{mz_0^2}kV_{\mathrm{end}}x - \frac{2q}{mr_0^2}V_{\mathrm{rf}}\cos(\omega_{\mathrm{rf}}t)x. \tag{2.21}$$

Making the substitution

$$a_x' = -\frac{4qkV_{\mathrm{end}}}{m\omega_{\mathrm{rf}}^2 z_0^2}, \tag{2.22}$$

[1]When a DC offset is also applied to create unequal tunes, as in Section 4.8, an extra term, U, must be included here.

$$q'_x = -\frac{4qV_{\rm rf}}{m\omega_{\rm rf}^2 r_0^2}, \tag{2.23}$$

$$\tau = \frac{\omega_{\rm rf} t}{2}, \tag{2.24}$$

the equations then take the form of the canonical Mathieu equation,

$$\frac{d^2x}{d\tau^2} + (a'_x + 2q'_x cos(2\tau))x = 0. \tag{2.25}$$

Again, from the Floquet theorem [54] it follows that the Mathieu equation has a solution of the form $\omega_x(\tau)e^{i\phi_x(\tau)}$ where $\omega_x(\tau)$ is periodic and $\phi_x(\tau)$ depends on a' and q'.

Figure 2.4 shows the Mathieu stability diagram for different values of a' and q'. Using square voltage pulses instead of varying the voltage sinusoidally does not alter this diagram significantly [55]. In the case of S-POD and IBEX, the end-cap voltage can be neglected so that $a' = 0$ (when equal transverse focusing is used). Changing the amplitude of the voltage $V_{\rm rf}$ applied to the rods moves the trap along the q' axis of the diagram in Fig. 2.4. In mass spectrometry, a trap with shorter central regions is used, so the end-cap voltage can be used to ensure that only ions within a small range of masses are stored.

There is interest in using an LPT to study the second, much smaller, stability region (also shown in Fig. 2.4), for potential applications in FFAs [56].

2.4 The IBEX experimental setup

The IBEX Linear Paul Trap (LPT) consists primarily of 4 stainless-steel cylindrical rods with a 11.5 mm diameter. These rods are divided into three sections, the central rods (75 mm in length) which define the region in which ions are trapped, and the end caps, two shorter sections of cylindrical rod (14 mm in length) at either end, as shown in Fig. 2.3. Each end

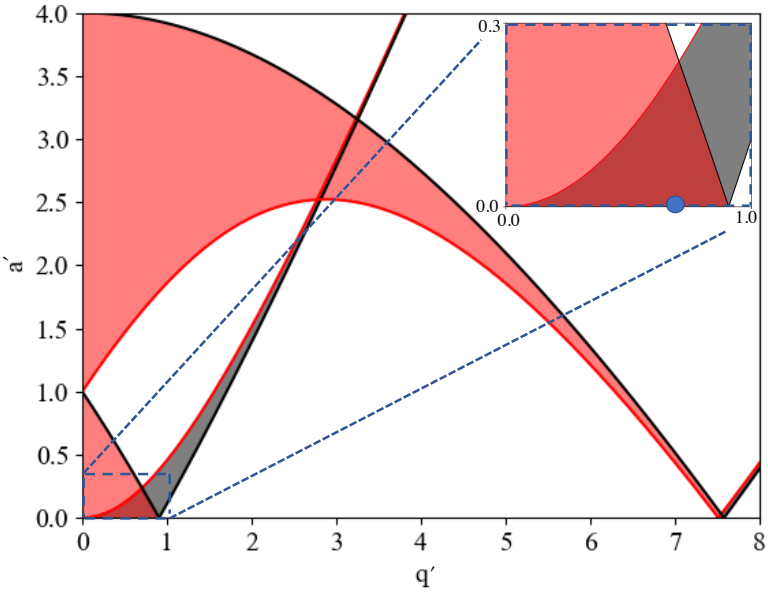


Figure 2.4: Stability diagram for the Mathieu equations. The stability region for the x direction is shown in grey, and the y in red. This plot is inverted about the line $a' = 0$. A Paul trap is only stable in the region where these two overlap. The inset shows an enlargement of the first stability region. The blue point represents trapping in the IBEX trap with $V_{\mathrm{rf}} = 68\,\mathrm{V}$.

cap is electrically isolated from the adjacent central rod by three ceramic spheres, placed to ensure the rods are correctly aligned. These dimensions were carefully chosen to ensure that ions could be confined using easily achievable voltages, and so that a sufficient charge density to study space-charge effects could be accumulated [51].

The IBEX experiment is a small-scale, single-room experiment, as shown in Fig. 2.5. It consists of the LPT itself, which is mounted in the base of a custom-built, multi-port, vacuum vessel, as well as two racks of electronics and a desktop computer. Argon gas is supplied from a gas cylinder. The IBEX vacuum vessel is significantly larger than the current trap and features several spare ports, allowing for future upgrades. Two of the ports contain vacuum-safe glass, one of which allows light to pass from a phosphor screen to a CCD camera, providing an image of the ion distribution.

The transverse-confining potential is created by applying an alternating voltage, $V_Q(t)$, to the cylindrical rods. The voltage applied is either a sinusoid or a square wave. The rf

trapping voltage is supplied using two synchronised channels from a Tabor 1074 Arbitrary Wavefunction Generator (AWG), created separately, with the rf components 180 degrees out of phase. These channels are then amplified independently using two Falco WMA300 amplifiers (supplying the end caps) and two custom-built amplifiers [57], supplying the central rods. The rods are powered in pairs, with opposing rods electrically connected. The IBEX trap is operated most often with a sinusoidal voltage of 1 MHz, and the transverse focusing is controlled by varying the amplitude of the applied voltage.

The amplifiers are connected to grounded feed-throughs on the vessel ports with BNC cables. On the inside of the vessel, the feed-throughs are connected to the rods using kapton coated, ultra-high-vacuum-safe wire.

The end caps also have the alternating trapping voltage $V_Q(t)$ applied to them, however, a positive DC offset (V_{end}) is added by an AWG before amplification. This creates a longitudinal potential well. As the end caps are short compared to the central rods, a rectangular potential is assumed, leading to a longitudinally homogeneous ion distribution.

The main difference between the IBEX and S-POD traps is that the S-POD traps contain two trapping regions, separated by a third set of end caps, known as the gate electrodes. Ions are accumulated in one trapping region and can at a later stage be transferred to the second [58].

Vacuum and ion creation

The IBEX vessel is held at the ultra-high vacuum of 10^{-10} mbar. To reach this vacuum level two pumps, an Edwards nXDS10i scroll pump and an Oerlikon Leybold vacuum Turbovac 450iX turbopump (attached to the base of the vessel), are used. The vessel is then baked out at $\sim 130^\circ$ (limited so as not to damage sensitive components) for 36 to 48 hours. Furthermore, all gaskets are made from copper, and the lid of the vessel uses a custom-made aluminium seal. When experiments are performed, argon gas is introduced to the entire vessel though a VAT Series 59 variable leak valve in the base, to pressures within the range

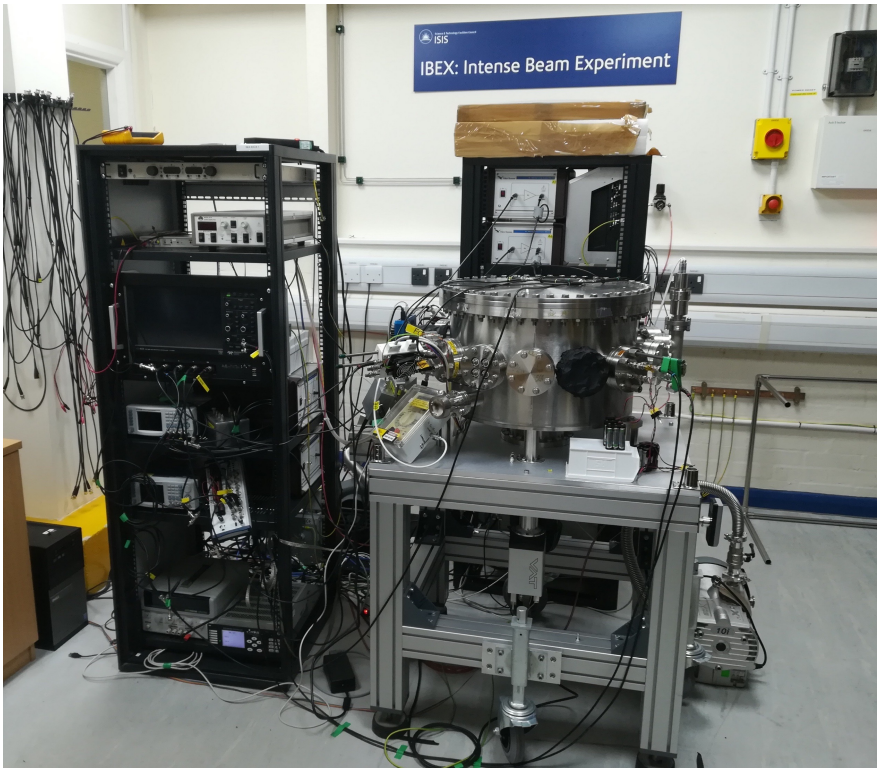


Figure 2.5: Photograph of the IBEX laboratory.

4.0×10^{-9} mbar to 2.9×10^{-7} mbar, with an accuracy of $\sim 1.0 \times 10^{-9}$ mbar. The VAT valve allows precise control of pressure, and room temperature is maintained constant to within $\pm 2°$ with air conditioning. A low-cost electron gun (from Tuoma, Japan) is used to ionise the argon gas in the trapping region, producing $^{40}Ar^{+}$ ions. The gun is expected to produce a current of between $10\,\mu$A and $100\,\mu$A depending on filament current and grid voltages. The number of ions produced is controlled by the length of time the electron gun is on, but is also pressure dependent.

Before the argon gas is introduced, the line supplying the gas is purged using a second Edwards nXDS10i scroll pump. This ensures that a higher purity of argon gas is introduced into the vessel. Any other ion species introduced into the trap will not be stored, due to the difference in charge to mass ratio, and will be lost over the argon accumulation period.

Vacuum is maintained for as long as possible between experiments, as once an electron gun has been used it cannot once again be exposed to air, and must be replaced if the vessel is opened. Using a thermionic gun in a custom setup requires a series of spot welds to correctly connect the power supplies, which is a difficult process that is avoided whenever

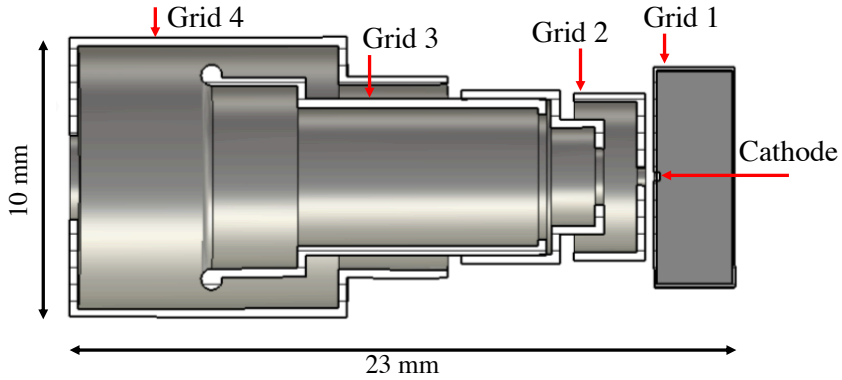


Figure 2.6: Diagram of the IBEX electron gun [60].

possible. Therefore, each time the electron gun is switched on it must be conditioned to extend its lifetime, which is achieved using a custom-built power supply [59]. The supply slowly increases the filament current applied to the electron gun over half an hour. The beam of electrons is switched on by applying voltages to two regions of the gun, grid 2 and grid 4 (see Fig. 2.6), where grid 2 accelerates electrons away from the filament and grid 4 both accelerates and focuses the electron beam [60].

The electron gun has previously been modelled in CST studio, by a former summer student, which allowed appropriate grid voltages to be found [60, 61]. An electron gun was then tested in a separate vacuum vessel, using a phosphor screen to establish the electron beam diameter as between 3 mm and 5 mm, depending on the settings used.

Ion number

It is helpful to estimate the number of ions produced in IBEX for a given electron-gun current. The ideal gas law,

$$PV = NK_BT \quad \text{or} \quad n_a = P/K_BT, \tag{2.26}$$

is used to describe the argon gas in the vessel, where n is the number density of argon atoms within the vessel, P is the gas pressure, T the temperature, and K_B Boltzmann's constant.

The number density of electrons in the beam produced by the electron gun, n_e, is estimated from the current, I, and cross sectional area, A, of the beam produced by the electron gun,

$$n_e = \frac{I}{Av_e q}, \tag{2.27}$$

where q is the electron charge and v_e, the electron velocity, which is estimated from the acceleration voltages applied to the electron gun.

Equation 2.28 gives the number of Argon ions (n_i) created per unit time, where σ is the cross section for the interaction, $\sigma = 2.33 \times 10^{-16}\text{cm}^2$ [62].

$$\frac{dn_i}{dt} = n_e n_a \langle \sigma v_e \rangle. \tag{2.28}$$

Such an estimation gives a rate of ion creation of $\sim 4.0 \times 10^8\,\text{s}^{-1}$. Not all of these ions are trapped, but this production rate is sufficient to trap between 10^3 and 10^7 ions, which is enough to study space-charge effects.

Ion detection

To extract ions from the trap, the DC end-cap voltage is removed from one end of the trap while the rf voltage is still applied. As the central rods are held at a slightly positive voltage, the ions are then extracted either towards a Faraday cup or a Micro Channel Plate (MCP), depending on from which end cap the DC voltage is removed. Both of these detectors are entirely destructive. A wire mesh located between the end caps and the detectors reduces the noise from the voltages applied to the rods and the fast switching of end caps but results in only 80% of the ions reaching the detector. A further Faraday cup sits under the trapping region, opposite the electron gun, for diagnostic purposes.

When ions are extracted onto the Faraday cup, the signal is amplified by a transimpedance amplifier of gain 2.80×10^6. The signal is then displayed and recorded using a high-definition

LeCroy oscilloscope. Similarly, ions extracted towards the MCP give either an integrated image of the ion distribution, which is captured by a CCD camera and saved, or an oscilloscope trace representing the current on the phosphor screen (again an amplifier, this time of gain 5.74×10^6, is used).

IBEX is automated by Labview controls (created by [63]) which perform a range of tasks, such as:

1. Using TTL signals to switch the electron gun on and off[2].
2. Sending waveforms to the AWGs.
3. Switching on the high-voltage supply to the MCP before ion extraction.
4. Removing the end-cap voltage to extract ions, with precise timing.
5. Reading and saving data from the oscilloscopes.

Waveforms for specific experiments are prepared in advance using a Python script [64]. The script creates CSV files which specify the number of AWG bits required to create the desired voltage.

MCP

The IBEX Micro Channel Plate is a two-stage Hamamatsu MCP with an effective diameter of 17 mm [65]. Ions are accelerated towards the MCP by a negative voltage applied to the front of the MCP (U_{in}) and the ion signal is amplified through the MCP by electron cascade, as illustrated in Fig. 2.7. The gain of the MCP is controlled by the voltage over the MCP, U_{MCP}, where $U_{\text{MCP}} = U_{\text{out}} - U_{\text{in}}$. Electrons leaving the MCP are accelerated towards a phosphor screen, currently a Hamamatsu P43 phosphor [66]. Electrons within the phosphor are excited and decay slowly, emitting photons. These photons are captured by an Alta F2000, grade S, CCD camera, with appropriate lens to focus on the phosphor screen [67].

[2] A TTL (Transistor-Transistor Logic) signal is used to switch between states based on whether a voltage is high or low. In IBEX a 5V TTL signal is used.

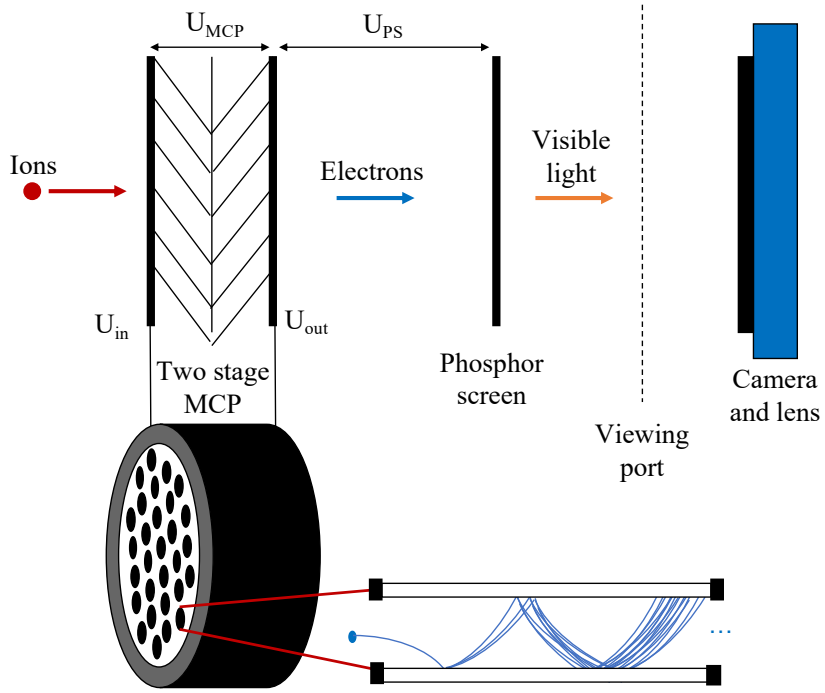


Figure 2.7: The IBEX MCP, phosphor screen and camera.

The MCP setup can be operated in two modes, "imaging mode" and "signal mode". In imaging mode, U_{in} is large and negative (∼-1300 V) and U_{out} is grounded. A positive voltage is applied to the phosphor screen so that electrons exiting the MCP are accelerated towards it. An image of the ions is created and captured by the CCD camera. In this setup, a current signal is not read directly from the phosphor screen, as additional electronics would be required to readout accurately while also applying a voltage.

However, in this thesis IBEX was operated most often in signal mode, with U_{in} ≈-1500 V and U_{out} ≈-300 V; these values are altered when a larger or smaller gain is required. The phosphor screen does not have a voltage applied to it. Instead, it is connected to an oscilloscope through an amplifier, allowing a signal proportional in size to the current on the phosphor screen to be saved. In this setup, two power supplies are used, a GLASSMAN high voltage supply, supplying U_{in}, and a Trek model 677B high voltage supply, supplying U_{out}.

The Trek power supply is operated in pulsed mode so that it supplies U_{out} for the shortest possible amount of time. This is necessary as the power supplies are connected through the capacitance of the MCP; if both power supplies are on for long periods this results in

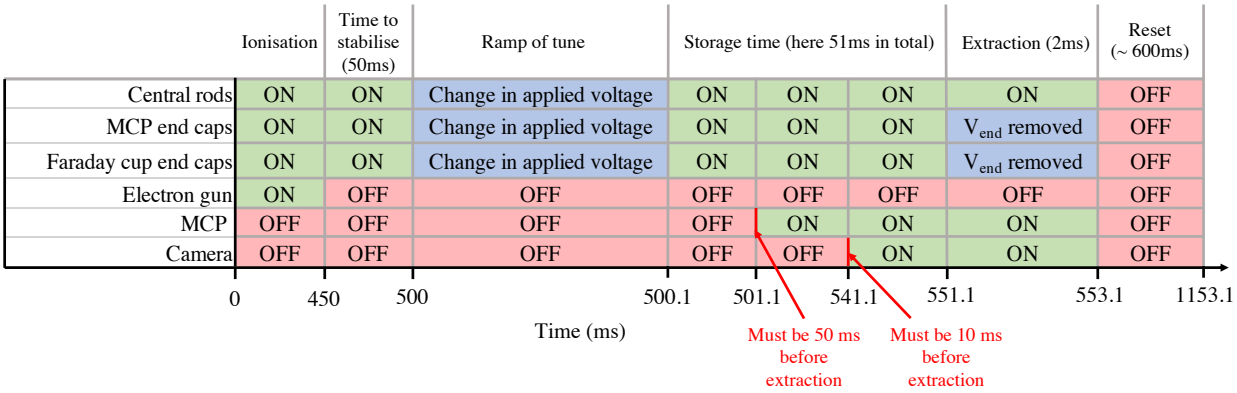


Figure 2.8: Typical timing structure of an IBEX experiment.

an incorrect value of U_{out} applied to the MCP. A small circuit was created by the ISIS Diagnostics group at RAL to allow the Trek power supply to be triggered by a rising TTL pulse, ensuring that in the event of an experiment stopping unexpectedly, $U_{\text{out}} = 0$, which will protect the MCP. The Trek power supply must be turned on 50 ms before the MCP is used to amplify an ion signal to ensure that the system is stable after the almost instantaneous increase in applied voltage. An example of the timing structure of an IBEX experiment where ions are extracted towards the MCP is shown in Fig. 2.8.

2.5 Previous Paul trap work

In this section, I will give a summary of previous work using Paul traps for accelerator physics, to highlight what has already been achieved and distinguish my original contribution.

In 2004 the Princeton plasma physics trap, known as the Paul Trap Simulator Experiment (PTSX) was first characterised, proving that the trap could confine ions without distorting the radial profile for significant fractions of a second [68]. A laser-induced fluorescence diagnostic system was then developed for a non-destructive measurement of beam profiles, using barium ions, with the intention of studying beam halo and filamentation [68]. However, such measurements proved to be experimentally difficult, the signal-to-noise ratio was degraded by background light scattered by the exciting laser, and there were difficulties acquiring data over long integration times (detector systems have an efficiency of $\sim 10^{-4}$) [69].

A detailed study into the compression of an ion distribution transversely was performed using the PTSX, where the period and strength of the applied voltage are changed both smoothly and instantaneously [69]. They found that for voltage changes of up to $\sim 50\%$ the transition could be considered adiabatic for as few as four rf periods. Furthermore, they found excellent agreement between experimental results and Warp simulations (see Section 2.6).

The effects of noise on an alternating focusing lattice were studied using the PTSX, by adding a small, random, noise component to the voltage applied to the trapping electrodes. Experimental observations showed that this noise led to an increase in transverse emittance and tails in the ion distribution [70, 71]. The emittance of the distribution was found to grow approximately linearly with the duration of the noise. The effect of coloured noise on artificially excited $m = 2$ collective oscillations was also investigated. Experimental results show coloured noise increased the emittance growth for these oscillations, suggesting that halo particles are ejected to a much larger amplitude [52].

The Beam Physics group at Hiroshima University have performed several studies using the S-POD trap for accelerator physics, also using the Warp code to simulate the experiment. Currently, argon is used to study space-charge physics; the available diagnostics are, as in IBEX, a Faraday cup and a MCP and phosphor screen. Therefore, experiments must be constructed so that the required information can be deduced from a measurement of the number of ions within the trap, or an integrated image of the distribution [72, 73].

At Hiroshima, integer resonances were excited within the trap and studied using the MCP and phosphor screen to image the distribution [58]. Resonance crossing was studied using the S-POD trap, simulating the parameters of the FFA, EMMA [74, 75]. Results agreed well with integer resonance crossing theory for a wide range of resonance strengths and crossing speeds, but when the crossing of multiple resonances was considered, it was found to be phase dependent. This experiment was the original basis of the collaboration between the intense beams group at RAL and Hiroshima University, which led to the construction of the IBEX trap.

Axial resonances have been excited in the S-POD trap by applying an additional rf voltage to the end caps [76]. The location of the axial resonances in tune space were also observed to shift with an increase in intensity. Furthermore, further work studying quadrupole noise, building on the study using the PTSX, was performed [77].

More recently, the S-POD trap has been adapted to measure the transverse dipole and quadrupole collective oscillations of the ion distribution [78]. Kicks were applied to excite the low-order oscillations, the perturbations were then removed, and the rods used to detect the image charges induced by the oscillating ions. The signal was electronically filtered and amplified to remove the frequency of the confining quadrupole field.

Several studies involving coherent resonances have been performed, which are discussed in detail in Section 4.2, as the work in Chapter 4 builds directly on these results.

Finally, the Beam Physics group has recently designed and built a multipole trap, which will be discussed in Chapter 7 [42], and has designed, and intends to construct, a short linear Paul trap which will allow space-charge effects in drift-tube linear accelerators to be studied [79].

In Chapter 3, I characterise the IBEX trap, as it is important that the experimental system is well understood. However, I do not repeat the accelerator-physics experiments performed on other traps; where results from previous experiments on S-POD or PTSX are assumed the relevant papers are referenced. Previously, Paul traps have mainly been used to study effects qualitatively. In this thesis, I build on this work to study resonant effects quantitatively and to create more complex lattices within the Paul trap, with a specific phase advance and beta function.

2.6 Simulations with Warp

The Particle-In-Cell (PIC) code Warp was originally designed to simulate space-charge-dominated ion beams for a range of applications [80]. Warp is written in Fortran and C,

with a Python interface, making it easy to adapt Warp simulations to use Python packages such as NumPy and Matplotlib to analyse and visualise data. Warp can be used to track the time evolution of particles in an accelerator, or in our case a Paul trap, by using macro-particles. Each macro-particle represents a number of real particles, and the charge of each macro-particle is weighted to reflect this. The macro-particles interact via their space-charge forces, and also with externally applied fields.

A uniform grid is used to implement the space-charge forces, with the charge density from the macro-particles interpolated onto the mesh. The electrostatic potential is then calculated and interpolated at the position of the macro-particles. The macro-particles then advance by a predefined time step, positions and velocities are updated based on the electric fields [81].

Warp has several features that make it useful when simulating a Paul trap. Metal conductors (in our case the four cylindrical IBEX rods) can be introduced, and a time-varying voltage applied to them. Particle scraping can be modelled on these conductors so that large-amplitude particles are lost [82]. A range of particle distributions can be introduced, and particles are easily tracked, with or without space-charge effects.

The Warp simulations presented in this thesis are adapted from a Warp xy slice simulation of a Paul trap equivalent accelerator lattice, initially written for S-POD at Hiroshima University. This code was written by one of the creators of Warp, S.M. Lund, and H. Sugimoto from the Beam Physics group at Hiroshima University. These simulations only include the 2D, transverse motion within the trap. The longitudinal motion is neglected to decrease computational time, as the thermal longitudinal motion within the Paul trap is much slower than any transverse oscillations, making it equivalent to a long coasting bunch with no longitudinal oscillations.

In Section 3.3, the longitudinal temperature in the IBEX is found to be $0.2846 \pm 0.0358\,\mathrm{eV}$. Using $v = \sqrt{\frac{T}{m}}$, where T is the temperature and v the particle speed, to approximate the time taken for an ion to travel from one end of the trap to the other, the end to end travel time is found to be greater than 100 rf periods.

The Warp release used in the simulations was from 21 Nov 2017, and simulations using Warp were run on the Oxford particle physics Linux batch farm, using scientific Linux release 6.10 and Python 2.7.

2.7 Chapter summary

In this chapter, I have explained how Paul traps can be used to study accelerator physics. Although there has always been a strong link between the fields of accelerator physics and ion trapping, the idea of using ion traps to study accelerator physics is relatively modern. This chapter showed that the transverse Hamiltonian in a linear Paul trap is equivalent to that of an accelerator, derived in Chapter 1. Mathematical descriptions from accelerator physics were used to describe the envelope motion of the ions within a Paul trap.

I have described in detail the experimental setup of the Intense Beam Experiment (IBEX), and the ways in which the ions can be detected as they leave the trap.

Both the S-POD and PTSX traps have previously been used to study accelerator physics. In this chapter, I gave a summary of their work. A range of interesting and useful accelerator-physics experiments have been performed, and strong agreement with the simulation code Warp shown. Due to this, we chose to use Warp in our simulations of the IBEX trap.

Chapter 3

IBEX characterisation

To use IBEX as a tool for accelerator physics, we must understand the Paul trap as well as possible. It is particularly important to understand any effects which may limit the validity of our experiments, or the analogy of the Paul trap to an accelerator.

The hardware of the IBEX linear Paul trap was first assembled in 2015, with the first ions successfully trapped in February 2017. During my DPhil, commencing in October 2016, I commissioned the IBEX Paul trap. This allowed us to perform a range of advanced experiments, as described in detail in Section 4.8 and Chapter 6. The later chapters of this thesis build on the understanding of the trap gained through the calibration and initial experiments described in this chapter.

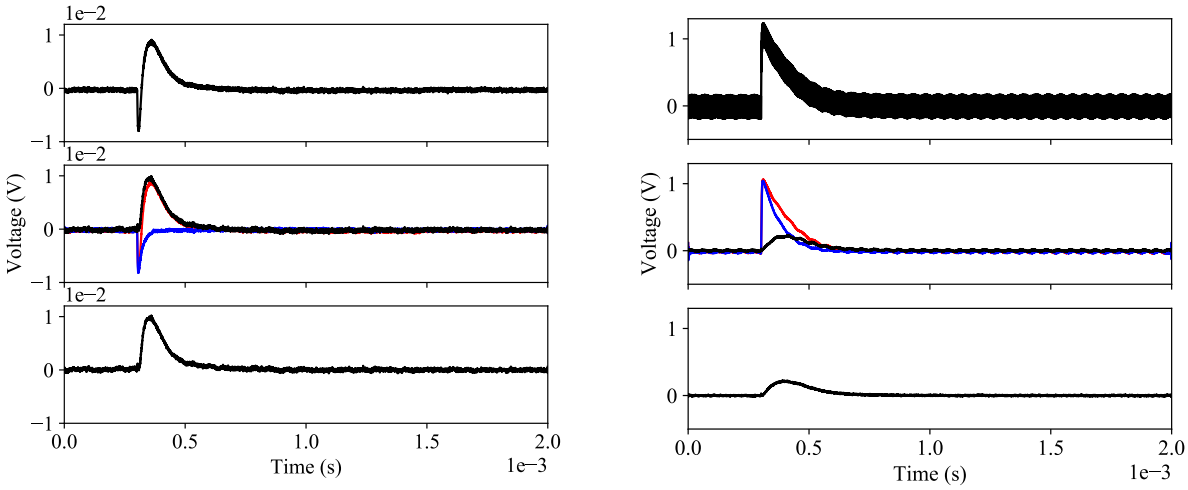
In this chapter, several key trap parameters are investigated: the ion number, ion lifetime, longitudinal temperature and the emittance. Firstly, as the Faraday cup is used to determine the number of ions within the trap accurately, in Section 3.1, I describe the process of noise reduction on the Faraday-cup signal. Section 3.2 presents a series of studies of the ion accumulation and lifetime within the trap. In Section 3.3, the longitudinal temperature of the ions within the trap is measured. The calibration of both the MCP and the voltages applied to the trap are described in sections 3.4.5 and 3.5, with Section 3.6 describing the determination of the upper limit of the emittance within the trap for small ion numbers.

3.1 The Faraday cup

All accelerator physics experiments conducted in an LPT require accurate knowledge of the number of ions stored, to determine whether space-charge effects are expected. During the first stages of commissioning, the Faraday cup was the only way to detect the number of ions extracted from the trap, as the MCP had not yet been installed. As the Faraday cup was later used to calibrate the MCP, details of which can be found in Section 3.4.5, the ability to extract an ion number accurately from a Faraday-cup signal was vital. In the initial stages of operation of the trap, large amounts of noise were observed on the signal from the Faraday cup (recorded using a high-precision oscilloscope). One source of this noise was ringing caused by the ramp down of the end-cap voltage, V_{end}, as a custom-made fast switch and DC power supply were initially used to apply this voltage. To reduce the ringing from the fast switching, the voltage V_{end} was instead applied via the AWG by adding it to $V_Q(t)$ before amplification.

Furthermore, there was a consistent noise at a frequency of $\sim$3 kHz on the Faraday-cup signal. Noise at this frequency was particularly problematic as the wavelength of the noise was comparable to the time taken to extract ions from the trap ($\sim$200 μs), making it hard to filter from the ion signal with hardware. The source of this noise was found to be the turbopump used to maintain the ultra-high vacuum. Vibrations created by the pump were affecting the transimpedence amplifier used to amplify the signal from the Faraday cup, which was connected externally directly to one of the vessel ports. Microphonics then led to noise on the electronic ion signal at harmonics of the revolution frequency of the turbopump (1 kHz).

Measures were taken to minimise this noise, such as installing anti-vibration feet on the vessel. In principle, it is possible to use an electrically floating wire to subtract the noise. A floating wire was installed in the vessel, wrapped around the wire connecting the transimpedence amplifier to the Faraday cup. The signal from the floating wire was amplified using a second transimpedence amplifier, with the intention of subtracting this second signal, containing only the noise, from the ion signal. However, the different capacitance in each



(a) Faraday cup.

(b) MCP.

Figure 3.1: Noise reduction on the signals from the Faraday cup and MCP. The top panel shows the initial oscilloscope trace. The middle panel shows, (in red) the trace with the 1 MHz filter applied, (in blue) the noise only signal with 1 MHz filter applied, and (in black) the subtraction of the noise from the signal. The bottom panel shows the signal with the periodic noise removed.

case, due to the termination of one wire on the Faraday cup, resulted in a different amplitude of noise so that a difference of the two signals could not be taken. Despite this, the installation of the floating wire significantly reduced the noise on the ion signal, potentially due to the damping of vibrations.

I removed the known frequencies of noise from the signal in post-processing (as continuing to experiment with real-time noise removal was not an efficient use of experimental time). As the noise was regular and sinusoidal, due to the rotation of the pump, by saving data over a larger time frame, the noise could be parameterised and removed using a Python script. In the same script, a bandpass filter was applied to remove the 1 MHz noise (and higher harmonics) expected from the 1 MHz rf voltage applied to the rods. The number of ions detected by the Faraday cup was then found from the integral of the Faraday-cup signal, as the gain of the amplifier is known.

Despite reducing the ringing, by ramping down the voltage offset V_{end} from the end caps more slowly, the sudden change in end-cap potential still resulted in a peak in the Faraday-cup signal. This was again removed in post-processing, by saving data from a run where no

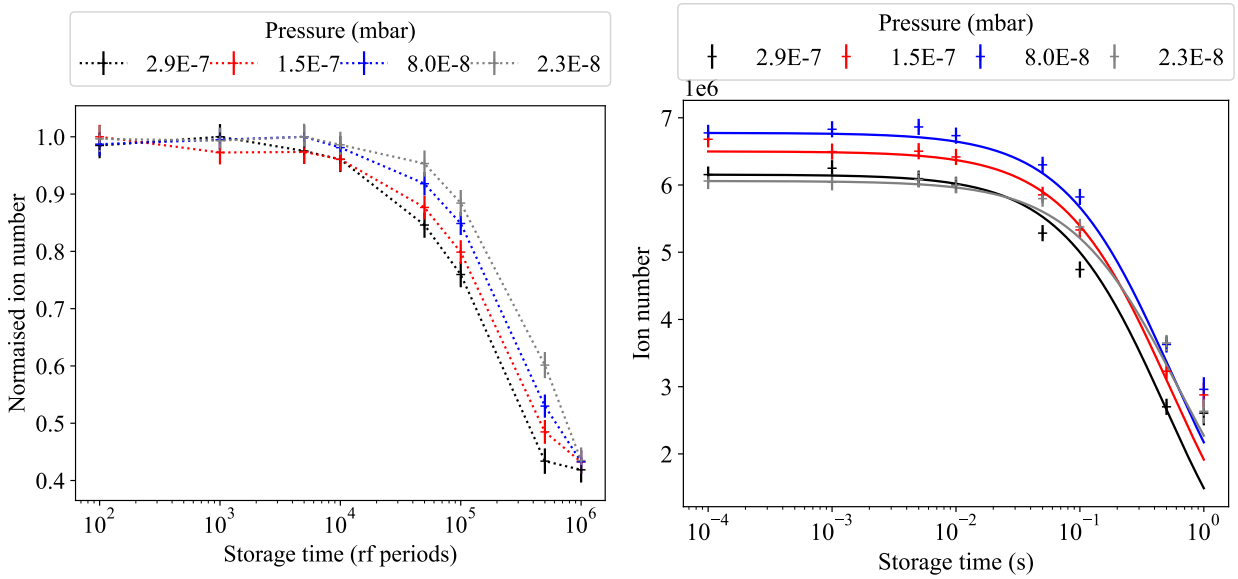
ions were stored and subtracting the integral of the noise-only peak. This process is shown in the central panel of Fig. 3.1. Note that the Faraday-cup signals have been inverted so that the ion signal is always positive.

All data presented in this thesis are averaged over a number of experiments. An example of tune scans taken at large ion number, using the Faraday cup to detect the number of ions extracted from the trap, is given in Appendix A.1. Each point in Fig. A.1 is averaged over five experiments; the data appears noisy when compared to Fig. 4.1 as the Faraday cup was used before the installation of the floating wire. These experimental results showed that the IBEX trap was working as expected and capable of producing data comparable to the S-POD trap, showing an intensity-dependent shift in the location of resonances in tune space.

3.2 Ion accumulation and lifetime

To change the number of ions accumulated in the IBEX trap, two methods can be used. Either the pressure of argon within the vessel (Eqn. 2.27) or the duration for which the electron gun is on can be varied. Changing the argon pressure has the disadvantage of affecting the lifetime of the ion distribution, due to ion collisions with the background gas. This section presents a series of short studies to understand ion accumulation and lifetime in IBEX.

There are several causes of ion loss that limit ion-trapping lifetime in a Paul trap, other than resonant excitation. During the period of ion accumulation, the electron gun is switched on, and an alternating voltage is applied to the confining rods. This results in the beam of electrons moving transversely within the trapping region [60]. Some of the ions produced in the ionisation of the argon gas will not be trapped, as they lie outside the stability region of the trap [83]. Additional ions will be lost if they possess a stable trajectory with an amplitude larger than the size of the trap, due to scraping on the central rods. In both of these cases, the ions will be lost over a short time scale (fewer than 100 rf periods).



(a) Normalised ion number.

(b) Ion loss model and data.

Figure 3.2: Ion number over a range of storage periods for four different argon pressures. Ions were stored at a cell tune of 0.15, each data point is averaged over 5 experiments and data was taken using the Faraday cup. In (a) the initial ion numbers are normalised for comparison, (b) shows the model for ion loss alongside the experimental data.

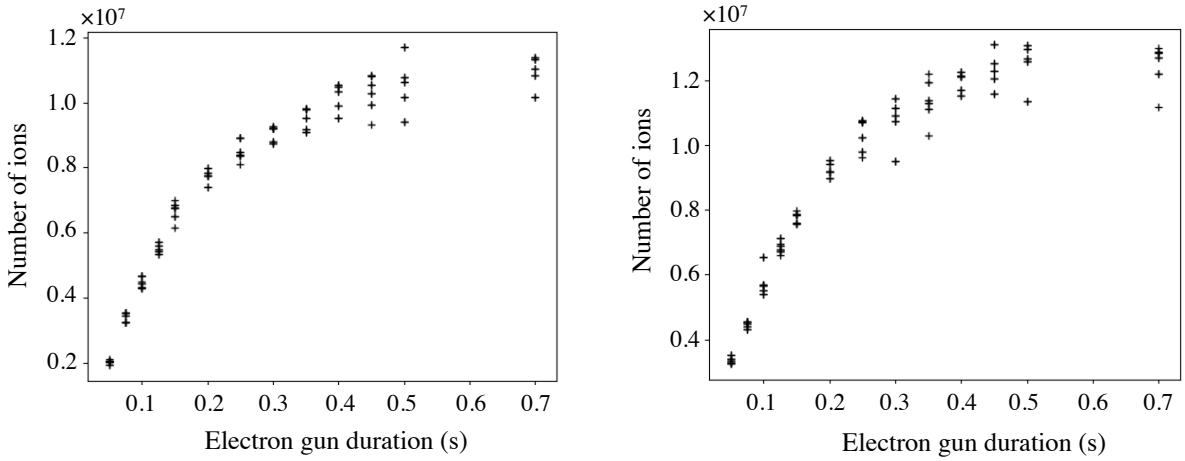
Furthermore, ions can be lost either due to interactions with neutral background argon atoms or with other ions. Collisions can result in damping, elastic scattering, and inelastic scattering. Due to a collision, the trajectory of an ion may become unstable, resulting in the ejection of the ion from the trap. The frequency of collisions of an ion with the background argon gas can be estimated using the equation

$$\nu_I = n_0 \sigma_s \sqrt{\frac{K_B T_I}{m_I}}, \tag{3.1}$$

where T_I and m_I are the temperature and mass of the ions, n_0 is the density of the background gas, and σ_s is the cross section for the collision [84]. Using $\sigma_s = 5 \times 10^{-15}\,\mathrm{cm}^{-2}$ [84], the collision frequency[1] for an ion with background gas is $\sim 1.3\,\mathrm{Hz}$ when the pressure in the vessel is $1.5{\times}10^{-7}\,\mathrm{mbar}$.

Figure 3.2 shows the reduction in the number of ions within the trap with increased storage time for four different pressures. I used the simple model

[1]The inverse of the mean free time between collisions.



(a) Argon pressure of 1.5×10^{-7} mbar.

(b) Argon pressure of 2.9×10^{-7} mbar.

Figure 3.3: The number of ions created within the trap, varying electron-gun duration at two different argon pressures. Data was taken using the Faraday cup and each point represents a different experiment.

$$\frac{dN}{dt} = -(k_2 N^2 + k_3 p N), \tag{3.2}$$

to describe the decay in the number of trapped ions, where N is the total number of ions within the trap, and p is the pressure in mbar [83]. This model assumes that all collisions lead to particle loss. The term including k_2 is due to ion-ion collisions, and the second term, including k_3, represents ion-neutral collisions. The ion loss is best described with $k_2 = 2.6 \times 10^{-7}$ and $k_3 = 2.2 \times 10^6$, as shown in Fig. 3.2b, where the discrepancy between the data and fit at storage times of 1 s may be due to the large signal-to-noise ratio of the Faraday cup for smaller ion numbers. Therefore, for a pressure of $1.5{\times}10^{-7}$ mbar and $4{\times}10^6$ trapped ions, the ion-ion collision rate dominates, as $k_2 N^2 > k_3 p N$. However, this will not be the case at smaller ion numbers. Our results agree well with data from similar Paul traps [52, 83].

From the data shown in Fig. 3.2, the rate of ion-neutral collisions which lead to ion loss, for a background gas pressure of $1.5{\times}10^{-7}$ mbar, is $\sim$0.33 Hz. This suggests that only a quarter of ion-neutral collisions lead to ion loss. By limiting experiments to on the order of 0.1 s, the effects of these collisions can be avoided.

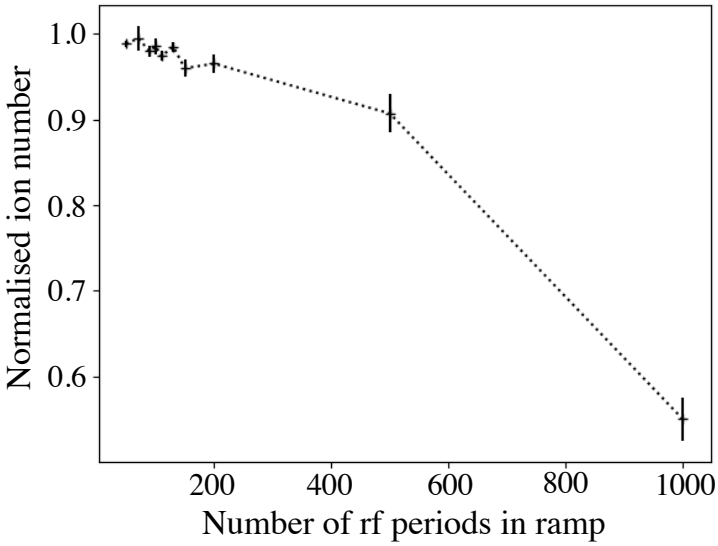


Figure 3.4: Ion number variation with ramping time between cell tune of 0.15 and 0.3.

Data was also taken to study ion accumulation for a range of electron-gun durations at a number of pressures, as shown in Fig. 3.3. The data shows that above $\sim 10^7$ ions there is a large variation in the number of ions produced for a given electron-gun duration, but for lower ion numbers the relationship between electron-gun duration and the number of ions produced is linear[2]. Therefore, the trap was operated with ion numbers below 10^7. The data in Fig. 3.3 was used to create specific numbers of ions by controlling the electron-gun time, as described in Section 4.8.

In experiments using the Paul trap, ions are often accumulated at a cell tune of 0.15, as the small beta function at this tune means that many ions can easily be trapped. In most experiments, the tune is then changed adiabatically to a different tune by slowly altering the amplitude of the voltage applied to the rods. Figure 3.4 shows the effect of the speed of tune ramping on ion loss, when the cell tune within the trap is changed between a cell tune of 0.15 and 0.3 by altering the amplitude of V_{rf}. Usually, 100 rf periods are used to alter the tune in S-POD. Figure 3.4 (and other similar studies) shows that no ion loss was observed for this ramping time, and so the same ramping time was adopted in IBEX. The ion loss over longer ramping times is due to the slow crossing of the resonance at a cell tune of 0.25.

[2]The large variation at ion numbers $> 10^7$ may be due to oscillatory self-emptying from the resonant excitation of some part of the beam at large space-charge tune shifts [83].

3.3 Temperature measurement

An accurate knowledge of the longitudinal temperature in the IBEX and S-POD Paul traps is desirable for several measurements (for example, the work in Chapter 4). If the temperature is known, the effective length of the ion distribution can be estimated using a model of the longitudinal potentials in the trap, which in turn gives an accurate representation of the line density.

In an LPT the longitudinal potential well is created by the voltage V_{end} applied to the two sets of end caps. As the central rods are significantly longer than the end caps, it is assumed that the potential well is almost rectangular and that the ion distribution is longitudinally homogeneous; this has been confirmed through simulation.

To measure the ion temperature, a number of experiments were performed, in which the confining voltage, V_{end}, applied to one set of end caps was slowly decreased. Any ions which escaped the potential were detected by the Faraday cup. To escape the trap, the ions must have had a longitudinal energy greater than the depth of the potential well. By recording the number of ions detected at each end-cap voltage, the energy distribution of the ions was reconstructed.

The ions in the trap are assumed to be in thermal equilibrium. Treating the ion distribution as a collisionless gas, the ions have a velocity distribution described by the Maxwell-Boltzmann distribution, and in each direction the velocity of the ions can be described by

$$f_v = \sqrt{\frac{m}{2\pi K_B T}} e^{\frac{-mv^2}{2K_B T}}, \tag{3.3}$$

where K_B is the Boltzmann constant, m the mass of the ions, T the temperature, and v the velocity. Starting from the three-dimensional momentum distribution of the ions, using the formula $E_{\text{tot}} = |\vec{p}|^2/2m$ to describe the kinetic energy of a particle, and applying the equipartition theorem, the energy in the longitudinal direction is found to be described by

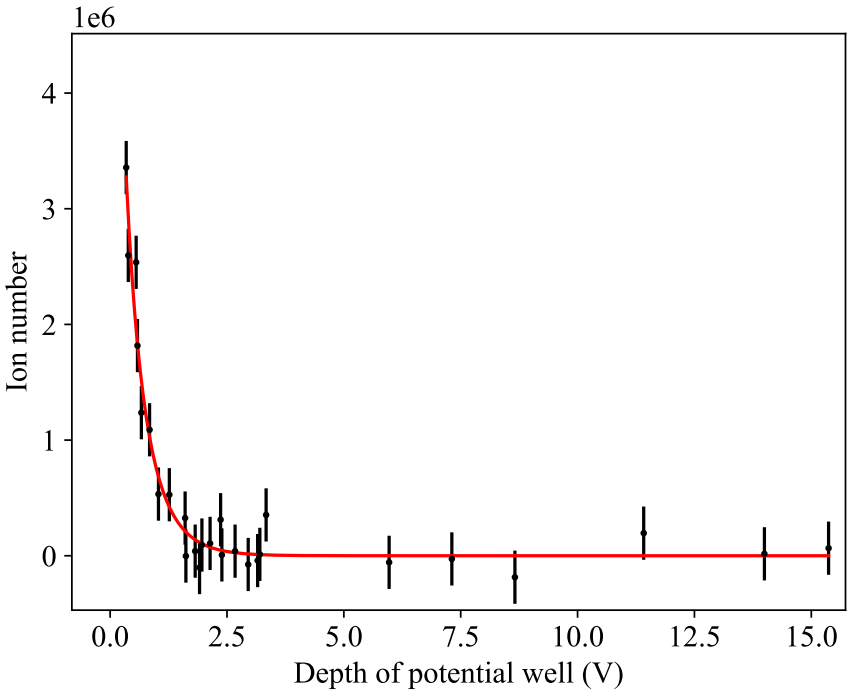


Figure 3.5: The number of ions extracted from the trap at different depths of the longitudinal potential well. The red line shows the fit to this data used to extract the temperature.

$$f_E = \sqrt{\frac{1}{E\pi K_B T}} e^{\frac{-E}{K_B T}}. \tag{3.4}$$

For this experiment, 4×10^6 ions were stored for 1000 rf periods at a cell tune of 0.15. The number of ions detected on the Faraday cup for a given height of the longitudinal potential well is shown in Fig. 3.5.

Fitting to the experimental data using the predicted distribution of ion energies in Eqn. 3.4 gives a longitudinal temperature of $0.285 \pm 0.036\,\text{eV}$, which is in good agreement with previous S-POD longitudinal temperature estimates of $\sim 0.3\,\text{eV}$ [72]. This close agreement is expected due to the similarity in trap design and electron gun between IBEX and S-POD.

To calculate the effective plasma length in S-POD and IBEX (which have the same longitudinal geometry, shown in Fig. 2.3), a 2D Mathematica model was used [85]. Assuming that the ions in the trap occupy a cylinder along the longitudinal axis, which ends where the depth of the potential well equals the temperature of the plasma, an effective length was

calculated. With the end-cap voltages used in experiments conducted on the S-POD trap, the length was found to be 65.50 ± 0.64 mm. This effective length is later used in Section 4.7 to produce numerical values describing high-intensity experiments in the S-POD LPT.

With an estimation of the effective length of the longitudinal distribution within the trap, it is possible to estimate quantities such as the Debye length [84],

$$\lambda_D = \sqrt{\frac{\epsilon_0 K_B T_I}{n_I q^2}}, \tag{3.5}$$

where n_I is the number of ions per unit volume. The Debye length represents the scale length of the shielding of a charged particle in the distribution. Using the calculated length of the trap, and typical emittance and temperature values (calculated in Section 4.7), for 4×10^6 ions the Debye length is ∼0.65 mm. As this is smaller than the transverse RMS size of the beam, collective effects are expected at this ion number [86].

3.4 MCP characterisation

Throughout this section, I will refer to the voltages applied to the MCP as first described in Section 2.4, where a diagram of the MCP can also be found.

Once the initial calibration of the trap was complete, the vessel was opened, and the MCP installed. The MCP allowed us to image the ion distribution, detect significantly smaller numbers of ions, and calibrate the trap more accurately. The MCP was required to accurately create more complex lattices within the trap, as described in Chapter 6. However, to use the MCP effectively it first had to be calibrated. The calibration of the system is described in the following sections.

3.4.1 CCD camera

To choose a suitable exposure time for the CCD camera, the duration of the light signal from the phosphor screen was estimated. Figure 3.6 shows an example of the time structure of a

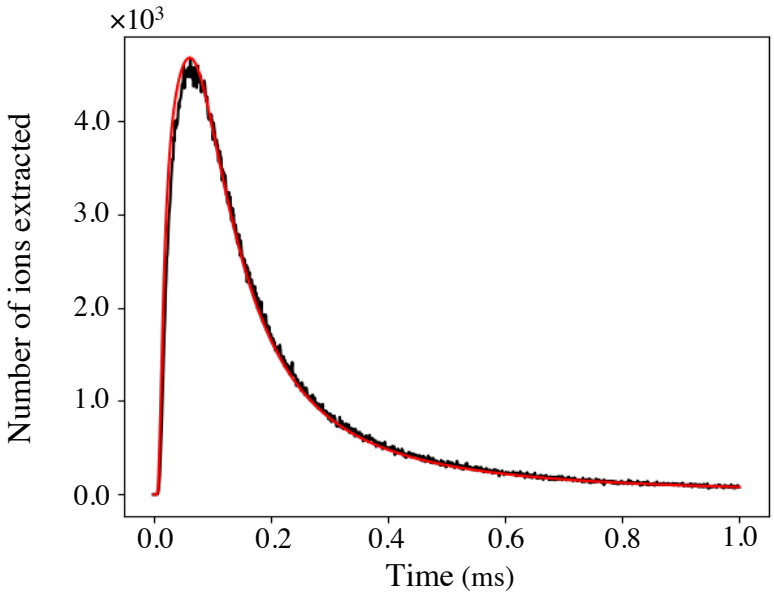
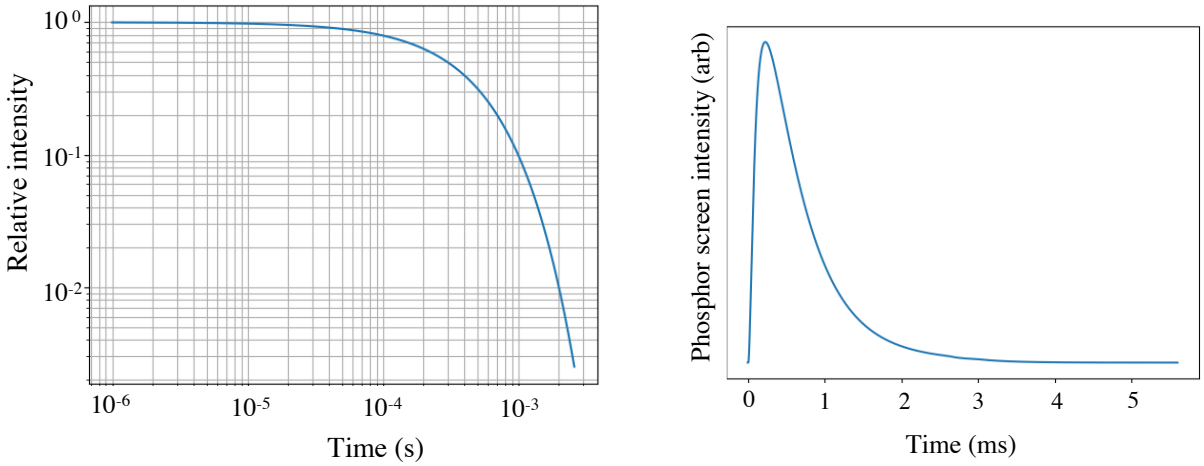


Figure 3.6: A histogram (black) of ion arrival times at the MCP produced by a simple Monte Carlo model where 10^6 particles were trapped in a cylinder of charge with a Gaussian transverse distribution and $U_{in} = -1825\,\mathrm{V}$. The red line shows the analytical description of this case, from the equation given in appendix A.2.

typical ion distribution leaving the trap, from both a simple Monte Carlo simulation and an analytical description of the trap. Further details on the assumptions made in this model can be found in Appendix A.2. The extraction time does not depend on the transverse focusing within the trap, only the longitudinal ion speed, therefore, the extraction time is dominated by the time taken for ions to move the length of the trap.

To calculate the expected duration of the light signal from the phosphor screen, several simplifying assumptions were taken. First, I assumed that the electron cascade through the MCP occurs almost instantaneously, and second, that the light of the signal from the phosphor screen decays exponentially according to the curve in Fig. 3.7a (using the 1 ms decay time to 10% of the original luminosity [66]). A convolution of the signals shown in Fig. 3.6 and Fig. 3.7a gives a prediction for the time duration of the light signal from the phosphor screen, shown in Fig. 3.7b. From this, the exposure time of the camera should be at least 4 ms to capture all light.

The minimum exposure time of the Alta F2000 camera is 20 ms, and due to the relatively



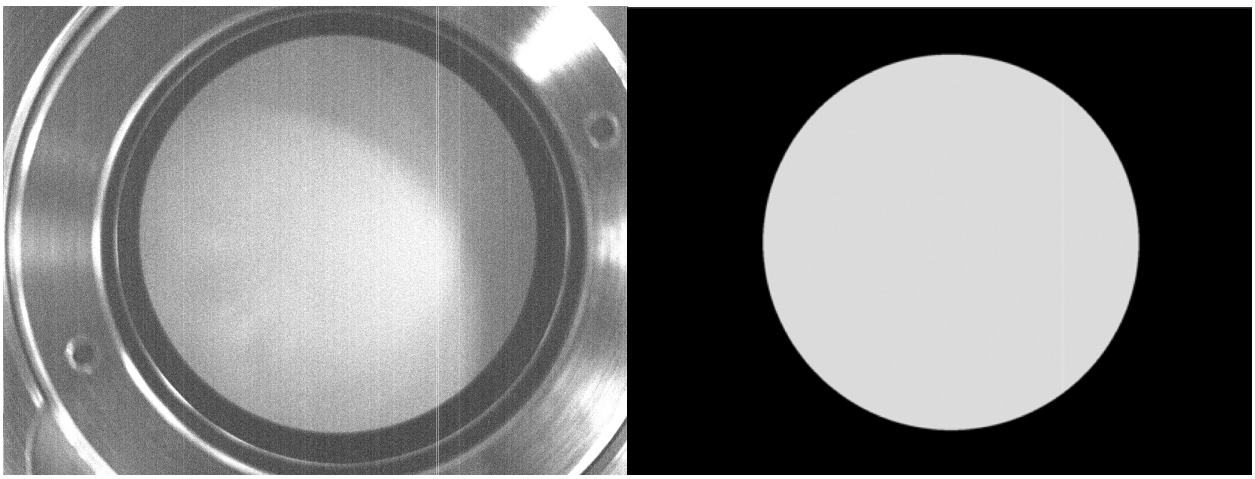
(a) Intensity from the P43 phosphor. (b) Expected intensity from the phosphor screen.

Figure 3.7: Predicted time structure of the light signal from the phosphor screen.

slow clock cycle of the camera, it must be triggered 10 ms before the ions are extracted from the trap [67]. The 20 ms exposure time ensures that all light is still captured. To reduce the noise on the camera, blackout material was used to protect the CCD camera and glass ports of the vessel from external sources of light, and the shortest CCD exposure time was used.

To process the images taken by the CCD camera, an analysis code was developed, adapted from a series of Python scripts written by a Masters student [87]. Three images are required, the first is an image of the phosphor screen taken with a 1 ms exposure time while light is introduced into the vessel from the second glass port; an example of this image is shown in Fig. 3.8a. A second calibration image is taken when all light has been blocked from the trap, the short exposure time of 20 ms is used, and no ions are trapped or extracted towards the MCP. The final image is taken under the same conditions as the second, but with ions stored and extracted from the trap towards the MCP.

A circular mask is created using the first image of the phosphor screen [88]. This is then applied to the other two images so that pixels outside the phosphor screen are automatically set to zero, as any signal from these pixels is by definition noise. An example mask is shown in Fig. 3.8b. The image of the phosphor screen containing no ion signal is then subtracted from the image containing the ion distribution, to remove any systematic noise due to the CCD camera. This leaves the ion signal with the addition of random background noise,



(a) Image of phosphor screen with 1 ms exposure.(b) Mask from the image of the phosphor screen.

Figure 3.8: Creation of the mask from the phosphor screen.

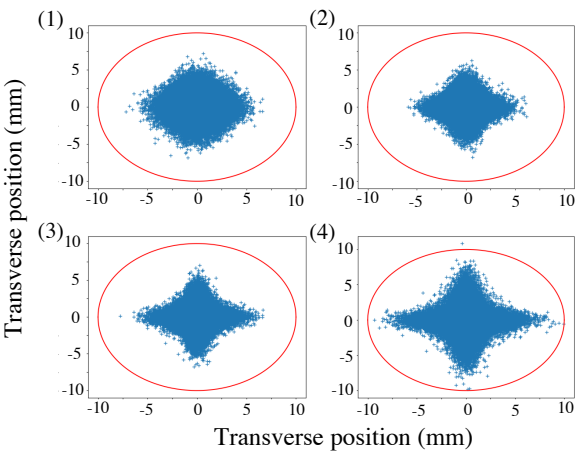
distributed about zero in each pixel. The resulting image is then rotated through 45 degrees to match the conventional x and y axis of an accelerator. Later, in Section 3.4.3, I will describe how an ion number is extracted from these images.

3.4.2 Monte Carlo simulation of transverse distribution

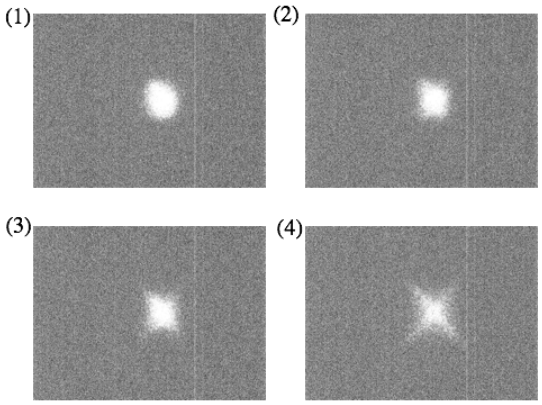
A simple Monte Carlo simulation was created in Python to confirm that the image of the ion distribution observed on the phosphor screen matched our expectations based on the dynamics within the trap.

A cylinder of 10^6 ions was assumed to be confined by the longitudinal potential well of the trap. Each ion was assigned a position and a longitudinal velocity assuming the temperature found in Section 3.3. Using a 2D Mathematica simulation, it was confirmed that the four confining rods and the mesh (located at the end of the trap) shield the ions within the trap from the large, negative, voltage U_{in} ($< -1500\,\text{V}$). Therefore, ions continue to move longitudinally within the trap with their initial velocity until they reach the end of the trap (at the end where $V_{\text{end}} = 0$).

When an ion reached the end of the trap in the simulation it was assigned a transverse position and momentum based on the Twiss parameters within the trap at that point in time. The Twiss parameters from a confining potential created by a 1 MHz sinusoidally



(a) Ion distribution from simulation.



(b) Ion distribution from the experiment.

Figure 3.9: A comparison between the expected image of the phosphor screen based on a simple Monte Carlo Model (a), and the image taken experimentally by the CCD camera (b). (1), (2), (3) and (4) show cell tunes of 0.1, 0.2, 0.3 and 0.4 respectively. Note: there is a 45 degree rotation between the axis of the trap and the model. The images in (b) are before processing. The red line in (a) shows the extent of the phosphor screen.

varying voltage were used. A Gaussian transverse distribution was assumed, as was the value of the emittance within the trap. Ions were then accelerated towards the MCP by U_{in} (it was assumed that this acceleration only affected the longitudinal velocity of the ion) and the transverse position of the ion at the MCP was saved. All space-charge forces were neglected in this simple simulation.

Figure 3.9 shows the output of this simulation at four different tunes, compared to the images of the ion distribution experimentally obtained at each of these tunes. The images in Fig. 3.9b have not been processed in any way. It is immediately apparent that the simulation results qualitatively match the experimental distributions, leading to a more pronounced cross shape at larger tunes.

Previously, it has been assumed that the projection of the ion distribution extracted from the CCD camera image onto the x or y axis can be approximated as a Gaussian distribution [87]. The simulations in Fig. 3.9 show that while this is a good approximation at a tune of $\sim$0.1, it is not a good approximation at larger tunes. Furthermore, as the potential difference between the trap and the Faraday cup is much smaller than the potential difference between the MCP and the end of the trap (U_{in}), the ions are extracted towards the Faraday cup with

much lower longitudinal acceleration. This means that for larger cell tunes, not all ions are collected by the Faraday cup due to the increased divergence of ions (as shown in Fig. 4.3). For this reason, the calibration of the MCP against the Faraday cup was performed at a cell tune of 0.15. However, very low cell tunes should also be avoided due to the increase in the average size of the beta function.

3.4.3 Relationship between ion number and luminosity

The gain of the MCP is controlled by U_{MCP} (where $U_{\mathrm{MCP}} = U_{\mathrm{out}} - U_{\mathrm{in}}$), however, altering U_{in} changes the detection efficiency of the MCP. Changing U_{PS} (the potential between the MCP and the phosphor screen, see Fig. 2.7) will alter the acceleration experienced by the electrons travelling between the MCP and the phosphor screen, and therefore the luminosity and size of the distribution imaged by the phosphor screen. However, altering U_{PS} should not impact the integral of the signal when the phosphor screen is used in signal mode, as all electrons will still hit the phosphor screen.

Following the MCP calibration procedure described in reference [72], the relationship between the number of electrons leaving the MCP and the integrated luminosity of the image on the phosphor screen was determined. Data was taken with the phosphor screen in signal mode, as described in Section 2.4, and at a cell tune of 0.15.

To extract the integrated luminosity from the image of the phosphor screen, the post-processing of the image described in Section 3.4.1 was first performed. Any pixels which contained a negative value (due to the subtraction of the noise) were then set to zero as negative values are unphysical. A projection of the signal onto the x and y axis was taken. As all negative pixel values were removed, the remaining histogram had a transverse extent determined by the diameter of the mask applied to the image. The histogram contained both the ion signal and the random noise not excluded by setting negative values to zero. As the experiment was performed at a low ion number, the ion signal was assumed to be Gaussian. Therefore, the projection onto the transverse axis was fitted by the sum of a Gaussian distribution and a semi-circle of known radius (to fit to and subtract the background). Both

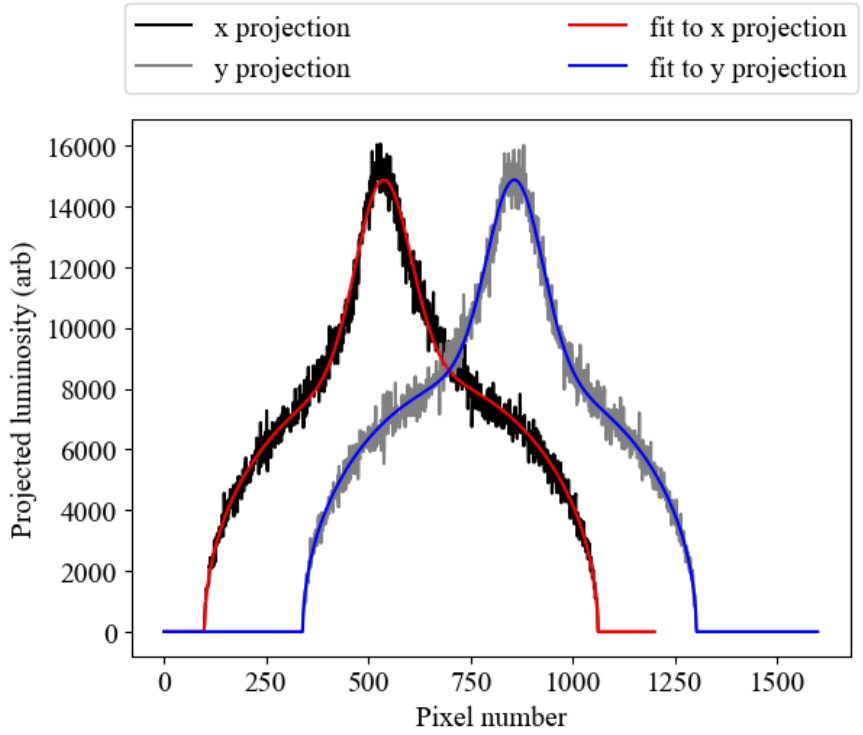


Figure 3.10: An example of the projection of the CCD image onto the x and y axis at a cell tune of 0.15, and the fitting process used to extract the luminosity.

the x and y projections were fitted simultaneously to increase the accuracy of the fit, as the amplitude of the noise should be the same in each case. An example of this fitting process is shown in Fig. 3.10.

For two different values of U_{PS}, U_{in} was altered for a fixed number of ions hitting the MCP, changing the gain and therefore the number of electrons leaving the MCP. The results of this experiment are shown in Fig. 3.11, where error bars are larger at low electron numbers due to the low luminosity of the image on the phosphor screen. There is a linear relationship between integrated luminosity and the number of electrons detected, showing that the phosphor screen has not saturated for these current densities [89].

3.4.4 Saturation of the MCP

It is well known that MCPs saturate due to space-charge effects when large numbers of electrons pass through the channels [72]. This may result in a nonlinear relationship between the number of electrons detected by the phosphor screen and the number of ions extracted

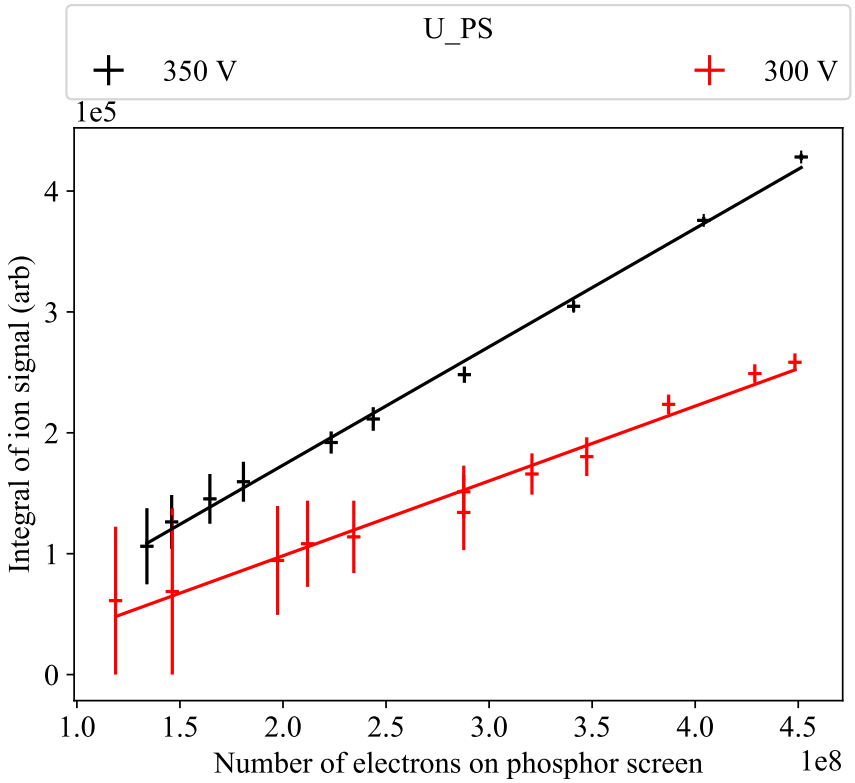


Figure 3.11: Comparison of the number of electrons collected by the phosphor screen to the integrated luminosity of the signal, with a linear fit applied to the data. The two lines show the change in sensitivity with the change in U_{PS}.

from the trap. However, I found experimentally that the amplifier used to amplify the signal from the phosphor screen saturates at a current of 400 nA. For currents, and therefore electron numbers, below this limit, the relationship between the number of electrons detected on the phosphor screen and the number of ions detected on the Faraday cup is linear (as shown in Fig. 3.12). This shows that the amplifier saturates before the MCP. As long as the experiment is operated in a regime where the signal from the amplifier is not saturated, there is no non-linearity.

Running the MCP in imaging mode, it may be desirable to operate in a regime where the central part of the MCP is saturated, for example, to produce a higher luminosity image and study the tails of a distribution in detail. In such a case the image luminosity would need to be corrected in post-processing, as described in [72]. However, IBEX is not currently equipped to apply a voltage to the phosphor screen while also reading out an electron signal. As a result of this, the saturation factor describing the MCP cannot accurately be determined, and the MCP must be operated in the regime where there is no saturation.

3.4.5 Calibration against Faraday cup

To find the gain of the MCP, the MCP was calibrated against the Faraday cup. As the Faraday cup is only capable of detecting ions accurately above $\sim 1\times10^6$ ions, the calibration was initially performed using ion numbers in the range 1×10^6 to 8×10^6. At constant pressure, the duration of the electron gun was varied to produce ion numbers in this range and the voltages applied to the MCP were not changed during the calibration. For the calibration measurement, only a small gain across the MCP was required, with $U_{\text{in}} = -1500\,\text{V}$ and $U_{\text{out}} = -620\,\text{V}$ (again operating in signal mode).

Ions were extracted first towards the Faraday cup and then the MCP (in a second experiment). The number of ions detected on the Faraday cup and the number of electrons detected by the phosphor screen were recorded and are shown in Fig. 3.12. By applying a linear fit to this data, it was possible to convert from the number of electrons detected on the phosphor screen to the number of ions extracted from the trap for these MCP settings,

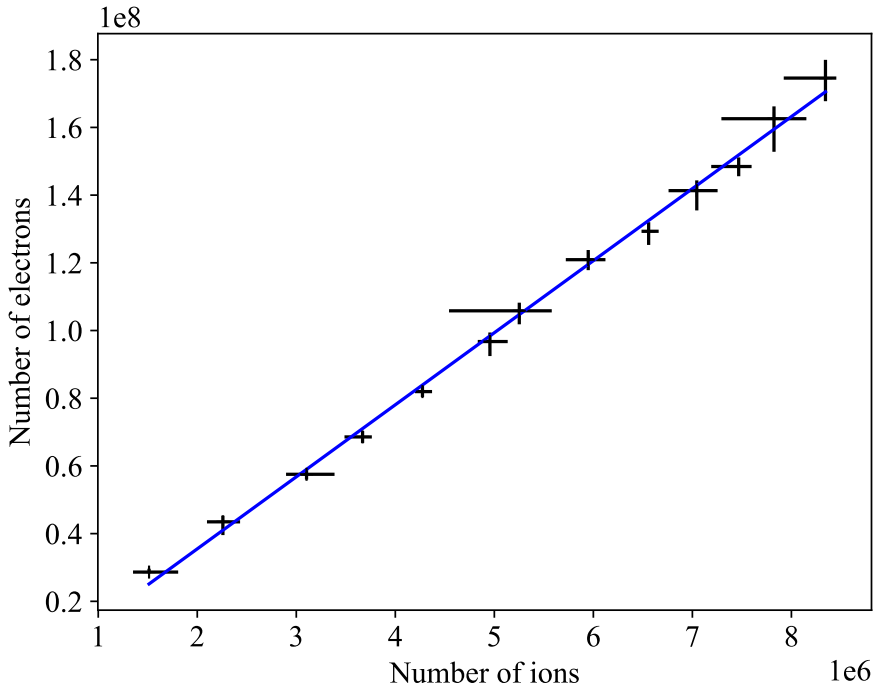


Figure 3.12: Comparison of the number of electrons collected by the phosphor screen with the number of ions collected by the Faraday cup. Each black cross represents the average of ten data points, error bars represent the range of the data taken. Here $U_{\mathrm{MCP}} = 880\,\mathrm{V}$.

giving a value for the gain of the MCP at this value of U_{MCP}.

When calculating the gain for larger values of U_{MCP}, smaller ion numbers were studied to avoid saturation of the amplifier. The ion number was controlled using both the argon pressure and the electron-gun duration. U_{in} was held at a constant value and U_{out} was varied to change the gain. As the number of electrons collected by the phosphor screen was used for this calibration, the variation in U_{PS} was unimportant. U_{PS} was large enough that all electrons were collected. Initially, $\sim 2\times10^{6}$ ions were stored and detected using the MCP in signal mode, with the MCP set at the voltages used to produce Fig. 3.12. The potential across the MCP, U_{MCP}, was then increased, increasing the gain. The gain for this new value of U_{MCP} was found by comparing the number of electrons detected to the initial value. This process was repeated for a range of U_{MCP} values, decreasing the number of ions stored each time.

The values of the gain for each U_{MCP} are shown in Fig. 3.13. These values are for voltages below those reported graphically in the Hamamatsu MCP data sheet [66]. The data were

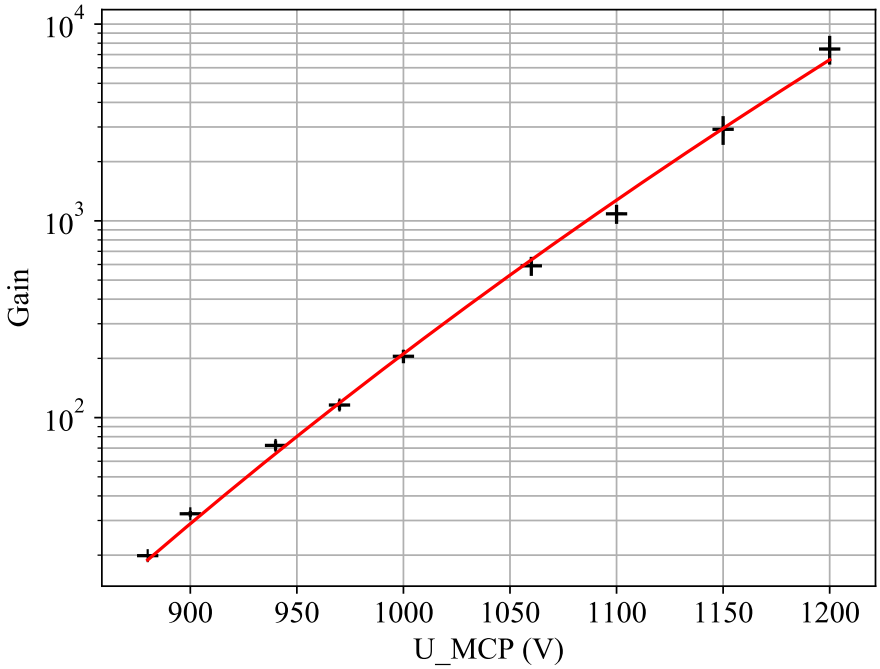


Figure 3.13: Gain of the MCP for different values of U_{MCP}, data points in black. The red line shows the fit to this data as described in the text.

fitted using a simple model for a two-stage MCP,

$$\mathrm{Gain} = \left(\left(\frac{U_{\mathrm{MCP}}}{\alpha b} \right)^{\alpha/4} \right)^2, \tag{3.6}$$

where α is the open area ratio of the MCP [65], and b is a property of the MCP material that should be between 9.5 and 10. Fitting with this model gave $\alpha = 37.74$ and $b = 9.97$. While this α value is lower than expected ($\sim$60), this is not surprising as the simple model in Eqn. 3.6 assumes that an MCP acts like a series of dynodes, amplifying the electrons, and all effects between the two stages are neglected [89, 90]. The fit shown in Fig. 3.13 holds in this range of U_{MCP}, but should not be extrapolated to larger values.

After this calibration, it was possible to detect down to $\sim 8 \times 10^3$ trapped ions. This was achieved using the smallest argon pressure that the VAT valve can regulate.

3.5 Calibration of applied voltages

The four oscilloscope channels used to monitor typical experiments (one for each pair of central rods, and one for each end-cap pair on the end of the trap from which ions are extracted, see Fig. 2.3) were calibrated so that the trap could be operated accurately. To find the relative gain of each amplifier, a 1 MHz, 1.6 V_{ptp} (peak to peak), sinusoidally oscillating signal was generated using an AWG. This amplitude was used as the gain of each amplifier was expected to be ∼50, and 80 V_{ptp} applied to the rods after amplification corresponds to a stable trapping tune. The signal was sent to each of the four amplifiers in turn and measured through each of the four oscilloscope probes and channels. This method produced enough data to calculate the relative gain of each amplifier with respect to the others, allowing a correction to be applied so that each amplifier outputted the same signal. However, the voltage measured by the oscilloscope still may not represent the true value due to inaccuracies introduced by the oscilloscope probes.

To correct for this, as well as to account for any errors in the inscribed radius of the trap, r_0, the trap was calibrated at low ion number. As no space-charge forces are present at low ion numbers, the theoretical location of the resonances are known and described simply by Eqn. 1.40. A small number of ions, $\sim 10^4$, were confined in the trap for 100,000 rf periods. They were then extracted towards the MCP. A range of cell tunes between 0.1 and 0.4 were studied by first creating ions at a cell tune of 0.15 and then adiabatically ramping them to the tune of interest over 100 rf periods. They were stored at this tune for 100,000 rf periods before extraction towards the MCP. Where a resonance had been experienced the number of ions detected by the MCP was reduced, as shown in Fig. 3.14. Between cell tunes of 0.1 and 0.4, 300 data points were studied, with ten samples taken at each data point. A pressure of 4.0×10^{-9} was used, the lowest possible pressure in IBEX. This tune scanning process is described in further detail in Section 4.3.

The cell tune was calculated by transforming each voltage data point measured by the oscilloscope into a focusing matrix. Equation 2.9 gives the strength of focusing for a given voltage datum, and the multiplication of many thin-lens matrices with the correct focusing

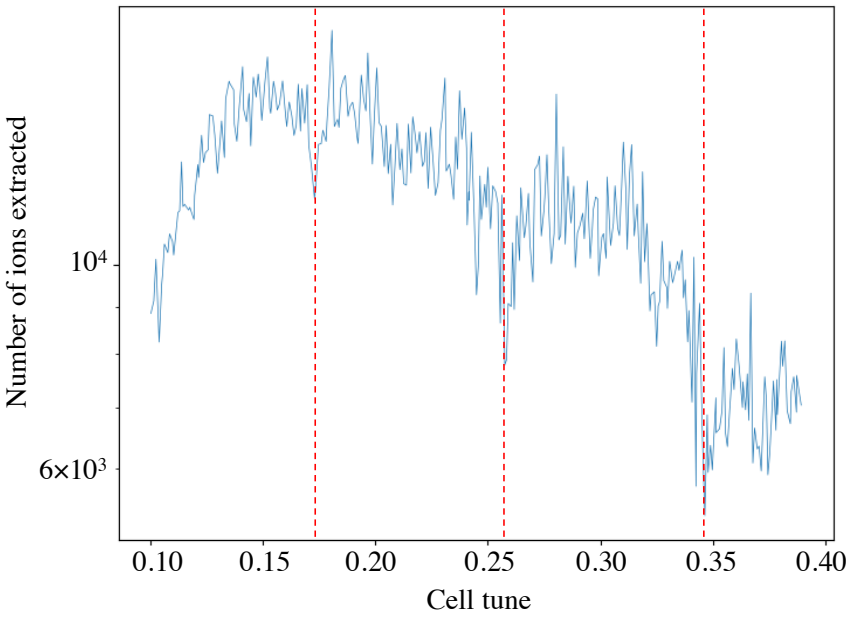


Figure 3.14: A calibration tune scan showing the number of ions extracted for cell tunes in the range 0.1 to 0.4, for small ion numbers and large confinement times. Red lines show the tunes at which significant ion loss occurs, before the calibration procedure has been performed.

strengths, described by Eqn. 1.39, gave the tune of the lattice.

Figure 3.14 shows the tune scan at low ion number, before calibration, with the ion loss on resonance highlighted in red. It is immediately obvious that the points of reduced ion number do not match the theoretical locations of the resonances. Therefore, to calculate the correct tune experienced within the trap, a calibration factor, f, was introduced so that

$$K_{\mathrm{p}}(\tau) = \frac{2qV_Q(\tau)}{fmc^2r_0^2}. \tag{3.7}$$

The value of f was changed iteratively, and the tune recalculated from the oscilloscope data points until the sum of the distance between the theoretical location of each resonance and the point of greatest ion loss was below a certain threshold. The calibration factor was found to be $f = 1.024$. The experiment was repeated using square waves instead of sinusoidal confinement voltages and f was found to take the same value.

3.5.1 Voltage correction

When performing an arbitrary tune scan over cell tunes in the range 0.1 to 0.4, it is not problematic if the voltage delivered to the trap by the amplifiers does not match the voltage desired due to limited bandwidth. The difference in voltage is likely to be small, and the tune is calculated directly from the oscilloscope trace.

However, for experiments such as those described in Section 4.8 and Chapter 6, precise control of the voltage is required. To achieve this, I mapped between the voltage requested by the control software and the voltage recorded on the oscilloscope by fitting to the curve of desired voltage against the voltage produced by the amplifiers.

3.6 Emittance estimate

The images of the ion distribution produced by the MCP gave the opportunity to estimate the emittance in the IBEX trap experimentally, using the simple simulation model described in Section 3.4.2.

For four different cell tunes (0.1, 0.2, 0.3, and 0.4), the emittance was varied between values of 0.5×10^{-9} m rad and 5×10^{-9} m rad in a series of simulations. A Gaussian transverse distribution of trapped ions was assumed. The simulation tracked the transverse position of ions as they were extracted from the trap. The integrated distribution on the MCP was projected onto the x and y axis and the Full-Width Half-Maximum (FWHM) was recorded. The data from these simulations is shown in Fig. 3.15. By fitting to the data, the relationship between the emittance in the trap and the FWHM of the distribution on the MCP at each tune was identified. In the simulations U_{in} = -1925 V was used.

An experiment was performed to check the simulation, using U_{in} = -1925 V and U_{out} = -700 V. A large, negative value of U_{out} was used to minimise any transverse divergence of electrons between the MCP and the phosphor screen and to ensure a larger image luminosity. A small number of ions were trapped to avoid space-charge forces affecting the distribution.

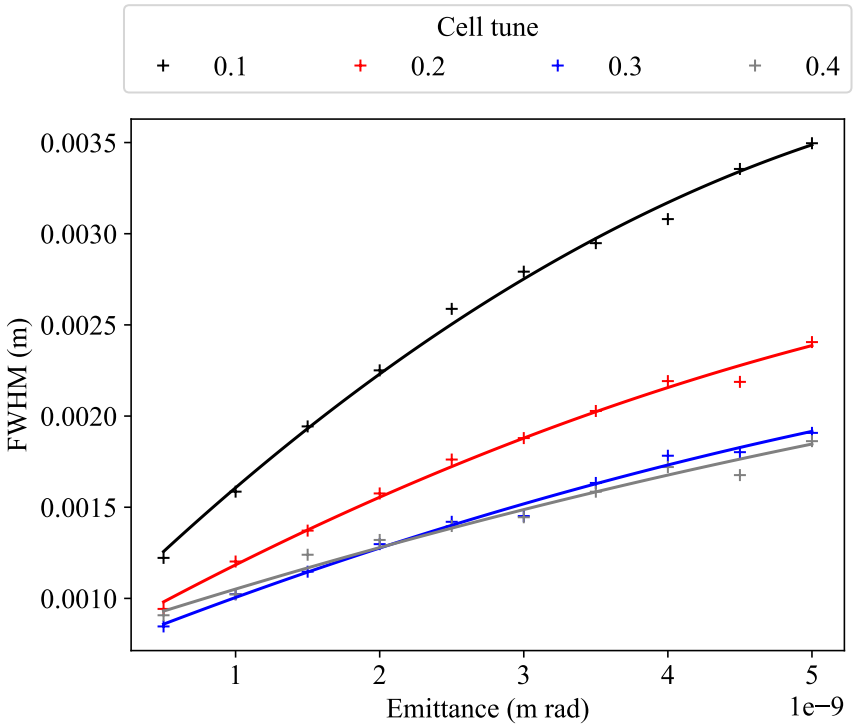


Figure 3.15: Simulated data showing the FWHM of the extracted ion distribution at the MCP for a range of emittance values. Four different cell tunes were investigated.

Images of the ion distribution were then saved for cell tune of 0.1, 0.2, 0.3, and 0.4 after the ions were stored for 1000 rf periods.

To analyse images taken by the CCD camera, the procedure to analyse the images outlined in Section 3.4.1 was followed. A threshold value was then applied to pixels, with all pixels below the threshold classed as noise and set to zero. A median filter was applied to the remaining image and projections onto the x and y axis were taken [91]. From this, the FWHM values were extracted.

One major difference between the experimental data and the simulated data is the difference in FWHM observed for the cell tunes of 0.3 and 0.4. In the simulated data, the FWHM values are the same for these two distributions, as shown in Fig. 3.15, despite an obvious difference in the shape of the distributions, shown in Fig. 3.9. However, in the experimental data, a clear difference was found between the FWHM values for these two cases. This suggests that as the distribution for a cell tune of 0.4 has large tails, part of the distribution was removed along with the noise in the threshold step. Due to this, I chose

to use the cell tune of 0.1, where the distribution can be approximated as Gaussian, for the comparison between the simulated and experimental data. Using the known radius of the phosphor screen to convert the distribution size to a value in millimetres, I found an emittance of 2.16×10^{-9} m rad.

This value is an upper bound only on the emittance within the trap, due to the assumptions made within the simulation.

3.7 Chapter summary

In this chapter, I have described the successful commissioning of the IBEX Paul trap. I have shown that the trap can store large numbers of ions for up to a second, and that an intensity-dependent tune shift was observed within the trap. I performed several short, but vital, studies to understand the creation and lifetime of ions within the trap, including the effect of collisions with the background argon gas on the number of trapped ions.

As accurate knowledge of the number of ions within the trap is necessary for all studies using the Paul trap, I identified and removed sources of noise from the Faraday-cup signal. The MCP, capable of detecting much smaller ion numbers, was then calibrated against the Faraday cup, and ion numbers as small as 8×10^3 were detected. Again, as the MCP is a necessary tool for precise experiments using the trap, I ensured that I had a clear understanding of the MCP, phosphor screen, and CCD camera.

Calibration of the trap ensured precise control of the voltages applied to the rods. The calibration allowed a calculation of longitudinal ion temperature (0.285 ± 0.036 eV) and an estimation of the effective length of the ion distribution within the trap (65.50 ± 0.64 mm). The emittance within the trap was estimated for small ion numbers (2.16×10^{-9} m rad). The accelerator physics experiments described later in this thesis are all dependent on the insight into the Paul trap gained through the experiments outlined in this chapter.

Chapter 4

A study of coherent and incoherent resonances

This chapter describes two experiments, one using the S-POD trap carried out during a visit to Hiroshima University and one using the IBEX trap after the initial commissioning was completed. The aim of both of these experiments was to study space-charge-driven resonances in intense beams using a Paul trap.

The theory describing coherent space-charge-driven resonances, as described in Section 4.2, has been developed over the last 50 years. However, the distinction between coherent and incoherent resonances is an ongoing subject of research and debate. In Section 4.3, I describe an experiment conducted on the S-POD trap to extract an expression for the location of the greatest particle loss, in tune space, for Gaussian beams of equal transverse tunes at a range of intensities.

A series of short simulations in Warp were used to understand further the dynamics within the trap and the expected results of the experiment. These simulations are shown in Section 4.4. I chose to focus on the resonance at a cell tune of $\frac{1}{4}$ in further detail to compare my results to the significant body of previous work at this tune. In Section 4.6, I present the analysis of the experimental data using insight gained from the simulation results. The experimental results are compared to theory and simulation studies performed at Hiroshima

University in Section 4.7.

Section 4.8 describes the first accelerator physics experiment conducted on the IBEX trap, a comparison of the resonance at a cell tune of $\frac{1}{4}$ with unequal and equal transverse tunes, as accelerators are most often operated with differing transverse focusing.

4.1 Published works

The work presented in this chapter has already been published in two separate locations. Sections 4.3, 4.4, 4.5, and 4.6 were published in the New Journal of Physics, in reference [92]. Section 4.8 was published first in the peer-reviewed conference proceedings of IPAC19 [93]. I am the first and corresponding author for both of these publications. Both are published under a creative commons license, [94], allowing the use of the material in this thesis. I performed the data taking, analysis, and writing for each paper, with input from the co-authors who acted in a supervisory role. The contents of [92] have been included with some addition of further detail for clarity. Some information has been reformatted for context, and information from new and relevant publications has been included. The initial setup of the S-POD trap and MCP, which was used to take some of the data in this chapter, was performed by K. Ito, assistant professor at Hiroshima University. IBEX was still in the commissioning phase when this work was completed. The published work in [93] has been added to more significantly, in light of further experimental work.

4.2 Coherent and incoherent resonances

In this section, I will introduce the theory describing the coherent and incoherent excitation of particle beams. As described in Section 1.4.4, it is known that a single particle experiences a resonance when its tune agrees with the frequency of a periodic driving force. In one dimension, this is described by the resonant condition

$$Q_0 = \frac{n}{m}, \tag{4.1}$$

where Q_0 represents the bare tune of the particle (not including any tune shift from space-charge forces) and n and m the harmonic and order of the perturbing driving force, respectively. Here $m = 1$ corresponds to a dipole perturbation, $m = 2$ to a quadrupole perturbation and so on.

Including the tune shift due to incoherent space-charge forces, ΔQ, Eqn. 4.1 becomes

$$Q_0 + \Delta Q = \frac{n}{m}, \tag{4.2}$$

where ΔQ is negative, known as the tune depression. For a lattice with a given super periodicity, N, this becomes

$$Q_0 + \Delta Q = \left(\frac{n}{m}\right) N. \tag{4.3}$$

In the past, accelerators were designed so that the incoherent tunes of the particles in the beam avoided this resonant condition [95]. However, the increased space-charge forces at high intensity can result in the beam responding as a whole to a perturbation. This can lead to a collective motion of the beam, known as coherent oscillation [96, 97, 98].

It is thought that the coherent oscillation of a beam leads to the excitation of the greatest number of particles and therefore the greatest beam loss [47]. In the case of coherent oscillation, a self-consistent solution to the equations of motion of the beam is necessary to describe the resonant response. For a quadrupole (m=2) coherent oscillation, this is found by considering the envelope equations, used to describe the beam motion along the trajectory s,

$$\frac{d^2a}{ds^2} + K_a(s)a - \frac{\epsilon_x^2}{a^3} - \frac{K_{\rm sc}}{2(a+b)} = 0, \tag{4.4}$$

$$\frac{d^2b}{ds^2} + K_b(s)b - \frac{\epsilon_y^2}{b^3} - \frac{K_{\rm sc}}{2(a+b)} = 0. \tag{4.5}$$

These equations were first derived in Section 2.2.2.

By applying the smooth approximation and solving the envelope equations, the new resonant condition is found to be

$$Q_0 + C_2\Delta Q = \frac{n}{2}, \tag{4.6}$$

where ΔQ is now the RMS incoherent tune depression of the beam. Where the tunes in both transverse directions are equal, two modes of oscillation are possible. One mode is symmetric and the transverse envelope oscillations are in phase; this mode is described as "breathing" and $C_2 = \frac{1}{2}$. The second mode is anti-symmetric, with $C_2 = \frac{3}{4}$ [47]. In the rest of this chapter, it is assumed that the anti-symmetric mode of coherent oscillation occurs when this resonant condition is satisfied, as this is more likely to be excited by quadrupole magnets [79].

The resonant condition can be generalised to higher-order, m, by the linearised Vlasov-Poisson equation. The Vlasov-Poisson equation can be directly derived from Liouville's equation (Eqn. 1.30), where the right-hand side of this equation can be considered as containing two parts, one describing time-dependent space-charge interactions, and one due to collisions between particles [23]. Taking the collisionless limit gives Vlasov's equation,

$$\frac{d\Psi}{dt} = \frac{\partial\Psi}{\partial t} + \Big(\frac{\partial\Psi}{\partial x}\Big)\dot{x} + \Big(\frac{\partial\Psi}{\partial p}\Big)\dot{p}, \tag{4.7}$$

where Ψ describes the particle distribution. The right-hand side of Eqn. 4.7 equals zero in the absence of damping [17].

An unperturbed equilibrium solution, Ψ_0, which is a function of the unperturbed Hamiltonian, can then be assumed, with small perturbations, Ψ_1, taken about it. Linearising the resulting equation gives a partial differential equation that can be solved through integration, leading to the resonant condition

$$Q_0 + C_m \Delta Q = \frac{n}{m}. \tag{4.8}$$

The factor C_m is independent of the driving term of the resonance; it is the same for external or space-charge-driven resonances.

In references [99] and [100], eigenmode analysis of the perturbed equations is used to determine if a particle distribution, Ψ_1, is amplified by the space-charge forces it creates, in a periodic focusing channel. Stability is investigated for a range of modes and tune depressions.

The C_m factor now present in the resonant condition depends on the mode of coherent oscillation that the beam is experiencing. The notation C_{mk} is also commonly used, where m denotes the azimuthal mode of oscillation and k the radial mode. Here k is dropped, $m = k$ is assumed as these rigid modes are more likely to be excited by accelerator components [96].

It has been analytically shown that the C_m factors all lie in the range $0 < C_m < 1$, with the special case of $C_1 = 0$ for a dipole perturbation [47, 96]. As the order of the coherent oscillation increases, so does the C_m factor, so that $C_1 < C_2 < C_3$... etc. As the C_m factors are less than 1 this gives a small increase in the high-intensity beam limit, as for a given tune the intensity can be increased further before the resonant condition is met.

This work was later extended by Okamoto and Yokoya, where no smooth approximation was applied [101]. The theory presented in [101] shows that, when alternating gradient focusing is considered, space-charge-driven resonances emerge at twice the density in tune space, according to the resonant condition

Order of coherent resonance (m)	1	2	3	4
C_m	0	$\frac{3}{4}$	$\frac{11}{12}$	$\frac{31}{32}$

Table 4.1: Analytically calculated C_m values for a 2D KV beam [47].

$$Q_0 + C_m \Delta Q = \frac{1}{2}\left(\frac{n}{m}\right). \tag{4.9}$$

The growth rate and stop-band width of these space-charge-driven resonances were found to be proportional to the intensity of the beam. Such resonances, also referred to as structure space-charge instabilities or coherent parametric instabilities [23], are therefore neglected at low intensities.

Analytical values of C_m have been calculated (initially in [47]) assuming a Kapchinski-Vladimirskij (KV) distribution, where the space-charge forces provide linear defocusing in both planes. These values can then be used to describe different particle distributions, assuming RMS equivalent beams. These C_m values are presented in Table 4.1.

Additionally, the transverse distribution of the beam itself can influence whether a beam is excited coherently. Hofmann, in reference [102], shows that KV distributions can be excited coherently by higher-order modes, but that for more realistic beam models, such as waterbag or Gaussian distributions, the spread in particle tunes may lead to Landau damping of coherent modes higher than $m = 2$. This effect is not included in the resonant condition, as by linearising the Vlasov-Poisson equation, higher-order terms are lost, and therefore the incoherent tune spread is not accounted for [103]. However, for higher-order modes, the significant overlap between the incoherent tunes in the distribution and the tune of the coherent resonance can lead to an energy transfer from the coherent excitation of the distribution to the incoherent excitation of particles within the beam, so that coherent oscillations never form [104].

These resonant conditions are further complicated when coupling resonances are considered. In a recent paper ([105]) Ito *et al.* propose a generalised 2D resonance condition,

$$k(Q_{0x} - C_m) + l(Q_{0y} - C_m) = \frac{n'}{2}. \tag{4.10}$$

Here n' is an integer, which can only be odd for space-charge-driven resonances, notably the C_m factor still depends only on the order of the resonance.

Previous work

Clarifying the distinction between coherent and incoherent resonances, investigating the mechanisms of beam loss, and calculating the value of the C_m factors have been active areas of research for a number of years. For example, at ISIS, extensive experimental and simulation work (using a frozen space-charge model) has been performed in an attempt to understand beam loss as the half-integer resonance is approached [106, 107]. The half-integer resonance is considered to be a major driver of beam loss, limiting the intensity of ISIS and similar rings.

A significant amount of previous work exists using S-POD to show the overlap in high-intensity beams of external-field-driven resonances (satisfying the resonant condition in Eqn. 4.8) and space-charge-driven resonances (meeting the resonant condition in Eqn. 4.9) [105]. Furthermore, the splitting between the location of the externally driven coherent dipole resonance and the self-driven coherent quadrupole resonance at integer tunes, due to the differing C_m factors, has been shown qualitatively [108]. As expected, this splitting becomes more pronounced as intensity is increased.

In reference [41], Ohtsubo *et al.* applied a quadrupole error to the S-POD trap to excite resonances, and ion loss was studied at three different intensities. They qualitatively draw the conclusion that the C_m factors for $m = 2$, $m = 3$ and $m = 4$ "appear to be less than unity" at high intensities. However, the underlying assumptions of this study do not allow the result to be quantified. This chapter describes a quantitative study of resonances in high-intensity Gaussian beams over longer time scales, an advance on previous qualitative Paul-trap studies.

The resonances occurring at a cell tune of $\frac{1}{4}$ have been studied in simulation several times [109, 110, 111]. Simulations clearly show the competition between the fourth-order incoherent excitation of the beam and the second-order coherent resonance at this tune.

However, the definition of coherent and incoherent oscillation is still highly debated, as are the mechanisms for beam loss in many intense accelerators, and the literature is confused by a large number of terms used to describe the same mechanisms [112].

Recently, resonances have been classified as coherent or incoherent using the FFT spectrum of individual particles tracked in simulation [113]. Incoherent resonances are defined as those with a peak in the FFT spectrum at the frequency of the resonance, signalling that fixed points exist in the phase space, which have trapped individual particles. However, the obvious disadvantage of this method is that it assumes that simulations can be performed that perfectly describe the experimental case. One potential solution is to compare the Debye length (Section 3.3, Eqn. 3.5) with the transverse size of the distribution to classify the resonance [86]. However, this method finds a large region where the beam oscillations are classed as a mixture of coherent and incoherent excitation and makes no prediction of the location of dangerous resonances in tune space.

In this chapter, I describe an experiment using the S-POD LPT to understand space-charge-driven resonances and to study experimentally how the tune corresponding to maximum beam loss changes with intensity. Several resonances of different orders were studied, in the hope of providing values useful in accelerator design.

In this chapter, I do not assume that resonances are either coherent or incoherent, only that the resonance condition for maximal beam loss can be defined as

$$Q_0 + A_m \Delta Q = \frac{1}{2}\left(\frac{n}{m}\right). \tag{4.11}$$

I used the S-POD LPT to extract values of A_m, which are of practical use in the design of high-intensity accelerators.

The cell tune (tune per focusing period) in the S-POD LPT was varied over a wide range and the location of the resonances experienced at a range of intensities was studied. No external error fields were applied to the trap, resonances were either driven by space-charge forces or by small multipole fields from slight trap misalignment. Therefore, in the high-intensity regime in which this experiment was conducted, space-charge-driven resonances dominated [41]. From this data, I extracted a numerical value for the location of four resonances of different orders at different ion numbers. By fitting to this, I extracted A_m, which I then compared to the C_m factors predicted for purely coherent resonances.

To understand the experiment further, the setup was simulated using Warp, details of which are given in Section 4.4.

4.3 Experimental procedure using S-POD

The experimental data were taken using the S-POD II trap, one of three LPTs at Hiroshima University. To study space-charge-driven resonances, several experiments were conducted, each using a different cell tune between 0.1 and 0.4. This ensured that a wide range of resonances could be investigated. The number of ions stored in the trap was increased and the process was repeated. As coherent oscillations arise due to space-charge forces in high-intensity beams, large numbers of ions were stored in the trap for these experiments. Measurements were taken for eight different ion numbers between 10^6 and 10^7.

Identical waveforms were applied to each rod pair (180 degrees out of phase, as shown in Fig. 2.3, page 33) so that the transverse tunes were always the same.

At each tune value, a new experiment was performed with the following steps:

1. Argon gas was introduced into the vessel.
2. A sinusoidal voltage was applied to the confining rods with an amplitude that gave a cell tune of 0.15, at which tune the largest possible number of ions are captured by the trap.

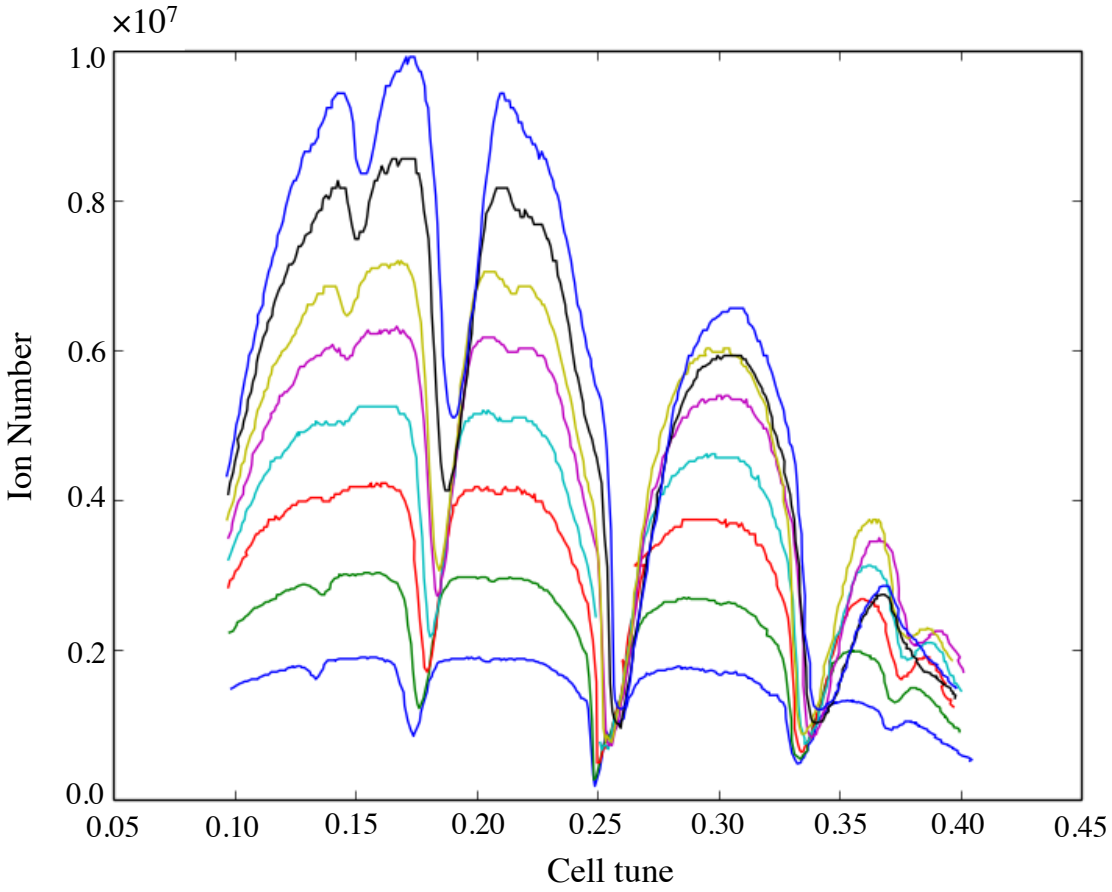


Figure 4.1: Measured ion number extracted from the S-POD trap, against cell tune. Different colours represent the different ion numbers initially trapped. Each coloured line is comprised of 330 data points. Each data point represents a separate experiment where ions are created, stored and extracted.

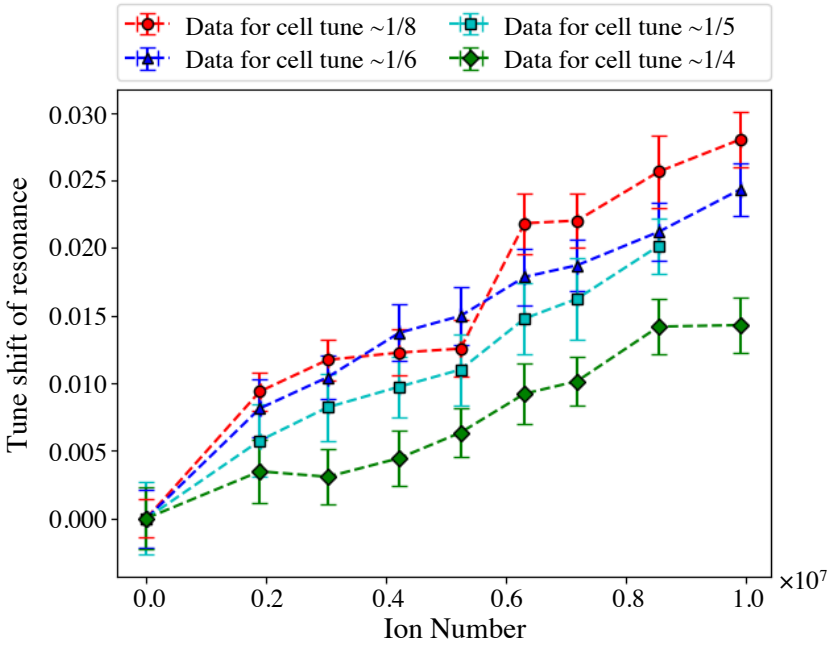


Figure 4.2: Tune shift against ion number for the four resonances at lowest tune in Fig. 4.1. Error bars are determined from the width of the resonance minima.

3. The electron gun was switched on for less than 1 s to ionise the argon gas.

4. The captured ions were stored in the trap for 50 ms to reach equilibrium.

5. The amplitude of the voltage applied to the confining rods was altered smoothly over 100 focusing periods until the tune at which the experiment should take place was reached. At all points, tunes are the same in both transverse directions.

6. At this tune, the ions were stored for 100 ms, equivalent to 10^5 focusing periods.

7. The remaining ions were extracted by setting to zero the DC voltage on the end cap closest to the MCP.

8. The signal from the MCP, taken from the phosphor screen, was recorded to calculate the number of ions extracted.

We changed the number of ions stored in the trap and repeated these steps over the same tune range. The number of ions stored in the trap was altered by changing the length of time for which the electron gun was producing electrons. Pressure changes inside the trap were avoided to keep ion-neutral collision rates constant.

In total $\sim$ 330 experiments were performed within the range of tunes, each for a given beam intensity. S-POD is automated and capable of taking one measurement approximately every 10 s, so recording the ion loss over this wide range of tunes took only $\sim$ 1.5 hours. The relationship between the applied voltage and the cell tune in the trap was calibrated using data taken at a very low ion number ($\sim 5 \times 10^3$), as described in Section 3.5.

Figure 4.1 shows the raw data from the experiments at large ion number, with the calibration applied. When the beam encountered a resonance, the resultant beam loss led to a reduction in the number of ions extracted. Resonances are represented by local minima in Fig. 4.1.

Figure 4.2 clearly shows that as the number of particles stored in the trap is increased, the location of the resonance shifts to a higher bare tune, as expected due to the increased space-charge tune depression. The ion loss observed as the cell tune approaches 0.1 and 0.4 is due to an increase in the maximum beta function at these tunes (as illustrated in Fig. 4.3), reducing the number of ions that can be stored. Furthermore, the depth of the pseudo-potential created by the trap changes with the amplitude of the rf voltage; together, these effects characterise the maximum number of ions that can be stored at a given tune [83].

Note that two effects are not included in the discussion of this experiment, as their effects are negligible. First, S-POD was operated with equal transverse tunes, which is often avoided in accelerator operation due to the difference resonance $Q_{0x} - Q_{0y} = 0$. However, no emittance growth was experienced due to this resonance; the emittance was the same in both transverse planes, resulting in no emittance exchange.

At the start of this chapter, the Vlasov-Poisson equation was used to describe the ion distribution in the collisionless limit. This is reasonable since, as shown in Section 3.2, the characteristic collision time for an ion with background gas is ~ 0.77 s, which is several times larger than the timescale of this experiment, limiting the effect of collisions. Furthermore, the resonance was experienced by the ions immediately after the tune ramp, just 1 ms after the ions had been left to stabilise. At this time, very few ion-neutral collisions had occurred,

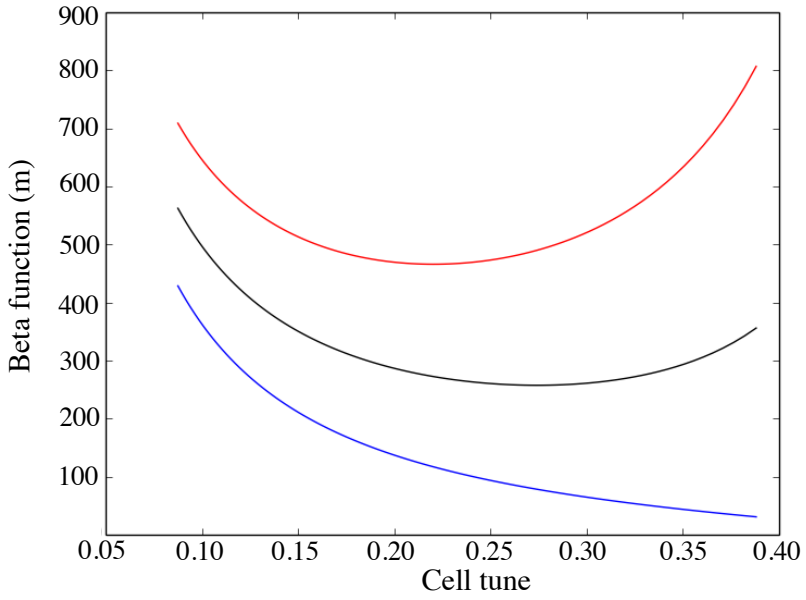


Figure 4.3: Variation the beta function with cell tune. The red line shows the maximum of the beta function, the black line the mean and the blue line the minimum.

with minimal impact on the ion distribution. As ion-neutral collisions are a non-conservative process they are not included in the Hamiltonian of the LPT. However, similar collisions will also take place in an accelerator, where Intra-Beam Scattering (IBS) can also lead to emittance growth [114]. In this chapter, I describe the effect of the resonant excitation only.

4.4 Simulation of the experiment

I used the PIC code Warp ([80], described in Section 2.6) to simulate the experimental setup in 2D, including space-charge forces. An ideal LPT was simulated, with no misalignment in the trapping rods. As the rods are cylindrical, not hyperbolic, higher-order external fields were still present in the simulated trap. Any rod misalignment in the real system will create additional higher-order fields.

The simulation was designed to mimic the experiment as closely as possible, except for the total storage time. A matched distribution of argon ions was injected into the trap at the starting cell tune of 0.15. The ions were trapped at this tune for 50 focusing periods

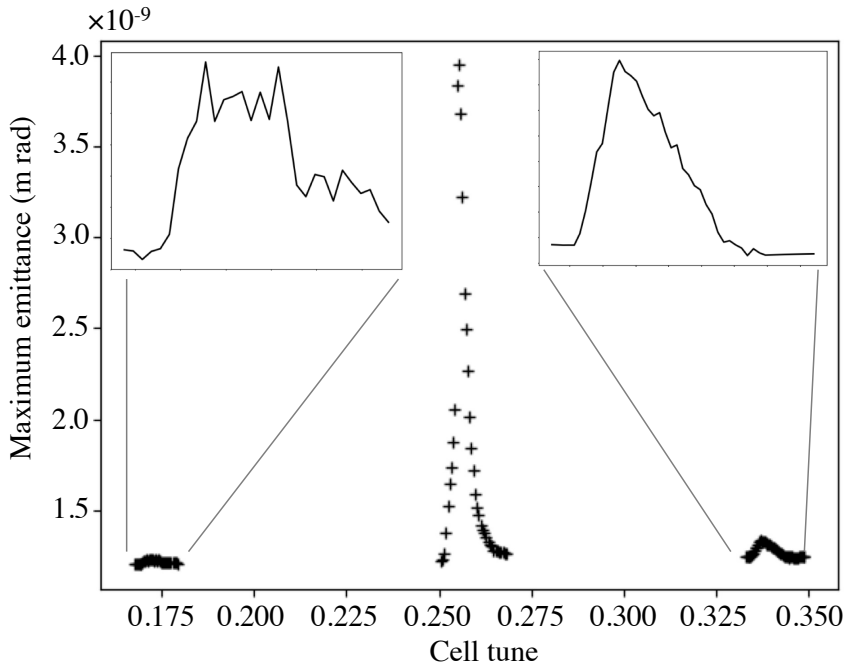


Figure 4.4: Simulated RMS emittance growth at the cell tunes $\frac{1}{6}$, $\frac{1}{4}$ and $\frac{1}{3}$. Left and right insets show enlarged versions of the $\frac{1}{6}$ and $\frac{1}{3}$ resonances, respectively.

before the tune was ramped to the tune of interest by changing the amplitude of the voltage applied to the confining rods. As in the experiment, this change in tune occurred over 100 focusing periods regardless of the final tune. The ions were then stored in the trap for 550 focusing periods at the final tune, so the simulation ran for 700 focusing periods in total.

In the simulation, ions were stored for only a fraction of the 10^5 focusing periods used in the experiment. This was due to the significant computational time required to simulate even 550 focusing periods, highlighting the importance of LPTs in understanding resonant effects over longer time scales.

Emittance growth was studied instead of particle loss as little, if any, loss occurred over such short timescales. Furthermore, any loss that occurred after only 550 focusing periods was due to the loss of halo ions and therefore provided very little information on the ion distribution as a whole. I used this method to study the increase in the emittance of the distribution at the resonances at cell tunes $\sim \frac{1}{6}$, $\sim \frac{1}{4}$, and $\sim \frac{1}{3}$, focusing in greater detail on the resonance at $\sim \frac{1}{4}$. In each simulation, the growth in emittance was recorded as well as the evolution of the phase space and any particle loss due to scraping on the rods.

Figure 4.4 shows the RMS emittance growth at the three resonances for 2×10^6 trapped argon ions[1]. From the phase-space distributions extracted from each simulation, I found that even after such a short time the $\frac{1}{4}$ resonance showed signs of coherent motion (see the inset phase space plots in Fig. 4.7b). However, at cell tunes of $\frac{1}{6}$ and $\frac{1}{3}$ this was not observed. This may be due to the relatively short timescale of the simulation, limited space charge, or due to the Landau damping of coherent higher-order modes, as predicted by Hofmann in reference [102].

The Warp simulations provided the opportunity to study the effect of the ramp in tune on the distribution of the trapped ions. When trapped ions were ramped to a cell tune of 0.25 or below, the change in emittance during the ramp was negligible. However, when the ions were ramped through a cell tune of 0.25, the emittance was increased, the magnitude of this increase depending on the final tune and therefore the rate of resonance crossing. This information was then used to guide the analysis of the data presented in Section 4.6.

[1] 100,000 macroparticles were used on a 300 by 300 grid, extending from $-(r_0 + \rho)$ to $(r_0 + \rho)$.

4.5 Detailed simulation at a cell tune of 0.25

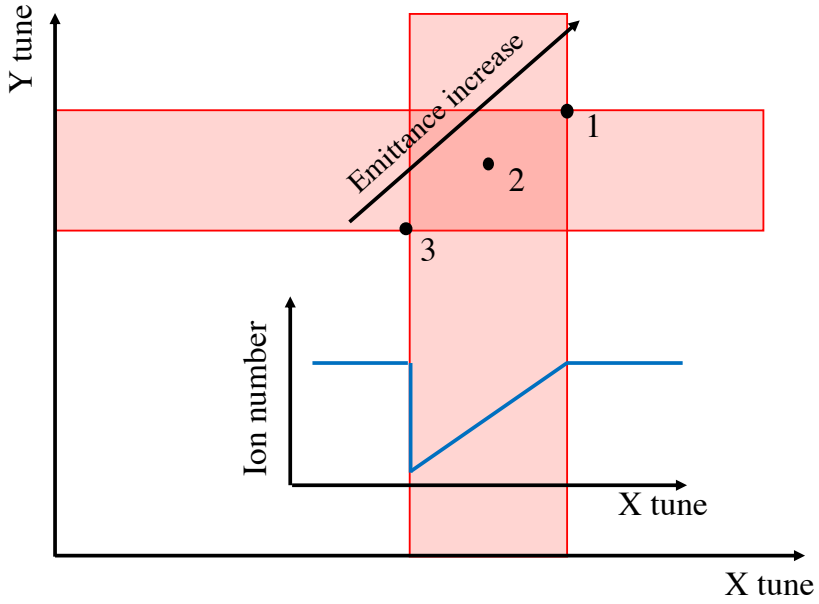


Figure 4.5: Diagram showing the shape of coherent resonance due to the finite width of the stopband (depicted as shaded red bands). Particle distributions with coherent tunes at position (1) spend minimal time within the stopband, as emittance increase reduces the tune depression, moving the tune in the direction indicated by the arrow. Distributions with tunes represented by point (3) are within the stopband for the maximum time; those at (2) give the intermediate case.

In the case of the resonance at a cell tune of 0.25[2], I chose four tunes across the resonance to study in greater detail. Throughout this section, the cell tune will be referred to in decimal form for ease of reading. At each of these tunes I tracked the ions in the Warp simulation, and from the positional information used Numerical Analysis of Fundamental Frequencies (NAFF [115]) to extract the tunes of individual macroparticles. I also calculated the kurtosis, a measure of the shape of the distribution [116], at the same point in every focusing period.

The code used for Numerical Analysis of the Fundamental Frequency (NAFF) in this thesis is adapted from a script written by K. Ruisard, written for the UMER project, which is described in further detail in Section 5.3.2 [117, 118].

Methods to analyse frequencies which vary over a small number of samples were initially

[2]The location of this resonance can also be described as at 90°, as is the case for much of the literature [23].

developed to measure weakly chaotic motion [115]. The algorithm for NAFF provides greater accuracy over a simple Fourier transform and so is useful in the analysis of dynamical systems. However, there is an increase in computational time for the algorithm. A first guess of the frequency is initially provided to the algorithm by a Fast Fourier Transform (FFT). The NAFF code increased the accuracy by fitting to the recorded positional data points with a sine wave, extracting a frequency that is not limited by the number of data points [118].

I chose to study the resonance at cell tune 0.25 as the competition between the fourth-order incoherent resonance and the second-order coherent resonance (also known as the envelope instability) at this tune is the subject of much previous work. Simulations by Hofmann and Boine-Frankenheim in reference [109] show that these two resonances overlap, with the fourth-order exciting particles initially and the stronger envelope instability taking over as the simulation progresses. In reference [110], the fourth-order resonance was found to dominate on smaller timescales and its width was measured at GSI.

Once the emittance growth due to either the coherent or incoherent resonance is so great that the tune of the beam no longer falls within the stopband of the envelope instability, the distribution can no longer be excited [111]. This leads to the characteristic shape of the coherent resonance, with a sharp increase in particle loss on the lower tune side of the resonance and a gentler gradient on the high tune side, as illustrated in Fig. 4.5.

On the other hand, the fourth-order resonance has the potential to excite particles over much longer time scales, trapping them in the stopband. Our simulations agree very well with these previous results. Figure 4.6 shows that the simulated resonance has the characteristic shape of a coherent resonance with the addition of areas of emittance growth outside this coherent region (for example, the region between bare cell tunes of 0.251 and 0.253 in Fig. 4.6a), where the emittance growth is significantly reduced, but not yet negligible.

In Fig. 4.6a, a small difference in the emittance growth between the horizontal and vertical directions indicates that the second-order resonance dominates at those tunes. The second-order resonance is a strong instability and small, random, differences in initial conditions influence in which plane the emittance grows first [23]. In Fig. 4.6a, the four tunes that

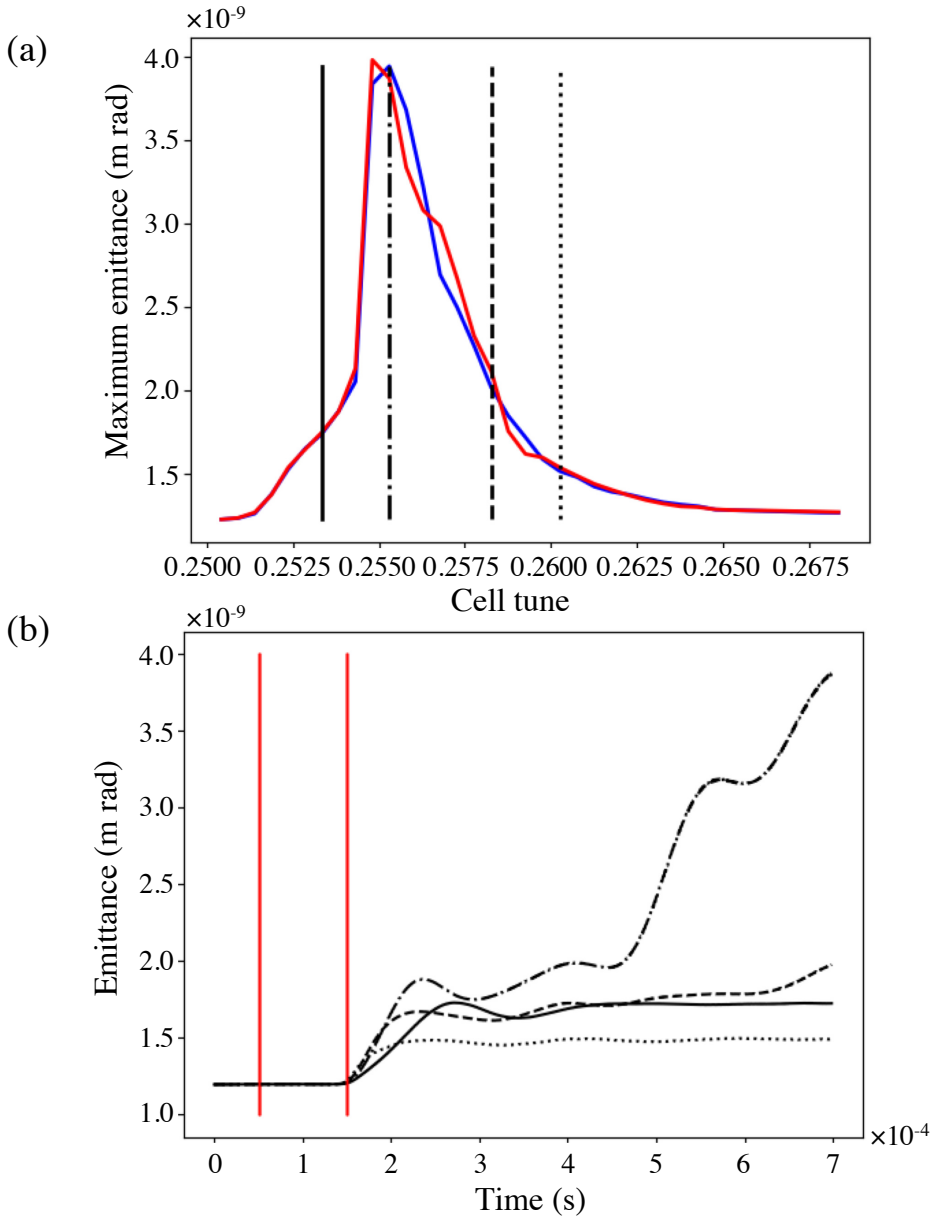


Figure 4.6: A detailed study of the resonance at a tune of 0.25. (a) shows the RMS emittance growth in the horizontal (blue) and vertical (red) directions, with the four tunes studied in greater detail highlighted by vertical lines. (b) shows the RMS emittance growth as a function of time for each of the four highlighted tunes; the vertical lines represent the start and end of the voltage ramp.

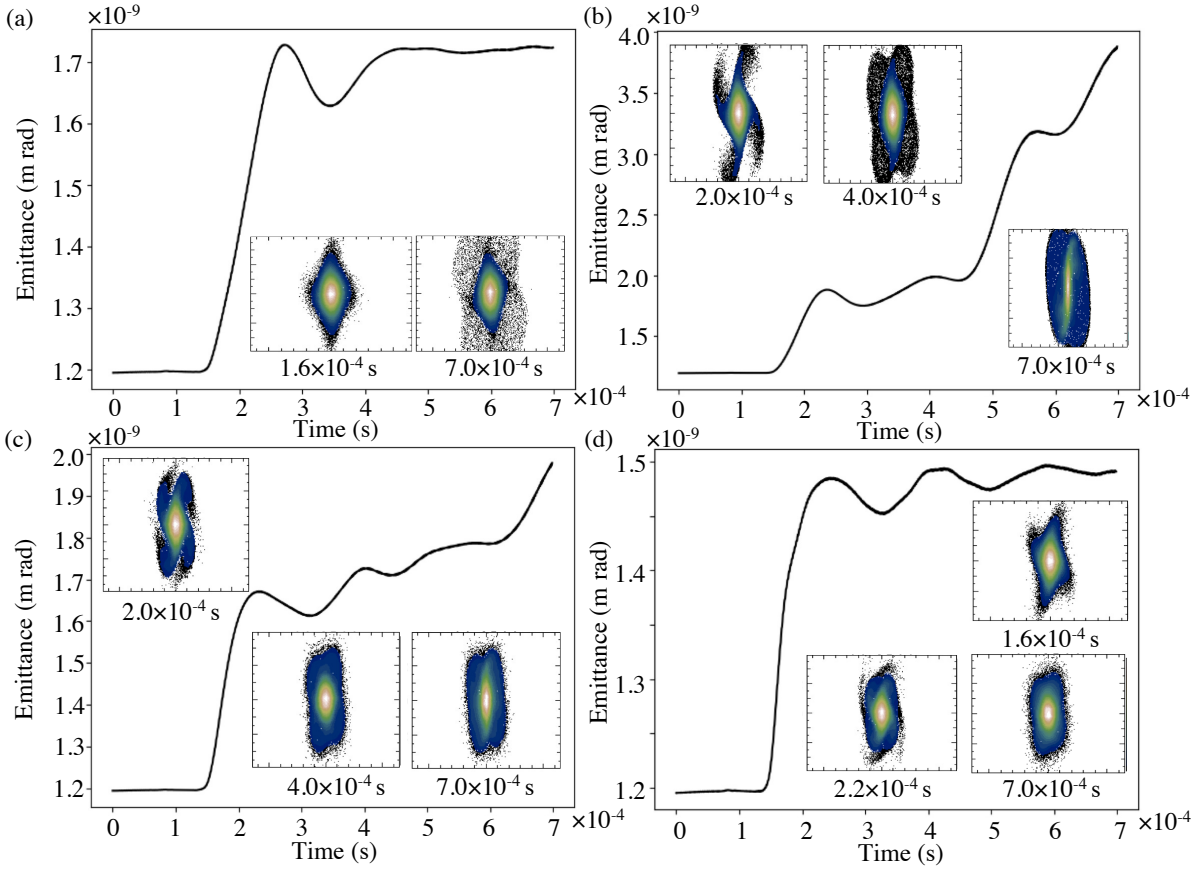


Figure 4.7: Emittance growth (RMS) in the horizontal direction at bare cell tunes (a) 0.253, (b) 0.255, (c) 0.258 and (d) 0.26. Emittance growth in the vertical direction is very similar in each case. Insets show the x (horizontal axis) x' (vertical axis) phase space at points of interest.

were studied in greater detail are highlighted with vertical lines and the emittance growth as a function of time at each of these tunes is shown in the lower panel.

Figure 4.7 shows the evolution of the phase space at the four tunes studied in detail. Together Fig. 4.6, Fig. 4.7a, and Fig. 4.7d show that the outer regions of emittance growth (at the higher and lower tunes within the resonance) are due to the excitation of particles through the fourth-order resonance, with this excitation at the lower tune side of the resonance leading to the formation of a large halo, which can lead to particle loss over a shorter timescale. In the centre of the resonance, the phase-space plots in Fig. 4.7b and Fig. 4.7c clearly show a fourth-order excitation followed by the stronger envelope (second-order) instability, leading to an initial growth in the emittance, a plateau, and then further emittance growth.

The kurtosis of the distributions is shown in Fig. 4.8. The kurtosis represents the peakedness of the ion distribution. Here I use Fisher's definition of the kurtosis [119], where

$$\text{kurtosis} = \frac{\sum_{i=1}^{N}(X_i - \bar{X})^4/N}{\sigma^4} - 3, \tag{4.12}$$

in which $\bar{X}$ is the mean, σ the standard deviation, and N the number of data points. Using this definition, a Gaussian distribution has a kurtosis of 0. Larger positive values indicate a more pointed shape, whereas larger negative values indicate that the distribution is more square. The incoherent fourth-order excitation of particles leads to a positive value of the kurtosis as a small number of particles are excited to large amplitudes. In the case of halo formation at a bare cell tune of 0.253 (Fig. 4.8a), the kurtosis remains large, showing that the halo remains an important feature over a large number of cells. In the case of the incoherent excitation at a bare cell tune of 0.26 (Fig. 4.8d) the kurtosis returns to 0, showing that although the emittance increases the ions can redistribute and return to an approximately Gaussian shape.

In the regions of coherent excitation (Fig. 4.8b and Fig. 4.8c) the kurtosis first returns to 0 and then becomes negative as the beam is excited as a whole.

The tune footprint for the four tunes studied is shown in Fig. 4.9. The tunes are calculated over 50 focusing periods, firstly at the start of the simulation (at cell tune of 0.15 in each case), then immediately after the tune ramp and finally at the end of the simulation. For each tune footprint, the RMS tune and the theoretical location of the coherent envelope instability is also plotted.

Figure 4.9 shows that the maximum emittance growth does not occur at the theoretical location of the coherent resonance, but rather at a bare cell tune of 0.255 (Fig. 4.9c), instead of the predicted theoretical value of closer to 0.259. This is due to the initial fourth-order excitation of the ions, which alters the ion distribution, in turn reducing the tune depression. This, coupled with the finite width of the resonance, means that the coherent resonance does not occur at the tune predicted by the C_m factor. At at tune of 0.255, fourth-order excitation

pushes the distribution onto the coherent envelope instability, the ions spend the maximum time within the coherent stopband and therefore the emittance growth is maximised. At 0.258, the distribution is moved towards the exit of the stopband of the envelope instability by the fourth-order incoherent excitation, the time spent within the coherent stopband is reduced and so is the emittance growth.

Through further simulation, I confirmed that this remains true even when simulations are extended to a total length of 1350 focusing periods, after which time the coherent emittance growth has plateaued. Simulations that introduced a matched distribution to the trap directly at the tune of interest, without the voltage ramp, verified that this effect is not due to the slow ramp onto the resonance.

To summarise, PIC simulations at a cell tune of 0.25 show that the distribution is first excited incoherently, increasing the emittance and altering the distribution. Coherent second-order excitation is later observed.

Returning now to the experimental work with the S-POD LPT, we therefore expect our experimental results to show evidence of this effect, with the extracted value of A_m (equation (4.11)) at a cell tune of $\sim \frac{1}{4}$ smaller than $C_2 = \frac{3}{4}$.

4.6 Analysis of S-POD data

When analysing the experimental data I chose to focus on only the four resonances at the lower tune values. These resonances are distinct and it is possible to locate the cell tune where the fewest ions are extracted from the trap for each resonance. Furthermore, the simulations presented in Section 4.4 suggest that at a cell tune higher than 0.25 the emittance will be increased, due to the transition of the fourth order resonance at a cell tune of 0.25, complicating the data analysis for these resonances.

The point of maximum beam loss was located for the four resonances studied. The tune corresponding to this point was extracted from the data by a minimum-finding algorithm.

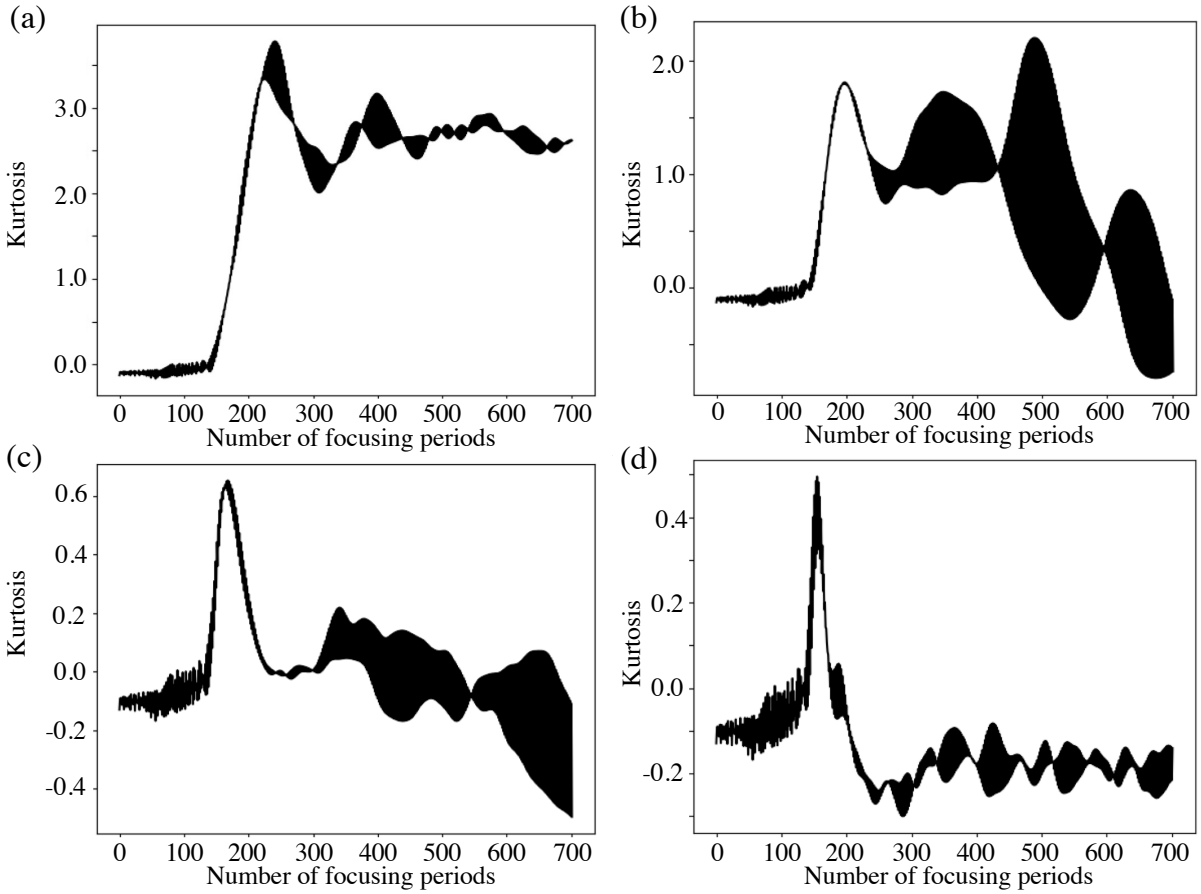


Figure 4.8: Kurtosis in the horizontal direction at bare cell tunes of (a) 0.253, (b) 0.255, (c) 0.258 and (d) 0.26. Kurtosis in the vertical direction is very similar in each case.

The change in the tune at which the resonance is located is plotted against the ion number to give Fig. 4.2.

Several steps are required to extract A_m (from Eqn. 4.11) from the data in Fig. 4.2. Firstly, the expected single-particle tune shift at each intensity must be calculated. To do this, a value of the emittance of the ion distribution and the longitudinal length of the distribution in the trap are required. Then, a linear fit can be applied to a plot of the tune shift of each resonance multiplied by the emittance, against the ion number in the trap (Fig. 4.10). Any deviation from the expected single-particle tune shift indicates that A_m deviates from 1. Final values for A_m are presented in Fig. 4.11.

It should be noted that the data in Fig. 4.10 deviate from a straight line. This may be due to a number of complex factors, including the interplay between incoherent and coherent

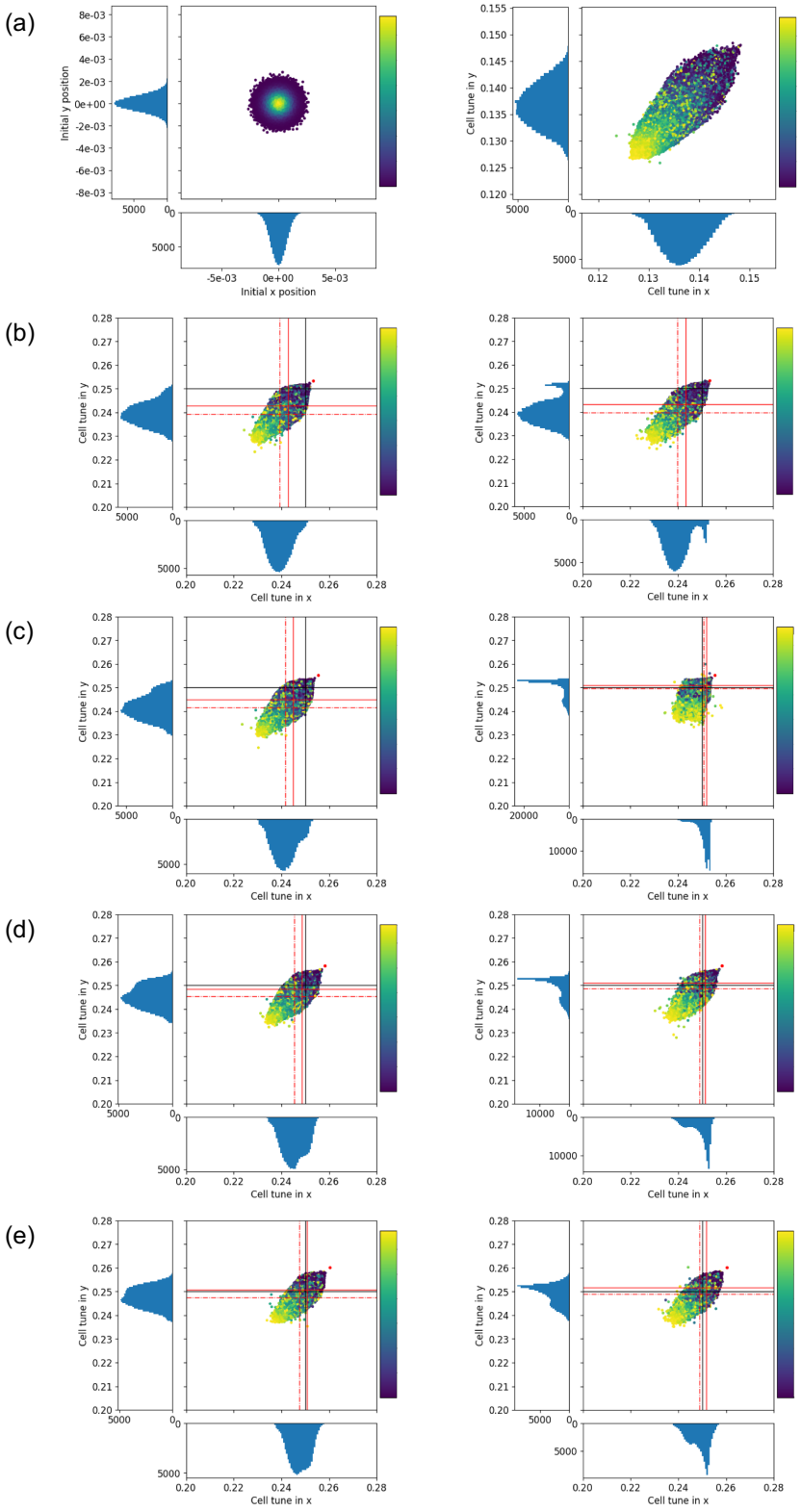


Figure 4.9: Tune footprints for bare cell tunes of (b) 0.253, (c) 0.255, (d) 0.258 and (e) 0.26. Plot (a) shows the initial distribution in space (left) and the starting tune footprint before the ramp (right). For subplots (b), (c), (d) and (e), the left plot shows the tune footprint immediately after the voltage ramp and the right-hand plot shows the tune footprint at the end of the simulation. Distributions are coloured to highlight the relationship between the initial location of the particle in the distribution and the tune. Red dots represent theoretical bare tune based on the applied voltage and solid black lines highlight the location of a tune of $\frac{1}{4}$. Broken red lines show the RMS of each tune footprint and solid red lines show the theoretical location of the coherent resonance, assuming $C_2 = \frac{3}{4}$.

resonances at different intensities. To avoid complicating the analysis further these effects were not considered and a linear fit was used.

To calculate the expected single-particle tune shift, the ions are assumed to occupy a cylinder with a transverse Gaussian distribution and length L, as described in Section 1.5.1 [22]. As ion motion in the Paul trap is non-relativistic, magnetic forces can be neglected and the RMS tune shift of the equivalent beam is

$$\Delta Q = -\frac{\lambda_{\mathrm{rf}} r_p}{8\pi} \frac{N}{L\epsilon_x}, \tag{4.13}$$

where N is the number of ions stored in the trap, ϵ_x is the RMS emittance, r_p is the classical particle radius and λ_{rf} the wavelength of the applied rf voltage.

A Gaussian distribution was assumed, based on significant evidence from previous S-POD experiments in which the MCP was used to image the ion distribution [75, 120]. Calculating ΔQ from Eqn. 4.13 gives a result that agrees very well with the RMS tune shift calculated from the Warp simulations through NAFF.

The ion distribution length, L, was determined experimentally using IBEX, as described in Section 3.3. IBEX was used due to restrictions on the experimental time available on S-POD. As both traps are designed to be longitudinally identical and the same model of electron gun was used, the result applies to both S-POD and IBEX.

Using the equations first presented in Section 2.2.2 and the experimentally determined value for the longitudinal distribution length, the emittance was calculated for each ion number. From the definition of the emittance in Eqn. 1.28 and using

$$K_B T = \frac{\langle p_x^2 \rangle}{m}, \tag{4.14}$$

following references [36] and [51], the emittance can be expressed as

$$\epsilon_x = a\sqrt{\frac{K_B T}{mc^2}}. \tag{4.15}$$

Using this definition and assuming a stationary ion distribution ($d^2a/d\tau^2 = 0$), Eqn. 2.19 can be rearranged to give an expression for the RMS size of the beam in terms of transverse temperature,

$$a = \frac{c}{\omega_q}\sqrt{\frac{K_B T}{mc^2} + \frac{N_L r_p}{2}}. \tag{4.16}$$

Here ω_q is the angular frequency of the betatron oscillations of the trapped ions.

Rearranging this equation and defining the effective value of the incoherent phase advance as

$$\phi^2 = \phi_0^2 - \frac{N_L r_p}{2}\left(\frac{\lambda_{\mathrm{rf}}}{a}\right)^2, \tag{4.17}$$

where ϕ_0 is the bare phase advance and ϕ is the shifted (depressed) phase advance, the following expression for transverse temperature in terms of tune depression can be derived,

$$T = \frac{N_L r_p mc^2}{2K_B}\left(\frac{1}{1-\eta^2} - 1\right). \tag{4.18}$$

The tune depression is defined to be $\eta = \phi/\phi_0$.

A single emittance value cannot be assumed, as the increased space-charge forces at a higher intensity will distort the potential experienced by the ions (the Debye-shielding effect). Furthermore, the electron gun is on for a different length of time to create each ion number, potentially altering the emittance. The tune depression for the resonance at a cell tune of $\frac{1}{6}$ was used to calculate the RMS tune depression, at first assuming $A_m = 1$. This was then used to calculate the transverse temperature. The temperature was used to find a value for the RMS beam size and finally the RMS emittance.

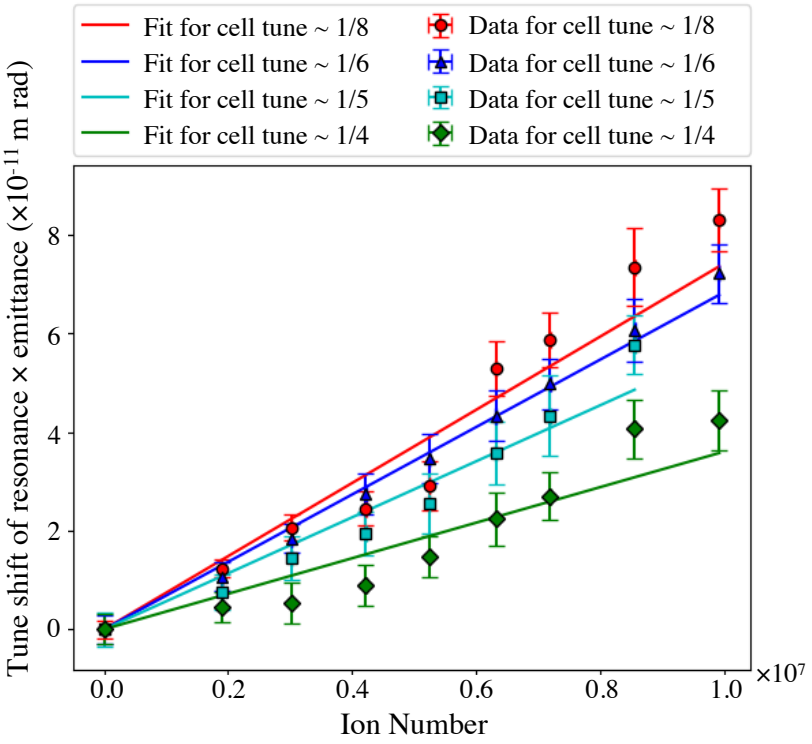


Figure 4.10: Tune shift multiplied by the emittance, for the four resonances studied, against the ion number. Here error bars include the error on the emittance values and the solid lines show the gradient of a linear fit to the data.

The data in Fig. 4.2 was combined with the results of the emittance calculation at each ion number and a linear fit was applied, as shown in Fig. 4.10. The gradient of the fit gives A_m for the resonance (using Eqn. 4.13), as

$$\frac{\epsilon_x \Delta Q_R}{N} = \frac{\lambda_{\mathrm{rf}} r_p}{8\pi} \frac{A_m}{L}, \tag{4.19}$$

in which Q_R describes the tune where the greatest ion loss is observed.

This process was repeated iteratively for the $\frac{1}{6}$ resonance until the factor of A_m included in the calculation of the RMS tune depression equalled the factor extracted from the fit. The emittance values for this case are presented in Table 4.2.

This analysis relies on the further assumption that the tune change from a cell tune of 0.15 (where the ions are collected) to the operating point is adiabatic, and that during this process no ions are lost. This assumption is well supported by the Warp simulations.

Ion number ($\times 10^6$)	Transverse temperature (eV)	RMS beam size (mm)	RMS emittance ($\times 10^{-9}$ m rad)
1.897	0.144 ± 0.003	0.670 ± 0.008	1.318 ± 0.030
3.026	0.190 ± 0.004	0.779 ± 0.008	1.760 ± 0.036
4.223	0.211 ± 0.005	0.837 ± 0.009	1.998 ± 0.045
5.245	0.244 ± 0.006	0.906 ± 0.010	2.320 ± 0.052
6.316	0.252 ± 0.006	0.934 ± 0.010	2.430 ± 0.054
7.192	0.275 ± 0.006	0.981 ± 0.010	2.664 ± 0.056
8.554	0.291 ± 0.007	1.024 ± 0.011	2.886 ± 0.064
9.917	0.297 ± 0.006	1.051 ± 0.011	2.967 ± 0.063

Table 4.2: The transverse temperature, RMS beam size and RMS emittance calculated for each ion number studied.

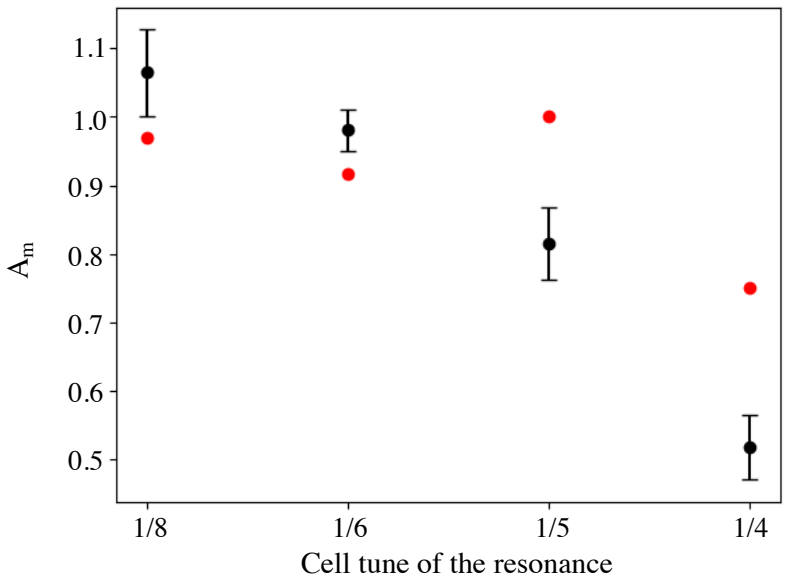


Figure 4.11: Values of A_m from the fitting process in Fig. 4.10, with error bars based on the fit in Fig. 4.10 and the calculation of the emittance at each ion number. The red points represent the theoretical C_m values for the lowest-order space-charge-driven resonance at each cell tune.

4.7 Discussion

In the experimental data in Fig. 4.1, the resonance at a cell tune of $\frac{1}{4}$ shows the characteristic shape of a coherent resonance (i.e. the dip in ion number in tune space is asymmetric, with a much steeper slope for tunes lower than the point where the ion number reaches a minimum), with the addition of ion loss at higher and lower tunes. This additional ion loss is explained by the Warp simulation as from the excitation of a subset of ions through the fourth-order resonance. The shape of the experimental ion-loss data agrees well with the emittance growth in the Warp simulation (Fig. 4.6), supporting the idea that emittance growth is a good predictor for ion-loss; the shape of the resonance does not vary much as the intensity is increased.

The other resonances studied experimentally ($\frac{1}{8}$, $\frac{1}{6}$ and $\frac{1}{5}$) do not have the sharp increase in ion loss that usually indicates a coherent resonance, suggesting that ion loss may not be due to coherent oscillations.

The fitting process was performed for all four resonances and the results of this fit are shown in Fig. 4.11, alongside the C_m factors for purely coherent resonances. The values of A_m extracted from the resonances at tunes of $\frac{1}{8}$ and $\frac{1}{6}$ are consistent with 1, within error, rather than the C_m factor for the coherent resonance which is expected to occur at that tune (also plotted in Fig. 4.11), again suggesting that these resonances may not be coherent. As it cannot be claimed that the excitation of a subset of particles is simply an incoherent effect, as the motion of these particles affects the rest of the beam through the Coulomb interaction, it is interesting to note that the peak ion loss still occurs approximately at the tune with the highest particle density (see Fig. 4.11).

A value of $A_m = 0.517 \pm 0.091$ is extracted for the $\frac{1}{4}$ resonance. This is smaller than the other resonances and indeed smaller than the analytically predicted value of 0.75. This agrees with the Warp simulations, we expect to see a smaller value than theoretically predicted due to the fourth-order resonance first increasing the emittance of the beam and the stopband width.

Any resonances present in an LPT are clearly complex and the product of competing sources of perturbation, as in an accelerator. Whether these resonances are coherent or incoherent, the values of A_m presented in Fig. 4.11 show the relative location of the beam loss for a resonance of a given order in a Gaussian beam. These factors help us understand the real behaviour of an accelerator and are directly relevant in future accelerator design.

Further work is possible to build on this study. The strong resonances at cell tunes of $\sim \frac{1}{4}, \sim \frac{1}{6}$, and $\sim \frac{1}{8}$ can be studied with a lower storage time to verify that the values of A_m remain unchanged. Further simulation work to study the resonance at a cell tune of $\frac{1}{4}$ at increasing intensities is also desirable to determine the effect of intensity on the relationship between the fourth-order resonance and the envelope instability.

In a recent paper ([79], published after the publication of the work in this chapter), the beam physics group at Hiroshima University tested the resonant condition proposed in Eqn. 4.10 through a series of short (200 alternating gradient focusing periods) simulation studies using Warp. These simulations used three different distributions, Gaussian (with the tail truncated at 1% to avoid complications from incoherent oscillations of the tail), waterbag and parabolic, to study externally driven resonances of order $m = 2$, $m = 3$ and $m = 4$. The centre of the stopband was defined as the point at which the emittance growth first exceeded 1%. From these simulations, the C_m factors were extracted. The results for beams with equal transverse tunes, for the three different particle distributions and perturbation orders, are reported in Table 4.3.

The apparent reversal in the $C_1 < C_2 < C_3$... trend for the Gaussian distribution is attributed to the tails of the distribution lowering the C_m factor. There is a notable difference between these simulation results and our experimental conclusions. These simulations also appear to contradict an earlier experimental work from the same group ([41]), where the splitting of a resonance in two, with loss occurring at two different cell tunes, is attributed to the difference in the C_2 and C_4 factors. In [41], where a Gaussian distribution is used, the fourth-order resonance appears at a larger bare cell tune, which is only possible for a larger C_m factor. This difference in results may be due to limited simulation length, or due

Distribution	$m = 2$	$m = 3$	$m = 4$
Gaussian	0.78 ± 0.05	0.77 ± 0.06	0.71 ± 0.06
Waterbag	0.71 ± 0.04	0.87 ± 0.03	0.92 ± 0.01
Parabolic	0.73 ± 0.05	0.85 ± 0.04	0.87 ± 0.02

Table 4.3: The values of C_m for round beams extracted from simulation in [79].

to a fundamental difference between the locations of the largest emittance growth and the greatest ion loss.

Highlighting the ongoing debate over the mechanism of particle loss in intense beams, a comment on reference [79] was recently published ([103]), questioning the validity of the C_m values extracted in the case of a Gaussian beam. They argue that an incoherent picture of particle loss, as given in reference [121], is sufficient to describe particle loss over long timescales, and is not described well by short Warp simulations. In reference [121], a frozen space-charge model and the incoherent excitation of particles is used to describe a resonance driven by sextupoles in the SIS18 synchrotron at GSI, accurately describing the tune of greatest particle loss. They find that in both experiment and simulation, for a coasting beam, the presence of space charge mitigates beam loss, due to amplitude-dependent detuning (Note: in the data presented in Fig. 4.1 we see no mitigation of the resonance at a tune of $\frac{1}{3}$ with additional space charge, in fact, the fractional ion loss increases by a small amount). However, they also acknowledge that a frozen space-charge model is not sufficient to accurately describe the total amount of beam loss. The authors of the original publication respond in reference [122], clarifying their results further, and arguing that their mechanism for beam loss also well describes the experiment at GSI.

Furthermore, the publication [79] reiterates the difficulties in experimentally measuring C_m factors. The Beam Physics group at Hiroshima University have recently built a multipole trap (discussed further in Chapter 7) capable of exciting higher-order resonances externally. This will allow higher-order resonances to be driven at arbitrary tunes. Using the above analysis method it should be possible to determine more accurate C_m values. Additionally, there is the possibility of detecting higher-order coherent modes of oscillation (if they are present) using an extension of the method presented in [78], in which the quadrupole

oscillation mode is detected using the confining rods.

To understand fully the mechanism behind beam loss at these resonances, further diagnostics are required in the experimental setup. Further diagnostics would also allow for an emittance measurement to be made at each ion number, which would improve the accuracy of the extracted values of A_m.

4.8 Tune splitting

Once the initial commissioning of the IBEX experiment was completed and we had successfully performed a range of tune scans, shown in Appendix A.1, I used the IBEX trap to study the resonance at a tune of 0.25, using both equal and unequal tunes in the transverse directions.

This experiment was the first performed using IBEX and was primarily to test our understanding of the system, as well as the ability to create predefined tunes precisely, as described in Section 3.5.1. This experiment was performed before the MCP was installed, so ions were detected using the Faraday cup.

The experiment is an interesting step forward from the work described in the previous section, as analytically two different values of C_m are predicted for equal and unequal transverse tunes, as shown in Table 4.4. Many accelerators operate with different tunes in the x and y directions to avoid coupling resonances, so this study is directly relevant for real machines. Having previously found signs of coherent oscillation at a cell tune of 0.25, we were interested in testing the analytic predictions for these two values quantitatively, to see if, as analytically predicted, the value of A_m is smaller for the case of unequal tunes than for equal tunes.

As the MCP, which is required for detailed calibration of the trap, had not been installed, we chose to simply study the relative magnitude of A_m in each of the two cases, finding the ratio $A_{2_{\text{unequal}}}/A_{2_{\text{equal}}}$.

Where equal transverse tunes were studied, a voltage of $V_Q(t) + V_{\text{DC}}$ was applied to the rods and the amplitude of $V_Q(t)$ $(= V_{\text{rf}} \cos(\omega_{\text{rf}} t))$ was used to vary the tune. In the unequal-tune case, a voltage of $V_Q(t) + V_{\text{DC}} \pm U$ was applied to the rods, where $\pm$ denotes the difference between the rod pairs, and U is a small DC voltage. The voltage U allowed different tunes in the horizontal and vertical directions. Examples of the voltages applied are shown in Table 4.5. The required voltages were found using a Newton-Raphson root finder [123].

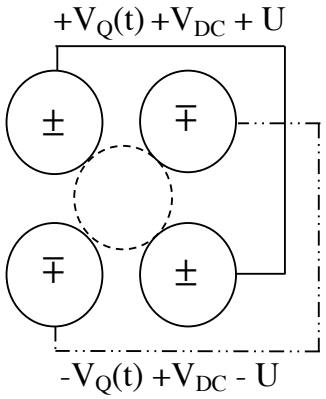


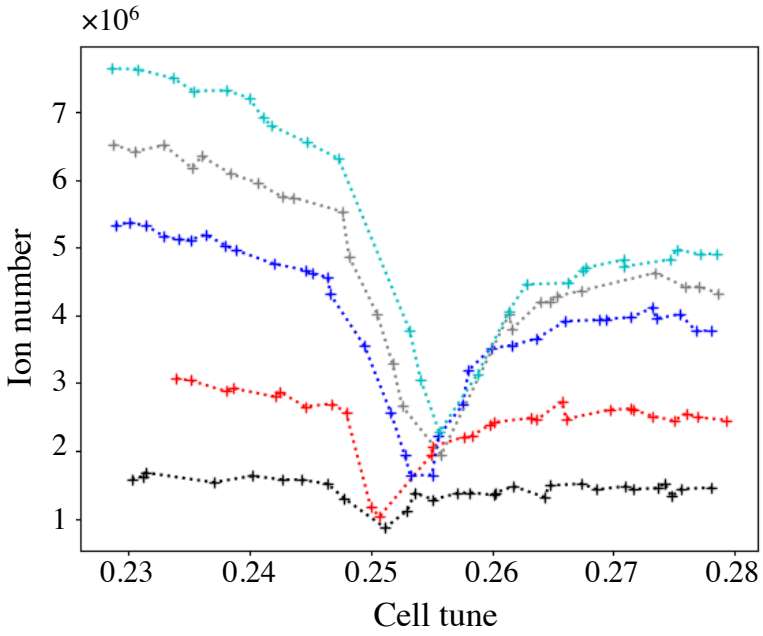
Figure 4.12: Diagram showing the voltages applied to the IBEX rods to create unequal transverse tunes.

C_m (1D)	C_m (2D equal tunes)	C_m (2D unequal tunes)
$\frac{3}{4}$	$\frac{3}{4}$	$\frac{5}{8}$

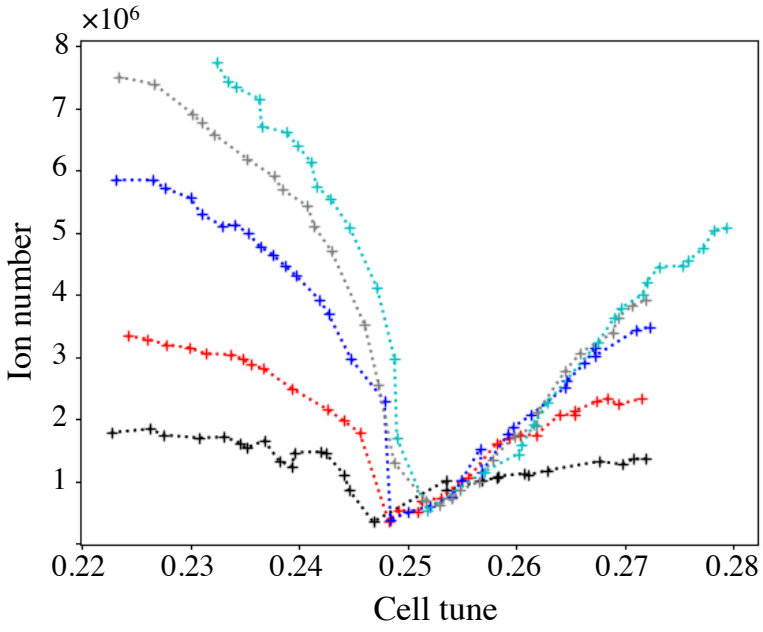
Table 4.4: The difference in C_2 for the cases of equal and unequal tunes ([47]).

Experiments with unequal transverse tunes have previously been performed on S-POD. In reference [105], 2D tune scans at three different intensities are shown, however, I am not aware of any attempt to extract numerical values to describe this qualitative data. The experiment described in this section was the first time that differing transverse tunes were created using the IBEX trap.

To study the location of the resonance at a cell tune of 0.25, with equal and split transverse tunes, experiments were performed at a range of tunes and intensities. The number of ions in the trap, and therefore the intensity, was controlled by the amount of time for which the electron gun was on. Although ion numbers slightly greater than 10^7 are achievable using IBEX, these ion numbers were found to be less reproducible for a given electron-gun time (shown in Section 3.2), so were not used in this experiment. Alternating gradient focusing was achieved by applying a time-varying sinusoidal voltage to the confining rods. At a given intensity, the ions were accumulated at a cell tune of 0.15 in both the horizontal and vertical directions ($U = 0\,\mathrm{V}$, frequency $=1\,\mathrm{MHz}$). The tunes were then ramped to the tunes of interest over 100 rf periods following the method described in Section 4.3.



(a) Unequal transverse tunes.



(b) Equal transverse tunes.

Figure 4.13: A selection of experimental data showing ion loss against horizontal cell tune for the resonance at a cell tune of ~ 0.25, in the case of equal and unequal transverse tunes, where the vertical cell tune is fixed at 0.15. Each coloured line represents a different number of accumulated ions.

V_{rf} (V)	**U** (V)	**Vertical tune**	**Horizontal tune**
55.953	3.407	0.150	0.251
56.249	3.501	0.150	0.253
56.397	3.545	0.150	0.255

Table 4.5: Example voltages for unequal cell tunes, where the rf voltage is a sinusoid with a frequency of 1 MHz.

In the case of equal transverse tunes, the tunes were altered over 100 rf periods by only varying the voltage, V_{rf}, applied to the rods so that the tunes in both transverse directions remained the same. However, to create unequal tunes, V_{rf} was changed and a small DC offset, U, was introduced, meaning that the horizontal tune was altered while the vertical tune was fixed at 0.15. Using this method, at each intensity the ion distribution was ramped to many different tunes across the resonance.

At the tune of interest, the ions were stored for 100 ms and extracted onto the Faraday cup. To study a different tune, the process was repeated, creating new ions using the electron gun. It was confirmed experimentally that the same number of ions were stored after ramping to a cell tune slightly below the 0.25 resonance in both the equal and unequal-tune cases.

The voltages, after amplification, were recorded using a high-precision oscilloscope. Each data point in the waveform was then converted into a transfer matrix and used to calculate the tune in the trap. The ion-loss data for a number of cell tunes and a range of intensities are shown in Fig. 4.13a and Fig. 4.13b, for the unequal-tune and equal-tune cases, respectively.

We were able to confirm using the oscilloscope trace that the vertical tune was held at 0.15. As we were interested only in the cell tunes around 0.25, we did not scan the full tune space in each experiment, which is reflected by the limited number of data points in Fig. 4.13a and Fig. 4.13b. Despite the limited tune region explored in the experiment, the total ion number originally stored was known due to the linear relationship between electron-gun duration and ion number, shown in Fig. 3.3. Data shown were averaged over five experiments at each tune.

From Fig. 4.13a and Fig. 4.13b, it is apparent that a large source of error is the limited

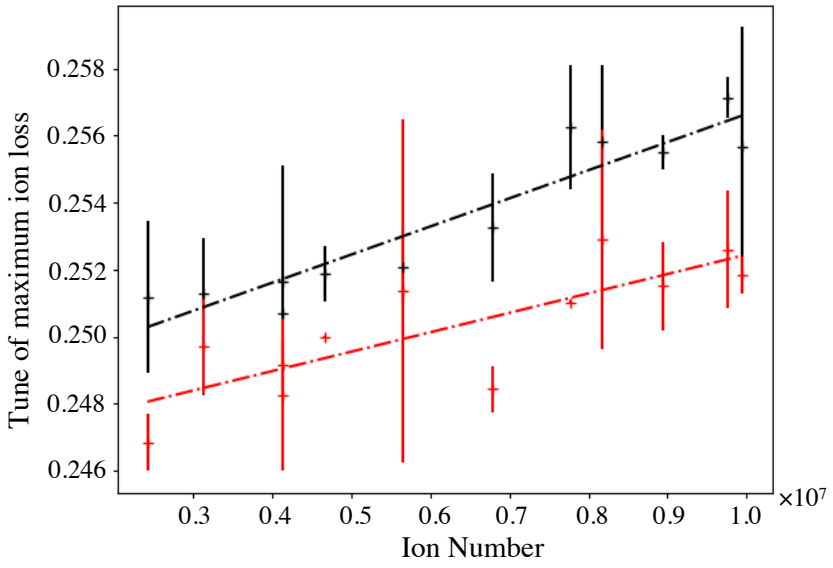


Figure 4.14: Ion number against the tune corresponding to the greatest ion loss. Red points correspond to equal tunes and black points to the unequal-tune case. The dashed line shows the linear fit for each case.

number of data points, resulting in uncertainty in the tune value for which maximum ion loss occurs. To quantify this error, I fitted to the ion-loss data with a skewed Gaussian distribution. The error was then taken to be the difference between the minimum of the fitted curve and the minimum data point.

Figure 4.14 shows the cell tune at which the minimum number of ions was extracted from the trap plotted against the ion number. The error bars describe the distance from this point to the minimum of the fitted curve.

Figure 4.14 contains data points at which maximum ion loss occurs at cell tunes smaller than 0.25. This is because the data was taken before the installation of the MCP, meaning that only ion numbers greater than $\sim 10^6$ were detectable. Due to this, the calibration at low ion number was imperfect, as space-charge forces were still present (the calibration process is described in detail in Section 3.5). However, this does not impact this qualitative study.

It is immediately obvious from the comparison of Fig. 4.14 with Table 4.4 that the experimental data does not match the analytical prediction, which states that the unequal tune resonance should occur at lower cell tunes.

4.8.1 Simulation

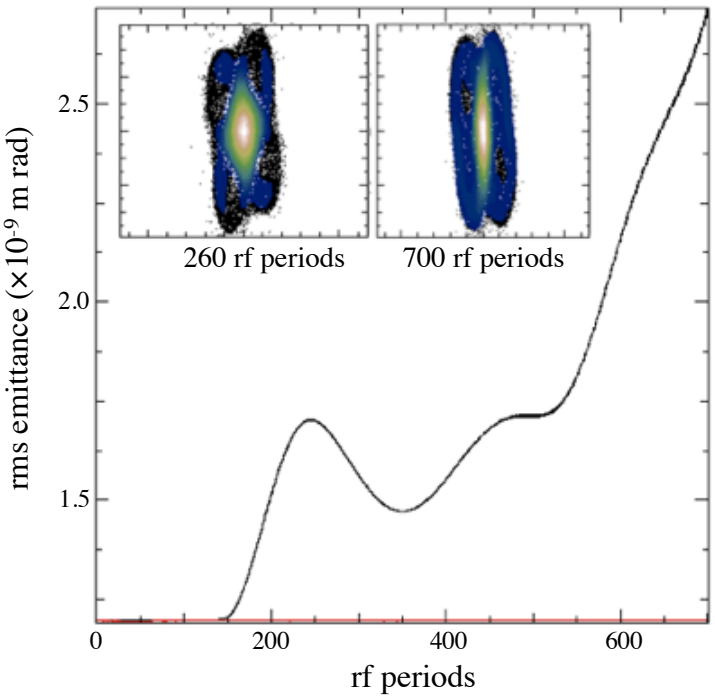


Figure 4.15: The emittance growth over time at a cell tune of Q_x =0.254, Q_y =0.15 The black line shows horizontal emittance and the red line the vertical emittance. Insets show the horizontal phase space at two different rf periods.

To understand the experiment further I performed a series of simulations using Warp, again using only 700 rf periods, and recorded the emittance growth of the ion distribution. An ideal Paul trap was again simulated, with no misalignment in the confining rods.

A matched ion distribution was created in the simulated trap at a cell tune of 0.15. These ions were stored for 50 rf periods before the tune was ramped to the value of interest over 100 rf periods. The ions were then stored at the final tune for 550 rf periods so that the simulation ran for 700 rf periods in total. The phase space and the emittance in both transverse planes were recorded, as was any ion loss. This method is the same as described in Section 4.4.

Figure 4.15 shows the emittance growth for the unequal-tune case at the cell tune corresponding to maximum emittance growth, as well as the horizontal phase space at two points in this simulation. Figure 4.16 shows the comparison between the emittance growth for the

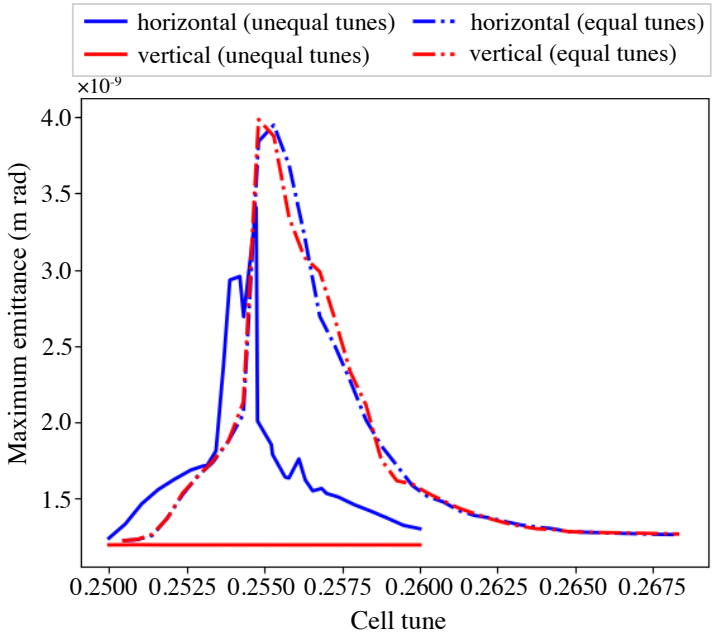


Figure 4.16: Comparison of emittance growth in simulation for equal and unequal tunes.

equal-tune and unequal-tune cases.

Figure 4.15 shows that in simulation, for the unequal-tune case the distribution is first excited by a fourth-order incoherent resonance, which at the tune of maximum emittance growth becomes a second-order coherent excitation at longer time scales. This is also true for equal tunes, as shown in Section 4.5.

Figure 4.16 shows that the maximum emittance growth with unequal tunes is expected to occur at a slightly smaller tune than that of equal tunes (even when the small factor from Eqn. 4.21 is accounted for). This is equivalent to a slightly smaller factor A_m in the unequal-tune case, agreeing qualitatively with the analytical prediction of $C_2 = 0.625$ for the unequal-tune case and $C_2 = 0.75$ for the equal-tune case [96]. For these analytical values, $C_{2_{\text{unequal}}}/C_{2_{\text{equal}}} = 0.83$.

4.8.2 Discussion

There are two main features of Fig. 4.14, which shows the results of this experiment. Firstly, the equal tune resonances occur at lower cell tunes than the unequal tune resonances.

Secondly, there is a difference in the gradients of the two linear fits to the data.

The fact that the equal-tune resonances appear to occur at lower cell tunes than the unequal-tune resonances suggests that the A_m factor is smaller for the equal-tune case, disagreeing with the analytical prediction. However, such a difference could also be explained by a difference in stopband width or a slight systematic offset from the calculation of the tune from the oscilloscope traces. Due to this, the linear fits shown in 4.14 were not forced to pass through the same cell tune value at an ion number of zero.

From the gradients of the two linear fits in Fig. 4.14,

$$\frac{\text{Gradient for unequal tunes}}{\text{Gradient for equal tunes}} = 1.4. \tag{4.20}$$

However, for fixed transverse emittance and intensity, a different transverse tune will lead to a different beam size, as a direct consequence of the difference in the average beta function. This is accounted for in the calculation of the RMS tune shift, ΔQ_x, by the factor,

$$\left\langle \frac{a}{a+b} \right\rangle \approx \frac{1}{\langle 1 + \frac{b}{a} \rangle} = \frac{1}{\sqrt{\langle \beta_y \rangle \epsilon_y / \langle \beta_x \rangle \epsilon_x} + 1}, \tag{4.21}$$

where the angular brackets denote the average [22]. As $\epsilon_x = \epsilon_y$, the factor in Eqn. 4.21 equals 0.5 in the equal-tune case and 0.463 in the unequal-tune case, where the average beta functions at cell tunes of 0.15 and 0.25 were used. These average beta-function values are shown in Fig. 4.3. The factor given by Eqn. 4.21 affects the location of the resonance in tune space, as illustrated clearly by simulations produced by the Beam Physics group at Hiroshima University, in [79].

For the tunes studied, this gives an extra factor of 1.08 in the ratio shown in Eqn. 4.20, so that experimentally

$$\frac{A_{2_{\text{unequal}}}}{A_{2_{\text{equal}}}} = 1.6. \tag{4.22}$$

The simulation and analytical prediction do not match with the experimental results, as shown in Fig. 4.14. Experimentally, resonances in the unequal-tune case seem to occur at larger cell tunes with increasing intensity. The ratio in Eqn. 4.22 shows that we find a larger value of A_m for the unequal-tune case.

However, it is emittance growth that is studied in simulation, not the ion loss. Over the 700 rf periods of the simulation, no ions are lost at the location of the coherent resonance due to the limited number of rf periods. This lack of ion loss may explain the difference between the simulation and the experimental results, as currently the impact of ion loss on continual emittance growth is not well understood. Neither the analytically predicted C_m values, nor the simulation, include the effects of beam loss. In the unequal-tune case, fewer ions will be lost from the distribution as the beam is only excited in one dimension, which may affect the emittance change and tune depression of the distribution as a whole.

Longer simulations in which ion loss could be observed were not performed as they would have taken a prohibitively long time to run. Furthermore, the IBEX Paul trap was designed to be used instead of such simulations, and so results should be verified through further experimentation. As there are now two Paul traps used for accelerator physics studies, this experiment should be repeated on the S-POD trap to confirm the observed results. The addition of the MCP to IBEX, and the development of the experimental techniques described in Chapter 6, represents a significant step forward experimentally. A possible future study is to use the MCP and an image of the ion distribution to study the relationship between emittance growth and ion loss in intense beams.

4.9 Chapter summary

This chapter presents the first quantitative study of the interaction and difference between coherent and incoherent resonances in a Paul trap. Additionally, simulation results were used to explain why the experimental results differ from those theoretically predicted. An LPT has previously been only qualitatively used to study the behaviour of a beam, showing the

shift in resonance location with beam intensity. Here we extract numerical values describing the locations of resonances at high intensity. We have shown through simulation using the PIC code Warp that in an LPT, as in an accelerator, we expect to see coherent oscillation at a cell tune of $\frac{1}{4}$. Here the second-order coherent resonance competes with the incoherent fourth-order resonance, which has a wider stopband. For 2×10^6 ions, simulations show that, even at tunes where coherent oscillations occur, ions are first excited by the incoherent fourth-order resonance. By analysing the tunes of trapped ions with NAFF, the tune footprints at several tunes across the resonance were extracted. This showed that the peak in emittance growth did not occur at the location predicted by the C_m factor for coherent resonances. We identified that this was due to both the finite width of the envelope instability and the fourth-order excitation.

The shape of the ion loss as a function of cell tune at the $\frac{1}{4}$ resonance agrees well with the shape of increased emittance growth in the Warp simulation. The experimental results show that the C_m factor for a second-order coherent resonance does not accurately predict the location of the resonance due to the interaction between the fourth-order incoherent resonance and the second-order coherent resonance at this tune, agreeing with Warp simulation predictions.

Simulation over 700 focusing periods did not show any signs of coherent oscillation for the resonances at cell tunes $\frac{1}{3}$ and $\frac{1}{6}$. The experimental ion loss for the resonances at cell tunes $\frac{1}{3}$ and $\frac{1}{6}$ did not show the characteristic shape of coherent resonance. Furthermore, the location of the peak in ion loss occurred in a location consistent with the RMS of the tune distribution, suggesting that at this tune, coherent oscillation may indeed be Landau damped for a Gaussian beam.

I performed an additional experiment using the IBEX trap, studying the resonance at a cell tune of $\frac{1}{4}$ with unequal transverse cell tunes. I found that my data qualitatively disagrees with both analytical results and simulation, suggesting that short simulations that study emittance growth are not sufficient to describe particle loss over large time scales.

Chapter 5

Future high-intensity accelerators

In this chapter, I introduce the concepts of Nonlinear Integrable Optics (NIO) and Quasi-integrable optics (QIO), and their application to intense beams. I then briefly describe the two accelerators in which QIO will be tested and outline the previous simulation studies that have been performed for QIO. In Section 5.5, I show how the octupole strength required to test QIO using IBEX can be derived from the Hamiltonian of a Paul trap, and explain the benefits of using a Paul trap to test this concept.

5.1 Introduction to novel high-intensity accelerators

High-intensity hadron accelerators must deliver both high power and small emittance. The choice of machine depends on several parameters, including the energy of the beam and the expertise of the institute where the accelerator will be built [124]. For higher particle energies synchrotrons are used, as greater acceleration can be more efficiently achieved through the repeated use of accelerating cavities. However, linacs tend to be able to provide smaller emittance beams, as the injection process in a synchrotron often leads to emittance growth. The specific requirements imposed by the varied applications of intense beams continue to drive the development of new types of machines.

There are currently two proposals (one in the UK and one in the USA) for future high-

power hadron accelerators that use novel accelerator concepts. The first, in the UK, is an upgrade to the ISIS spallation neutron source. The ISIS accelerator at the Rutherford Appleton Laboratory will soon be upgraded to provide MW beams. A Fixed Field Alternating Gradient (FFA) accelerator is a potential option for the new ring. Although only a handful of FFAs have been built, an FFA ring may provide several advantages for ISIS users, such as high average current, good energy efficiency, and a high repetition rate, leading to a flexible time structure of pulses [125].

At Fermilab, the goal of the US high energy physics program over the coming 20 years is to measure the mass hierarchy and CP violation of neutrinos. To achieve this, the Fermilab accelerator complex will be upgraded to provide protons at higher intensities (multi MW) for the Deep Underground Neutrino Experiment (DUNE) [126]. As intensity is fundamentally limited by the beam physics effects discussed previously in this thesis, interesting new designs for high-intensity machines are under investigation. One of these designs relies upon Nonlinear Integrable Optics (NIO), which will be the topic of the remainder of this thesis.

The flexible nature of the IBEX experiment makes exploration of these novel concepts possible. Aspects of FFA accelerators have been studied by the Oxford, Hiroshima, and RAL beam physics groups previously (in [75]), but will not be explored further in this thesis. Instead, I will focus on demonstrating the feasibility of testing NIO in a Paul trap, as such an accelerator physics concept stands to benefit from the kind of proof-of-principle tests which IBEX can provide.

5.2 The theory of Nonlinear Integrable Optics

5.2.1 What is an integrable lattice?

A system consisting of N degrees of freedom is integrable if there are also N linearly independent invariants of the motion. Consequently, a time-independent system in one dimension is always integrable [118]. A 2D Hamiltonian is, therefore, integrable if it can be transformed

into a set of coordinates where it is separable into two independent equations. A coordinate transform capable of this is often hard to find, meaning that there is no simple way to find the invariant of a system and that it is difficult to prove that a given Hamiltonian is integrable.

Accelerators are primarily designed using linear components, such as dipole and quadrupole magnets. The equations of motion describing a single particle travelling in a linear accelerator lattice are integrable. As there is no coupling between the horizontal and vertical directions, two uncoupled Hill's equations describe the motion of such a particle [127].

Through the introduction of the Twiss parameters α, β, and γ, the Hamiltonian associated with the motion of a single particle in a linear lattice can be made time-independent. Furthermore, it can be separated into two equations, the horizontal and vertical Hamiltonians. These equations are then solvable so that the motion of the particle can be perfectly described. The invariant of such a system is the Courant-Snyder invariant.

Realistically, accelerators cannot be constructed only from linear magnets, as linear systems are susceptible to perturbations from a range of sources, leading to resonances, as discussed in Section 1.4.4, and later in Chapter 4.

Furthermore, sextupole magnets are generally required to correct the spread in tune associated with a range of particle momenta, known as the chromaticity. Higher-order magnets can be used to create a tune spread within the beam, leading to Landau damping (Section 1.6). However, using these strong, 'thin', nonlinear components limits the phase space where the particle motion is non-chaotic, reducing the dynamic aperture [127].

As nonlinear components (which break the integrability condition) are essential additions to modern linear lattice designs, either intentionally or through error, it is desirable to make an integrable lattice which is inherently nonlinear, providing all the advantages of a large tune spread without limiting dynamic aperture. It is possible to find a combination of nonlinear fields along the particle orbit that leads to a set of equations with two invariants (here longitudinal motion is neglected and only two degrees of freedom are considered, horizontal

and vertical). The main challenge in doing this is that the fields must also obey the Laplace equation, so that they are physically realisable within an accelerator, and result in stable orbits.

Previous attempts have been made to find a fully integrable nonlinear accelerator lattice, for example in [128]. In [127], Danilov and Nagaitsev simplify the problem by considering a focusing lattice that provides a thin-lens linear kick, followed by a thick nonlinear element that creates the integrable potential. If the linear kick meets several conditions, described in more detail in Chapter 6, then the motion through the nonlinear region is quasi-periodic.

If the nonlinear lattice is integrable, then even when errors such as momentum deviation, magnet misalignment, and space charge are included, the system will always be close to an integrable system, provided that these errors are small. According to the KAM theorem, this ensures that the particle motion remains almost regular [129], which is not true for a purely linear system [130]. Therefore, resonances are absent, and the large tune spread created by the nonlinear lattice can be used to suppress collective instabilities without loss of dynamic aperture.

5.2.2 Danilov and Nagaitsev's integrable solution

Considering only the effects of transverse fields that satisfy the Laplace equation, Danilov and Nagaitsev produce a time-dependent Hamiltonian that is fully integrable.

The Hamiltonian for a linear lattice with equal focusing in the transverse planes is given by

$$H = \frac{p_x^2}{2} + \frac{p_y^2}{2} + K(s)(\frac{x^2}{2} + \frac{y^2}{2}), \tag{5.1}$$

where $K(s)$ is the strength of the linear focusing. The coordinate transform

$$z_N = \frac{z}{\sqrt{\beta(s)}}, \tag{5.2}$$

$$p_N = p\sqrt{\beta(s)} - \frac{\beta'(s)z}{2\sqrt{\beta(s)}}, \tag{5.3}$$

where z is either x or y, and p is either p_x or p_y, is introduced. Here $\beta(s)$ is the horizontal or vertical beta function, as a function of position in the ring, and

$$(\sqrt{\beta})'' + K(s)\sqrt{\beta} = \frac{1}{\sqrt{\beta^3}}. \tag{5.4}$$

The Hamiltonian can be expressed as

$$H_N = \frac{1}{2}(p_N^2 + z_N^2). \tag{5.5}$$

In Eqn. 5.4, the differentiation is with respect to s, and the betatron phase is described by $\phi' = \frac{1}{\beta(s)}$. From this, two invariants can be found.

Adding an s-dependent potential to the Hamiltonian in Eqn. 5.1 gives,

$$H = \frac{p_x^2}{2} + \frac{p_y^2}{2} + K(s)(\frac{x^2}{2} + \frac{y^2}{2}) + V(x, y, s). \tag{5.6}$$

Making the same coordinate change again, and assuming that the beta functions in the horizontal and vertical directions are the same ($\beta_x(s) = \beta_y(s) = \beta(s)$), the new Hamiltonian can be expressed as

$$H_N = \frac{p_{xN}^2 + p_{yN}^2}{2} + \frac{x_N^2 + y_N^2}{2} + \beta(\phi)V[x_N\sqrt{\beta(\phi)}, y_N\sqrt{\beta(\phi)}, s(\phi)], \tag{5.7}$$

which can be simplified to

$$H_N = \frac{p_{xN}^2 + p_{yN}^2}{2} + \frac{x_N^2 + y_N^2}{2} + U(x_N, y_N), \tag{5.8}$$

where

$$U(x_N, y_N) = \beta(\phi)V[x_N\sqrt{\beta(\phi)}, y_N\sqrt{\beta(\phi)}, s(\phi)]. \tag{5.9}$$

Since $U(x_N, y_N)$ is time-independent, the system has at least one invariant of the motion, the Hamiltonian.

Fully integrable solution

A subset of potentials, $U_{\mathrm{I}}(x_N, y_N, \phi)$, are separable in some set of variables and are therefore fully integrable. In [127], Danilov and Nagaitsev find solutions that are separable for three different sets of coordinates, elliptical, polar, and parabolic. Further details of this are given in Appendix A.3.

Quasi-integrable solution

Although potentials with two integrals of motion do exist, 2D systems with only one invariant are slightly easier to realise in practice. Although these potentials are not fully integrable, the particle motion is stable about a closed orbit [127]. One example of this is an octupole potential of the form

$$V(x, y, s) = \frac{k}{\beta(s)^3}(\frac{x^4}{4} + \frac{y^4}{4} - \frac{3x^2y^2}{2}). \tag{5.10}$$

The coordinate transform in Eqn. 5.2 and Eqn. 5.3 can be applied to the octupole potential, giving

$$U(x_N, y_N) = k(\frac{x_N^4}{4} + \frac{y_N^4}{4} - \frac{3x_N^2y_N^2}{2}). \tag{5.11}$$

This potential is time-independent, ensuring at least one invariant of the motion. This is referred to as quasi-integrable nonlinear optics (QIO).

Achieving equal focusing in the horizontal and vertical planes

An accelerator lattice with equal focusing in the transverse directions in the region between the nonlinear inserts (a requirement of NIO), can be created either using solenoid magnets or through strong focusing. A strong-focusing lattice of quadrupole magnets should have the transfer matrix of a thin, axially symmetric lens. Such a strong-focusing lattice, called a T-insert, should leave a drift region of equal beta functions where the nonlinear magnets can be installed. Further information regarding these lattices, and details of the implementation of the T-insert lattice in IBEX, are given in Chapter 6.

5.2.3 Nonlinear decoherence and Landau damping

The effect of a nonlinear integrable lattice is that particle trajectories are bounded, but the particle distribution still has a large spread of frequencies. A periodic perturbation can still excite particles within the distribution, but as these particles oscillate at larger and larger amplitudes, their tunes will change and the particles will no longer be excited by the resonance. This is known as nonlinear decoherence (see Section 1.6), which is a separate effect from Landau damping. Nonlinear decoherence is a property of the accelerator lattice, whereas Landau damping depends upon properties of the confined particles [131]. Fortunately, this means that the effects of nonlinear decoherence can be observed regardless of the distribution of particles.

In reference [131], nonlinear decoherence is demonstrated using a halo driven by the breathing of a central distribution (due to betatron oscillation) and a fully integrable lattice. A "pre-halo" of particles is first introduced into a linear lattice with a mismatched beam core. The mismatched beam-core's periodic oscillations drive the pre-halo to large amplitudes. However, when an integrable elliptical lattice is used instead, the beam tends towards a stationary solution. This work was extended in reference [132], where the QIO lattice was simulated. The pre-halo starts to show a distinctive fourth-order shape, due to space-charge forces, however, the formation of a larger halo is still suppressed.

In the nonlinear simulations described in reference [132], the beam must be matched to the nonlinear elliptical lattice; details of how this is achieved are given in references [133] and [134].

5.3 An introduction to IOTA and UMER

Since the discovery of realisable NIO lattices in 2010, two accelerators have made significant progress towards studying integrable optics. The Integrable Optics Test Accelerator (IOTA) has been built specifically for this purpose, and the University of Maryland Electron Ring (UMER) has been adapted to study QIO. In this section, I briefly describe both experiments to report the work already done in the field of integrable optics and to highlight how testing QIO in a Paul trap can contribute to the field.

5.3.1 IOTA

IOTA is a storage ring at Fermilab, US, built to study advanced beam physics [135]. The IOTA ring is compact, with a circumference of 40 m, and aims to test the Nonlinear Integrable Optics (NIO) theory using an elliptical potential, as well as several other new concepts, such as stochastic cooling and the use of electron lenses to introduce a tune spread. The ring will first operate with 150 MeV electrons from the FAST LINAC, and then later with 2.5 MeV protons.

A large amount of research and development guided the design and manufacture of the IOTA ring. IOTA aims to test both the fully integrable and quasi-integrable potentials previously discussed. The design and manufacture of a lattice with the required precision for the fully integrable case is a challenge, and so the first stage of the experiment will use octupole magnets to test the quasi-integrable theory [126, 136].

As IOTA is a small ring, it has a large natural chromaticity. However, in reference [137] it is shown that both dispersion and chromaticity break integrability for NIO. To regain

integrability, zero dispersion is required in the region where the nonlinear magnet will be installed, and the chromaticity in the transverse planes must be equal. Normal chromatic correction schemes can still be applied but they may reduce the dynamic aperture of the ring.

IOTA octupole magnets

In the elliptical nonlinear magnets designed for IOTA, both the field strength and the magnet aperture must vary across the nonlinear region [138, 139]. Due to this, a total of 20 smaller magnets will be installed across the section to approximate the ideal elliptical potential. These magnets are designed so that the field does not deviate by more than 1% within the good field region, and so that the good field region extends as close to the physical aperture as possible. The tolerance of the alignment of these magnet segments is 50 μm. Such complex magnets are challenging to create, again motivating the use of octupole magnets to test the QIO case first [140].

The potential created by the elliptical nonlinear magnets can be described in normalised coordinates as

$$U(x_N, y_N) = t \cdot Re\left[(x_N + iy_N)^2 + \frac{2}{3c_I^2}(x_N + iy_N)^4 + \frac{8}{15c_I^4}(x_N + iy_N)^6 + \frac{16}{35c_I^6}(x_N + iy_N)^8 + \dots\right]. \tag{5.12}$$

In the testing of NIO, the nonlinear strength (t, in Eqn. 5.12) will be varied from 0 to 0.5, the same range of strengths will be used for the octupole channel for QIO. The octupole channel to be tested in IOTA consists of 17 identical, air-cooled, octupole magnets. Simulations show that octupole field errors on the order of 10% can be tolerated and should not alter the dynamics of the system [141].

The octupole magnets were designed to be simple. The octupoles sit on a dedicated girder with 10cm between the centres of adjacent magnets (each magnet is 7cm in length, with the

magnetic field extending to 7.5cm), the girder supports the magnets at three points, allowing them to be positioned accurately in three dimensions. The strengths of higher harmonics were measured to be less than 1% for all orders at the reference radius (8.5 mm, 2/3 of the radius of the vacuum chamber), with the largest term $m = 6$ and $m = 12$ [141].

Testing

In 2019 the first tests were performed at IOTA with the octupole inserts. First, the dynamic aperture of the system was studied [142]. Precise and accurate beam alignment is important to ensure that the integrability condition is satisfied. To achieve this IOTA used a range of diagnostics, including wall-current monitors, electrostatic beam-position monitors (BPMs) and synchrotron-light cameras. To determine the dynamic aperture, the beam was kicked out in both planes simultaneously. The strength of the kick was increased until loss of beam lifetime was observed, which defined the limit of the DA. The tune shift was also studied using turn-by-turn data from 17 BPMs. The tests showed that 60% - 70% of the predicted performance from simulation studies was achieved. This reduced performance is thought to be due to power-supply drift issues and lack of chromatic correction. Upgrades, including the addition of six more sextupoles, aim to improve performance.

The decoherence within the lattice was also studied [143]. The beam was again kicked outwards using two kickers, horizontal and vertical. The oscillations of the beam were observed. Faster decoherence was observed with the nonlinear magnet switched on; however, observations of this decoherence did not match well with predictions from models.

In both the DA and decoherence studies, significant beam loss was observed when the octupole channel was switched on [142, 143].

5.3.2 UMER

The University of Maryland Electron Ring (UMER) is an extremely small (11.52 m diameter) ring designed to study space-charge physics. The ring, like IBEX, is a scaled experiment.

However, UMER is used to store 10 keV electrons. This extremely low electron energy results in large space-charge forces of $\frac{Q}{Q_0} = 0.85 \rightarrow 0.14$ [144, 145]. Any space-charge physics studied will also be relevant to higher-energy hadron machines [146].

The ring is relatively low cost and flexible, using printed circuit quadrupoles [144]. One unique feature of the UMER ring is the very small rigidity of the beam. The beam is significantly affected by background fields, such as the earth's magnetic field, which contributes $\sim$ 20% of the bending force around the ring. As a result, electrons no longer travel in straight lines between bending magnets [147]. In the context of QIO, this introduces a further challenge, as the beam must be well centred through the octupole region otherwise the dynamic aperture is significantly reduced [118, 148]. Because of this, precise beam steering is required, which is a challenge in a small ring with few corrector magnets and a low number of BPMs. A Robust Conjugate Directional Search (RCDS) optimiser is used to find the best closed orbit [147].

The octupole magnets in UMER are also made from flexible printed-circuit boards (PCBs), which are wrapped around the beam pipe. One advantage of this is that the octupole magnets can easily be overlapped and stacked to create a close approximation to a smoothly varying octupole field [149]. UMER currently uses seven equally spaced octupole magnets to create the strength variation of $1/\beta^3$, which is required to create the time-independent potential (see Eqn. 5.10). The insertion is capable of meeting the octupole requirements within an RMS error of 2% [150]. Simulation using Warp has been used to guide the design choices in the UMER ring. The original design used a segmented octupole insert. Due to space limitations, the longest element that can be placed in UMER is 25 cm long. To create a longer insert, a segmented octupole channel, 64 cm long and including two dipole bends, was designed. This lattice had a fractional tune of 0.263, giving a large tune spread. However, in simulation, this lattice showed significant particle loss along the $Q_x + Q_y = 0.5$ coupling resonance. The beam distribution showed a clear fourth-order shape, suggesting that resonance was driven by the octupole.

Due to this, UMER is currently operating with one shorter octupole insert and a fractional

tune of 0.13 [151, 152]. This tune was chosen as higher tunes require either multiple inserts or a smaller waist in the drift region, leading to a larger beta function in the rest of the ring, which can cause scraping. Furthermore, using the shorter insert allows UMER to operate closer to its normal operating parameters, increasing stability. As UMER has individual power supplies associated with each magnet, it is possible to measure the beta function at each quadrupole, ensuring that the conditions for integrability are met. This measurement has taken place and the octupole channel has been installed. The lattice was then re-optimised to get the best transmission.

In reference [149], an average tune shift of 0.126, approximately half of the maximum predicted value, was observed when a 0.6 mA 10 keV electron beam passed through the octupole channel. In reference [152], these measurements are updated, showing the tune shift in both transverse directions once the steering was optimised.

Investigations into a distributed octupole lattice, with four short octupole magnets placed around the ring with a π phase advance between each octupole, were also conducted at the University of Maryland [153]. This configuration allows minimal disruption to the usual UMER ring; however, the condition $\beta_x = \beta_y$ is not met and the magnets are not capable of perfectly meeting the $1/\beta^3$ requirement. Simulations showed a much larger variation in the invariant in the distributed lattice.

5.4 Past simulation work

Significant simulation work has been attempted to advance the understanding of NIO and QIO. Although much of this simulation work is beyond the scope of this thesis, here, I will summarise the results relevant to testing QIO with IBEX. In Section 7.6 symplectic space-charge simulations are briefly discussed.

Many simulations approximate the T-insert as a thin-lens kick, reducing the computational time required. Reference [134] describes such a method, which is implemented in [154] (a Python script). In [154], a series of "drift kicks" are used to implement the nonlinear

region; the effect of the nonlinear kick given is found by taking derivatives of the elliptical potential with respect to x_N and y_N. I adapted this code to represent the octupole case in a Paul trap and used it to benchmark simulations in Warp (discussed in Chapter 7).

Simulations of QIO all show a distinctive aeroplane-shaped tune spread, similar to Fig. 7.7. Throughout all simulation studies, the three main metrics used to determine the quality of the QIO lattices are: the size of the dynamic aperture, the tune spread, and the conservation of the Hamiltonian over time. The dynamic aperture can be estimated by the distance to the unstable fixed points of the Hamiltonian. Where $p_{xN} = p_{yN} = 0$, the dynamic aperture is given by $|x_N| = |y_N| = 1/\sqrt{2k}$, where k is the strength of the octupole potential from Eqn. 5.11 [126]. This aperture is further reduced to $|z_N| = 0.6/\sqrt{k}$ by a small region where motion is bounded but chaotic.

The dynamic aperture shrinks for octupole-channel configurations with fewer magnets. Although the IOTA octupole channel is not perfectly continuous, it is still expected to show significant improvement over a single octupole, with a larger dynamic aperture and frequency spread [126].

For low octupole strengths, the maximum amplitude of particle oscillations is limited by the physical aperture, and as the strength of the octupole increases so does the tune spread. For large octupole strengths, and therefore tune shifts, the aperture is limited by particle loss on resonances. The optimal octupole strength is that which maximises dynamic aperture and tune spread simultaneously.

Simulations in reference [151] show that at small amplitudes in physical coordinates the particle motion is regular. At larger amplitudes, but still within the DA, the motion is chaotic and bounded, where bounded is defined to mean that a small error in the initial condition grows by less than a factor of 10 over 100 oscillations.

Finally, simulations show that the QIO channel is more robust with respect to small errors in the linear lattice than the NIO channel. Errors of $\Delta Q = 10^{-2}$ in the QIO lattice led to only a reduction in the dynamic aperture of $\sim 10\%$.

5.5 Comparison between an octupole in an accelerator and in a Paul trap

Here, the derivation given in Section 2.2.1, which shows the equivalence between the Hamiltonian of a linear Paul trap and a linearly-focusing accelerator, is extended to include octupole terms. The Hamiltonian in an accelerator, including quadrupole and octupole terms, is

$$H = \frac{p_x^2 + p_y^2}{2} + \frac{1}{2}k_2(x^2 - y^2) + \frac{1}{24}k_4(x^4 - 6x^2y^2 + y^4), \tag{5.13}$$

where

$$k_m = \frac{1}{B\rho}\frac{\partial^{m-1}B}{\partial x^{m-1}}. \tag{5.14}$$

The equivalent Hamiltonian in the Paul trap is

$$H = \frac{p_x^2 + p_y^2}{2m} + \frac{qV_Q(t)}{r_0^2}(x^2 - y^2) + \frac{qV_O(t)}{r_0^4}(x^4 - 6x^2y^2 + y^4). \tag{5.15}$$

Using the change of scale

$$\frac{H}{mc^2} \to H, \quad \frac{p_x}{mc} \to p_x, \quad \frac{p_y}{mc} \to p_y, \tag{5.16}$$

and scaling the independent variable as $\tau = ct$,

$$H = \frac{p_x^2 + p_y^2}{2} + \frac{qV_Q(\tau)}{r_0^2mc^2}(x^2 - y^2) + \frac{qV_O(\tau)}{r_0^4mc^2}(x^4 - 6x^2y^2 + y^4). \tag{5.17}$$

This can then be directly expressed in accelerator terminology

$$k_2 = \frac{2V_Q(\tau)}{mc^2r_0^2}, \quad k_4 = \frac{24qV_O(\tau)}{mc^2r_0^4}, \tag{5.18}$$

when all four rods of the Paul trap are powered.

The IOTA octupole channel built to test the integrable case will have the octupole field strength [155],

$$\frac{\partial^3 B}{\partial x^3} = \frac{16t}{c_I^2}\frac{B\rho}{\beta(s)^3}. \tag{5.19}$$

This gives

$$k_4 = \frac{16t}{c_I^2}\frac{1}{\beta(s)^3}. \tag{5.20}$$

Equating both of these expressions for k_4 gives the strength in the octupole channel as

$$V_O = \frac{2}{3}\frac{mc^2 r_0^4}{q}\frac{t}{c_I^2\beta^3}. \tag{5.21}$$

In the fully integrable case, c_I gives the location of the singularities of the potential. These singularities should correspond with the side of the beam pipe, meaning that in IOTA $c_I^2 = 1$ cm. In reference [155], it is shown that for values of t (nonlinear strength) greater than 0.4, the tune spread does not increase, but the dynamic aperture shrinks.

I used a value of $t = 0.3$ and $c_I = r_0/\sqrt{\beta_{\text{center}}}$, where β_{center} is the beta function at the centre of the drift region, to estimate a reasonable octupole strength to use in initial simulations.

5.6 The benefits and drawbacks of using IBEX to test NIO

The first obvious limitation in using IBEX to test QIO is that it is currently a linear system, in which higher-order multipoles cannot be controlled. However, an upgrade to an octupole trap is possible and is described in detail in Chapter 7. Once we have control over octupole

terms, the advantage of using IBEX to test QIO is the flexibility of the experimental setup; a wide range of experimental configurations can be tested simply by altering the voltages applied to the trap.

So far, the main challenge in testing QIO in UMER is steering the beam correctly through the nonlinear region. IBEX will not face similar issues as particles are not accelerated in a longitudinal direction and therefore focusing is independent of momentum. This also means that IBEX does not experience dispersion or chromatic effects, which are potentially limiting factors in the compact IOTA ring.

In the simulations of NIO, the particle beam must be correctly matched to the lattice, including the nonlinear potential, to avoid beam loss [156]. Additionally, in both reference [142] and reference [143], there is significant beam loss when the octupole channel is switched on. This is tolerable for a low-current, low-energy electron beam, however, when protons are injected into the ring a much more sophisticated matching is required. In IBEX, there is the potential to either accumulate ions with the nonlinear section switched on, or to adiabatically increase the strength of the octupole while studying emittance growth. Such adiabatic manipulations of the beam using IBEX may act as a proof of concept; if they are not possible in the relatively simple IBEX system, then they will not work in real machines with dispersion and chromaticity [157], further detail can be found in Section 7.4.1.

Finally, recent work questions whether the number of nonlinear magnets used can be reduced. In reference [158], symplectic integrators are used to design lattices that preserve the Hamiltonian over realistic time scales. Two different schemes using octupoles are suggested. In the first of these schemes, five nonlinear magnets are used, with unequal spacing and with a different scaling of the octupole strength with beta function:

$$V(x, y, s) = \frac{h a_0}{4\beta^2(s)}[x^4 + y^4 - 6x^2y^2], \tag{5.22}$$

where a_0 is a strength parameter and h is related to the magnet spacing. The second suggested scheme uses only three octupole magnets. Furthermore, this method of lattice

design is independent of the nonlinear element, and so sextupoles could also be used. The extreme flexibility of the IBEX system means that testing these alternative configurations should be straight forward.

In the 2014 workshop on High-Intensity, High-Brightness and High-Power Hadron Beams, investigations into studying NIO in a Paul trap were strongly encouraged by the community:

> "Paul traps ... with adaptable electric focusing might prove amenable to economically explore long path length transport aspects of NIO. We advocate exploring this more fully. Given funding issues with IOTA, trap experiments might provide a more rapid and economical partial step to explore concept viability" [159].

There are, however, some challenges in using IBEX to test QIO. Firstly, diagnostics are limited as the MCP and Faraday cup both give an integrated image of the beam, meaning that it is difficult to measure the beta function at a single point in time. This issue is addressed in Section 6.4, but this may limit the ways in which QIO can be tested.

Furthermore, Paul traps have not traditionally been operated in this highly quantitative way, mimicking accelerator lattices with precise properties. Due to this, several experiments must be performed before QIO can be tested to ensure that we can create linear lattices with the required precision, and octupole terms with the required strength. We must also understand any limitations of the experiments we can perform using the Paul trap.

5.7 Chapter summary

Nonlinear integrable optics is a mathematical concept, where particle motion is stable if there are two invariants of the motion. A lattice with a complex, nonlinear, elliptical magnet has previously been designed to test this concept. Physically, the particles within such a machine should have a large range of tunes while the machine maintains a large dynamic aperture.

As a very precise linear lattice and a series of complex nonlinear magnets are required to test nonlinear integrable optics, a version with only one invariant of the motion (quasi-

integrable nonlinear optics) will first be tested. To test quasi-integrable nonlinear optics the elliptical magnets can be replaced with octupoles and the tolerances on the linear lattice relaxed slightly.

Two accelerators currently exist to test quasi-integrable nonlinear optics, IOTA and UMER. However, both face challenges, such as correctly steering the beam and accounting for chromaticity and dispersion.

Therefore, we want to test the concept of quasi-integrable nonlinear optics in the IBEX Paul trap, where these longitudinal effects are not experienced by confined ions. However, new levels of precision in operating a Paul trap for accelerator physics will be required, as well as an upgrade to the trap to allow the control of octupole fields. Chapter 6 addresses the issue of creating precise lattices in a Paul trap, while Chapter 7 describes the nonlinear upgrade and simulations of the octupole lattice.

Chapter 6

Experimental creation of a T-insert with IBEX

To test nonlinear quasi-integrable optics experimentally in a Paul trap, two things are required. First, a linear focusing region that meets the requirements of nonlinear integrable optics, and second, an upgrade to the current trap, which is linear, so that the octupole potential can be included. This chapter describes the development of a strong focusing linear lattice, known as a T-insert, which can be realised on the IBEX trap. In Section 6.1, the constraints on the T-insert and the design process are outlined. Sections 6.2 and 6.3 describe the experimental creation and testing of the T-insert. Towards the end of the chapter, in Section 6.4, I describe a new method to measure the beta function and emittance in a Paul trap, with the intention of using similar methods to verify that we have successfully created a T-insert lattice.

6.1 T-insert design for IBEX

The potential given in Eqn. 5.10 is quasi-integrable, but the magnets that create this potential are not sufficient to create a physically realisable accelerator, as linear focusing is still required to create a stable solution. Because of this, the nonlinear magnets which create the

integrable potentials must be placed in the drift region of a linear focusing lattice.

In the derivation of the integrable nonlinear potential described in Section 5.2.2, equal beta functions in the horizontal and vertical direction were assumed in the nonlinear region. A phase advance of $n\pi$, where n is an integer, is also required between the nonlinear regions. The phase advance of $n\pi$ ensures quasi-periodic motion through the nonlinear region. Furthermore, $n\pi$ phase advance (as opposed to $2n\pi$, which would ensure that particles enter the nonlinear insert at the same point in phase space at which they left it) is a sufficient condition for quasi-integrability, as the nonlinear potential in Eqn. 5.10 is dependent only on x_N and y_N raised to even powers.

A linear focusing accelerator lattice with equal focusing in the horizontal and vertical directions can be created through strong focusing, using a lattice with the transfer matrix of a thin, axially symmetric lens. Such a strong-focusing lattice, called a T-insert, can be used to create a drift region where the horizontal and vertical beta functions are equal. The nonlinear magnets are then installed in this drift region [126].

The transfer matrix of an ideal T-insert is given by

$$M_{\text{T-insert}} = \begin{pmatrix} 1 & 0 & 0 & 0 \\ -k & 1 & 0 & 0 \\ 0 & 0 & 1 & 0 \\ 0 & 0 & -k & 1 \end{pmatrix}, \tag{6.1}$$

where k is the focusing strength, equal in both transverse directions. The beta function across the drift region is given by

$$\beta(s) = \frac{l - sk(l-s)}{\sqrt{1-(1-\frac{lk}{2})^2}}, \tag{6.2}$$

where l is the length of the drift region in meters, and s denotes the position across that drift region [127].

The first step toward testing NIO in a Paul trap is to design and test the underlying T-insert lattice. Several conditions must be met by the T-insert; as previously discussed some of these are due to requirements imposed by the theory of NIO, and others come from constraints in the IBEX experimental setup. For the T-insert to be suitable for NIO, there must be a drift region where the beta functions are equal in the horizontal and vertical directions, which means that the lattice must be left-right symmetric and have both a horizontal beta function, vertical beta function, and dispersion with a derivative of zero at the point of symmetry. Fortunately, in the case of an LPT, dispersion is always zero, and we do not observe momentum dependent effects. Combining these conditions with the requirement for $n\pi$ phase advance gives 6 parameters that have to be controlled precisely, $\alpha_{x,y}$, $\beta_{x,y}$, and $Q_{x,y}$.

A further constraint is the maximum beta function in both the horizontal and vertical directions. If the beta function is too large, the ions will scrape on the confining rods and will be lost. This has the potential to limit the number of ions stored. It is also advantageous to have beta functions that are similar in both transverse directions, keeping the beam as round as possible to avoid unequal scraping. Additionally, the phase advance over the drift region should be close to $0.3\times2\pi$ to ensure a large tune spread when the octupole is introduced, as illustrated further in Chapter 7.

Finally, the voltage applied must be in line with the limitations of the IBEX wave function generators and amplifiers. The maximum voltage of the square wave circuit is $\sim \pm150\,\mathrm{V}$ and the rise and fall time is amplitude-dependent, but on the order of $\sim$90 ns. Due to this, the safe operational limit is a pulse of width $\sim$90 ns. This results in pulses that are sawtooth in shape, instead of square. However, simulations indicate that it is still possible to create a T-insert with the correct optics using these amplifiers.

The S-POD trap at Hiroshima University uses Metal Oxide Semiconductor Field-Effect Transistors (MOSFETs), to create square waveforms with greater accuracy, by switching quickly between two voltages [105]. A similar circuit could be used on IBEX as a relatively simple upgrade if required. However, a MOSFET-based circuit requires a DC voltage source

Constraint	Source	Priority
$\beta_x = \beta_y$	NIO theory	High
$\phi_x = \phi_y = n\pi$	NIO theory	High
fractional Q_x = fractional $Q_y \approx 0.3$	Maximise tune spread	Medium
β_{x,y_Max} = minimal	IBEX trap size	Medium
Limit on voltage amplitude	IBEX electronics	High
Lower bound on voltage pulse length	IBEX electronics	High
Lattice as simple as possible	Ease of optimisation	Low

Table 6.1: The constraints on a T-insert lattice for the IBEX trap.

to supply the voltage of the square pulse, driving the fast switch to that voltage. As a DC power supply is therefore required for each voltage, it is much simpler to step between only one positive voltage value and one negative voltage value when using a MOSFET circuit.

A summary of the constraints on a T-insert for the IBEX trap can be found in Table 6.1.

6.1.1 A first attempt at T-insert design

The IBEX trap allows a great deal of flexibility when designing a lattice, however, this leads to a highly under-constrained problem. Initially, it was also unclear if the current IBEX electronics would be able to create a T-insert with a sufficiently precise phase-advance and beta-function control. To simplify the problem, I chose to create a T-insert in which only the length of each voltage pulse varied, keeping the amplitude of each pulse constant.

Such a T-insert design has the advantage that it could also be achieved using a simple MOSFET circuit if one was required, or using the S-POD trap [160]. Furthermore, using a fixed voltage amplitude ensured a constant rise and fall time across the lattice for pulses longer than $\sim$90 ns and with a relatively small amplitude. This was done to simplify the process of optimising the lattice for the correct phase advance and beta function.

In this lattice design, I chose to use the relatively low amplitude of 25 V for each voltage pulse. As a result of this, longer square voltage pulses were required to create sufficient focusing. Such pulses are more easily achieved with the IBEX amplifiers than shorter pulses with large amplitudes; however, this low-voltage and long-pulse design led to larger beta

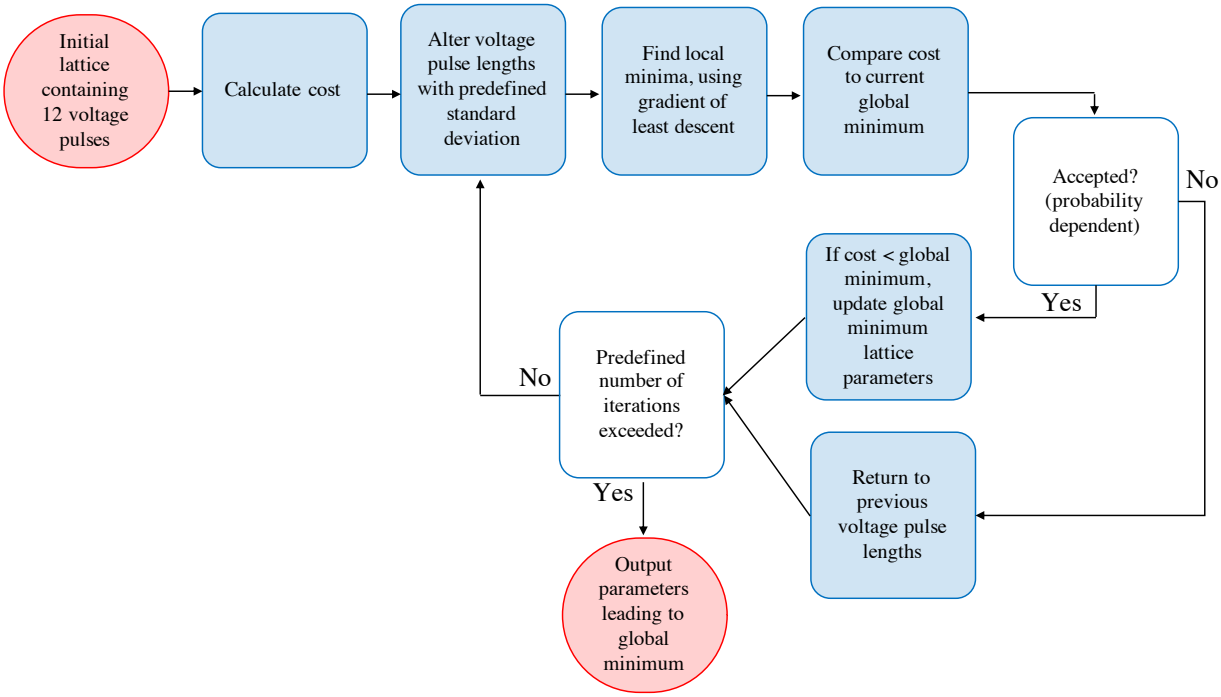


Figure 6.1: Flow diagram of the T-insert lattice design process.

functions in the trap.

For each of the six parameters to be controlled by the T-insert, a variable in the lattice design was required. As all pulses have the same, non-variable, amplitude in this design, six independent voltage pulses of variable duration were necessary. This meant that the simplest solution was a symmetric system of twelve square voltage pulses between nonlinear insertion sections [118].

To design the T-insert, I created a Python script to turn an array of voltages into transfer matrices and extracted the Twiss parameters for the lattice, calculating the phase advance over both the T-insert and the lattice as a whole. When optimising the lattice design, I used a basin-hopping algorithm [161]. From a reasonable starting lattice, the algorithm calculated the cost of the lattice. Here, the cost is defined as the distance of the lattice parameters from their required values, a cost of 0 corresponds to a lattice which meets all of the requirements. I calculated the cost using weighted values of the distance of the phase advance ($\phi_{x,y}$) from $n\pi$, as well as $\beta_x - \beta_y$, $\alpha_{x,y}$ in the centre of the drift region, and maximum beta function. The values for the length of the voltage pulses were optimised to find the local minimum. The algorithm then changed the voltage pulse lengths randomly, with a predefined standard

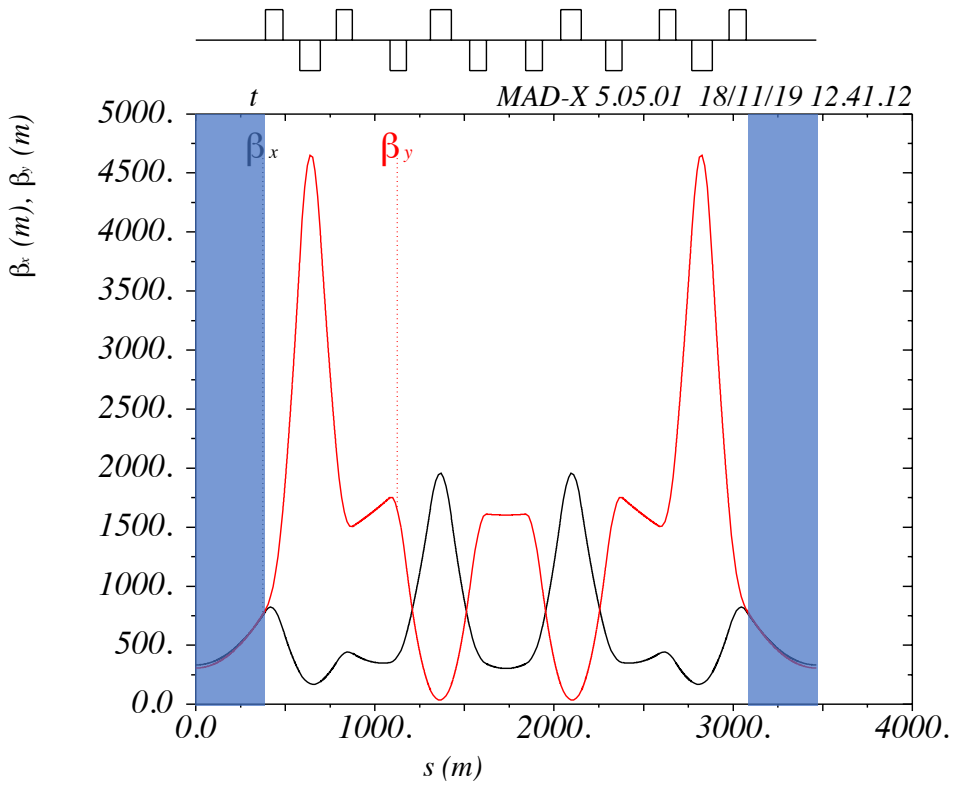


Figure 6.2: Optics of the first T-insert design, where voltage pulses have an amplitude of 25 V. The shaded blue region shows the drift region where the nonlinear potential would be.

deviation, after which the cost was evaluated again and the local minimum found. If the new minimum was close to the global minimum then this point was "accepted" with a certain probability, and the parameters were changed randomly from this point again. If the point was not accepted, or if the lattice was unstable, the parameters reverted to the previous set and the random step was taken again from the previously accepted parameters. This continued for a pre-specified number of steps until finally the global minimum and the corresponding lattice parameters were outputted. This process is summarised in Fig. 6.1.

I did not include space-charge effects on the beta function of the lattice in the basin-hopping process, as this is prohibitively computationally intensive. The nonlinear dynamics of the system will be tested initially in the low-intensity regime, where space-charge forces can be neglected, and so a solution meeting the above conditions for NIO, in this case, was required. A discussion of the effects of space-charge forces on a T-insert can be found in Section 7.6.

Lattice parameter	Value
Horizontal phase advance over T-insert (2π)	1.0086
Vertical phase advance over T-insert (2π)	1.0063
Horizontal phase advance over drift (2π)	0.2777
Vertical phase advance over drift (2π)	0.2936
Minimum β_x in drift (m)	333.33
Minimum β_y in drift (m)	307.29

Table 6.2: The design parameters for the first T-insert design, where all voltage pulses have a constant amplitude.

The basin-hopping method produced the lattice shown in Fig. 6.2, where MAD-X was used to confirm the lattice parameters, which are summarised in Table 6.2.

Throughout the rest of this thesis, "T-insert" refers to the linear part of the focusing lattice over which the phase advance is $n\pi$, excluding the drift region where the octupole will be applied.

6.2 Experimentally creating the T-insert

In January 2019, a first attempt was made to create the T-insert lattice on the IBEX Paul trap; however, no trapped ions were detected using the Faraday cup. At this point in the commissioning of the IBEX trap, the MCP had not yet been installed in the system. We suspected that the T-insert was confining ions, but fewer than we could detect with the Faraday cup alone ($< 10^6$).

Since simulations predicted that ions should be trapped, yet none were observed, further diagnostics were required to determine the discrepancy between our expectation and the experimental results. We decided to stop T-insert testing and install the MCP. During this time we also upgraded the amplifiers to the central IBEX rods from the commercially available WMA300 amplifiers to a pair of amplifiers custom-built by Oxford particle physics central electronics [57].

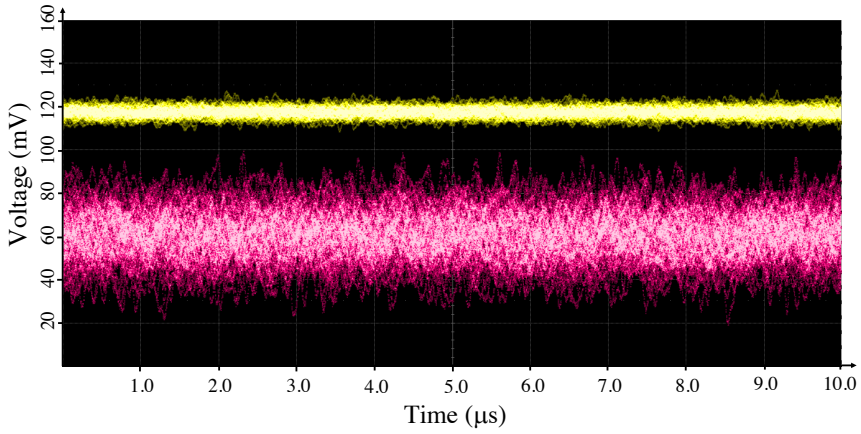


Figure 6.3: Oscilloscope trace showing the noise, with no load, on the WMA300 amplifier (pink) and the custom built amplifiers (yellow). A vertical offset was introduced simply to allow better comparison of the two traces.

Impact of experimental upgrades

The upgrade of the amplifiers to the central rods increased the bandwidth available and reduced the amplitude of the noise applied to the rods (from $\sim 60\,\mathrm{mV}$ to $\sim 10\,\mathrm{mV}$ peak to peak, with no load applied, as shown in Fig. 6.3).

The installation of the MCP resulted in the ability to detect down to $\sim 10^3$ ions. This ensured that the calibration of the trap was in a regime where space-charge forces could be neglected, and therefore increased its accuracy. The increased sensitivity to lower ion numbers allowed us to study the impact of the beta function on the number of ions confined by the trap.

Finally, the installation of the MCP allowed an estimate of the emittance at low ion number in the IBEX trap to be made, using the image of the ion distribution on the phosphor screen and a simple simulation. Further details of this measurement can be found in Section 3.6. This measurement led to an upper bound on the expected beam size for a given beta function.

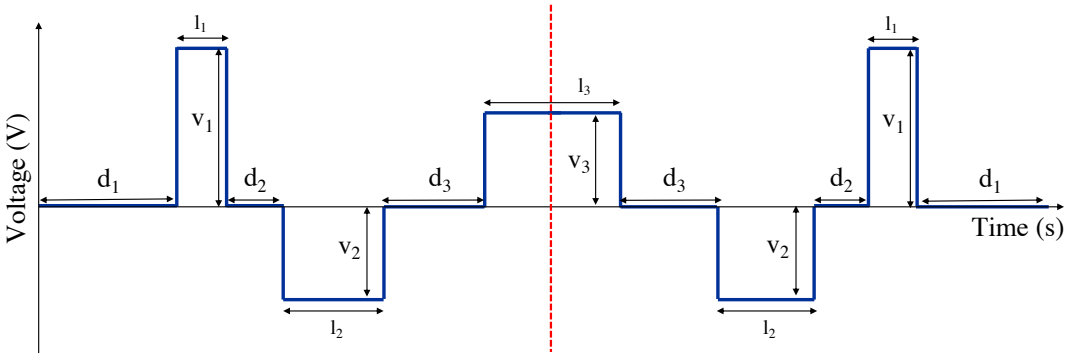


Figure 6.4: Diagram showing the structure of the T-insert lattice and drift region, for a phase advance of $0.135\times2\pi$ over the drift. The same waveform with opposite polarity was applied to the opposing set of central rods. The dotted red line shows the line of symmetry for the lattice.

Lattice parameter	**Element number**		
	1	2	3
d (drift length (ns))	500.3	300.2	600.4
l (quadrupole length (ns))	266.9	600.4	600.4
d (effective drift length (m))	150	90	180
l (effective quadrupole length (m))	80	180	180
v (quadrupole voltage (V))	26.83	-16.70	13.64

Table 6.3: The parameters of lattice L_1, in the configuration shown in 6.4.

Lattice parameter	**Value (2π)**
Horizontal phase advance over T-insert	0.4999
Vertical phase advance over T-insert	0.5001
Horizontal phase advance over drift	0.1358
Vertical phase advance over drift	0.1358

Table 6.4: The design parameters common between lattices L_1, L_2 and L_3, the phase advance.

	Lattice number		
	L_1	L_2	L_3
Scaling factor (κ)	1	2	3
Maximum β_x (m)	2457.84	1737.96	1419.03
Maximum β_y (m)	1977.79	1398.51	1141.88
Minimum β in drift (m)	330.00	233.34	190.53

Table 6.5: The scaling relation between lattice L_1, L_2 and L_3. Lengths are scaled by $\frac{1}{\sqrt{\kappa}}$ and voltages by κ, resulting in a beta function that scales by $\frac{1}{\sqrt{\kappa}}$.

A new T-insert design

During the installation of the MCP and the new amplifiers, a new T-insert was designed. This was a consequence of the experimental evidence that the initial design was unable to trap a large number of ions ($\sim 10^6$ ions, which would have been detectable using the Faraday cup). Although during the initial testing in the low-intensity regime, this may not have been a problem, in the later stages of testing of QIO, large numbers of ions are required to study the impact of space-charge forces on integrability. To increase the number of ions stored we required a T-insert with a lower beta function. This required voltages pulses that were larger in amplitude and shorter in duration, as shown in Eqn. 6.2.

As the voltage pulses become shorter, the rise and fall times become pulse-length dependent, as the limited bandwidth of the amplifiers cannot accurately reproduce a perfect square wave. Due to this, I chose to redesign the T-insert, varying both the height and width of the pulses and producing a much shorter lattice, consisting of only five voltage pulses, as previous work showed that this is the minimum number required [162].

To limit the maximum beta function in the T-insert, I reduced the phase advance across the drift from $\sim 0.3 \times 2\pi$, in the first lattice design, to $\sim 0.135 \times 2\pi$. As the phase advance is given by $\phi(s) = \int \frac{ds}{\beta s}$, creating a large phase advance over the drift region is achieved either by reducing the beta function in the drift region or increasing the length of the drift, both of which tend to increase the maximum beta function within the T-insert. Furthermore, as the strength of the octupole required in the nonlinear region scales as $1/\beta^3$, reducing the beta function in the drift will lead to larger octupole voltage required to produce the same tune spread. As it is desirable to use a similar amplifier to the WMA300 to apply voltages to four metal plates (described in Chapter 7), creating the octupole potential as described in Eqn. 5.10, this must be considered in the T-insert design. If the required octupole is too large, a higher-specification amplifier may be required.

Although IOTA is hoping to operate at a phase advance of $0.3 \times 2\pi$, UMER will test QIO with a tune of 0.13 over the drift as they experience the similar experimental limitations

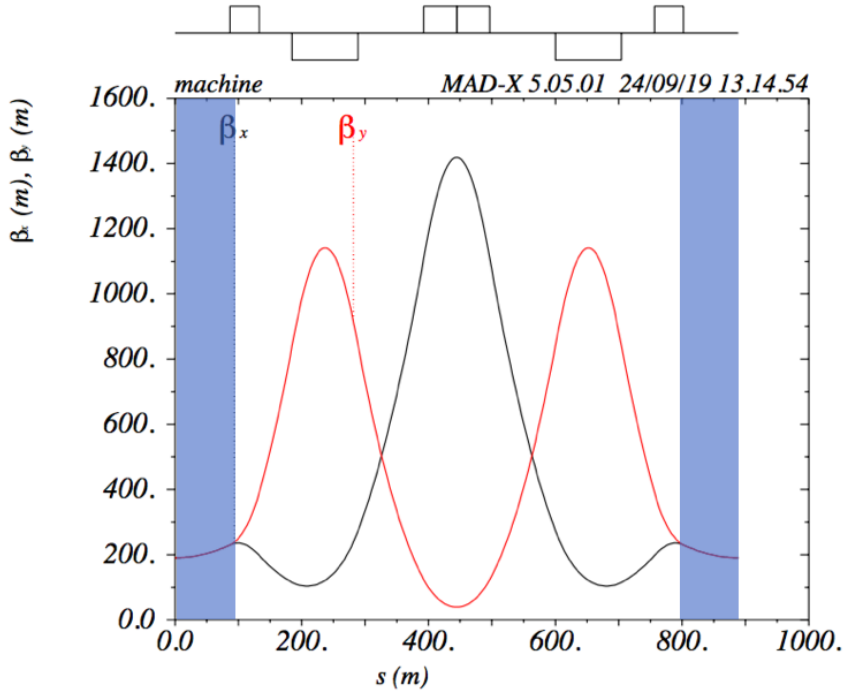


Figure 6.5: Optics of the lattice L_3, verified in MAD-X, with the drift region where the octupole potential will be highlighted in blue.

to those found with IBEX [150, 151]. Furthermore, based on the simulation results from UMER, described in Section 5.3.2, I have chosen to avoid fractional tunes close to 0.25. A smaller phase advance over the drift limits the maximum tune spread in the lattice.

Once the structure of the new lattice, L_κ, was finalised (shown in Fig. 6.4) we chose to study three different lattices, related to each other through a scaling factor, κ. The parameters of the longest lattice, L_1, with the lowest amplitude voltage pulses, are shown in Table 6.3. For lattices L_2 and L_3, the lengths of both the drifts and the voltage pulses are scaled by $1/\sqrt{\kappa}$ and the amplitudes of the voltage pulses are scaled by κ [163]. Here L_κ denotes a lattice including both the T-insert and drift region.

Each lattice, whose parameters are given in Table 6.4, has the same phase advance across both the drift region and the lattice as a whole. However, as the length of the lattice changes, the magnitude of the beta function is scaled, as is shown in Table 6.5. This illustrates the competition between different constraints upon the lattice, as the lattice with the smallest maximum beta function, L_3, will also require the largest octupole potential to create the same tune spread.

Lattice	Number of ions extracted			
	After 100 periods	After 1000 periods	After 0.513 ms	After 5.13 ms
L_1	3.23×10^4	3.85×10^4	3.23×10^4	3.85×10^4
L_2	4.85×10^5	1.67×10^5	1.16×10^6	2.05×10^5
L_3	3.25×10^6	2.20×10^6	3.08×10^6	1.74×10^6

Table 6.6: The largest number of ions extracted from the three L_κ lattices after different trapping times. Results show the average over 5 experiments.

6.3 Testing the T-insert

When testing the new T-insert on IBEX, the lattice L_1 was used initially, as the amplitudes of the voltage pulses were easily reachable with both the WMA300 and custom IBEX amplifiers. The lattice L_1 was applied periodically to both the central rods and the end caps, even during the ion accumulation period, while the electron gun was switched on. Ions were extracted towards the MCP by removing the DC offset applied to the MCP end caps. Initially, using the MCP as an ion counter and the phosphor screen to give an image of the distribution, no ions were observed.

In previous experiments, it has been shown that ions are not well accumulated at larger values of tune, so ions were accumulated at a tune of 0.15 and the tune adiabatically varied to the final value. Based on this experimental experience, ions were first trapped using a square wave at a tune of 0.15, and then transitioned immediately into the T-insert lattice. Using this method, a small number of ions were detected, extracted after 1000 lattice periods.

It is well known that if the Twiss parameters are not well matched when moving between two different lattice regions, the particle distribution can experience filamentation, emittance growth and ultimately particle loss. The immediate transition from the square-wave lattice to the T-insert is highly mismatched. We suspected, due to this, that ion loss was occurring at the transition.

To improve the trapping process, we chose to operate IBEX more like an accelerator, matching correctly between the two regions with a series of voltage pulses instead of an adiabatic voltage change. The amplified waveforms applied to the IBEX rods were measured

Lattice	Number of ions extracted		
	Matching into and out of L_3	Matching into L_3 only	No matching
L_3	3.26×10^4	2.28×10^4	2.44×10^4

Table 6.7: The number of ions extracted from the lattice L_3 with and without matching.

using high-definition oscilloscopes and oscilloscope probes. The traces describing the voltages applied to the central rods were saved and each voltage datum was transformed into a transfer matrix. Multiplying these transfer matrices together allowed the optics of the lattice that we had created within the trap to be calculated and compared to the design optics.

From the optics calculation, the Twiss parameters at the end of the accumulation FODO lattice and the Twiss parameters at the centre of the drift region in the lattice L_κ were extracted and used as inputs into a simple MAD-X script. The MAD-X script calculated the required amplitudes of five voltage pulses of predefined length to create a simple matching section.

A Python script automatically extracted the voltage amplitudes from the MAD-X output file and created CSV files to be sent to the AWGs. This process is entirely automated, requiring only that the experiment should be restarted using the Labview controls for the matching to be updated. This allowed fast re-matching when changes were made to the T-insert, or in the case of slow amplifier drift over time. The matching process is summarised in Fig. 6.6. Figure 6.7 shows the oscilloscope trace of the voltage applied to the rods. Region (1) in Fig. 6.7 shows the initial alternating gradient lattice in which the ions accumulated. Region (2) shows the matching section and region (3) the lattice L_κ. The difference in bandwidth between the WMA300 amplifiers (supplying the end caps) and the custom-built upgrade (supplying the central rods) is easily observable.

We found that this process of matching increased the number of ions detected using the MCP. Table 6.7 shows the impact of the matching section on the number of ions detected when ions were extracted after 100 periods of lattice L_3. Only a small number of ions were stored in this experiment to reduce space-charge effects.

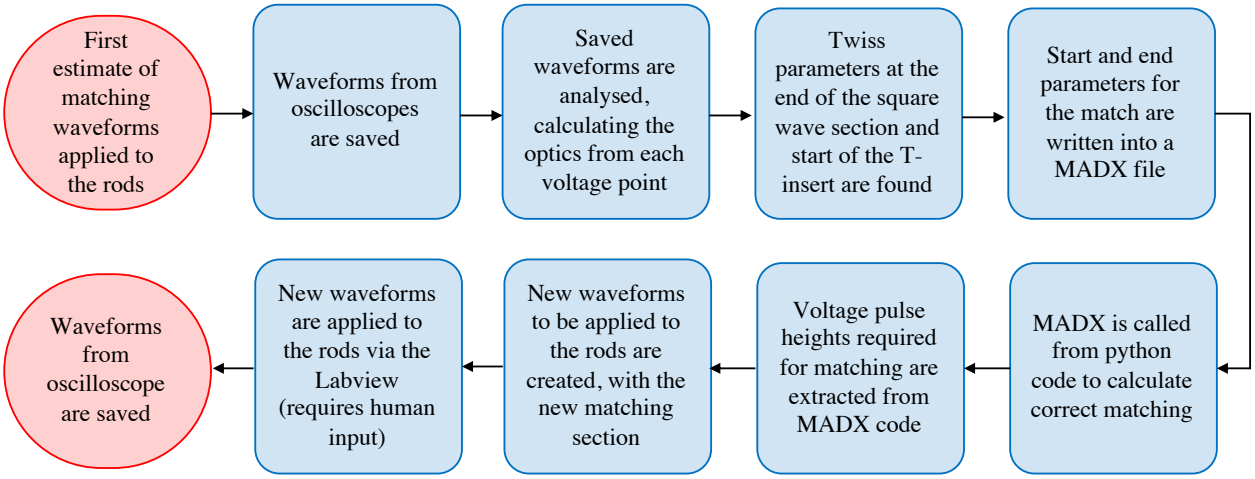


Figure 6.6: Flow diagram of the matching process.

However, even with matching, the number of ions stored by lattice L_1 still seemed to be limited by the large beta function of the lattice. Although ions were trapped, not enough were stored to study space-charge effects. Lattices L_2 and L_3 were both tested, increasing the amplitude of the voltage pulses and reducing the length of the lattice to reduce the beta function. In the case of lattice L_3, the WMA300 amplifiers did not have the required bandwidth to create the T-insert on the end caps. This can be seen in Fig. 6.7, which shows an oscilloscope trace where the end-cap voltage is lower than required within the T-insert region. This will have two effects, firstly a possible reduction in the effectiveness of the longitudinal trapping, secondly, the ions will have to pass through an incorrect T-insert potential as they pass through the end caps on extraction. This T-insert will have different optics, will not be matched to the central rods, and may not even be stable, resulting in ion loss. This will give an inaccurate measurement of the number of ions stored. To reduce the ion loss from this effect, the ion distribution was matched back to the initial confining alternating-gradient cell before extraction, as shown in Fig. 6.8.

Figure 6.9 shows an example of the image obtained using the phosphor screen and CCD camera in the case where the lattice L_3 is applied to the end caps when the ions are extracted, and the case where ions are first matched back to the FODO cell. Figure 6.9a shows an asymmetric distribution as the beta functions differ in the horizontal and vertical directions in the case where an imperfect lattice L_3 was applied to the end caps. Figure 6.9b shows a

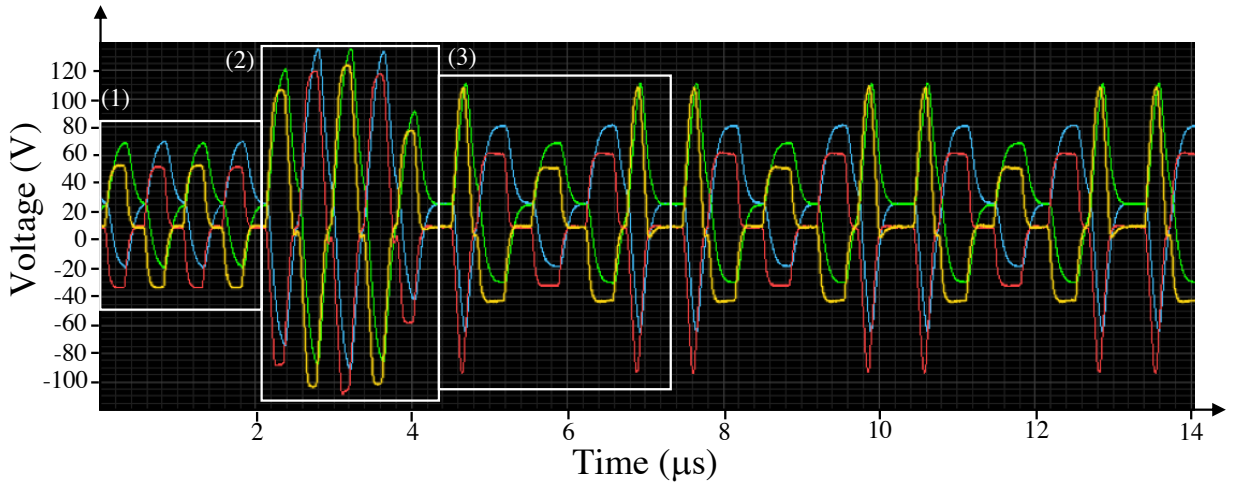


Figure 6.7: Oscilloscope trace showing the experimental setup for trapping with lattice L_3 with the lattice also applied to the end caps. Red and yellow traces show the voltages applied to the two pairs of central rods, where the custom amplifiers are used. Blue and green traces show the voltages applied to the end caps. Region (1) shows the initial confining square wave, (2) shows the matching section and (3) the lattice L_3, consisting of T-insert and drift region.

much rounder distribution once matching back has taken place, as the beta functions in the horizontal and vertical direction are mirrors of one another, and $\alpha_{x,y}$ is reduced.

After testing all three lattices, with matching, on IBEX, we found that as the maximum beta function was reduced, the number of ions stored increased, as shown in Table 6.6. For lattice L_3, 2.2×10^6 ions were stored for 1000 T-insert periods. The results given in Table 6.6 were taken with the maximum number of ions stored, the argon pressure was 1.5×10^{-7} mbar and the electron gun was on for 0.475 s. At these ion numbers, we expect to see moderate space-charge effects. Table 6.6 shows the largest observed number of ions stored with lattice L_3 for 100 and 1000 lattice periods. When the storage time was increased to 10,000 lattice periods, the ion number was reduced to 5.25×10^5.

Furthermore, it was possible to accumulate ions while the lattice L_3 was applied to the rods, however, a much smaller number of ions were detected upon extraction, suggesting that accumulation with the T-insert creates an ion distribution with a larger emittance.

As far as we are aware, prior to this work the most complex lattice created in a Paul trap is of the form FODODOFO [105], and non-adiabatic matching has not previously been

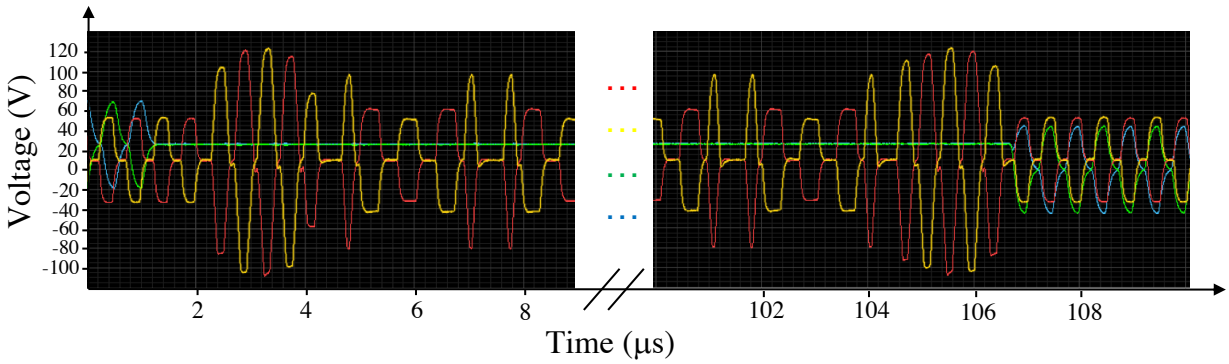
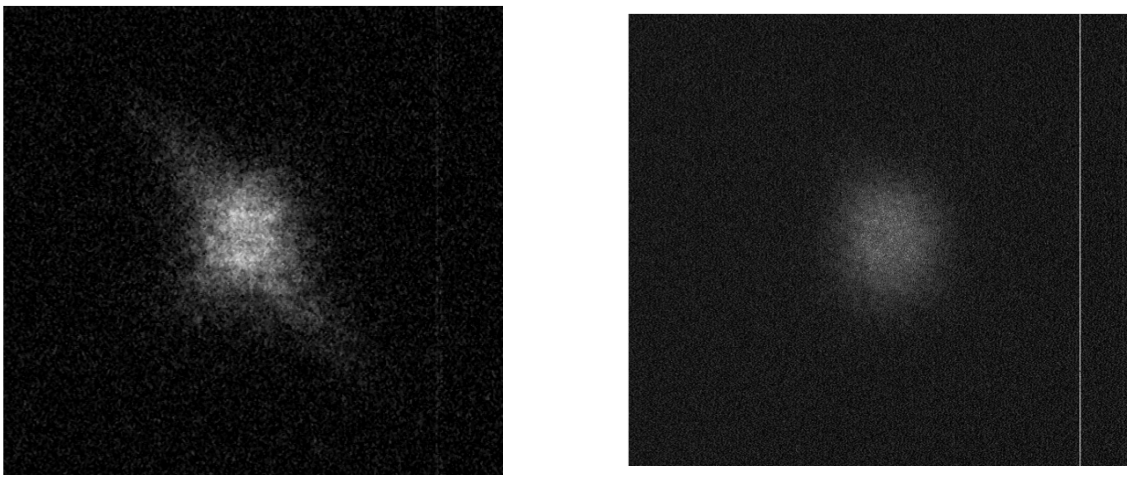


Figure 6.8: Oscilloscope trace showing (left) matching from a FODO lattice to the lattice L_3 and (right) reversing the process to match back to the FODO lattice. Red and yellow traces show the voltages applied to the two pairs of central rods, where the custom amplifiers are used. Blue and green traces show the voltages applied to the end caps.



(a) lattice L_3 is applied to the end caps.

(b) Matching back occurs before extraction.

Figure 6.9: An example ion distribution on the phosphor screen, when the lattice L_3 is also applied to the end caps during ion extraction and when matching back to the original FODO lattice is used.

attempted.

6.3.1 Quadrupole perturbation

Simply trapping ions with a T-insert lattice and the appropriate drift region is not sufficient evidence that a T-insert has been produced. We also need to show that the lattice we have created meets the requirements for quasi-integrable optics with the required precision.

As described in Section 3.5, the careful calibration of the trap should allow the optics of the lattice to be extracted from the voltage trace read out from the oscilloscope, which shows the amplified voltages applied to the rods. However, this is not enough to prove that we meet the T-insert requirements; we would like to verify this experimentally. The first step towards this is to verify that the tune of the entire lattice, L_κ (the T-insert and the drift region), is the same as the tune predicted from the optics extracted from the oscilloscope trace. To do this, I applied a quadrupole perturbation to the lattice L_κ during trapping. The perturbation was sinusoidal and applied continuously for 500 rf periods before the perturbation was removed and the ions extracted. The quadrupole perturbation was added to the CSV file describing the waveform before it was sent to the AWGs and amplifiers. I performed a series of experiments, in each experiment a perturbation of a slightly different frequency was applied. Frequencies close to twice the frequency predicted by the correctly calibrated oscilloscope trace were used, as $m = 2$ for quadrupole resonances.

When the frequency of the perturbation is twice the tune, we expect the quadrupole perturbation to resonantly excite the ions, leading to ion loss. This ion loss was detected as a reduction in the number of ions detected by the MCP on extraction. The experiment was performed at a low ion number to avoid complications due to space-charge effects. As the beta function is large in the T-insert, only a small perturbation amplitude of 0.1 V was required to give ion loss. Figure 6.10 shows the result of this experiment for lattice L_3.

For lattice L_3, the tune calculated from the oscilloscope trace agreed very well with the frequency of maximum ion loss in Fig. 6.10. The optics from the trace predicted a tune of

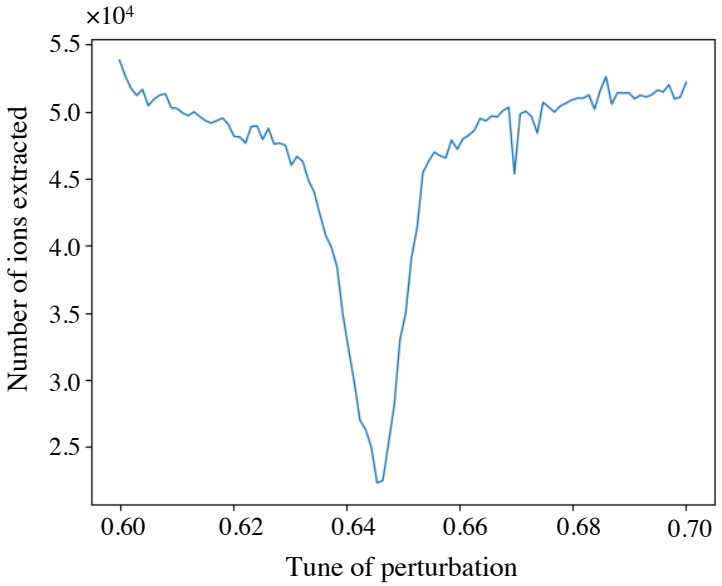


Figure 6.10: The number of ions extracted from lattice L_3, when a quadrupole perturbation of 0.1 V is applied at a range of frequencies.

0.6455; the minimum in extracted ion number occurred at a tune of 0.645. This indicates that the calculated optics accurately represent the optics within the trap. This result was reproduced in two separate experiments. Lattice L_3 was altered, increasing the height of each voltage pulse by 1%. The experiment was then performed again. For this slightly altered lattice, with slightly altered optics, the measured tune again matched the tune calculated from the voltage traces. This suggests that using the calibration factor, we can understand well the optics within the trap from the oscilloscope traces.

However, this was not the case for lattice L_2, this is likely due to the calibration process. The system is calibrated using a square wave at 1MHz and a range of voltage amplitudes from $\sim$ 30 V to $\sim$ 100 V. Included in the calibration process is the response of the scope probes, which is known to vary with voltage frequency and amplitude. As the frequencies and voltage amplitudes used in lattice L_3 are close to those used in the calibration process the calibration is valid. However, for lattices L_1 and L_2, where much lower voltages are used, the calibration is not appropriate. Due to this, further verification that the applied lattice meets the T-insert parameters may be required.

The lattice L_3, though the best so far in terms of ion number, is not a perfect T-insert.

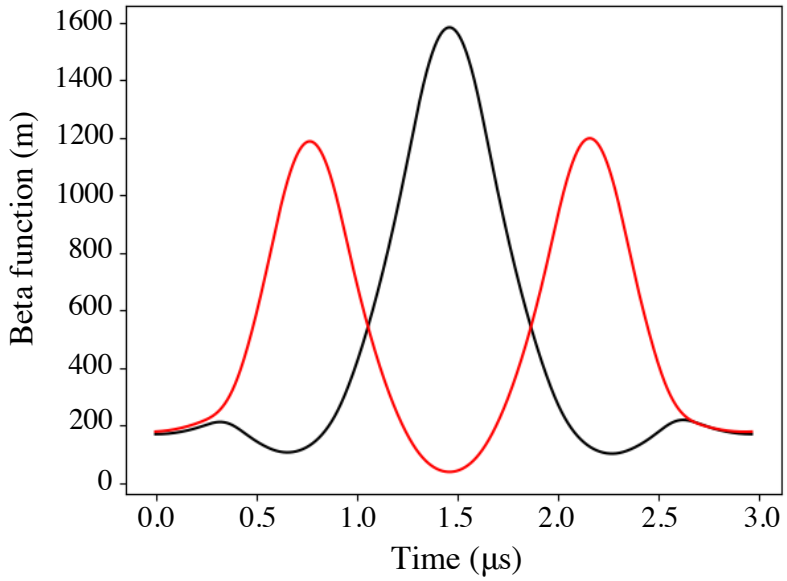


Figure 6.11: The optics of lattice L_3, reconstructed from a recorded oscilloscope trace, the voltages used to reconstruct these optics are shown in Fig. 6.12. The black line shows the beta function in the x direction and the red line in the y. A comparison to the design optics in Fig. 6.5 shows that further work is still required to optimise the lattice.

The optics do not quite meet conditions for QIO, due to the rise and fall time of the voltage pulses and the finite resolution of the AWGs (100 MHz). Further work is required to alter the amplitude of voltage pulses slightly, iterating towards a perfect T-insert solution and compensating for amplifier overshoot. The optics of the latest L_3 lattice (where a first attempt to account for the overshoot was made), reconstructed from the oscilloscope trace, are shown in Fig. 6.11, with the corresponding voltage in Fig. 6.12. These optics differ slightly from the design optics in Fig. 6.5.

Lattice precision

From the width of the dip in the extracted ion number in Fig. 6.10, an estimation can be made of the precision of control that we have over the tune in the lattice, assuming zero tune spread. The width of the dip in ion number, at half of the maximum ion loss, is approximately 0.01. This estimation does not take into account the width of the stopband of

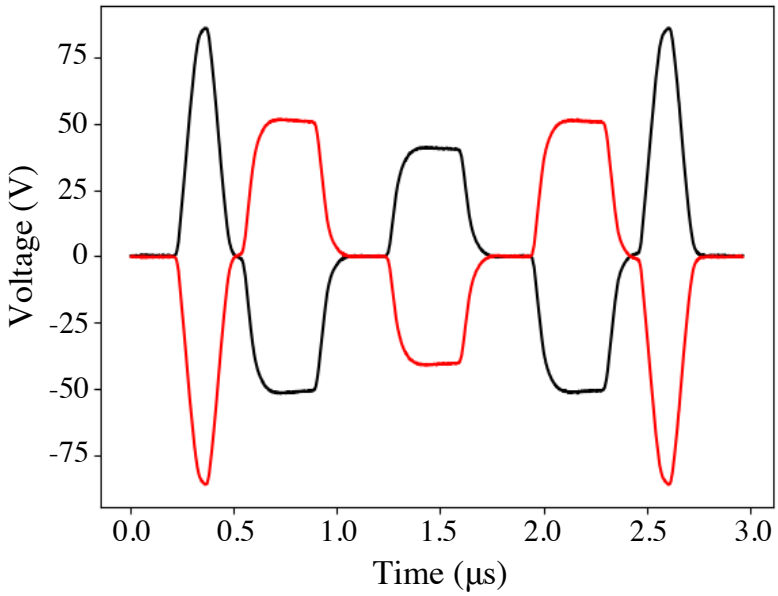


Figure 6.12: Experimentally applied voltages for lattice L_3, with the calibration factor applied. The black line shows the voltage applied to one pair of central rods, and the red line the opposing pair.

the resonance but agrees well with the variation in the tune calculated from the oscilloscope trace, which also varied over a range of 0.01, as shown in Fig. 6.13. This indicates that we can achieve the desired control over the lattice tune, as specified in Section 5.4.

Details of the error study performed on the lattice L_3 can be found in Appendix A.4. Appendix A.4 also shows the relationship between the total lattice tune, the phase advance over the T-insert, and the beta function in the centre of the drift.

6.4 Beta-function measurement using dipole kicks

Due to the need to verify that a T-insert lattice has been correctly created, a new method to measure the beta function and emittance at a specific point in time in an LPT has been developed. This method involves detecting ion loss when a dipole kick is applied to the ion distribution.

The experimental testing of this method was performed using the S-POD LPT during

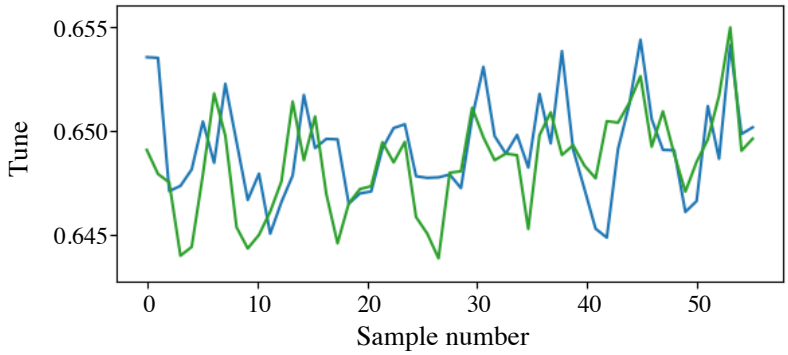


Figure 6.13: An example of the tunes (Q_x) calculated from successive oscilloscope traces of lattice L_3. The blue line shows the tune when no perturbation is applied and the green when a perturbation is applied.

a visit in the summer of 2017 when the IBEX trap was not yet operational. It should be noted that S-POD III was used, a different trap than was used to collect the data in Chapter 4. This trap is identical to the other S-POD traps, apart from a difference in central rod length, but this does not impact the following experiment.

This work has previously been published in the peer-reviewed proceedings of the International Particle Accelerator Conference 2018 [164]. I am responsible for the development of the method, the data taking, data analysis and writing of the short paper in reference [164], which was published under a creative commons license, [94], which allows me to use the content here. However, the initial setup of the S-POD trap was performed by Dr K. Ito, assistant professor at Hiroshima University.

6.4.1 Dipole oscillation

In accelerators, a dipole kick causes (coherent) centroid oscillation about the equilibrium orbit [165]. The same is therefore true in an LPT, where the oscillations are no longer a function of distance, s, but of time, t.

When a single kick is applied there is an angular change of θ applied to the ion distribution, while the position of the ions does not immediately change. The transfer matrix in

Eqn. 1.36 can be used to track the oscillations created by this dipole kick, as the particle moves around the ring, giving,

$$x_2 = \theta\sqrt{\beta_1\beta_2}\sin(\phi_{12}). \tag{6.3}$$

Here x_2 is the transverse coordinate of the centre of the ion distribution at t_2 (a point in time after the dipole kick has been applied), β_1 is the beta function at the time of kick (t_1), and ϕ_{12} the betatron phase difference between the two points.

Concentrating on the motion in one transverse direction, x, the angular kick corresponding to a dipole perturbation can be calculated. In the case of a dipole kick given by two infinitely long parallel plates, the transverse acceleration, a, experienced by particles is uniform and so the distance travelled due to this acceleration can be described using $x = \frac{1}{2}at^2$. As, for small angles,

$$\theta = \frac{x}{l} = \frac{1}{2}\frac{at^2}{l} = \frac{al}{2c^2}. \tag{6.4}$$

In this case, $F = \frac{qV}{r_0}$, so that θ can be expressed as

$$\theta = \frac{Fl}{2mc^2} = \frac{qV_Dl}{2mc^2r_0}, \tag{6.5}$$

where V_D is here the total potential difference applied between two plates and l is the effective length of the kick.

The angular deflection, θ, of the trapped ions is therefore given by

$$\theta = \frac{-q\zeta}{2mc^2r_0}V_Dct, \tag{6.6}$$

where V_D is the applied dipole voltage and t is the length of time that it is applied. To account for the geometry of the rods, a factor, ζ, is included. In S-POD, $\zeta = 0.795$ [75].

This result can also be derived directly from the Hamiltonian of the Paul trap, assuming that the dipole voltage is applied for a short time only so that the quadrupole can be assumed to be static,

$$H_{\text{paul}} = \frac{(p_x^2 + p_y^2)}{2m} + qV_D(t)\frac{x}{r_0}. \tag{6.7}$$

From Hamilton's equations $p_x' = -\frac{\partial H}{\partial x}$, giving the transverse acceleration as $a = \frac{qV_D(t)}{mr_0}$, which in turn can be integrated to give the transverse displacement.

The transverse trajectory of the ions, therefore, depends on the strength of the dipole kick applied, and the beta function when the kick is applied.

S-POD III had no MCP, only a Faraday cup, so all measurements were taken using the Faraday cup to detect the number of ions extracted.

To use the Faraday cup to measure the beta function through orbit distortion, the ions must move enough transversely to scrape on the central rods. Some ions will be lost, so that fewer will be extracted from the trap. Applying the dipole perturbation at different points in the confining potential leads to a varying transverse displacement, and therefore varying beam loss, allowing a beta-function measurement. To do this, a Gaussian beam is assumed, as previously validated [75].

6.4.2 Experimental limitations

In this experiment, a rf sinusoidal voltage was applied to one pair of central rods to create the confining potential (at twice the voltage amplitude required if both pairs are powered). The dipole kick was applied to the remaining pair (Fig. 6.14).

The simplest method of generating the dipole kick was to directly output it from a wavefunction generator. In an ideal experiment, the dipole kick applied to the beam would be a delta function; in reality, the pulse will have a finite width based on the rise and fall time of the wavefunction generator (15 ns). The maximum kick possible using this method

was 10 V, as this is the maximum output from the wavefunction generator.

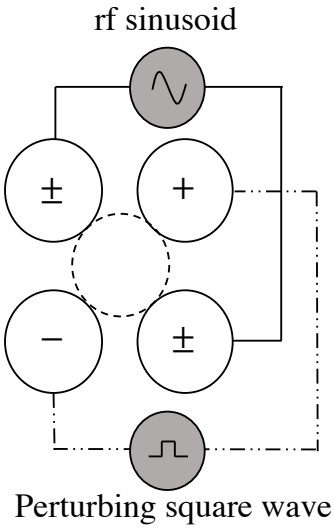


Figure 6.14: Schematic end view of S-POD rods, showing the voltages applied in the beta function measurement.

However, in normal S-POD operation (applying a voltage between 10 V and 100 V at a frequency of $\sim$ 1 MHz) a beta function on the order of 300 m is expected. Using Eqn. 6.3 and Eqn. 6.6 and assuming a dipole kick of length 100 ns, a voltage of $\sim$ 250 V is required to kick the ions to such an extent that all the ions are lost. A kick of 100 ns is assumed as this is short enough to achieve good resolution in the reconstruction. Longer voltage pulses will reduce the voltage required to give the same integrated strength, but will lead to a reduction in resolution.

Therefore, we applied a series of dipole kicks to the ions. If the kicks are applied in phase, the strength of the kicks adds linearly, producing the same effect as a single kick at a larger voltage. To be able to provide a series of dipole kicks at both the same phase advance and beta function, the cell tune of the trap was $\frac{1}{n}$, where n is an integer. Dipole kicks were applied every n rf periods to simulate a ring with integer tune. As a proof of principle experiment, we used alternating gradient lattices with cell tunes of $\frac{1}{5}$, $\frac{1}{7}$, and $\frac{1}{9}$ and a series of 25 dipole kicks. These tunes were chosen as, at low ion number, we do not expect to see strong resonances.

6.4.3 Measurement method

When converting the extracted ion number into a value for the beta function, the ion loss in phase space must be considered. When dipole kicks are periodically applied in a lattice, the result is closed orbit distortion. In the case of an integer tune, for periodic kicks, the phase space rotates about the origin in such a way that the same side of the phase-space distribution continuously collides with the confining rods, this is known as synchronous rotation. The same is not true away from the resonance, where an annulus in phase space is scraped instead [166].

If a single kick is applied, the motion is also synchronous. As the dipole kicks were on the integer resonance, their strengths simply add, acting as a single kick, and so we must consider the case of synchronous motion in phase space.

Accounting for this asymmetric loss in the phase space, the error function was used to calculate the fraction of ions lost. This method has been previously used and shown to match closely the measured ion loss [75]. After applying a dipole kick, the fraction of ions remaining is given by

$$\xi = \frac{1}{2} + \frac{1}{2}\mathrm{erf}(\frac{r_0 - x_{\max}}{\sqrt{2}\sigma_x}), \tag{6.8}$$

where $x_{\max}$ is the maximum transverse position of the centre of the trapped ions, σ_x their standard deviation, and erf the error function.

Three alternating gradient lattices were investigated, with tunes of $\frac{1}{5}$, $\frac{1}{7}$ and $\frac{1}{9}$. For each of the three lattices, the number of ions extracted was recorded when 25 dipole kicks were applied in phase (and at the same time, t_1) in an rf period. The process was repeated for many different values of t_1. At each t_1, the number of ions extracted was recorded as the dipole perturbation voltage was varied between 0 V and 10 V.

The experiment was conducted at an ion number of 10^6. Ideally, the experiment would be conducted at a lower ion number, where space-charge effects are not present, however,

Cell tune	Emittance from measurement ($\times 10^{-9}$ m rad)	$\beta_{\max}$ from measurement (m)	Expected $\beta_{\max}$ (m)
$\frac{1}{5}$	3.8 ± 0.2	451 ±6	469
$\frac{1}{7}$	6.1 ± 0.2	698 ±14	525
$\frac{1}{9}$	5.1 ± 0.5	621 ±17	604

Table 6.8: The maximum beta function and emittance, compared to expected values, when dipole kicks are used to give ion loss.

at lower ion numbers the signal to noise ratio was found to be too small for an accurate beta-function reconstruction. This was a consequence of using the Faraday cup as an ion detector. The storage time of the ions before extraction from the trap was set to 1 ms.

6.4.4 Results

By substituting Eqn. 6.3 and Eqn. 6.6 into Eqn. 6.8, and noting that for maximal ion loss $\sin(\phi_{12}) \approx \pm 1$, so that $x_{\max} \approx \theta\beta_1\beta_{\max}$, the fraction of ions remaining is found to be

$$\xi = \frac{1}{2} + \frac{1}{2}\mathrm{erf}\left(\frac{r_0 - \theta\sqrt{\beta_1\beta_{\max}}}{\sqrt{2\epsilon\beta_{\max}}}\right). \tag{6.9}$$

In the special case where the dipole kick is at the maximum beta function ($\beta_1 = \beta_{\max}$), this reduces to

$$\xi = \frac{1}{2} + \frac{1}{2}\mathrm{erf}\left(\frac{r_0 - \theta\beta_{\max}}{\sqrt{2\epsilon\beta_{\max}}}\right). \tag{6.10}$$

Firstly, the data from the dipole kicks at the value of t_1 that resulted in the greatest ion loss was fitted to using Eqn. 6.10. Figure 6.15 shows an example of one of these fits, where $\beta_{\max}$ and ϵ are the fitting parameters. The values found for $\beta_{\max}$ and ϵ are shown in Table 6.8.

Using these values of $\beta_{\max}$ and ϵ, the ion loss curves from different kick locations were

fitted to with Eqn. 6.9, and values for β_1 were extracted from each curve.

The result of this fitting for the three lattices that were studied is shown in Fig. 6.16.

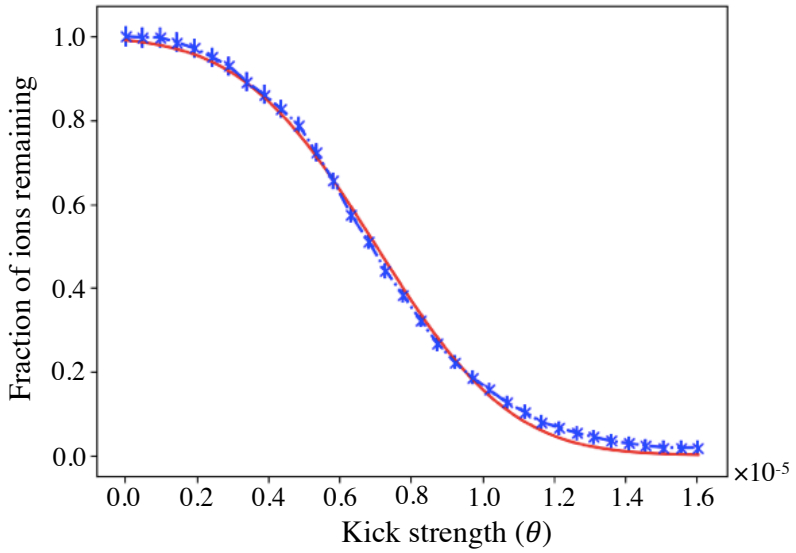


Figure 6.15: An example fit to data showing ion loss for different strengths of dipole kick. The blue points are experimental data points. The red curve is the fit to the data using Eqn. 6.10.

6.4.5 Discussion

Figure 6.16 shows the reconstructed beta functions with error bars, in comparison with the beta functions associated with the applied rf waveforms, where the optics of the periodic cell were calculated taking into account the transfer matrix associated with each voltage datum in the waveform. This shows that the reconstruction for a cell tune of $\frac{1}{5}$ worked very well, with the reconstructions diverging from the expected beta functions with increasing size of n.

This suggests that the deviation may be due to dephasing between kicks, or detuning of the ions due to nonlinear fields at large transverse amplitudes [167]. For the $n = 5$ case, the 25 kicks can be accomplished in 125 rf periods. However, for the case of $n = 7$ this is extended to 175 rf periods and for $n = 9$, 225 rf periods. These longer kicking times will amplify any error in the kick timings, resulting in kicks that are not precisely in phase. For

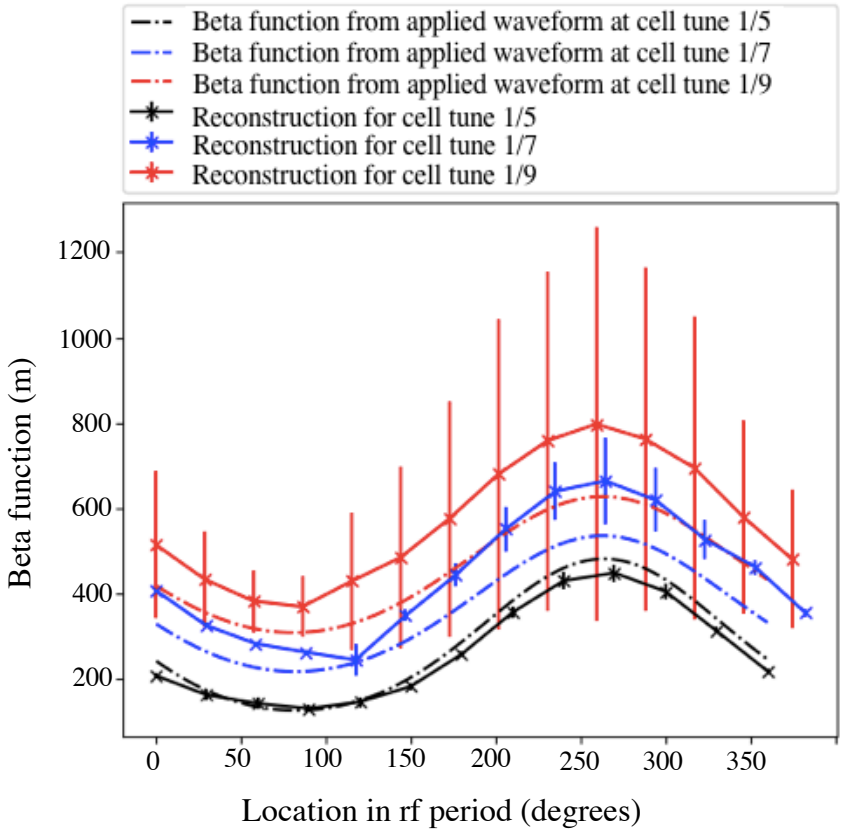


Figure 6.16: Comparison of reconstructed beta function for tunes $\frac{1}{5}$, $\frac{1}{7}$ and $\frac{1}{9}$, with the beta functions expected from the applied waveforms. Error bars are calculated from the error in the fits to the curves of kick strength against ion loss (Fig. 6.15).

such kicks, the kick strength no longer adds linearly and the total kick felt by the ions will be reduced, resulting in the upwards shift of the reconstructed beta functions in the $n = 7$ and $n = 9$ cases.

Furthermore, Table 6.8 shows that a large source of error in the reconstruction of the beta functions for tunes of $\frac{1}{7}$ and $\frac{1}{9}$ seems to come from the initial estimation of $\beta_{\max}$, which differs significantly from the expected value. Additionally, using the MCP as an ion counter in future experiments should increase the accuracy of the method.

The reconstruction of the beta function at a tune of $\frac{1}{5}$ strongly suggests that if a larger single-voltage kick is available, then this method is capable of reconstructing any beta function. The study also suggests that voltage does not need to be so high that the ions are lost completely, successful fitting occurred even when only 20% of the ions were lost.

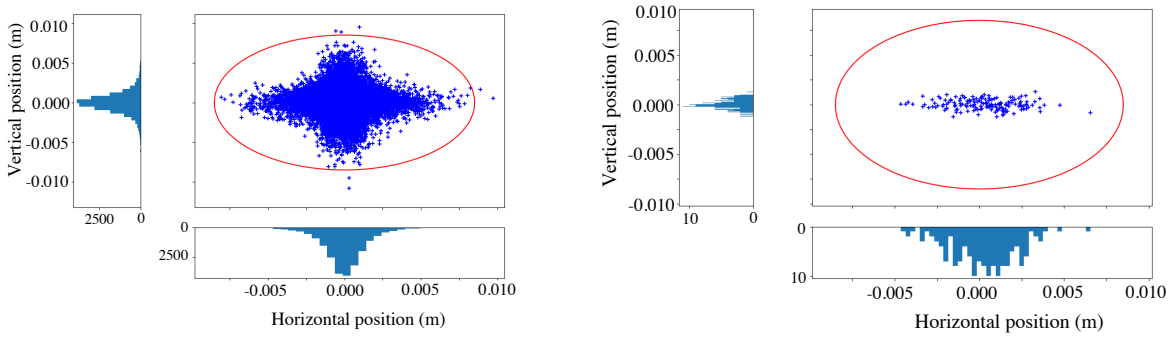
If a large enough voltage can be applied to the LPT in a single kick, this method can be used to extract the beta function and emittance from any lattice, not only when n is an integer, allowing more complex lattices such as the T-insert to be studied. It should be noted that scraping through closed-orbit distortion cannot be used to reconstruct the beta function in this way. However, as the highest possible precision is required when creating the T-insert, using only two rods to create the lattice, while applying the perturbation to the other pair, may not be possible.

The upgraded amplifiers from Oxford electronics are capable of applying up to a 20 V square-wave kick of variable amplitude and length on top of the T-insert waveforms. This kick is triggered by a TTL pulse sent to the amplifier. Currently, we have two custom amplifiers, each powering a pair of central rods. With two more of these amplifiers, the T-insert voltages could be applied to all four rods, at the same time as dipole perturbations in either the horizontal or vertical plane. As the beta function in the T-insert is relatively large, a smaller dipole kick would be required to see sufficient ion loss, especially if the emittance had first been increased.

6.4.6 Alternative methods

There is the potential to use the MCP and phosphor screen to take a time-resolved image of the ion distribution. When the ions are extracted towards the MCP, they can be accelerated by up to ∼1.8 kV. As the ions in the trap have a very low temperature (Section 3.3), the longitudinal velocity of the ions as they leave the trap is dominated by the acceleration due to the MCP voltage, U_{in}.

Due to this, ions arriving at the MCP at a given time will have a transverse distribution representative of the Twiss parameters at the time they left the trap. Therefore, if ions can be detected within a time window much smaller than an RF period, it should be possible to reconstruct the optics of the trap within that time window. Figure 6.17 shows the simulated distribution of ions arriving at the MCP for a 40 ns snapshot, 0.1 ms after the end cap is first switched off, compared to the fully time-integrated distribution. Details of how this



(a) Integrated over full extraction time.

(b) Integrated over 40 ns.

Figure 6.17: Simulations showing a comparison between the full extracted ion distribution on the MCP and a 40 ns snap shot. Blue crosses represent individual ions hitting the MCP. This assumes U_{in} = -1825 V. The red line shows the effective radius of the phosphor screen output from the MCP.

simulation was performed can be found in Section 3.4.2.

In the current setup, the MCP can be switched on and off by applying the voltage U_{out} for only a short time. However, this cannot be used to gate the MCP for the required time of $\sim$ 40 ns, as the MCP requires 50 ms to settle once U_{out} is switched on, otherwise the signal will not be correctly amplified. The signal from any ions arriving at the MCP within this time would be amplified, but with unknown and varying characteristics.

However, with a fast phosphor and a high-speed camera, it may be possible to image a snapshot of ions leaving the trap and reconstruct the beta function at a given point in time. The current phosphor screen is a P43 phosphor, with a slow decay time. A P47 phosphor, with a decay time (to 10% of the initial intensity) of 110 ns is available. Combined with a high-speed camera it may be possible to reconstruct the ion distribution with time resolution. However, much further work would be required to ensure that this method would be successful. The small number of ions arriving at the MCP in a 40 ns snapshot ($\sim$175 for an experiment containing 1×10^6 ions, as this timescale is much shorter than the extraction time) would make it necessary to reconstruct the distribution over many experiments, which may introduce large errors.

Further simulations show that the MCP should always be used to study the T-insert, as due to the large beta function and divergence within the lattice, not all of the confined ions

will be detected by the Faraday cup (described further in Section 3.4.2).

6.5 Chapter summary

In this chapter, I have described the experimental progress made towards testing QIO in a Paul trap. I described the process of designing two different T-insert linear lattices for the trap. One of these lattices is more complex, as all voltage pulses have the same amplitude, but is easily translatable to a MOSFET system of electronics. The second lattice is shorter, and voltage amplitudes are also allowed to vary.

I described the testing of the T-inserts on the IBEX Paul trap, using the MCP to detect the number of ions extracted from the trap. We found that the major factor limiting the number of ions that could be stored was the maximum beta function in the T-insert, but that by scaling lattice parameters it was possible to decrease the beta function while maintaining the correct phase advance over the T-insert.

Furthermore, we found that creating and trapping ions in a FODO lattice before matching into the T-insert, using 5 voltage pulses, increased the number of ions stored. To trap enough ions to see space-charge effects, custom-built amplifiers were used on the central rods and the ions were matched back into a FODO lattice before extraction towards the MCP. To test our understanding of the optics within the trap, we applied a quadrupole perturbation to the T-insert. The tune calculated from a calibrated oscilloscope reading matched the tune corresponding to the greatest ion loss from the quadrupole perturbation, and experimental results suggest that we can control the tune with a precision of 0.01, which should be sufficient to test QIO.

This represents a new regime for Paul traps in accelerator physics. Usually, measurements are much more qualitative, with FODO lattices often used to approximate more complex accelerator rings. In contrast, I have shown that it is possible to create a lattice that meets a specific set of constraints in phase advance and beta function.

Finally, I presented a proof-of-principle test of a method to directly measure the beta function in a Paul trap, using a series of dipole kicks and studying the ion loss through scraping. If large enough dipole kicks can be applied within the Paul trap, this is a promising method to extract the beta function throughout the cell.

Chapter 7

Simulation of Nonlinear Integrable Optics in a Paul trap

In Chapter 5, I introduced the ideas of Nonlinear Integrable Optics (NIO) and Quasi Integrable Nonlinear Optics (QIO), describing how a nonlinear potential is included in the drift region of a linear lattice to create a time-independent Hamiltonian. In Chapter 6, I described the progress that we have made towards creating a linear lattice that meets the requirements of integrable optics in IBEX. In this chapter, I will describe a planned upgrade to the IBEX Paul trap, which will allow the introduction of the octupole potential required for QIO. I will then present the results of Warp simulations showing the dynamic aperture and tune spread created by the addition of the octupole potential to the T-insert lattice. Throughout this chapter, space-charge forces are not included in the simulations, as QIO will initially be tested without space-charge forces.

In this chapter, I present the most recent and relevant simulation results, which extends the work previously published in reference [168][1].

[1]This conference paper was published in the peer-reviewed proceedings of the International Particle Accelerator Conference 2019, under a creative commons license [94], which allows me to use the content here.

7.1 Octupole trap

To test the concept of quasi-integrable nonlinear optics (QIO) in a Paul trap, IBEX will require an upgrade so that an octupole potential can be created. Furthermore, the trap will still need to be capable of creating a near-perfect quadrupole potential, so that the T-insert section of the lattice can be realised. We must be able to create the required octupole potential by applying realistic voltages within the trap. The goals of the simulations presented in this chapter are: to show that we can create an octupole potential good enough to test QIO, to investigate the impact of both a pure octupole and more realistic potentials on the dynamic aperture (as defined in the glossary) and tune spread of the ions, and to begin to explore ways of testing the stability of particle motion within the QIO lattice in the presence of a resonant excitation.

The Beam Physics group at Hiroshima University have already performed a study of several different designs for a nonlinear Paul trap, to control sextupole and octupole fields to drive nonlinear resonances [42]. Their study attempted to find a nonlinear trap design that is easy to manufacture and that has sufficient space to position the electron gun. A set of small cylindrical rods placed between the existing rods was initially investigated; however, their preferred solution was to insert four metal plates between the existing rods. These plates are easier to manufacture and hold in the correct position. As the plates cannot be too thin, for manufacturing reasons, a thickness of 1 mm is assumed, with a width of at least 4 mm. Figure 7.1 shows this transverse layout.

7.1.1 Multipole components

For a 1 mm plate thickness in the multipole trap, reference [42] shows that the $m = 6$ multipole can be almost completely eliminated if the plates are 8.5 mm from the centre of the trap (this value varies with plate thickness), allowing a high-quality quadrupole to be produced when the additional plates are grounded. As an initial step, I repeated these investigations using both Mathematica and Warp (as a Poisson solver), using the Mathematica results to

ensure a large enough grid, with sufficient grid points, was used in the Warp simulations. I investigated many trap configurations and found that although other configurations could produce a good quality octupole, they could not also produce a good quality quadrupole field.

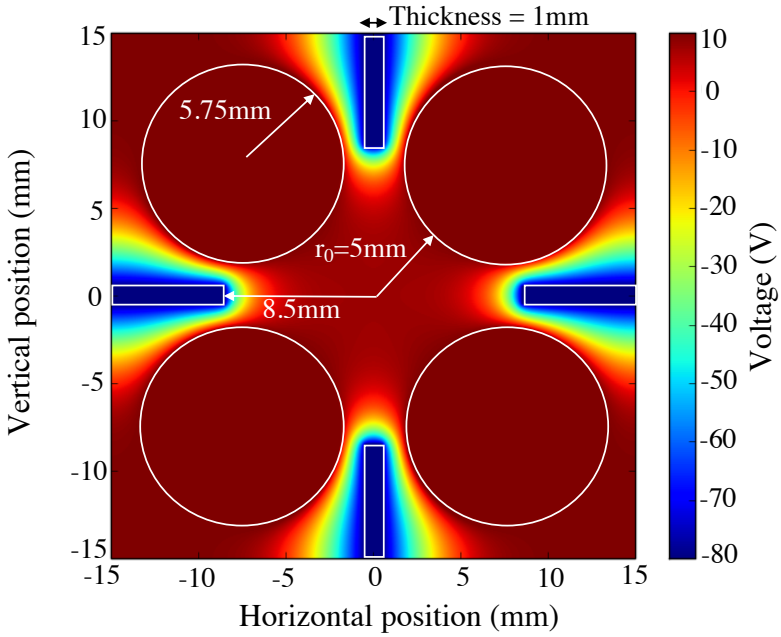


Figure 7.1: A transverse slice of the octupole trap design, with the potential within the trap shown when 10 V is applied to the rods and -80 V to the plates. As before, the trap is rotated 45 degrees from the accelerator axis.

For the experimental configuration shown in Fig. 7.1, I used both Mathematica and Warp to investigate the octupole field strengths possible within the trap. Currently, IBEX runs with a DC offset in the centre of the trap, to aid extraction onto the Faraday cup; this offset was also included in the octupole trap investigation. The strength of the octupole field in the centre of the trap was found by taking the voltage at points on a circle inside the trapping region at the reference radius (3 mm). The Fourier decomposition of the voltages at these points was then taken, giving the harmonic terms of the potential at this radius, which were then scaled to give the terms at the edge of the trap (a radius of 5 mm) [169, 170].

We then needed to establish whether this trap is sufficient to test QIO. As reference [42] contains a detailed analysis of the multipole fields created by applying voltages to the rods and plates, including the impact of misalignment, and my simulations agree with these

results exactly, I will not reproduce the data here. However, Fig. 7.2 compares the octupole field quality within the trap to the field requirements of the IOTA magnets (Section 5.3.1, [155]). The figure shows the sum of the higher-order harmonic coefficients of the field, both without alignment error and for a Gaussian error, with a standard deviation of 20 μm, on the positions of the rods and plates (averaged over ten simulations). This figure shows the radius at which the sum of the higher-order multipoles is greater than 100 units (where the octupole strength is 10,000 units). The required field quality of the IOTA octupole magnets is that no single higher-order coefficient should exceed 100 units within the good field region [155], meaning that the dashed line in Fig. 7.2 represents an even tighter constraint on the field quality. Using this definition, the good field region within IBEX extends to a radius of 2 mm with perfect alignment and ~1.6 mm when a realistic alignment error is included.

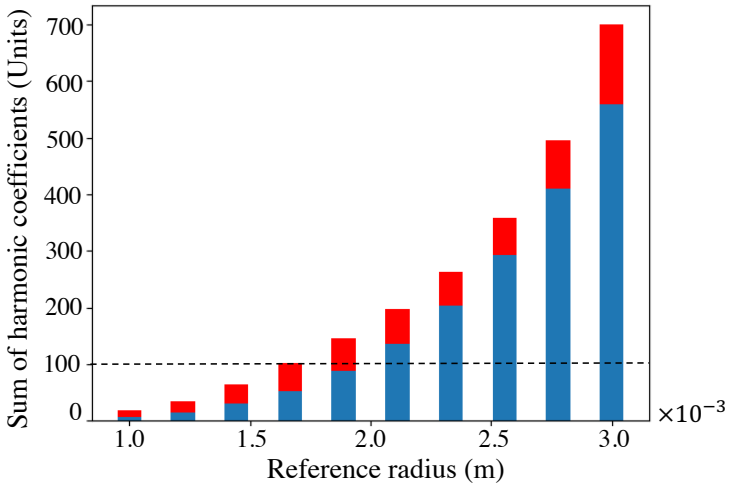


Figure 7.2: The sum of higher-order (m> 4) strength harmonics of the field, as a function of radius in the multipole trap. The red bars show the harmonics when a Gaussian error, with a standard deviation of 20 μm, is applied to the rod and plate locations and blue bars show ideal alignment. The misalignment data is averaged over 10 simulations and the dotted line is the required quality for the IOTA octupole magnets.

Currently, the IBEX trap contains only one trapping section. To test QIO we will have to create a trap in two sections, similar to the traps at Hiroshima University. This is because the geometry of the metal plates required to create the octupole will block the electron gun

from the trapping region. Ions will, therefore, have to be accumulated in one section of the trap, where only the four rods are present, and then transferred to a second trapping region containing both the rods and plates.

In a recent publication, [171], the Beam Physics group at Hiroshima University performed a detailed study of such a transfer of argon ions, experimentally showing that it is possible to transfer up to 50% of the initially trapped ions into a second trapping region.

7.1.2 Octupole strengths

Using the trap design in Fig. 7.1, it is possible to create an octupole potential of sufficient strength to investigate QIO. To determine the octupole field strength I varied first the voltage applied to the plates and then the rods, recording both the octupole voltage and the DC offset for each case. From this data I extracted the relationship,

$$\begin{aligned} V_{\text{offset}} &= 0.027V_{\text{plate}} + 0.973V_{\text{rods}}, \\ V_{\text{octupole}} &= 0.034V_{\text{plate}} - 0.034V_{\text{rods}}. \end{aligned} \tag{7.1}$$

In these equations, V_{plate} is the value of the voltage applied to the plates (here negative), and V_{rods} is the voltage applied to the rods (here positive). V_{offset} is the measured DC offset and V_{octupole} the measured octupole voltage. These equations can be solved to give the voltage that should be applied to the trap to produce the required octupole field and DC offset.

Figure 7.3 shows the beta function in the drift region of the lattice L_3, depicted first in Fig. 6.4. The octupole potential, at radius r_0, required to create the tune spread shown later in Fig. 7.5, Fig. 7.7, and Fig. 7.8, is shown in Fig. 7.3. The lower panel in this figure shows the voltages which would have to be applied to the rods and plates to achieve the required octupole potential, with a DC offset of 0 V.

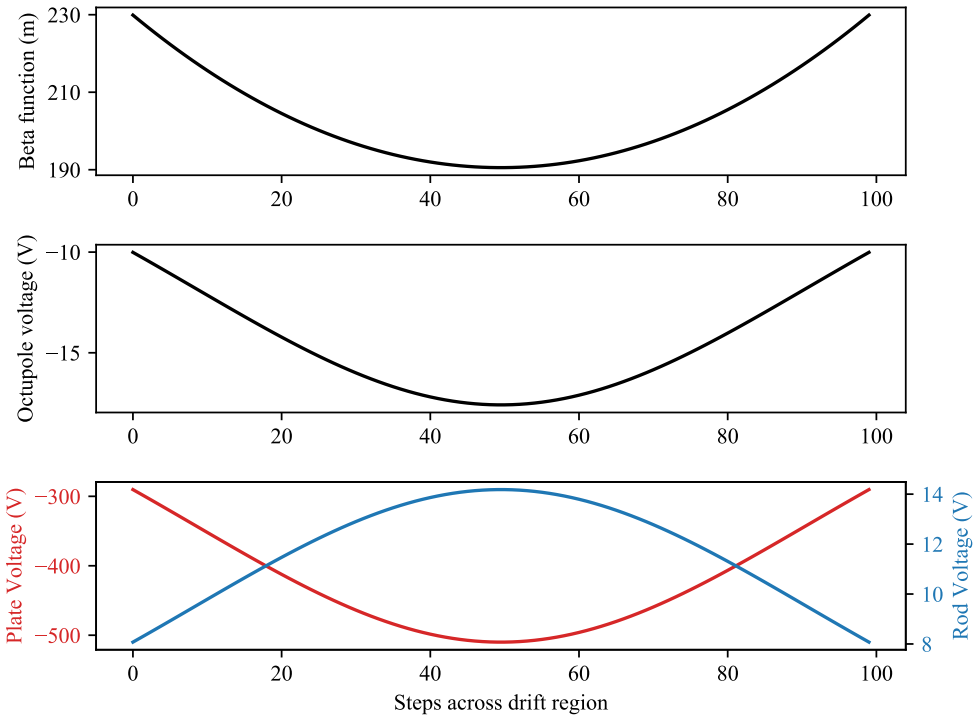


Figure 7.3: The top panel shows the beta function in the drift region of lattice L_3. The middle panel shows an example of the octupole potential required at these beta functions. The bottom panel shows the voltages required on the rods and plates, shown in Fig. 7.1, to create these potentials.

It should be noted that a simple way to decrease the voltage amplitude required on the plates is to increase the DC offset within the trap. A positive DC offset of 10 V reduces the most negative voltage required on the plates from -510 V to -395 V. However, the offset is limited by the bandwidth of the amplifier on the central rods, as the offset will also have to be applied during the T-insert.

7.2 Simulation of QIO

In this chapter, three different methods of simulation are used, all without space-charge, with increasing complexity to represent the proposed experimental setup:

1. The first simulation method represents the T-insert as a matrix kick to the ions. The matrix kick which describes the lattice L_3, shown in Section 6.1 (Fig. 6.4), is used. A pure octupole potential is applied in the drift region, either using Warp or a Python

script adapted from [154]. The octupole is applied in 100 steps across the drift region. This type of simulation is illustrated in Fig. 7.4a.

2. In the second type of simulation Warp is used. The T-insert (lattice L_3) is again represented by a matrix kick to the ions. However, the octupole potential is created by applying voltages to rods and plates, as shown in Fig. 7.1, creating a more realistic potential. The octupole potential is created by applying voltages to the rods and plates in 100 discrete time steps across the drift region. This type of simulation is illustrated in Fig. 7.4b.

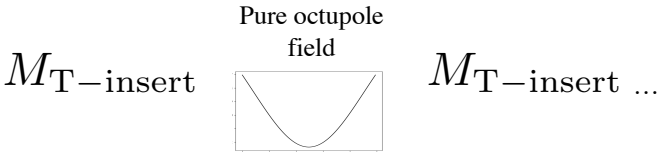
3. In the third type of simulation, Warp is used to create both the T-insert (lattice L_3) and the octupole potential, by applying voltages directly to the rods and plates[2]. This type of simulation is illustrated in Fig. 7.4c. The octupole is applied in 100 steps across the drift region.

For each of the three simulation methods, a transverse grid of ions with zero momentum was created with values of x and y up to 3 mm. The ions were introduced into the QIO lattice at the midpoint of the nonlinear region and tracked for a number of turns. Using NAFF, the tune spread was calculated for a given voltage amplitude and the dynamic aperture (DA) of the lattice was evaluated. The DA is defined here as the largest circle in real space within which no particles are lost over the whole simulation (usually 1000 lattice periods).

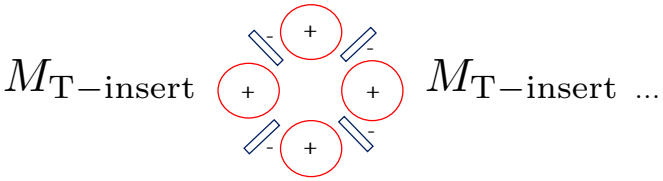
The tune spread and dynamic aperture in all simulations are qualitatively similar to those found by simulations of IOTA and UMER lattices. Throughout this section I present simulated data in a similar way to the UMER experiment, for example in reference [150], this is both for ease of comparison and because such plots are easy to interpret.

Figures 7.5, 7.6, 7.7, and 7.8 all show examples of the DA and tune spread from simulation. In each of these figures, only the ions that are still trapped at the end of the simulation are shown. Ions inside the DA are represented in colour, and ions outside of the DA are shown in grey. The colour of the ions inside the dynamic aperture is determined by the

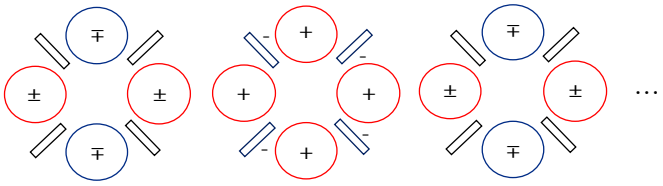
[2]In Warp a 1000 by 1000 grid is used, extending from -15 mm to 15 mm



(a) The most basic simulation implements the T-insert as a matrix kick and applies a perfect octupole potential in the drift region.



(b) Warp simulation implements the T-insert as a matrix kick but creates a realistic octupole by applying voltages to rods and plates.



(c) Warp is used to apply voltages to the rods and plates to create both the octupole and the T-insert.

Figure 7.4: Diagram showing the methods of simulation used in this chapter. $M_{\mathrm{T-insert}}$ is the single matrix representation of the lattice L_3, shown in Fig. 6.4 and Fig. 6.5.

logarithm of the difference in the tune of the ion between the first half and the second half of the simulation (dQ). Ions plotted in yellow have experienced a greater change in tune, either because they are in the region where motion is bounded but chaotic, or because they are close to a resonance. The tune shown in the right-hand panel of these figures is determined by the first half of the simulation only. The panels to the left of and below each figure show the projection onto the x and y axis, with the full surviving distribution in grey, and ions within the DA in black.

In all of the simulations in this chapter, when voltages are applied to the rods and plates to create a quadrupole or octupole potential, a DC offset of 0 V is assumed. Only minimal effort was made to increase the speed of simulations as they ran concurrently with the experimental Paul trap work.

Voltage strength (arb)	Dynamic aperture (mm)	Standard deviation of x tune spread within DA
1	2.60	0.0316
1.5	2.10	0.0309
3	1.45	0.0292
6	1.00	0.0276

Table 7.1: Change in the dynamic aperture and tune spread with octupole strength over 1000 lattice periods, for a simulation of the initial T-insert lattice, shown in Fig. 6.2. An ideal octupole and a matrix kick description of the t-insert over 1000 lattice periods was used in Warp.

Cell tunes larger than 0.5

As particle information is recorded by Warp once per lattice in the simulations described in this chapter, care must be taken for lattices with a cell tune greater than 0.5. In this case, under-sampling occurs and the FFT cannot resolve the correct tune [172]. Due to aliasing, the peak power in the FFT occurs at (1 − cell tune), which is corrected before the value is input into the NAFF algorithm described in Section 4.5.

7.3 A T-insert matrix kick and ideal octupole

The first type of simulation described in Section 7.2 was used to study the impact of a range of octupole strengths on DA and tune spread. As no scraping on the rods was included in this simulation, the dynamic aperture was limited by resonances. Table 7.1 shows the effect of varying octupole strength, confirming that as octupole strength increases, the DA shrinks. The values of dynamic aperture shown in Table 7.1 agree approximately with the estimate of dynamic aperture, $|z_N| = 0.6/\sqrt{k}$, first described in Section 5.4. For the results presented in Table 7.1 only, the original T-insert lattice design was used (Fig. 6.2), and slight deviations from the predicted DA are attributed to that fact that this lattice does not perfectly meet the integrability conditions. For all other simulations presented in this section, lattice L_3 was used.

Figure 7.5 shows an example of the DA and tune spread when 3600 particles were tracked through 1000 periods of the lattice L_3, with the octupole strengths shown in Fig. 7.3 applied. The aeroplane shape of the tune spread is present in all QIO simulations, and clearly shows why a tune of ~ 0.3 over the nonlinear region is desirable, since it will lead to the largest tune spread before the half-integer resonance is encountered (an example of such a tune spread is shown in Fig. A.5, in Appendix A.5). In Fig. 7.5, Fig. 7.7 and Fig. 7.8, the lines $Q_y = Q_x$, $Q_y = 2Q_x$ and $2Q_y = Q_x$ are plotted to highlight how particle tune is affected by these resonances, with particles clustering at these tunes. Although Table 7.1 shows that the standard deviation of the tune spread decreases slightly as the DA decreases, the maximum tune spread within the DA remains the same, as it is still limited by the half-integer resonance.

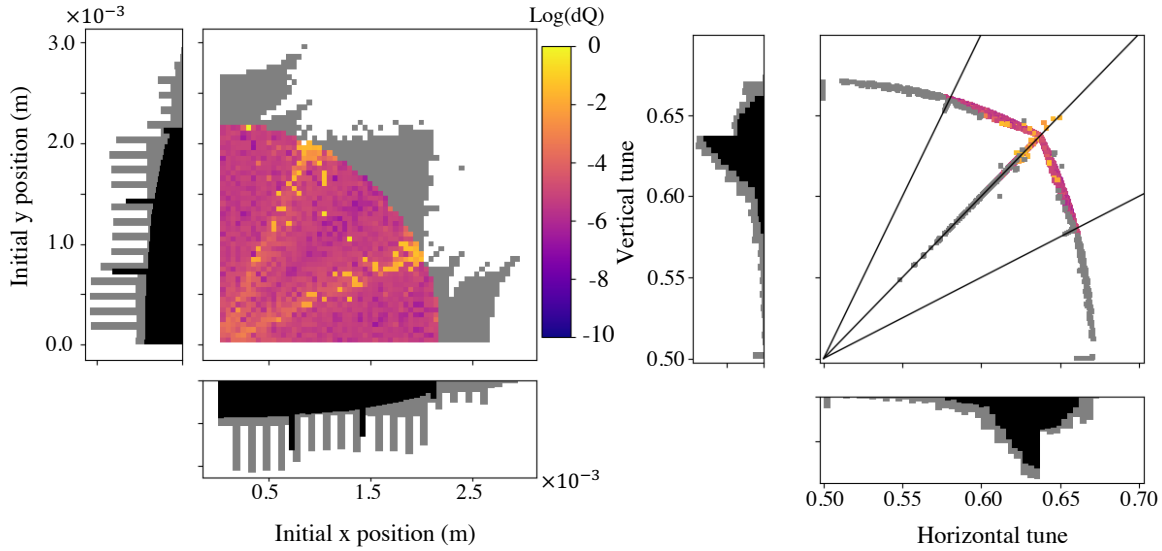


Figure 7.5: DA and tune spread, calculated using simulation method (1), where an ideal octupole is used and the T-insert is implemented through matrix multiplication of the ions. Here 1000 lattice periods are simulated and the dynamic aperture is found to be 2.2×10^{-3} m.

Figure 7.6 shows a more realistic version of the simulation in Fig. 7.5, where any scraping of the ion distribution in the T-insert is accounted for. This is achieved by tracking particles through the T-insert element by element, by a series of matrix multiplications, and removing any ions at a radius larger than 5 mm, the inscribed radius of the trap (r_0). In Fig. 7.6, the tune spread is now limited by the aperture of the trap and the beta function within the T-insert lattice, the dynamic aperture was found to be 1.7×10^{-3} m.

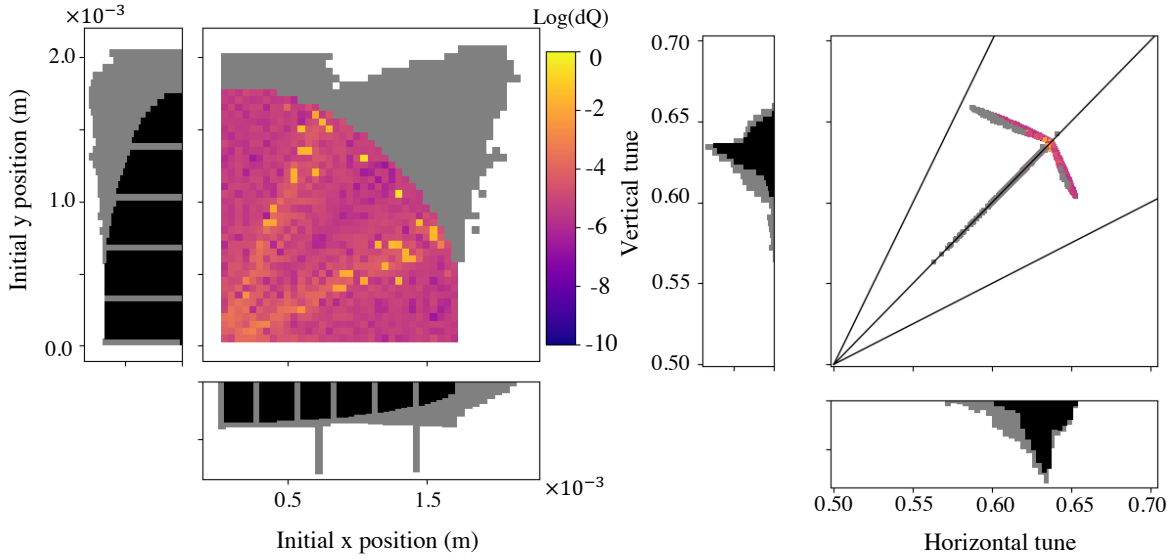


Figure 7.6: As in Fig. 7.5, now including scraping of particles outside of the radius 5 mm. The dynamic aperture is found to be 1.7×10^{-3} m.

In Chapter 6, I described the experimental process of finding a T-insert lattice capable of trapping sufficient ions to study space-charge effects. The lattice, L_3, in which we were able to confine a large number of ions, has a small beta function in the region where the octupole will be applied, meaning that a larger octupole field will be required. Using the estimate of the emittance in IBEX, described in Section 3.6, for the beta function in the drift region of the lattice L_3, two standard deviations of the ion distribution fall within a radius of $\sim$1.4 mm. This radius is well within the good field region of the octupole, even when misalignment errors are applied. In the IBEX trap, we have the flexibility to apply a range of octupole voltages.

It would be an interesting extension to move to very large octupole strengths, testing voltage strengths up to a DA of 1.4 mm, which would require the octupole voltages to be increased by a factor of $\sim$2.5 from those shown in Fig. 7.3. However, this may not be possible due to hardware constraints on the amplitude of voltages that can be applied.

A comparison between the Python simulation code and Warp, using an ideal octupole, can be found in Appendix A.5, where Fig. A.3 shows that the two agree well. I chose to use Warp to progressively build more complex simulations of the QIO lattice as Warp allows a

representation of the trap to be constructed, with voltages applied directly to the rods and plates instead of simply using perfect octupole potentials. Furthermore, space-charge forces can be included in Warp, which facilitates the next step of including space charge in future QIO simulations.

7.4 Using Warp to simulate a perfect T-insert and realistic octupole

Figure 7.7 shows a simulation in Warp, with voltages applied to the rods and plates to create the octupole potential (simulation method (2) is used). The dynamic aperture in this simulation is found to be 2.25×10^{-3} m, which is slightly larger than in Fig. 7.5 (in which simulation method (1) is used). This is because the simulation in Fig. 7.7 uses many more particles ($\sim 70\times$), giving a better resolution. This shows that creating the octupole by applying voltages to the rods and plates, i.e. moving from perfect octupole fields to more realistic ones, does not negatively impact the DA, even though the radius of the DA is slightly outside the good field region shown in Fig. 7.2.

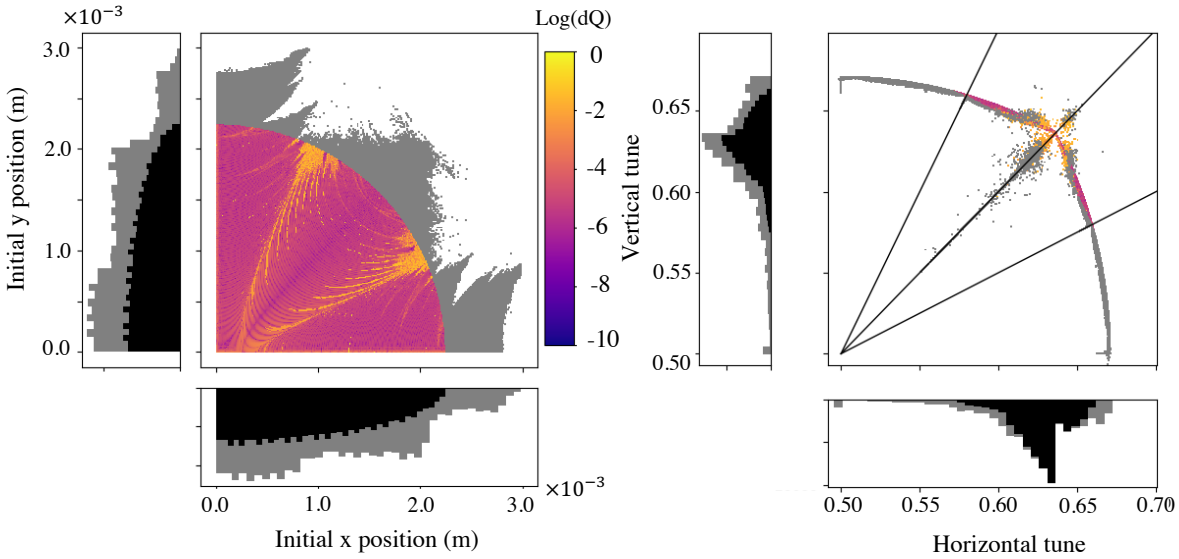


Figure 7.7: A Warp simulation of the lattice, the T-insert (lattice L_3) is implemented through a matrix kick. The octupole is created by applying voltages to the plates and rods. Here 1000 lattice periods are simulated, using 250,000 particles, the dynamic aperture is 2.25×10^{-3} m.

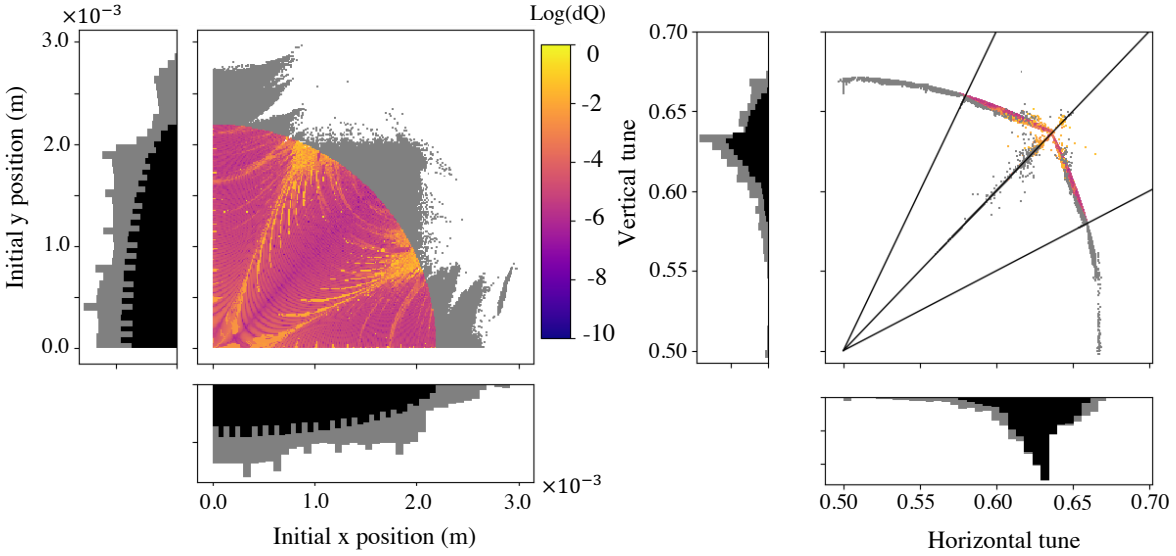


Figure 7.8: As in Fig. 7.7, now with a Gaussian error with a standard deviation of 20 μm applied to each rod and plate location. The dynamic aperture is 2.20×10^{-3} m.

In the nonlinear trap, there will be some error in the alignment of the rods and plates. Figure 7.8 shows the effect of a random misalignment with a Gaussian distribution and a standard deviation of 20 μm (based on the misalignment in IBEX, given in Appendix A.6), on the location of the rods and plates. The dynamic aperture was found to be 2.20×10^{-3} m. This small reduction in DA indicates that the QIO lattice is robust with respect to the misalignment of the octupole.

7.4.1 Introducing the octupole

A study of the impact of introducing the octupole potential to the linear lattice L_3 was performed, using a Gaussian distribution of ions (with an emittance of 2.16×10^{-9} m rad in both transverse directions) matched to the linear lattice. In these simulations, the T-insert was represented by a matrix kick and the octupole region created by applying voltages to rods and plates (simulation method (2)). In these simulations, 62,500 particles were tracked over 256 lattice periods. Figure 7.9 shows the change in the standard deviation of the ion distribution and the ion loss when the octupole term is switched on at the start of the simulation, when the octupole is turned on slowly over 100 lattice periods, and when the

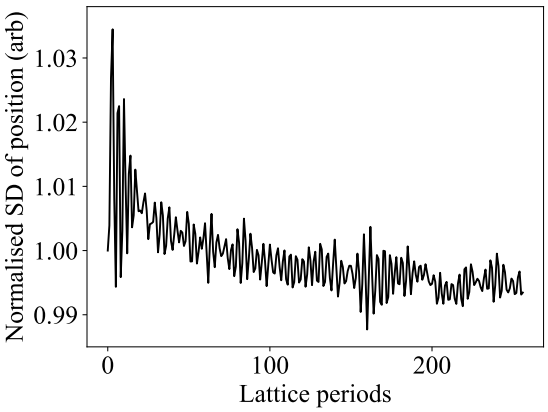
octupole is turned on slowly over 200 lattice periods. The maximum octupole voltages in each case are the same as in previous simulations, shown in Fig. 7.3.

It is important to note that any ion loss in this simulation is only through scraping applied in the drift region. Since the ion distribution is small in this region (due to the small beta function), ions are lost when they are pushed to radii outside the DA. The fact that the ion loss occurred at the same point in the ramp in the simulations shown in Fig. 7.9d and Fig. 7.9f suggests that the loss occurs as the DA shrinks and the tails of the distribution become larger than the DA. The simulations were extended to look at ion loss 550 turns after the octupole reached maximum strength in each simulation. Although the final ion numbers follow the expected trend, with 98.91% of ions remaining when the ramp is longer, 98.85% ions when the ramp is shorter and 98.64% when there is no ramp, ion loss was similar in all three cases, suggesting that for these octupole strengths the impact of any mismatch is small. Furthermore, ion loss was still very small, just 1.36% in the worst case.

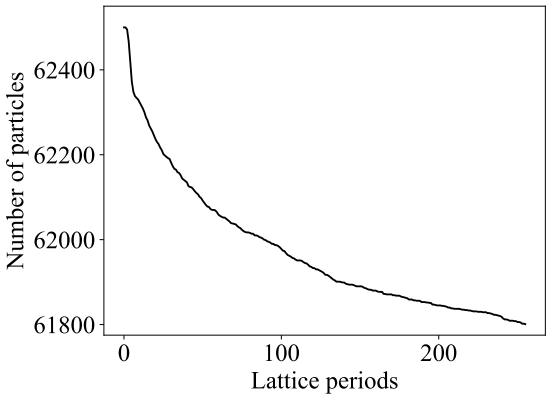
This, however, may not be true at larger octupole strengths or when space-charge effects are included. Recent studies for IOTA show that filamentation and significant emittance growth are expected when the nonlinear element is turned on for the fully nonlinear case, including space charge [173]. Our simulations should be repeated including space charge.

7.5 Introducing a perturbation

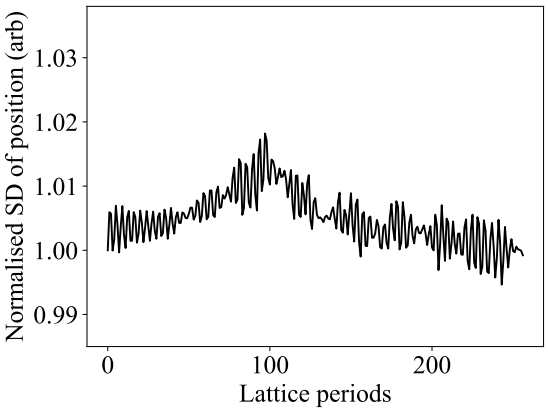
There are several proposed methods for testing QIO in an accelerator, as described in Section 5.3.1. So far, tests have been performed to find the dynamic aperture by transversely kicking particles until loss is observed, and decoherence has been tested by monitoring the damping of transverse oscillations following a transverse kick. It should be possible to use the former method to find the dynamic aperture in IBEX, kicking the ion distribution transversely as described in Section 6.4. However, testing the decoherence in IBEX may prove more difficult, as the integrated image on the phosphor screen would need to be used to monitor the change in the amplitude of transverse oscillations, yet ion extraction from the trap takes



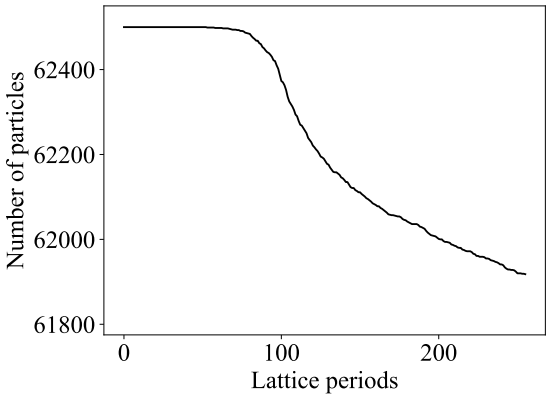
(a) Octupole initially on.



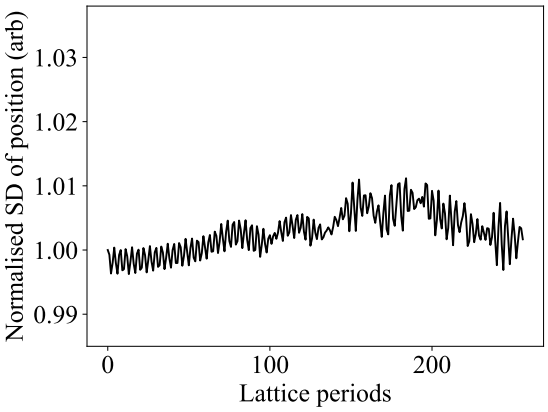
(b) Octupole initially on.



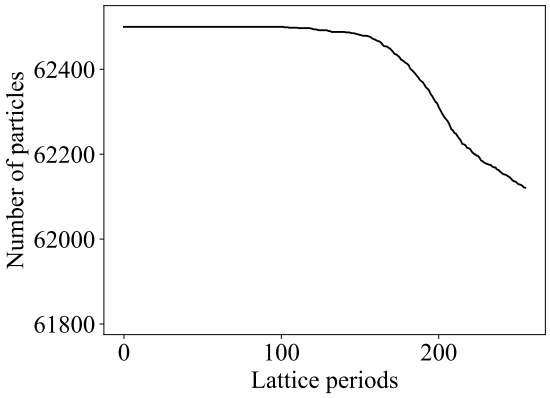
(c) Octupole ramped over 100.



(d) Octupole ramped over 100.

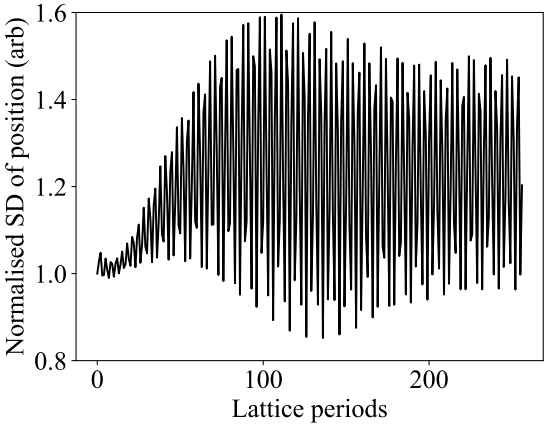


(e) Octupole ramped over 200.

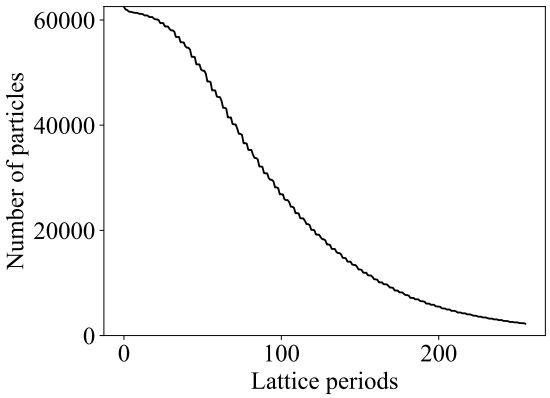


(f) Octupole ramped over 200.

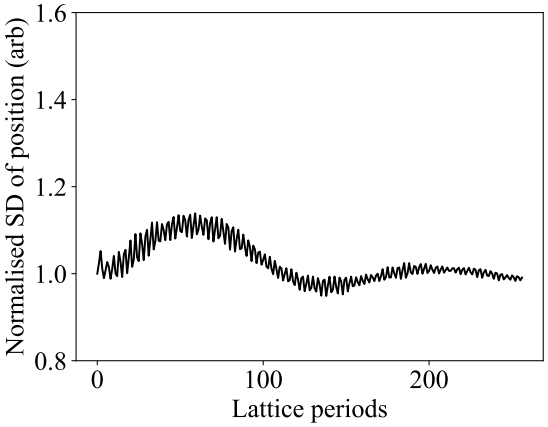
Figure 7.9: Particle loss and change in the standard deviation of the ion distribution in x, when the octupole potential is introduced to the linear lattice L_3. Initially the transverse ion distribution is Gaussian and matched to L_3. In (a) and (b) the octupole is turned on immediately, in (c) and (d) the octupole is turned on slowly over 100 lattice periods, in (e) and (f) the octupole is turned on slowly over 200 lattice periods.



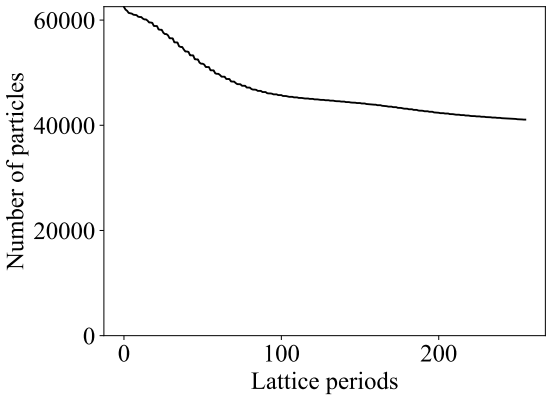
(a) Distribution change, no octupole.



(b) Ion loss, no octupole.

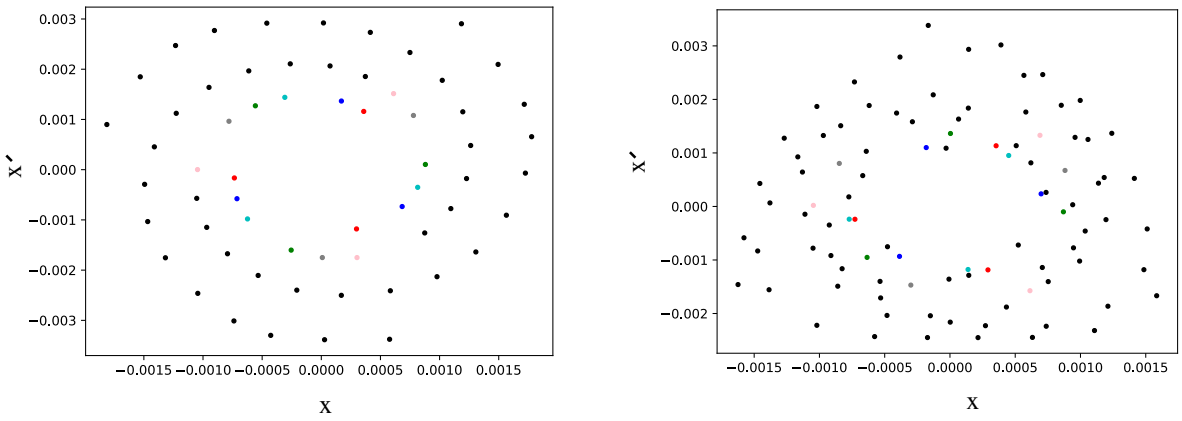


(c) Distribution change, with octupole.



(d) Ion loss, with octupole.

Figure 7.10: Particle loss and change in the standard deviation of the ion distribution in x, when a quadrupole perturbation is applied to an approximation of lattice L_3, with the octupole potential turned off ((a) and (b)) and on ((c) and (d)).



(a) With octupole switched off.

(b) With octupole switched on.

Figure 7.11: Poincaré plot showing the example of the motion of a single particle through phase space over 250 lattice periods, when a perturbation is applied, both with and without the octupole potential. The initial data points are plotted in colour for clarity, the first three points are in red, the following three in blue, etc.

many lattice periods, which may limit the accuracy of data.

One method to test QIO, much easier to achieve in a Paul trap than an accelerator, is to apply a perturbation to the trapped ions, which should be resistant to the effects of resonant excitation. This method is simple to implement using IBEX, where it is easy to apply a perturbation at any frequency. To investigate this method, both the T-insert and octupole potential were simulated by applying voltages to the rods and plates in Warp (simulation method (3)), as illustrated in Fig. 7.4c. Here I simulated an imperfect T-insert, using only ∼500 steps to describe the full lattice. Because of this, the lattice will not precisely meet the conditions for QIO (the DA and tune spread for this lattice are shown in Fig. A.4). The reduced number of simulation steps was firstly to speed up the simulation process, and secondly for later comparison with the perfect case, to note any differences caused by not exactly meeting the T-insert conditions. A Gaussian distribution of 62,500 ions, matched to the linear lattice L_3, was tracked over 256 lattice periods. Due to the imperfect nature of the lattice, there will be a small initial mismatch.

The simulation was then performed again, but with a quadrupole perturbation at a frequency of $2 \cdot 2\pi \cdot Q$ applied to the rods, where Q is the tune of the lattice with no octupole

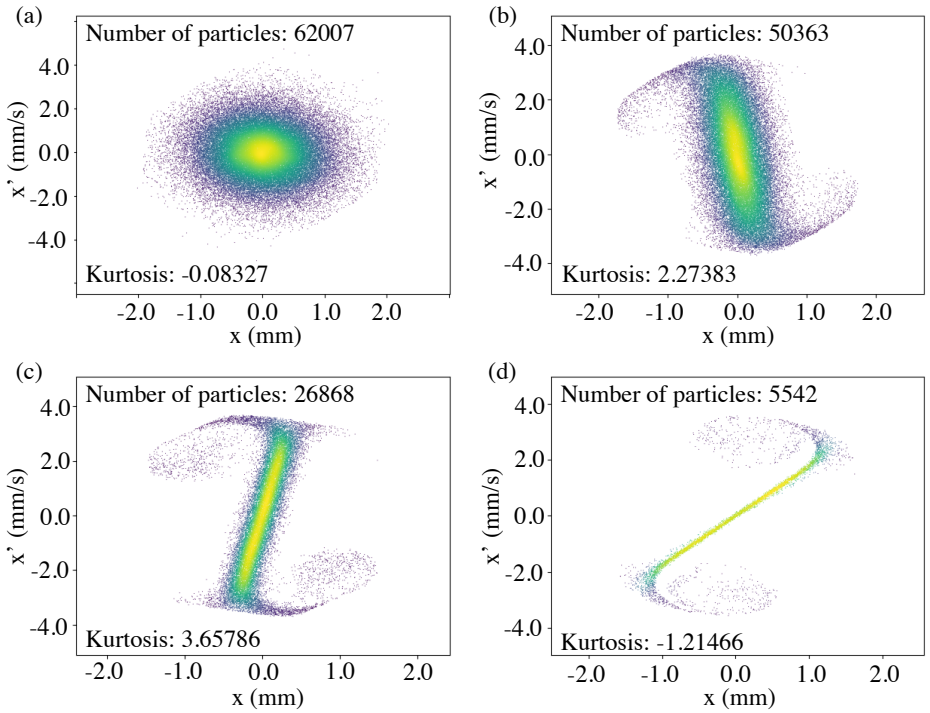


Figure 7.12: Phase space when a quadrupole perturbation is applied to a QIO lattice, at a frequency of $2 \cdot 2\pi \cdot Q$, with the octupole potential switched off. (a) is after 1 lattice period, (b) after 50 lattice periods, (c) after 100 lattice periods, and (d) after 200 lattice periods.

term. From previous experimental observations (shown in Fig. 6.10), a perturbation of 0.1 V is enough to cause ion loss, so this perturbation strength was used in the simulations. Figure 7.10b shows the ion loss in the case where the perturbation is applied and the octupole potential is turned off. Figure 7.10d shows the ion loss when the octupole is turned on. It is immediately obvious that the octupole term significantly mitigates the effects of the resonant excitation.

Figure 7.11 shows two Poincaré plots, illustrating the difference in the motion of one particle, with the same initial conditions, with and without the octupole term. Without the octupole, the particle is resonantly excited and ultimately lost (Fig. 7.11a). However, when the octupole potential is turned on the particle is initially excited, but after moving to higher amplitudes, away from the perturbing frequency, the motion is bounded and the particle is not lost (Fig. 7.11b). This process is highlighted by displaying the earlier points in colour in Fig. 7.11.

Figures 7.12 and 7.13 show the phase space in the x direction when the perturbation is

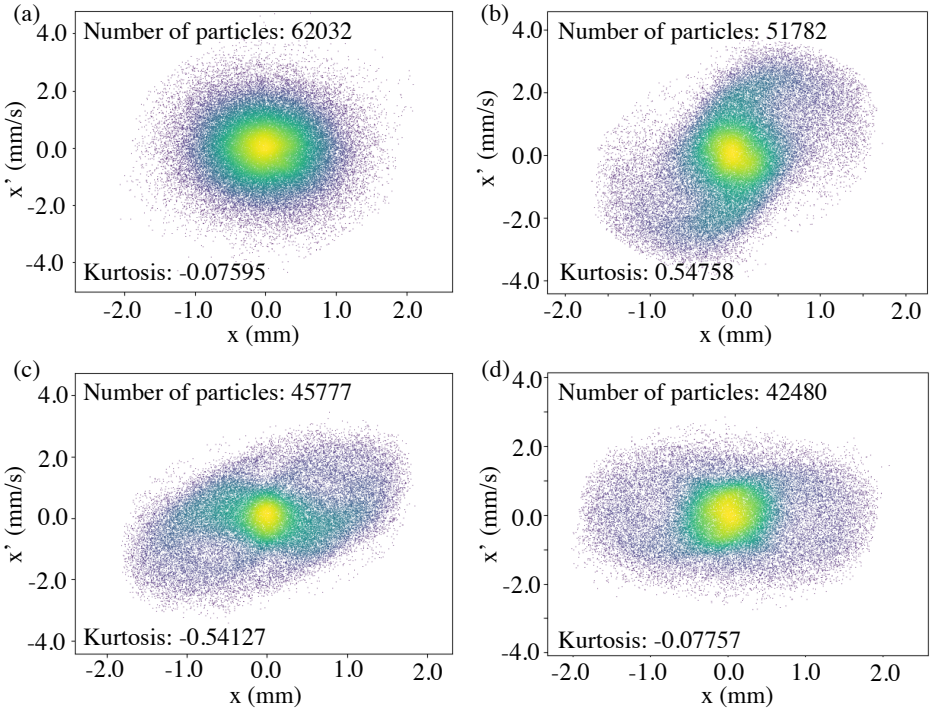


Figure 7.13: Phase space when a quadrupole perturbation is applied to a QIO lattice, at a frequency of $2 \cdot 2\pi \cdot Q$, with the octupole term switched on. (a) is after 1 lattice period, (b) after 50 lattice periods, (c) after 100 lattice periods, and (d) after 200 lattice periods.

applied to the lattice, with the octupole potential off and on, respectively. The phase space after 1, 50, 100 and 200 lattice periods is shown. Figure 7.13 clearly shows that although ions are still excited to larger amplitudes they then stay there and that by 200 turns, although the perturbation is still being applied, the distribution has returned to something resembling the initial distribution, but with a greater halo of particles at large amplitudes. This is shown further in Fig. 7.14, where the distributions are projected onto the x axis. However, this halo of particles is still potentially problematic in intense beams, as it can be driven to larger amplitudes by oscillations of the core (the same data, shown instead in the coupled coordinate system is given in Fig. A.6, in Appendix A.5).

7.6 Space charge

When large numbers of ions are confined using a QIO lattice, space-charge forces will alter the beta function in the lattice, potentially shifting parameters away from the required values

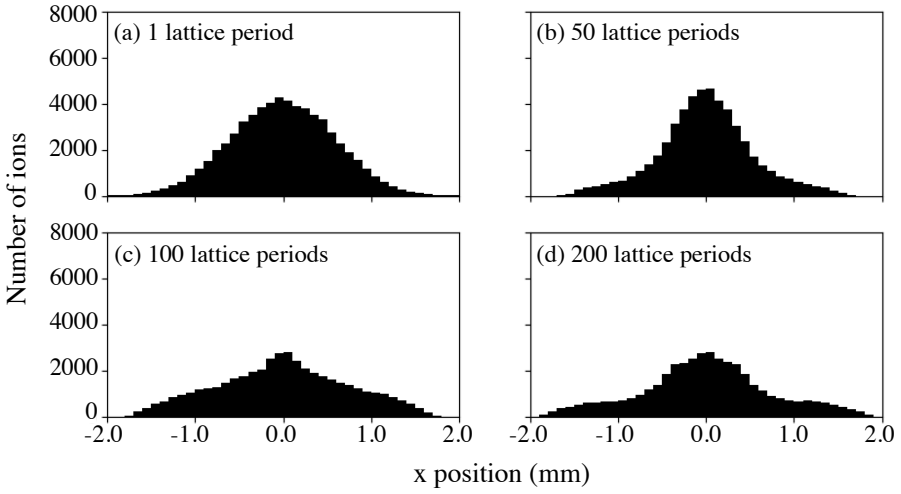


Figure 7.14: A projection of the phase space distributions shown in Fig. 7.13 onto the x axis.

for QIO. To investigate these effects, I created a Python script to find the matched Twiss parameters including space-charge effects. Starting from the initial Twiss parameters for the case without space charge, the envelope equations for the lattice were solved numerically using a fourth-order Runge-Kutta. The starting Twiss parameters were then altered, and the equations solved again until the lattice was matched.

Figure 7.15 shows the result of this for lattice L_3 for a relatively small ion number (2×10^6) and a relatively large emittance (3.5×10^{-9} m rad). Even for these values, there is a visible split in the beta functions within the drift. The transverse tunes (Q_x, Q_y) with space charge are (0.626, 0.624) for the full lattice and (0.489, 0.497) for the T-insert only. The beta functions at the centre of the drift split, becoming 188.5 m and 205.3 m.

The IOTA accelerator will face a similar problem, the lattice will have to be re-tuned slightly at each new intensity [174]. Proposals for re-matching with space charge consider only linear components of the beam, through second-order moments, which allows the lattice to be re-matched while maintaining the integrability conditions.

However, when the beam or ion distribution encounters a resonance, the distribution may shift, especially in the case of QIO, where the system is not fully integrable. Any change in the particle distribution will, in turn, alter the tune. There is currently not a

detailed theoretical understanding of the impact of space charge on NIO [175]. As discussed in detail in Chapter 4, we do not have a clear analytical understanding of space-charge-driven resonances, which makes it difficult to reconcile with NIO.

Space-charge forces add to the challenge of simulating NIO. Recently, advances have been made using the code IMPACT-Z to model NIO with space charge in IOTA [175]. Symplectic tracking with a second-order symplectic integrator is used, including space charge through a symplectic spectral space-charge solver. It is hoped that this method will help to avoid numerical artefacts, such as grid heating, in long simulations($\sim$ 10,000 turns for studies of beam stability and low-level particle loss). Grid heating refers to the increase in energy within the simulation as a consequence of treating time and space as discrete variables, it is particularly problematic as it leads to a nonphysical growth in the invariants of motion. However, the conservation of these invariants is essential for NIO, so it is important to be able to distinguish between spurious and real growth. Several other methods of symplectic space-charge tracking are also in use for IOTA studies [29, 176]. In addition, Warp has been used for studies of the UMER QIO lattice with space charge over a small number of turns [118].

The complexity of these simulations, and the dependence upon the choice of Poisson solver, the number of macroparticles, the number of grid points, and other variables, again highlights the benefits of using IBEX to study QIO alongside simulations.

7.7 Chapter summary

In this chapter, I have described a planned upgrade to the IBEX trap, based on the nonlinear trap at Hiroshima University, and shown that the desired, high-quality, octupole potential can be created by applying achievable voltages to the components of the nonlinear design.

I then presented several simulations, using both a Python code and Warp, showing the effect of the octupole potential on the tune spread and dynamic aperture, assuming the T-insert lattice described in Chapter 6. The strength of the octupole potential, misalignment

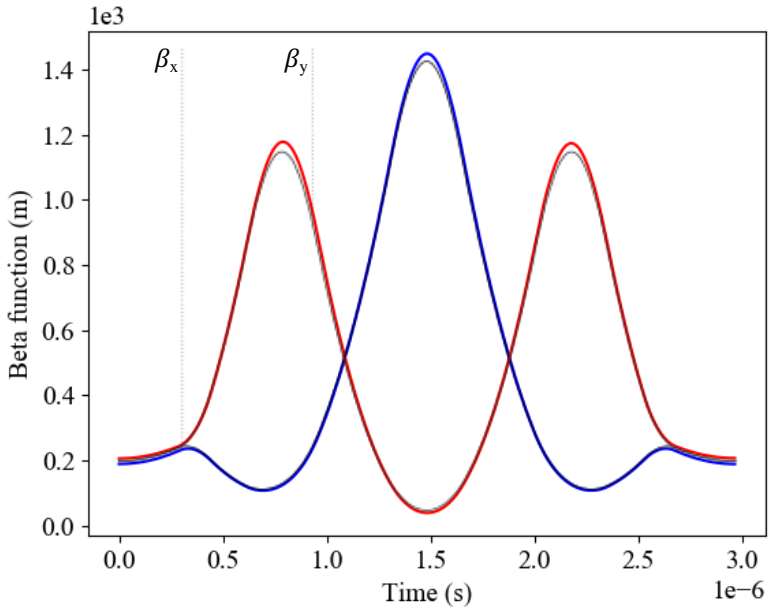


Figure 7.15: The change to the measured beta function (x in blue, and y in red) due to space-charge forces when 2×10^6 ions are stored with an emittance of 3.5×10^{-9} m rad in lattice L_3. Beta functions without space charge are shown by the thin black line.

within the trap, and effect of scraping in the T-insert lattice were studied, showing that misalignment of the expected order is not expected to limit the DA or tune spread.

The mismatch associated with the octupole potential was investigated with no space-charge forces, showing that although turning the octupole on slowly reduces ion loss, even when the octupole is turned on suddenly, ion loss is only of the order of 1%. A quadrupole perturbation was applied to an imperfect QIO lattice at the correct frequency to resonantly excite particles, mimicking a proposed IBEX experiment, and showing the effect of the nonlinear term on particle motion. Beam loss was significantly reduced, as expected, even when the conditions for QIO were not perfectly met.

7.8 Further work

I have performed basic simulations of a T-insert and octupole potential within the IBEX trap. Now that the basic simulation codes exist, further work can be performed. The next step in the simulation process is to create a field map of the quadrupole and octupole fields

within the trap, which can then be scaled with the octupole and quadrupole voltages so that the Poisson solver is not required in every step of the simulation. This should significantly increase the speed of simulations without space charge.

Simulations and analytical calculations should also be performed for the alternative method described in [158], first discussed in Section 5.6, which proposes a reduction in the number of nonlinear magnets and a change in their spacing. Furthermore, as the trap shown in Fig. 7.1 is also capable of creating a sextupole [42], the case in which sextupoles are used to create the non-linearity should also be investigated.

Simulations of QIO in IBEX, including space charge, should be attempted for small (~ 256) numbers of lattice periods. It should, however, be noted that these simulations are not trivial and that a significant amount of effort has previously gone into creating accurate simulations for NIO by the teams working on IOTA and UMER. As IBEX is designed to remove the need for lengthy simulations, effort should be concentrated on the experiment itself, with simulations used to guide the design of experiments using the trap.

The next step towards testing QIO in IBEX is to design and machine an octupole trap. As the trap is small and relatively simple, this process should not take long. Equally, machining the new parts will not be prohibitively expensive. Care should be taken to ensure the best possible alignment of rods and plates, not just with each other but throughout the different sections of the trap. It has been suggested ([177]) that the current longitudinal alignment system, using three ceramic spheres, should be redesigned, as they over-constrain the system, making it harder to align the rods correctly when constructing the trap and increasing the likelihood of damage to components. An investigation into the amplitude of voltages that can safely and accurately be applied to the plates should be conducted, as this will be limited by hardware, which will, in turn, limit the tune spread which can be investigated.

In Chapter 5, I described how nonlinear decoherence following a dipole kick is used to test the QIO lattice in IOTA. Comparisons of decoherence simulations and analytical predictions have been performed for the IOTA experiment. However, as yet these simulations do not include space charge [178]. The analytical prediction of decoherence time should be compared

against experimental results obtained using IBEX (although accuracy may be limited by the ion extraction time), and any deviations with increasing space charge investigated. When planning the experiments that will be performed to test QIO using IBEX, it is important that studies are designed so that they will assist with the design of real machines based on QIO. For example, in IBEX we can easily vary the number of steps used to create the octupole potential and study the impact on tune spread. In a real machine, a continuously varying octupole is not practical and so a series of magnets with fixed strengths and apertures will be used.

Chapter 8

Conclusions

This thesis has described the use of two linear Paul traps for accelerator physics studies.

A linear Paul trap can be used to study the transverse beam dynamics of intense accelerators, as the transverse Hamiltonian of ions within a Paul trap is equivalent to that of particles within an accelerator. A Paul trap is a useful tool for accelerator physics as it is relatively inexpensive, compact, and ion loss does not lead to damage or activation of components. However, in previous work, Paul traps have been used to study accelerator dynamics qualitatively. In this thesis, I have studied accelerator dynamics quantitatively with a Paul trap, to further understand coherent space-charge-driven resonances and to investigate novel designs for future intense machines.

The IBEX trap was commissioned at the Rutherford Appleton Laboratory, Oxfordshire, with the first trapping of ions achieved in February 2017. The trap was then characterised, as an understanding of the dynamics of ions is essential for the design of experiments, and to understand any experimental limitations. Using IBEX, we were able to trap up to $\sim 1.2\times10^7$ ions; however, experiments were limited to below $\sim 1 \times 10^7$ ions, as for greater ion numbers the shot-to-shot variation in ion number was large. Space-charge effects were observed for larger ($\sim 10^6$) ion numbers, and an intensity-dependent tune shift was observed in tune scans.

Experimentally, the longitudinal temperature within the trap was found to be 0.285 ± 0.036 eV. Furthermore, if experiments are limited to timescales on the order of 0.1 s, the impact of ion-ion and ion-neutral collisions on the ion distribution is small. Through the calibration of the MCP, I was able to detect down to $\sim 10^3$ ions, which allowed the trap to be calibrated in the zero space-charge regime. Using an MCP, phosphor screen, and CCD camera to image the ion distribution extracted from the trap, an upper bound of 2.16×10^{-9} m rad was placed on the value of the transverse emittance within the trap.

Using the S-POD trap during a visit to the Hiroshima University in 2017, a study of coherent and incoherent resonances was undertaken. A tune scan across cell tunes ranging from 0.1 to 0.4 was performed at eight different intensities, corresponding to ion numbers in the range 10^6 to 10^7. Ions were trapped for 100 ms (10^5 rf periods). Ions were first trapped at a cell tune of 0.15 and then ramped to the tune of interest over 100 rf periods. By looking for cell tunes where the number of ions extracted from the trap was minimal, resonances were identified, indicating that at this tune ions had been resonantly excited, scraped on the central rods of the trap, and lost. Due to space-charge forces, the location of the resonance in tune space changes with intensity. The cell tunes at which resonances occurred were extracted from the data.

The PIC code Warp was used to simulate the experiment; however, a much shorter timescale was used and emittance growth was studied, instead of ion loss, as running simulations for 10^5 rf periods would have taken a prohibitive amount of time. These simulations were used to guide the analysis of the data. For example, I found that ramping the tune through the resonance at a cell tune of 0.25 led to emittance growth. Due to this, so that the same emittance for all tunes at a given intensity could be assumed, only resonances at lower cell tunes than 0.25 were studied quantitatively. Furthermore, as expected from the literature, the simulation showed that at a cell tune of 0.25 an incoherent fourth-order resonance is first experienced by the ion distribution, with a second-order coherent excitation of the ions only dominating at later times.

From the literature, the location of a coherent space-charge-driven resonance is dictated

by a resonant condition, dependent on the order of the resonance through the term C_m. Due to competition between resonances of differing orders at a single cell tune, extracting a value of C_m for each order was not possible. Therefore, I assumed that the location of maximum ion loss can be described instead by the factor A_m. From the mathematical description of the ions within the trap, and data taken using S-POD, values of A_m were extracted and compared to the theoretically predicted values of C_m. For the resonance at cell tunes of $\frac{1}{8}$ and $\frac{1}{6}$, I found A_m values consistent with 1, suggesting no coherent oscillation. However, for a cell tune of 0.25, a value of 0.517 ± 0.091 was extracted. This is smaller than the predicted value of C_2 =0.75, which can be explained by the emittance increase due to the initial fourth-order excitation before the coherent second-order excitation of the distribution, as well as the finite width of the resonance stopband.

After IBEX was commissioned, a similar experiment was performed on the IBEX trap, qualitatively studying the difference between the resonant excitation and ion loss at a cell tune of 0.25, for equal and unequal transverse tunes. The experimental results obtained from the IBEX trap disagreed with both the analytical prediction and simulation results. I observed that the location (in tune space) of the resonance shifted further with increasing intensity in the case of unequal tunes ($A_{2_{\text{unequal}}}/A_{2_{\text{equal}}} = 1.6$). The discrepancy between the experimental results and the simulation, which studies only emittance growth, suggests that we may not yet fully understand the relation between emittance growth and ion (or beam) loss, as particle loss will, in turn, impact the space-charge forces within the distribution. However, this data was taken before the installation of the MCP and so errors associated with this data could be reduced in a further study.

The second half of this thesis aimed to answer the question, can we test nonlinear integrable optics in a Paul trap? Nonlinear integrable optics (NIO) is a novel design for future intense accelerators. A complex nonlinear magnet is installed in a drift region of a linear lattice which precisely meets several conditions. For example, the linear lattice must have a phase advance of $n\pi$, where n is an integer, and equal beta functions in the region of the nonlinear magnet. If the conditions are met, there are two invariants of the motion and the

system is integrable, resulting in bounded particle motion and reduced particle loss. As the complex nonlinear potential is difficult to achieve, a version using only octupole magnets has been proposed, known as quasi-integrable nonlinear optics (QIO). In QIO there is only one invariant of the motion. We aim to test QIO in the IBEX trap.

I designed and tested several T-insert lattices using the IBEX trap. The first T-insert lattice was designed using a basin-hopping algorithm. It consisted of twelve voltage pulses, each of 25 V but varying in length. This lattice could easily be created using a MOSFET circuit if the current IBEX electronics were unable to create precise-enough waveforms. This lattice had a large beta function and was unable to trap enough ions to study space-charge effects. Due to this, the lattice was redesigned, using only five voltage pulses of varying duration and amplitude. The phase advance across the region where the nonlinear section will be inserted was reduced from $0.3(\times 2\pi)$ to $0.135(\times 2\pi)$. This lattice was scaled so that the phase advance remained the same but the beta-function amplitude, the length of the lattice, and the amplitude of the voltage pulses, changed in each case. Three versions of this lattice structure were studied, each with a different maximum beta function. I found that to successfully trap a large number of ions in the T-insert lattice, ions had to be first accumulated at a cell tune of 0.15 using a FODO square-wave lattice, before being matched into the T-insert lattice. Five voltage pulses were used for this matching. Due to bandwidth limitations on the amplifiers, the ions had to be matched back to the FODO lattice before extraction. Using this method, I was able to trap enough ions to test QIO including space-charge effects.

To establish that the lattice created in IBEX met the requirements of a T-insert, the tune was verified by applying a quadrupole perturbation to the lattice at a range of frequencies and studying the ion loss. A method to measure the beta function in a Paul trap using a series of dipole kicks was designed and investigated using the S-POD trap. This method showed promising results; however, it requires that a large, short, voltage kick is applied to the ions, which is a challenge given the current IBEX hardware.

An upgrade to the IBEX trap, allowing an octupole potential to be created, was in-

vestigated. I showed that a trap with two sections (one for accumulating ions and one for testing QIO) and a design similar to that of the multipole trap at Hiroshima University can create an octupole potential of sufficient strength and quality to test QIO. Simulations were performed showing the impact of octupole strength, scraping, and misalignment on the dynamic aperture and tune spread. The response of the ion distribution to turning the octupole potential on, and to a perturbation applied to the QIO lattice, was investigated using Warp.

8.1 Further work

Now that the MCP has been installed in IBEX, several interesting studies are possible. For example, I have shown that the integrated image of the ion distribution on the phosphor screen is dependent upon the optics within the trap. Simulation studies should be performed to test if it is possible to detect small changes in either the ion distribution or the optics within the trap, using only the integrated image.

Several studies could be performed to build on the work presented in Chapter 4, attempting to bridge the gap between ion loss, typically monitored over longer timescales using a Paul trap, and emittance growth, studied over short timescales in simulations. The onset of resonance, starting from ~ 100 rf periods, should be studied with both images of the ion distribution from the phosphor screen, and through ion loss, as the phosphor-screen images can be used to track emittance growth. This could lead to a better understanding of the interplay between coherent and incoherent resonance over longer timescales.

Significant progress has been made towards testing QIO in the IBEX trap. A nonlinear trap should be designed, and the hardware required to apply a sufficiently large and precise voltage to the plates of the nonlinear trap should be investigated. The new trap can then be machined and installed within the IBEX vessel.

There is the potential to use a fast phosphor and high-speed camera to image ions leaving the trap over very short timescales. A large voltage is applied to the MCP, meaning that ions

are accelerated as they leave the trap. This acceleration results in longitudinal ion speeds much greater than those within the trapped distribution. Due to this, it may be possible to reconstruct the optics within the trap from a CCD image, as ions arriving at the MCP within a short period of time will all have experienced the same optics as they left the trap. However, as only a small number of ions will be detected in such a short time, a distribution would have to be built up over many experiments. As a high-speed camera would be an expensive addition to the IBEX hardware, a detailed simulation study should be performed before this is attempted.

An experimental program for testing QIO should be designed, based around the performance of the lattice in decoherence tests and when a perturbation is applied. Lattice parameters, such as the number and spacing of discrete octupole steps, should then be varied. The number of ions should then be increased, so that space-charge effects are included. The lattice will have to be re-matched and the effect of intensity on the lattice properties studied. Experiments should be designed so that they are directly relevant to the design of future accelerators using QIO.

Appendix A

A.1 IBEX tune scan data

To mark the completion of the first stages of the commissioning of IBEX, before the installation of the MCP, a tune scan was performed at a range of intensities, with ions extracted onto the Faraday cup, following the same experimental procedure as in Section 4.3. Fig. A.1 shows the result of this experiment.

It is immediately obvious by comparison of Fig. A.1 to Fig. 4.1, that the IBEX Faraday cup gives a noisier ion signal than the S-POD MCP. Furthermore, the ion signal is reduced at larger cell tunes as not all ions impact on the Faraday cup during extraction. However, the similarity between the two figures is also apparent, and we observe for the first time using IBEX the tune shift with increased intensity.

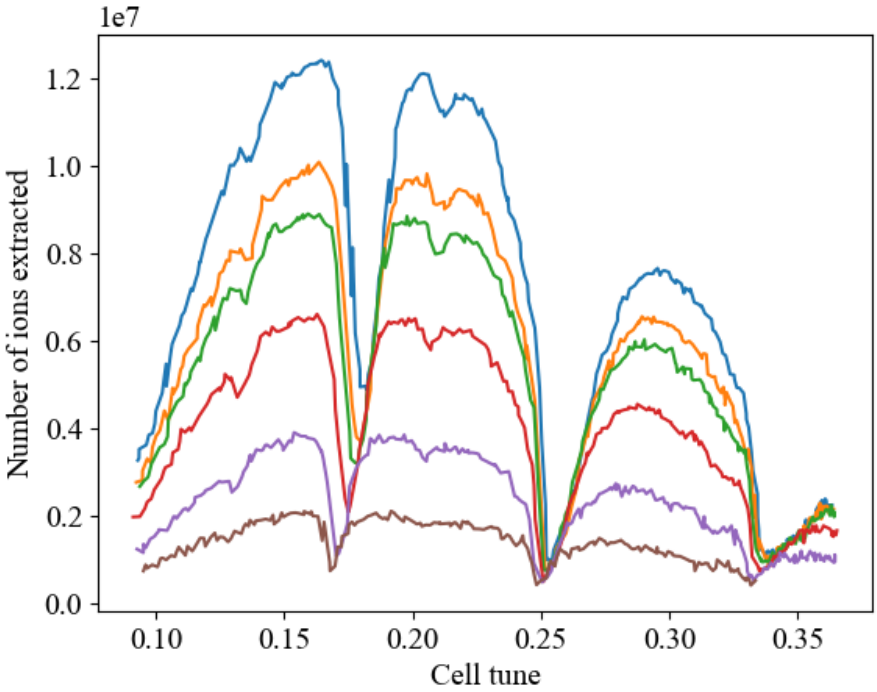


Figure A.1: Measured ion number extracted from the IBEX trap against cell tune. Each point on the lines represents a separate experiment where the ions are created, stored and extracted. Different colours represent the different ion numbers initially trapped. The Faraday cup was used to detect ions.

A.2 Ion distribution

This appendix describes the mathematical description of the ion distribution in time, at either the Faraday cup of the MCP. The following derivation is by Dr Christopher Prior, from the Intense Beams Group, RAL, and is included here for completeness.

Several basic assumptions are first made about the trap, which is considered only in one dimension:

1. The trap has a total length L and ions are distributed from $\frac{-L}{2}$ to $\frac{L}{2}$, with a density $f_X(x)$.
2. The ions have a velocity distribution $f_V(v)$.
3. The trap is open at one end, and closed at the other where ions are reflected.
4. The detector is positioned outside of the open end of the trap, at x = D.
5. There is no acceleration of ions as they leave the trap (this is later corrected to give a more realistic distribution).

$F_T(t)$ is the cumulative distribution function for the arrival time, T, of particles at the detector.

There are $f_X(x)dx$ ions in a thin slide, dx, at position x. These ions arrive at the detector before time t if their velocities are

$$v \geq \frac{D-x}{t}, \tag{A.1}$$

in the case where ions are already moving towards the open end of the trap, or,

$$v \leq -\frac{(x+L+D)}{t}, \tag{A.2}$$

in the case where ions are first reflected from the closed end of the trap.

The total number of ions to reach the detector by time t, where $t > 0$, is

$$F_T(t) = \int_{x=-L/2}^{L/2} f_X(x)dx \left[\int_{v=(D-x)/t}^{\infty} f_V(v)dv + \int_{x=-\infty}^{-(x+L+D)/t} f_V(v)dv \right]. \tag{A.3}$$

For a uniform distribution of n ions, $f_X(x) = \frac{N}{L}$, in the range $\frac{-L}{2}$ to $\frac{L}{2}$. As this is independent of x, the expression is evaluated by inverting the order of integration.

The first term in Eqn. A.3, becomes

$$\begin{aligned} &\int_{x=-L/2}^{L/2} f_X(x)dx \int_{v=(D-x)/t}^{\infty} f_V(v)dv \\ &\qquad = \frac{N}{L}\left[\int_{(D-L/2)/t}^{(D+L/2)/t} f_V(v)dv \int_{D-vt}^{L/2} dx + \int_{(D+L/2)/t}^{\infty} f_V(v)dv \int_{-L/2}^{L/2} dx \right] \\ &\qquad = \frac{N}{L} \int_{(D-L/2)/t}^{(D+L/2)/t} \left(\frac{L}{2} - D + vt \right) f_V(v)dv + N \int_{(D+L/2)/t}^{\infty} f_V(v)dv. \end{aligned} \tag{A.4}$$

The second term from Eqn. A.3 becomes

$$\begin{aligned} &\int_{-L/2}^{L/2} f_X(x)dx \int_{-\infty}^{-(x+L+D)/t} f_V(v)dv \\ &\qquad = \frac{N}{L}\left[\int_{-(3L/2+D)/t}^{-(L/2+D)/t} f_V(v)dv \int_{-L/2}^{-(L+D+vt)} dx + \int_{-\infty}^{-(3L/2+D)/t} f_V(v)dv \int_{-L/2}^{L/2} dx \right] \\ &\qquad = -\frac{N}{L} \int_{-(3L/2+D)/t}^{-(L/2+D)/t} \left(\frac{L}{2} + D + vt \right) f_V(v)dv + N \int_{-\infty}^{-(3L/2+D)/t} f_V(v)dv. \end{aligned} \tag{A.5}$$

The distribution function $f_t(t)$, is then found as the derivative of the cumulative distribution function $F_T(t)$. Applying this to the sum of Eqn. A.4 and Eqn. A.5 gives

$$f_T(t) = \frac{N}{L}\left[\int_{(D-L/2)/t}^{(D+L/2)t} v f_V(v)dv - \int_{-(D-3L/2)/t}^{-(D+L/2)t} v f_V(v)dv \right]. \tag{A.6}$$

Assuming a Gaussian velocity distribution,

$$f_V(v) = \frac{1}{\sqrt{2\pi\sigma^2}} e^{-v^2/2\sigma^2}, \tag{A.7}$$

as the distribution is thermal,

$$\int v f_V(v) dv = -\frac{\sigma}{\sqrt{2\pi}} e^{-v^2/2\sigma^2}. \tag{A.8}$$

Finally leading to

$$f_T(t) = \frac{\sigma}{\sqrt{2\pi}} \frac{N}{L} \left[e^{-(D-L/2)^2/2\sigma^2 t^2} - e^{-(D-3L/2)^2/2\sigma^2 t^2} \right]. \tag{A.9}$$

The initial basic assumptions can then be modified so that this equation more closely describes the experimental situation. The actual length of the ion distribution within the trap is known from the temperature measurement conducted on IBEX. The distance D is also modified to reflect the acceleration of ions from the trap towards either the MCP or the Faraday cup.

A.3 Fully integrable solutions

There is a subset of nonlinear potentials, $U_I(x, y, s)$, which have an additional invariant of the motion. The derivation of these potentials is outside of the scope of this thesis, but the outline is included here for completeness.

In [127], Danilov and Nagaitsev search for an invariant of the form

$$I = (ay_N^2 + c^2)p_{xN}^2 - 2ax_N y_N p_{xN} p_{yN} + ax_N^2 p_{yN}^2 + D, \tag{A.10}$$

where a and c are constants, and D is a function of x and y. The potentials can then be classified according to the values that a and c take. When $a \neq 0$, $c \neq 0$, and $a = 1$ the system in integrable in elliptical coordinates.

The potential $U(x_N, y_N)$, which has the invariant I, is given by the solution to the Bertrand-Darboux partial differential equation,

$$x_N y_N \Big(\frac{\partial^2 U}{\partial x_N^2} - \frac{\partial^2 U}{\partial y_N^2}\Big) + (y_N^2 - x_N^2 + c^2)\frac{\partial U}{\partial x_N \partial y_N} + 2y_N \frac{\partial U}{\partial x_N} - 3x_N \frac{\partial U}{\partial y_N} = 0. \tag{A.11}$$

The solution to this has the general form

$$U(x_N, y_N) = \frac{f(\xi) + g(\eta)}{\xi^2 - \eta^2}, \tag{A.12}$$

where f and g are arbitrary functions, and ξ and η are the elliptical coordinates

$$\xi = \frac{\sqrt{(x_N + c)^2 + y_N^2} + \sqrt{(x_N - c)^2 + y_N^2}}{2c}, \tag{A.13}$$

$$\eta = \frac{\sqrt{(x_N + c)^2 + y_N^2} - \sqrt{(x_N - c)^2 + y_N^2}}{2c}. \tag{A.14}$$

The second invariant of the system is then

$$I(x_N, y_N, p_{xN}, p_{yN}) = (x_N p_{yN} - y_N p_{xN})^2 + c^2 p_{xN}^2 + 2c^2 \frac{f(\xi)\eta^2 + g(\eta)\xi^2}{\xi^2 - \eta^2}, \tag{A.15}$$

where the positions and momenta are in the normalised coordinates. This invariant has the same units as the Hamiltonian. In elliptical coordinates

$$f(\xi) = \xi\sqrt{\xi^2 - 1}[d + t\cosh^{-1}(\xi)], \tag{A.16}$$

$$g(\eta) = \eta\sqrt{1 - \eta^2}[b + t\cos^{-1}(\eta)], \tag{A.17}$$

where b, c, d and t are arbitrary constants [131].

Time evolution of a Hamiltonian is a canonical transformation, as it preserves the form of the equations of motion. If a canonical transform can be found in which the new Hamiltonian equals 0, then all of the time variation is described by the canonical transform. A generating function capable of making such a canonical transform satisfies a the Hamilton-Jacobi partial differential equation [179].

The unusual potential described in this section can be analysed by converting the Hamiltonian in the normalised coordinates into a Hamilton-Jacobi equation and solving for the motion in separate elliptical coordinates.

From this, the phase space of the motion can be determined. The structure of the phase space is limited to those that can physically be realised in a vacuum pipe. This, in turn, limits the constants to those that describe systems where the motion is regular in the entire volume between singularities, and the fields can be created by electrodes or magnetic poles.

Examples of the particle motion expected due to the elliptical magnets in IOTA are shown in reference [29].

A.4 T-insert error study

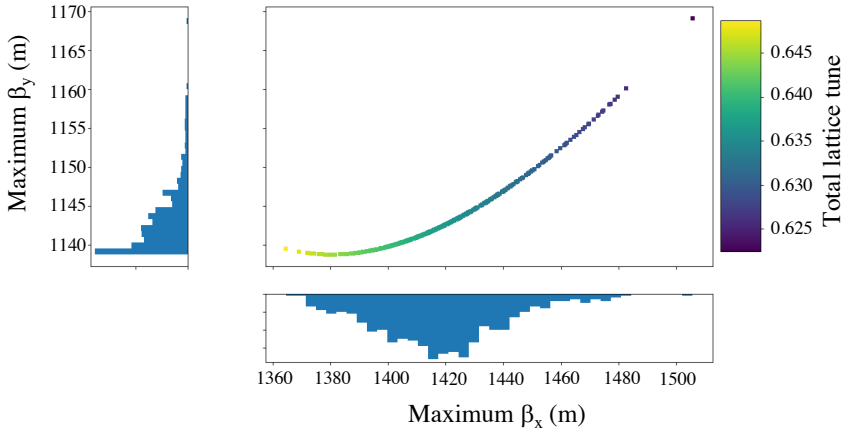
When testing the custom-built amplifiers made by Oxford electronics, the peak-to-peak noise when the amplifier was unloaded was found to be on the order of 10 mV. An error study of the T-insert lattice L_3 was then performed, accounting for this noise.

A lattice of 10,000 voltage points in length was used, with a Gaussian error term of mean 0, and standard deviation 10 mV, added to each of the voltage points. The simulation was repeated 500 times. The impact of this error on the maximum beta function in the horizontal and vertical directions, the beta functions at the centre of the drift region, and the phase advance over the T-insert was studied. The change in the total tune of the lattice was recorded, as this is the only quantity which we can currently measure.

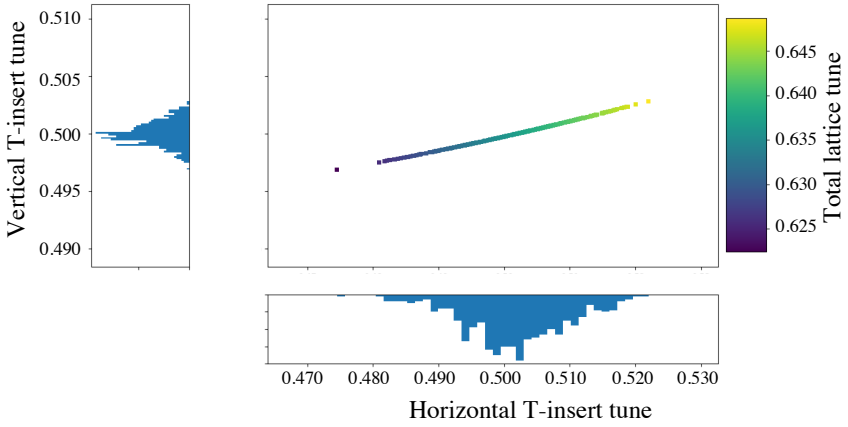
From this study, I found that such a small error led to a variation in total tune of only 4×10^{-5}. To find the source of the variation in total tune noted in the experiments described in Section 6.3.1, I looked at the variation in the maximum and minimum voltage recorded on the oscilloscope for lattice L_3 in each experiment. I found that these points varied with a standard deviation of $\sim$0.2 V.

The error study was repeated with an error term of mean 0 and standard deviation 0.2 V on each voltage point. Again this simulated error study produced a variation in the total tune which was smaller than that observed experimentally, this time $\sim$0.001. Experimentally, the tune variation was found to be $\sim$0.01. Through the error study I found that this variation in total tune could be reconstructed by applying a Gaussian error term to a voltage pulse as a whole, with a standard deviation of 0.2 V.

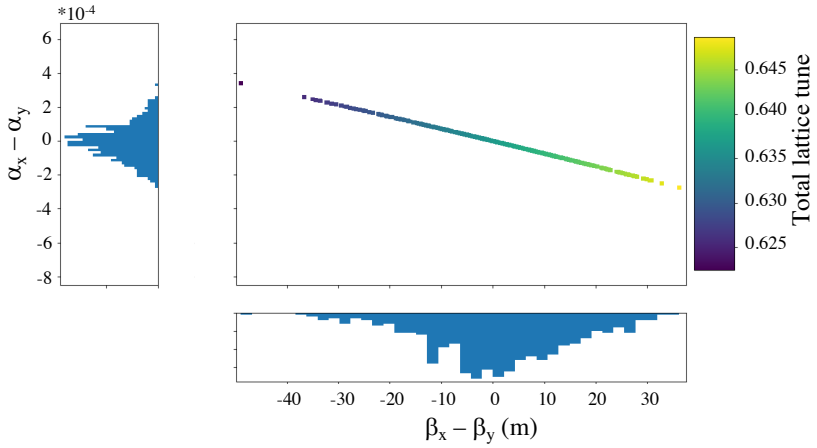
Furthermore, a range of simulations were performed, varying the height and length of voltage pulses and studying the impact on the total tune, our only observable. An example one of these studies is given in Fig. A.2. The variation of the phase advance over the T-insert for the observed tune variation over the full lattice L_3 is shown in Fig. A.2b. Interestingly, any errors seem to have a larger impact on the T-insert tune in the horizontal direction.



(a) Impact on maximum β_x and maximum β_y.



(b) Impact on horizontal and vertical T-insert tune.



(c) Impact on the Twiss parameters in the centre of the drift.

Figure A.2: Error study of lattice L_3 when a Gaussian error of mean 0 and standard deviation 0.2 V was applied to each voltage pulse so that all pulses are either larger or smaller than the design value. The simulation was repeated 500 times.

A.5 Further simulations of QIO

Figure A.3 shows a comparison of the dynamic aperture between two simulations of the initial T-insert design. In one simulation a Python script is used, with the octupole implemented through a series of "drift kicks". In the second simulation, Warp is used with an ideal octupole potential, as illustrated in Fig. 7.4a.

A different number of ions were used in each simulation, but both simulations ran for 1000 lattice periods. It is immediately obvious that the two produce very similar results, with a small discrepancy along the line $x = y$. This is because scraping is applied in the Warp simulation when particles are within the octupole channel. No scraping is included in the Python simulation.

Figure A.4 shows an imperfect version of the lattice L_3, simulated in Warp using only 513 steps across the lattice with simulation method (3) (described in Section 7.2). The lattice tune has been shifted from 0.635 to 0.65 and the tune spread is limited by scraping in the T-insert. The asymmetry in the plot of the dynamic aperture shown in Fig. A.4 is due to a difference in the tune between the x and y directions.

Figure A.5 shows the dynamic aperture and tune spread from the original lattice design, with the larger phase advance over the drift region leading to a larger tune spread. Again, the asymmetry in the plot of the dynamic aperture is due to a slight difference in the tune between the x and y directions.

Figure A.6 represents the same simulation as shown in Fig. 7.13, only with the coordinate system rotated through 45 degrees. In this coupled coordinate system the ions seem to be expelled from the centre of the trap, where the tune will equal the perturbation frequency.

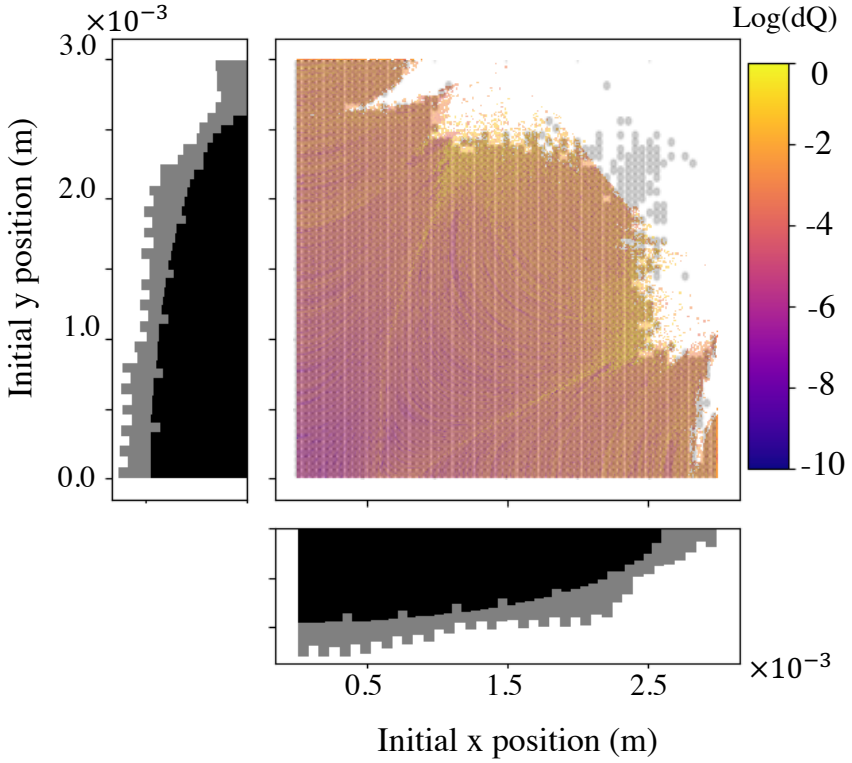


Figure A.3: A comparison of the dynamic aperture calculated by a python script and a Warp simulation using an ideal octupole potential. Coloured points are from the warp simulation, with the overlaid grey points from the Python simulation.

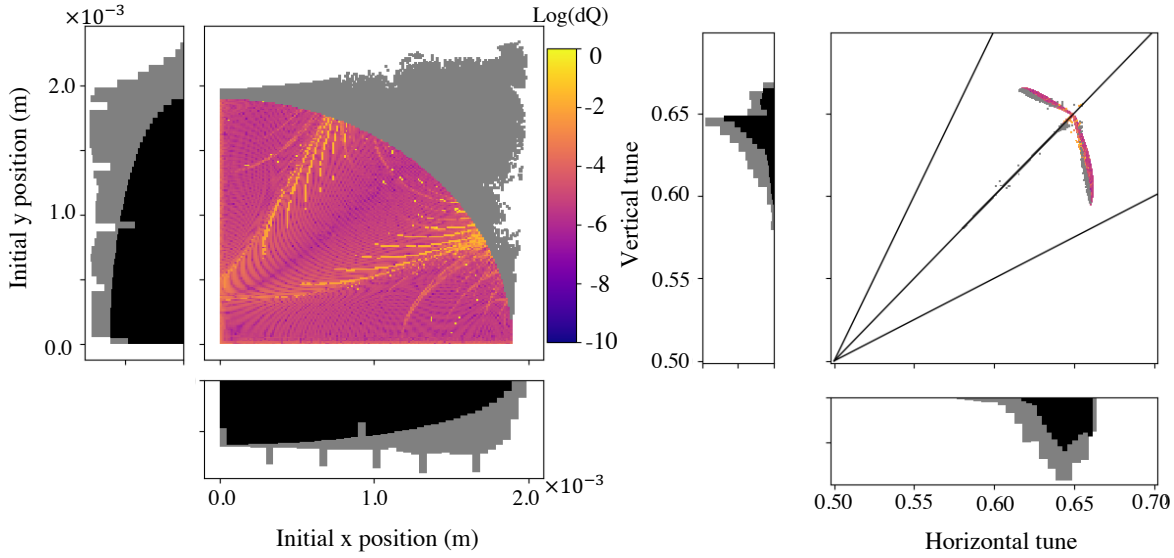


Figure A.4: Dynamic aperture and tune spread of the imperfect T-insert lattice to which a perturbation is applied in Section 7.5.

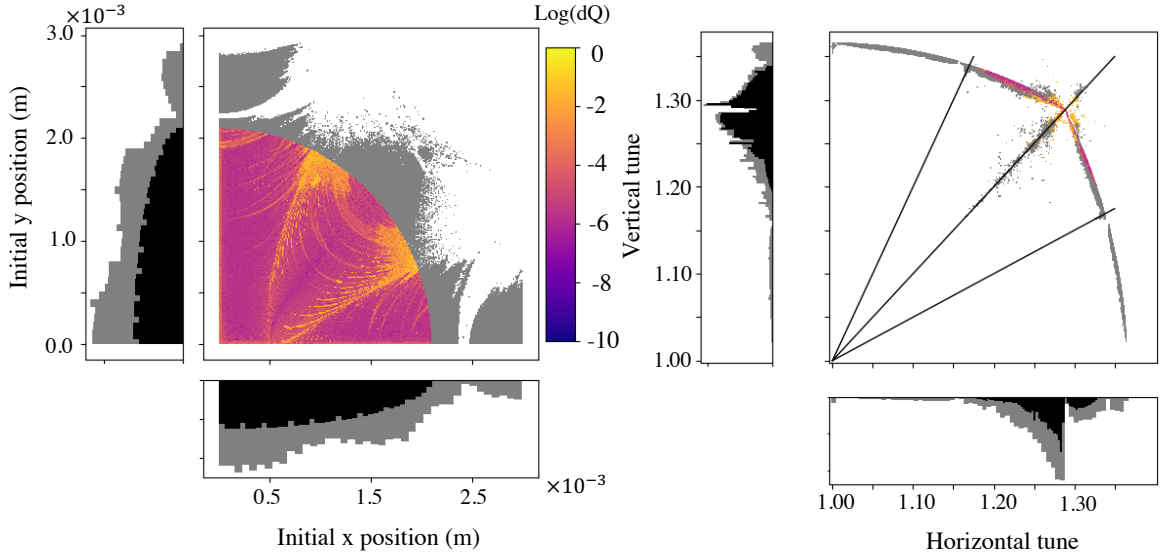


Figure A.5: Dynamic aperture and tune spread from the initial T-insert lattice design, when voltages are applied to the roads and plates to create the octupole and the T-insert is treated as a matrix kick (simulation method 2). Ions are tracked over 1000 lattice periods.

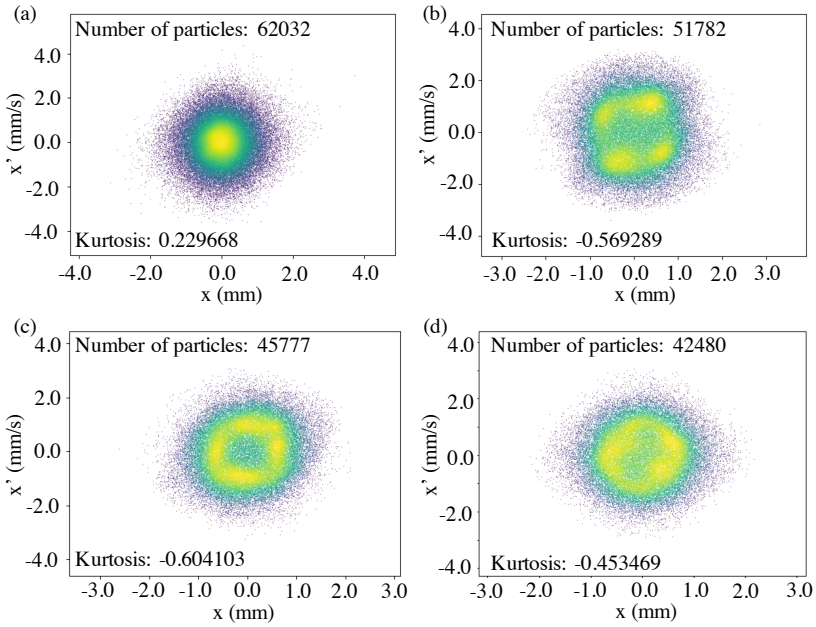


Figure A.6: Phase space in coupled coordinates when a quadrupole perturbation is applied to a QIO lattice, at a frequency of $2 \cdot 2\pi \cdot Q$, with the octupole term switched on. (a) is after 1 lattice period, (b) after 50 lattice periods, (c) after 100 lattice periods, and (d) after 200 lattice periods.

A.6 IBEX trap alignment

To ensure the greatest possible accuracy in the alignment of the IBEX trap the rods were both measured and aligned by the Dimensional Metrology and Additive Manufacturing Facility at Rutherford Appleton Laboratory, using a Coordinate Measuring Machine (CMM). The latest set of measurements from the trap are summarised below.

The central rods were measured at two positions, one to either side of the centre of the trap. The roundness of each electrode is recorded, as well as the coordinates of the centre of the trap, the inner diameter of the trap, and its roundness. Roundness is defined in [180]. The x and y coordinates are with respect to a reference datum.

Parameter	Actual (mm)	Nominal (mm)
Diameter of electrode 1	11.5054	11.5000
Diameter of electrode 2	11.5023	11.5000
Diameter of electrode 3	11.5015	11.5000
Diameter of electrode 4	11.5043	11.5000
Roundness of electrode 1	0.0026	0.0000
Roundness of electrode 2	0.0022	0.0000
Roundness of electrode 3	0.0029	0.0000
Roundness of electrode 4	0.0019	0.0000
Inner diameter rods 24	9.9809	10.0000
Inner diameter rods 13	9.9819	10.0000
Roundness of internal diameter	0.0010	0.0000
x position	34.1585	34.0000
y position	74.0239	74.0000

Table A.1: Alignment data at position 1.

Parameter	Actual (mm)	Nominal (mm)
Diameter of electrode 1	11.5039	11.5000
Diameter of electrode 2	11.5040	11.5000
Diameter of electrode 3	11.5012	11.5000
Diameter of electrode 4	11.5034	11.5000
Roundness of electrode 1	0.0017	0.0000
Roundness of electrode 2	0.0024	0.0000
Roundness of electrode 3	0.0023	0.0000
Roundness of electrode 4	0.0019	0.0000
Inner diameter rods 24	9.9783	10.0000
Inner diameter rods 13	9.9797	10.0000
Roundness of internal diameter	0.0014	0.0000
x position	34.1680	34.0000
y position	74.0358	74.0000

Table A.2: Alignment data at position 2.

Bibliography

[1] https://home.cern/science/accelerators/large-hadron-collider

[2] R.W. Thomae. "Recent developments in ion implantation accelerators", *Nuclear Instruments and Methods in Physics Research Section B: Beam Interactions with Materials and Atoms*, **50**, 1 (1990) 444 – 454. ISSN 0168-583X. http://www.sciencedirect.com/science/article/pii/0168583X9090398E

[3] https://www.isis.stfc.ac.uk

[4] https://www.diamond.ac.uk/Home.html

[5] https://www.isis.stfc.ac.uk/Pages/Neutron-techniques-used-to-study-1400\-BC-grave-goods-from-Egyptian-tomb.aspx

[6] E.O. Lawrence & N. Edlefsen. "On the production of high speed protons", *Science*, **72** (1930) 376. https://science.sciencemag.org/content/72/1867/372/tab-pdf

[7] A. Sessler & E. Wilson. "Engines of discovery: A century of particle accelerators". World Scientific Publishing Co. Pte. Ltd. (2007).

[8] E. Wilson. "An introduction to particle accelerators". Oxford University Press (2001). ISBN 0-19-850829-8.

[9] http://j-parc.jp/index-e.html

[10] http://neutrons.ornl.gov/facilities/SNS

[11] J.W.G. Thomason. "The ISIS Spallation Neutron and Muon Source—The first thirty-three years", *Nuclear Instruments and Methods in Physics Research Section A: Accelerators, Spectrometers, Detectors and Associated Equipment*, **917** (2019) 61 – 67. ISSN 0168-9002.

[12] G.H. Rees. "A Pulsed Spallation Source for Neutron Scattering Research", *IEEE Transactions on Nuclear Science*, **24**, 3 (1977) 989–992. ISSN 1558-1578.

[13] W.T. Weng. "Ultra-high intensity proton accelerators and their applications". In "Proceedings of the 1997 Particle Accelerator Conference (Cat. No.97CH36167)", volume 1, pages 42–46 vol.1 (1997).

[14] S.D. Holmes. "Low energy aspects of circular accelerators". In "Frontiers of Particle Beams: Intensity Limitations", pages 189–212. Springer, Berlin Heidelberg (1992). ISBN 978-3-540-46797-7.

[15] B. Pine. "Space charge induced beam loss on a high intensity proton synchrotron". D.Phil. thesis, University of Oxford (2016).

[16] `https://www.isis.stfc.ac.uk/Pages/How-ISIS-works.aspx`

[17] H. Wiedemann. "Particle accelerator physics". Springer, 3rd edition (2007). ISBN 978-3-540-49043-2.

[18] S.Y. Lee. "Accelerator Physics". World Scientific, 3rd edition (2012). ISBN 978-981-4374-94-1.

[19] A. Seryi. "Unifying physics of accelerators, lasers and plasma". CRC Press, Taylor and Francis group (2016). ISBN 978-1-4822-4058-0.

[20] A. Wolski. "Beam dynamics in high energy particle accelerators". Imperial College Press (2014). ISBN 978-1-78326-277-9.

[21] E.J.N. Wilson. "Nonlinear resonances". CAS - CERN Accelerator School : 5th Advanced Accelerator Physics Course, Rhodes, Greece, (1993). pp.15-41 (CERN-1995-006).

[22] K. Schindl. "Space Charge". `http://cds.cern.ch/record/941316`

[23] I. Hofmann. "The Physics of Particle Accelerators". Springer (2017). ISBN 978-3-319-62157-9.

[24] C. Prior. "Dynamics of non-linear beams with space-charge". Presentation, CAS, Bilbao, Spain (2011). `https://cas.web.cern.ch/sites/cas.web.cern.ch/files/lectures/bilbao-2011/priorbeamdynamics2.pdf`

[25] D. Møhl. "Sources of emittance growth". CAS - CERN Accelerator School: Intermediate Course on Accelerator Physics, Zeuthen, Germany, 15 - 26 Sep 2003, pp.245-270 (CERN-2006-002).

[26] W. Herr. "Introduction to Landau Damping". CERN Yellow Report CERN-2014-009, pp.377-403 (2016).

[27] V. Kornilov. "Laundau damping". Advanced CAS school lectures (2017). `http://cas.web.cern.ch/sites/cas.web.cern.ch/files/lectures/egham-2017/\kornilovld2.pdf`

[28] C. Prior. "Accelerator Simulations - Issues and Challenges". Workshop on advanced computing for accelerators, Cockcroft Institute (2013).

[29] S. Rexford & B. Erdelyi. "Numerical discretization of completely integrable nonlinear Hamiltonian systems", *Phys. Rev. Accel. Beams*, **21** (2018) 114601. `https://link.aps.org/doi/10.1103/PhysRevAccelBeams.21.114601`

[30] D.J. Kelliher. "Modeling". FFAG School, FFAG11, Daresbury (2011).

[31] H. Bruck. "Circular particle accelerators". Translated by Ralph McElroy Co, Inc., from initial publication from the Institut National des Sciences et Techniques Nucleaires (1974). http://inspirehep.net/record/19864?ln=en

[32] Nobel Media AB 2019. "The Nobel Prize". https://www.nobelprize.org/prizes\/physics/1989/summary/

[33] W. Paul. "Electromagnetic traps for charged particles". Nobel Lecture, Physikalisches Institut der Universität Bonn, Nussallee 12, D-5300 Bonn, F.R.G. (1989).

[34] In "Proceedings of the 7th International Conference on Trapped Charged Particles and Fundamental Physics (TCP 2018), Traverse City, Michigan, USA", (2018).

[35] H. Okamoto & H. Tanaka. "Proposed experiments for the study of beam halo formation", *Nuclear Instruments and Methods in Physics Research, Section A: Accelerators, Spectrometers, Detectors and Associated Equipment*, **437**, 2-3 (1999) 178–187. ISSN 01689002.

[36] H. Okamoto, Y. Wada & R. Takai. "Radio-frequency quadrupole trap as a tool for experimental beam physics", *Nuclear Instruments and Methods in Physics Research A*, **485** (2002) 244–254.

[37] R.C. Davidson, P.C. Efthimion, R. Majeski, H. Qin et al. "Paul trap experiment to simulate intense nonneutral beam propagation through a periodic focusing field configuration", *Nuclear Instruments and Methods in Physics Research A*, **464** (2001) 502 – 511.

[38] E. Gilson, R. Davidson, P. Efthimion, R. Majeski et al. "The Paul trap simulator experiment", *Laser and Particle Beams*, **21** (2003) 549 – 552.

[39] R. Takai, K. Ito, Y. Iwashita, H. Okamoto et al. "Design and fabrication of a linear Paul trap for the study of space-charge-dominated beams", *Nuclear Instruments and Methods in Physics Research Section A: Accelerators, Spectrometers, Detectors and Associated Equipment*, **532**, 1 (2004) 508 – 512. ISSN 0168-9002. International Workshop on Beam Cooling and Related Topics. http://www.sciencedirect.com/science/article/pii/S0168900204013026

[40] K. Izawa, K. Ito, H. Higaki & H. Okamoto. "Controlled Extraction of Ultracold Ions from a Linear Paul Trap for Nanobeam Production", *Journal of the Physical Society of Japan*, **79**, 12 (2010) 124502. https://doi.org/10.1143/JPSJ.79.124502

[41] S. Ohtsubo, M. Fujioka, H. Higaki, K. Ito et al. "Experimental study of coherent betatron resonances with a Paul trap", *Physical Review Special Topics - Accelerators and Beams*, **13** (2010) 044201.

[42] K. Fukushima & H. Okamoto. "Design study of a multipole ion trap for beam physics applications", *Plasma and Fusion Research*, **4** (2015) 1–18.

[43] S.L. Sheehy, D.J. Kelliher, S. Machida, C. Plostinar et al. "Overview of the design of the IBEX linear Paul trap". In "Proc. 7th Int. Particle Accelerator Conf. (IPAC'16), Busan, Korea", pages 3104–3106 (2016). ISBN 978-3-95450-147-2.

[44] K. Mølhave. "Construction of and Experiments with a Linear Paul Trap". Master's thesis, Institute of Physics and Astronomy University of Aarhus (2000).

[45] L. Deniau, H. Grote, G. Roy & F. Schmidt. "The MAD-X Program (Methodical Accelerator Design) User's Reference Manual". CERN, Geneva (2018).

[46] I.M. Kapchinski & V.V. Vladimirskiy. In "Proc. Int. Conf. on High Energy Acc. (CERN, Geneva, Switzerland, 1959)", page 274 (1959).

[47] F.J. Sacherer. "Transverse Space-Charge Effects in Circular Accelerators". D.Phil. thesis, University of California, Lawrence Radiation Laboratory, Berkley, California (1968).

[48] F.J. Sacherer. "RMS envelope equations with space charge", *IEEE Trans. Nucl. Sci.*, **18** (1971) 1105–1107.

[49] S. Machida. "Envelope equations in the Paul Trap". Internal note, Intense beams group, STFC, Rutherford Appleton Laboratory, Private communication (2018).

[50] K. Kojima, H. Okamoto & K. Ito. "A compact Paul ion trap for the study of space-charge effects in drift-tube linear accelerators", *Progress of Theoretical and Experimental Physics*, **9** (2019) 093G01. ISSN 2050-3911. `https://doi.org/10.1093/ptep/ptz098`

[51] D.J. Kelliher, S. Machida, C.R. Prior & S.L Sheehy. "Study of beam dynamics in linear Paul traps". In "Proc. HB2014, east-Lansing, MI", page 84 (2014).

[52] M. Chung. "Studies of Charged Particle Beam Dynamics on the Paul Trap Simulator Experiment Pure Ion Plasma". D.Phil. thesis, Princeton University (2008).

[53] J.R.C. Pita. "Design, Development and Operation of Novel Ion Trap Geometries". D.Phil. thesis, The Blackett Laboratory, Imperial College (2007).

[54] R. Dilao & R. Alves-Pires. "Nonlinear dynamics in particle accelerators". World Scientific publishing Co. Pte. Ltd. (1996). ISBN 981-02-2517-2.

[55] L. Ding & S. Kumashiro. "Ion motion in the rectangular wave quadrupole field and digital operation mode of a quadrupole ion trap mass spectrometer", *Rapid communications in mass spectrometry : RCM*, **20** (2006) 3–8.

[56] S.L. Sheehy, K.J. Peach, H. Witte, D.J. Kelliher et al. "Fixed field alternating gradient accelerator with small orbit shift and tune excursion", *Phys. Rev. ST Accel. Beams*, **13** (2010) 040101.

[57] Adam Baird. Oxford central electronics group.

[58] K. Ito, T. Okano, K. Moriya, K. Fukushima et al. "Experimental study on dipole motion of an ion plasma confined in a linear Paul trap", *Hyperfine Interactions*, **236**, 1-3 (2015) 29–37. ISSN 0304-3843. http://link.springer.com/10.1007/s10751-015-1196-y

[59] Neil Farthing. ISIS Neutron Source, RF group.

[60] K. Budzik. "Electron gun for IBEX". Internal presentation, Private communication (2016).

[61] CST Studio Suite. "CST Microwave Studio". http://www.cst.com

[62] R. Rejoub, B. G. Lindsay & R. F. Stebbings. "Determination of the absolute partial and total cross sections for electron-impact ionization of the rare gases", *Phys. Rev. A*, **65** (2002) 042713. https://link.aps.org/doi/10.1103/PhysRevA.65.042713

[63] Peter Griffin-Hicks. ISIS Neutron Source.

[64] Python Software Foundation. Python Language Reference. Version 3.5. http://www.python.org

[65] Hamamatsu Photonics. "MCP (microchannel plate) and MCP assembly". https://www.hamamatsu.com/resources/pdf/etd/MCP_TMCP0002E.pdf

[66] Hamamatsu Photonics. "Technical information: MCP assembly". https://www.triumf.ca/sites/default/files/Hamamatsu%20MCP%20guide.pdf

[67] Andor (Oxford instruments). "Alta F2000: High performance cooled CCD camera system". https://andor.oxinst.com/assets/uploads/documents/Andor/apogee/Apogee_Alta_F2000_Specifications.pdf

[68] E.P. Gilson, R.C. Davidson, P.C. Efthimion & R. Majesk. "Paul Trap Simulator Experiment to Model Intense Beam Propagation in Alternating-Gradient Transport Systems". PPPL Report (2004).

[69] E.P. Gilson, M. Chung, R.C. Davidson, P.C. Efthimion et al. "Transverse beam compression on the Paul trap simulator experiment", *Physical Review Special Topics - Accelerators and Beams*, **10**, 12 (2007) 124201. ISSN 1098-4402. https://link.aps.org/doi/10.1103/PhysRevSTAB.10.124201

[70] M. Chung, E.P. Gilson, R.C. Davidson, P.C. Efthimion et al. "Experimental investigation of random noise-induced beam degradation in high-intensity accelerators using a linear Paul trap", *Physical Review Special Topics - Accelerators and Beams*, **12**, 5 (2009) 1–11. ISSN 10984402.

[71] M. Chung, E.P. Gilson, R.C. Davidson, P.C. Efthimion et al. "Use of a Linear Paul Trap to Study Random Noise-Induced Beam Degradation in High-Intensity Accelerators", *Physical Review Letters*, **14** (2009) 45003.

[72] K. Ito, K. Nakayama, S. Ohtsubo, H. Higakl et al. "Determination of transverse distributions of ion plasmas confined in a linear Paul trap by imaging diagnostics", *Japanese Journal of Applied Physics*, **47**, 10 PART 1 (2008) 8017–8025. ISSN 00214922.

[73] M. Knoop. "Detection Techniques for Trapped Ions". Physics with Trapped Charged Particles : Lectures from the Les Houches Winter School, Imperial College Press, pages 25-42 (2013).

[74] H. Takeuchi, K. Fukushima, K. Ito, K. Moriya et al. "Experimental study of resonance crossing with a Paul trap", *Physical Review Accelerators and Beams*, **15** (2012) 074201.

[75] K. Moriya, K. Fukushima, K. Ito, T. Okano et al. "Experimental study of integer resonance crossing in a nonscaling fixed field alternating gradient accelerator with a Paul ion trap", *Physical Review Special Topics - Accelerators and Beams*, **18** (2015) 1–13. ISSN 10984402.

[76] H. Higaki, K. Ito, R. Takai, K. Nakayama et al. "Axial resonances of Ar+ ions observed in a linear Paul trap", *Hyperfine Interactions*, **174** (2007) 77–82.

[77] K. Ito, M. Matsuba & H. Okamoto. "Effect of quadrupole focusing-field fluctuation on the transverse stability of intense hadron beams in storage rings", *Progress of Theoretical and Experimental Physics*, **PTEP**, 2 (2018) 023G01. ISSN 2050-3911. 023G01. `https://doi.org/10.1093/ptep/pty004`

[78] K. Ito, T. Kurauchi, H. Higaki & H. Okamoto. "Experimental observation of low-order collective oscillation modes in a strong-focusing lattice". In "Proc. 10th Int. Particle Accelerator Conf. (IPAC'19), Melbourne, Australia", page 3130 (2019).

[79] K. Kojima, H. Okamoto & Y. Tokashiki. "Empirical condition of betatron resonances with space charge", *Phys. Rev. Accel. Beams*, **22** (2019) 074201. `https://link.aps.org/doi/10.1103/PhysRevAccelBeams.22.074201`

[80] A. Friedman, R.H. Cohen, D.P. Grote, S.M. Lund et al. "Computational methods in the warp code framework for kinetic simulations of particle beams and plasmas", *IEEE Transactions on Plasma Science*, **42(5)** (2014) 1321–1334.

[81] D.P. Grote et. al. "Warp Manual" (2000). `http://hifweb.lbl.gov`

[82] D. Grote, J.L. Vay, A. Friedman & S. Lund. `http://warp.lbl.gov`

[83] R.E. March & J.F.J. Todd. "Quadrupole Ion Trap Mass Spectrometry". John Wiley and Sons (2005).

[84] J.D. Huba. "NRL Plasma Formulary". Beam Physics Branch, Plasma Physics Division, Naval Research Laboratory, Washington, DC 20375 (2013).

[85] Wolfram Research, Inc. "Mathematica, Version 12.0". Champaign, IL, 2019. `https://www.wolfram.com/mathematica`

[86] G. Franchetti. "On the boundary between coherent and incoherent effects: a small study". Presentation at the 4th ICFA mini-workshop on space charge. (2019).

[87] E. Carr. "Development of an Ion Analysis Diagnostic Tool for IBEX". Master's thesis, University of Oxford (2017).

[88] T.E. Oliphant. "Circular and elliptical mask" (2015). `https://gist.github.com/teoliphant/7709098`

[89] B.W. Noel, M.R. Cates & L.A. Franks. "Advances in Electronics and Electron Physics: Increased gain of channel intensifier tubes by pulsed biasing", volume 74. Academic Press (1988).

[90] E.H. Eberhardt. "Gain model for microchannel plates", *Applied Optics*, **18**, 9 (1979) 1418.

[91] Median filter. `https://docs.scipy.org/doc/scipy/reference/generated/scipy.ndimage.median_filter.html`

[92] L.K. Martin, S. Machida, D.J. Kelliher & S.L. Sheehy. "A study of coherent and incoherent resonances in high intensity beams using a linear Paul trap", *New Journal of Physics*, **21** (2019) 053023.

[93] L.K. Martin, D.J. Kelliher & S.L. Sheehy. "Recent Studies of the Resonances at a Cell Tune of 0.25 Using the IBEX Paul Trap", *Journal of Physics: Conference Series*, **1350** (2019) 012133. `https://doi.org/10.1088%2F1742-6596%2F1350%2F1%2F012133`

[94] Creative Commons License. `https://creativecommons.org/licenses/by/3.0/`

[95] D.C. Morin. "Transverse Space-Charge Effects in Circular Accelerators". D.Phil. thesis, Madison, Wisconsin: Midwestern Universities Research Association (1962).

[96] R. Baartman. "Betatron Resonances with Space Charge". In "Proceedings of Space Charge Physics in High Intensity Hadron Rings (Shelter Island, New York, USA, 1998)", volume 448, page 56 (1998).

[97] P. Lapostolle. "Oscillations in a Synchrotron Under Space Charge Conditions". In "Proc. Int. Conf. on High Energy Acc. (Dubna, 1963)", page 1235 (1963).

[98] L. Smith. "Effect of Gradient Errors in the Presence of Space Charge Forces". In "Proc. Int. Conf. on High Energy Acc. (Dubna, 1963)", page 1232 (1963).

[99] I. Hofmann, L.J. Laslett, L. Smith & I. Haber. "Stability of the Kapchinskij-Vladimirski (K-V) distribution in long periodic transport systems", *Particle Accelerators*, **13**.

[100] C. Li & R.A. Jameson. "Structure resonances due to space charge in periodic focusing channels", *Phys. Rev. Accel. Beams*, **21** (2018) 024204. `https://link.aps.org/doi/10.1103/PhysRevAccelBeams.21.024204`

[101] H. Okamoto & K. Yokoya. "Parametric resonances in intense one-dimensional beams propagating through a periodic focusing channel", *Nuclear Instruments and Methods in Physics Research Section A*, **482** (2002) 51–64.

[102] I. Hofmann & O. Boine-Frankenheim. "Parametric instabilities in 3D periodically focused beams with space charge", *Physical Review Special Topics - Accelerators and Beams*, **20** (2017) 014202.

[103] I. Hofmann. "Comment on "Empirical condition of betatron resonances with space charge"", *Phys. Rev. Accel. Beams*, **23** (2020) 028001. `https://link.aps.org/doi/10.1103/PhysRevAccelBeams.23.028001`

[104] L. Landau. "On the vibration of the electronic plasma", *J. Phys.(USSR)*, **10** (1946) 25–34.

[105] K. Ito, H. Okamoto, Y. Tokashiki, et al. "Coherent resonance stop bands in alternating gradient beam transport", *Physical Review Accelerators and Beams*, **20** (2017) 064201.

[106] C. Warsop, D. Adams, B. Jones, B. Pine et al. "Studies of Loss Mechanisms Associated with the Half Integer Limit on the ISIS Ring". In "Proc. HB2014, East-Lansing, MI, USA", page 123 (2014).

[107] C. Warsop, D. Adams, B. Jones & B. Pine. "Simple models for beam loss near the half integer resonance with space charge". In "Proc. HB2016, Malmo, Sweden", pages 150–154 (2016).

[108] K. Moriya, M. Ota, K. Fukushima, M. Yamaguchi et al. "Double stop-band structure near half-integer tunes in high-intensity rings", *Physical Review Accelerators and Beams*, **19** (2016) 114201.

[109] I. Hofmann & O. Boine-Frankenheim. "Space-Charge Structural Instabilities and Resonances in High-Intensity Beams", *Physical Review Letters*, **115** (2015) 204802.

[110] D. Jeon, L. Groening & G. Franchetti. "Fourth order resonance of a high intensity linear accelerator", *Physical Review Special Topics - Accelerators and Beams*, **12** (2009) 054204.

[111] C. Li & Y.L. Zhao. "Envelope instability and the fourth order resonance", *Physical Review Special Topics - Accelerators and Beams*, **17** (2014) 124202.

[112] S. Machida. "Comments on coherent and incoherent views". Presentation at the 4th ICFA mini-workshop on space charge. (2019).

[113] D. Jeon. "Classification of Space-Charge Resonances and Instabilities in High-intensity Linear Accelerators", *Journal of the Korean Physical Society*, **72** (2018) 1523–1530.

[114] K. Kiyoshi, S.K. Mtingwa & A. Wolski. "Intrabeam scattering formulas for high energy beams", *Physical Review Special Topics - Accelerators and Beams*, **8** (2005) 081001.

[115] L. Laskar, C. Froeschle & A. Celletti. "The measure of chaos by the numerical analysis of the fundamental frequencies. Application to the standard mapping", *Physica D*, **56** (1992) 253–269.

[116] W.H. Press, B.P. Flannery & S.A. Teukolsky. "Numerical recipes in C: The art of scientific computing". Cambridge University press (1988).

[117] K. Ruisard. Private communication (14/03/18).

[118] K. Ruisard. "Design of a nonlinear quasi-integrable lattice for resonance suppression at the university of Maryland electron ring". D.Phil. thesis, University of Maryland (2018).

[119] Kurtosis. `https://docs.scipy.org/doc/scipy-0.14.0/reference/generated/scipy.stats.kurtosis.html`

[120] K. Ito, S. Ohtsubo, S. Higaki, K. Izawa et al. "Tune Depression of Ion Plasmas Observed in a Linear Paul Trap", *J. Plasma Fusion Res. Series*, **8** (2009) 959 – 962.

[121] G. Franchetti, O. Chorniy, I Hofmann, W. Bayer et al. "Experiment on space charge driven nonlinear resonance crossing in an ion synchrotron", *Phys. Rev. ST Accel. Beams*, **13** (2010) 114203.

[122] K. Kojima, H. Okamoto & Y. Tokashiki. "Reply to "Comment on 'Empirical condition of betatron resonances with space charge'"", *Phys. Rev. Accel. Beams*, **23** (2020) 028002. `https://link.aps.org/doi/10.1103/PhysRevAccelBeams.23.028002`

[123] Netwon-Raphson algorithm documentation. "scipy.optimize.newton". `https://docs.scipy.org/doc/scipy/reference/generated/scipy.optimize.newton.html` (2014).

[124] F. Gerigk. "Future High-Intensity Proton Accelerators". In "SRF'07, Beijing 15-19 October", (2007).

[125] S. Machida. "FFA-based ISIS Upgrade Options". ICFA Beam dynamics news letter (2019). `http://www.icfa-bd.org/Newsletter76.pdf`

[126] S.A. Antipov, S. Nagaitsev & A. Valishev. "Single-particle dynamics in a nonlinear accelerator lattice: Attaining a large tune spread with octupoles in IOTA", *Journal of Instrumentation*, **12** (2017) P04008. ISSN 17480221.

[127] V. Danilov & S. Nagaitsev. "Nonlinear accelerator lattices with one and two analytic invariants", *Physical Review Special Topics - Accelerators and Beams*, **13** (2010) 084002. ISSN 10984402.

[128] V. Danilov. "Practical solutions for nonlinear accelerator lattice with stable nearly regular motion", *Phys. Rev. ST Accel. Beams*, **11** (2008) 114001. `https://link.aps.org/doi/10.1103/PhysRevSTAB.11.114001`

[129] C.E. Wayne. "An Introduction to KAM Theory". Technical report (2008). `http://math.bu.edu/people/cew/preprints/introkam.pdf`

[130] N.N. Nekhoroshev. "An exponential estimate of the time of stability of nearly-integrable Hamiltonian systems", *Russ. Math. Surv.*, **32** (1977) 1.

[131] S.D. Webb, D.L. Bruhwiler, S. Nagaitsev, V. Danilov et al. "Suppressing transverse beam halo with nonlinear magnetic fields". In "IPAC 2013: Proceedings of the 4th International Particle Accelerator Conference", (2013). ISBN 9783954501229.

[132] S.D. Webb, D.L. Bruhwiler, D.T. Abell, A. Sishlo et al. "Effects of Nonlinear Decoherence on Halo Formation". arXiv:1205.7083 [physics.acc-ph] (2012).

[133] S. Webb et al. "Matching Beams for the Nonlinear Integrable Optics". Technical report, RadiaSoft LLC (2015).

[134] S.D. Webb, D.L. Bruhwiler, R. Kishek, S. Nagaitsev et al. "Experiences simulating nonlinear integrable optics". In "6th International Particle Accelerator Conference, IPAC 2015", (2015). ISBN 9783954501687. `https://web.fnal.gov/sites/Synergia/SitePages/`

[135] S. Antipov, D. Broemmelsiek, D. Bruhwiler, D. Edstrom et al. "IOTA (Integrable Optics Test Accelerator): Facility and experimental beam physics program", *Journal of Instrumentation*, **12** (2017) T03002. ISSN 17480221.

[136] G. Kafka. "Lattice design of the integrable optics test accelerator and optical stochastic cooling experiment at Fermilab". D.Phil. thesis, Illinois Institute of Technology (2015).

[137] S.D. Webb, D.L Bruhwiler, A. Valishev, S.N. Nagaitsev et al. "Chromatic and dispersive effects in Nonlinear Integrable Optics". In "Proc. HB2014, east-Lansing, MI", page 10 (2014).

[138] F.H. O'shea, R. Agustsson, Y.C. Chen, E. Spranza et al. "Non-linear magnetic inserts for the Integrable Optics Test Accelerator: State of the project". Technical report (2015).

[139] S. Nagaitsev & A. Valishev. "Design and simulation of a IOTA - a novel concept of integrable optics accelerator". In "IPAC 2012 - International Particle Accelerator Conference 2012", (2012).

[140] F.H. O'shea, R.B. Agustsson, Y. Chen, D.W. Martin et al. "Non-linear inserts for the IOTA ring". Technical report (2017).

[141] S. Antipov, A. Valishev, S. Wesseln, K. Carlson et al. "Design of octupole channel for Integrable Optics Test Accelerator". Technical report (2016).

[142] N. Kuklev, Y.K. Kim, S. Nagaitsev, A. Romanov et al. "Experimental demonstration of the Henon-Heiles quasi-integrable system at IOTA". In "Proc. 10th Int. Particle Accelerator Conf. (IPAC'19), Melbourne, Australia", page 386 (2019).

[143] C.C. Hall, D.L. Bruhwiler, J.P. Edelen, A.L. Romanov et al. "First measurements of nonlinear decoherence in the IOTA ring". In "Proc. 10th Int. Particle Accelerator Conf. (IPAC'19), Melbourne, Australia", page 3286 (2019).

[144] Y. Li M. Reiser R.A. Kishek, S. Bernal, M. Venturini & et al. "PIC code simulations of collective effects in the space charge dominated beam of the University of Maryland Electron ring (UMER)". In "Proc. 1999 Particle Accelerator Conf., New York", (1999).

[145] M. Reiser, S. Bernal, A. Dragt, M. Venturini et al. "Design features of small electron ring for study of recirculating space-charge-dominated beams", *Fusion Engineering and Design*, **32-33** (1996) 293 – 298. ISSN 0920-3796. Proceedings of the Seventh International Symposium on Heavy Ion Inertial Fusion. http://www.sciencedirect.com/science/article/pii/S0920379696004814

[146] S. Bernal, B. Beaudoin, H. Baumgartner, S. Ehrenstein et al. "Ultra-low current beams in UMER to model space-charge effects in high-energy proton and ion machines", *AIP Conference Proceedings*, **1812** (2017) 1–6. ISSN 15517616.

[147] L. Dovlatyan, K. Ruisard, B. Beaudoin & R. Kishek. "Steering optimizations for the University of Maryland electron ring". In "Proc. 9th Int. Particle Accelerator Conf. (IPAC'18), Vancouver, Canada, 2018", page 4913 (2018).

[148] K.J. Ruisard, H. Baumgartner, B. Beaudoin, S. Bernal et al. "Tuning low-current beam for nonlinear quasi-integrable optics experiments at the university of Maryland electron ring". In "Proc. 9th Int. Particle Accelerator Conf. (IPAC'18), Vancouver, Canada", pages 3585–3588 (2018). ISBN 9783954501847.

[149] H. Baumgartner, B. Beaudoin, I. Haber, T. Koeth et al. "Initial tests of nonlinear quasi-integrable optics at the University of Maryland Electron ring". In "Proc. 9th Int. Particle Accelerator Conf. (IPAC'18), Vancouver, Canada, 2018", page 3581 (2018).

[150] K. Ruisard, B. Beaudoin, I. Haber, T. Koeth et al. "Nonlinear Optics at UMER: Lessons Learned in Simulation". In "Proceedings, 13th International Computational Accelerator Physics Conference, ICAP2018: Key West, FL, USA, 20-24 October 2018", page TUPAG10 (2019).

[151] K. Ruisard, H. B. Komkov, B. Beaudoin, I. Haber et al. "Single-invariant nonlinear optics for a small electron recirculator", *Phys. Rev. Accel. Beams*, **22** (2019) 041601. https://link.aps.org/doi/10.1103/PhysRevAccelBeams.22.041601

[152] L. Dovlatyan, T.M. Antonsen, B.L. Beaudoin, I. Haber et al. "Preliminary Lattice Studies for the Single-Invariant Optics Experiment at the University of Maryland". In "Proc. 10th Int. Particle Accelerator Conf. (IPAC'19), Melbourne, Australia", (2019).

[153] B. Beaudoin I. Haber D. Matthews et al. K. Ruisard, H. Baumgartner. "Early tests and simulations of Quasi-integrable octupole lattices at the University of Maryland electron ring". In "Proc. HB2016, Malmö, Sweden", pages 511 – 516 (2016). ISBN 978-3-95450-178-6.

[154] S.D. Webb. "Computing the kick and invariants for nonlinear integrable optics". GitHub gist. https://gist.github.com/sdwebb/afda4f4eb3d09d46a4fb

[155] S.A. Antipov, S. Nagaitsev & A. Valishev. "Quasi-integrable nonlinear optics experiment at IOTA". In "AIP Conference Proceedings", (2016). ISBN 9780735414396. ISSN 15517616.

[156] K. Hwang, C. Mitchell & R. Ryne. "Particle loss study". IOTA physics meeting (2019).

[157] S.D. Webb. Private communication (30/11/19).

[158] S.S. Baturin. "Hamiltonian preserving nonlinear optics". arXiv:1908.03520 (2019).

[159] S.M. Lund, G. Franchetti & H. Okamoto. "Working Group C summary: Computational challenges, new concepts, and new projects". In "Proc. HB2014, East-Lansing, MI, USA", page 448 (2014).

[160] K. Ito. Private communication (01/05/2017).

[161] Basin hopping algorithm documentation. "scipy.optimize.basinhopping". https://docs.scipy.org/doc/scipy-0.14.0/reference/generated/scipy.\optimize.basinhopping.html (2014).

[162] A.A. Valishev. Private communication (20/05/19).

[163] D.J. Kelliher. "The study of scaling FFAGs in a multipole ion trap". Presentation, FFAG'17, Cornell University (2017). https://indico.bnl.gov/event/2764/contributions/7140/attachments/6419/7800/170908_kelliher_multipoletrap_final.pdf

[164] L.K. Martin, K. Ito, D.J. Kelliher, S. Machida et al. "A new method to measure the beta function in a Paul trap", *Journal of Physics: Conference Series*, **1067** (2018) 062016.

[165] "Dipole errors and correction". USPAS notes. http://uspas.fnal.gov/materials/12MSU/corrlect.pdf

[166] D.J. Kelliher. "Calculating the centroid amplitude in S-POD". Internal collaboration note, Private communication (2014).

[167] D.J. Kelliher. "Detuning in S-POD". Internal collaboration note, Private communication (2017).

[168] L.K. Martin, D.J. Kelliher & S.L. Sheehy. "Can a Paul Ion Trap Be Used to Investigate Nonlinear Quasi-Integrable Optics?", *Journal of Physics: Conference Series*, **1350** (2019) 012132. https://doi.org/10.1088%2F1742-6596%2F1350%2F1%2F012132

[169] J. Campmany, J. Marcos & V. Massana. "Determination of Magnetic Multipoles using a Hall Probe". In "Proceedings, 5th International Particle Accelerator Conference (IPAC 2014): Dresden, Germany, June 15-20, 2014", page THPRI105 (2014). http://jacow.org/IPAC2014/papers/thpri105.pdf

[170] A. Wolski. "Maxwell's equations for magnets". In D. Brandt, editor, "CERN Accelerator School, Bruges, Belgium", (2010).

[171] K. Ito, T. Masuda, H. Higaki & H. Okamoto. "Accumulating laser-coolable ions in a linear Paul trap for ultrahigh-density beam dynamics experiment". In "Proc. 10th Int. Particle Accelerator Conf. (IPAC'19), Melbourne, Australia, 2019", page 3134 (2019).

[172] C. Pearson. "High-Speed, Analog-to-Digital Converter Basics". SLAA510, Application report, Texas Instruments (2011).

[173] C. Mitchell & R. Ryne. "Proton Beam Filamentation in IOTA at High Current". Presentation, IOTA Physics Meeting February 24, 2020 (2020). https://indico.fnal.gov/event/23366/contribution/2/material/slides/0.pdf

[174] A. Romanov, A. Valishev, David Bruhwiler, Nathan Cook et al. "Adaptive Matching Of The IOTA Ring Linear Optics For Space Charge Compensation". Technical report (2018).

[175] C. Mitchell, R. Ryne & J. Qiang. "Advances in Symplectic Tracking for Robust Modeling of Nonlinear Integrable Optics". In "Nonlinear Dynamics and Collective Effects in Particle Beam Physics", pages 1–11 (2019).

[176] J. Edelen, D. Abell, D. Bruhwiler, N. Cook et al. "A Novel S-Based Symplectic Algorithm for Tracking With Space Charge". In "Proceedings, 10th International Particle Accelerator Conference (IPAC2019): Melbourne, Australia", page WEPTS068 (2019).

[177] D. Wilsher. Facility Manager, Dimensional Metrology and Additive Manufacturing Facility, STFC. Private communication (2018).

[178] C.C. Hall, D.L. Bruhwiler, N.M. Cook, J.P. Edelen et al. "Simulation of perturbative effects in IOTA". In "9th International Particle Accelerator Conference, IPAC18, Vancouver, Canada", (2018). ISBN 9783954501687. https://accelconf.web.cern.ch/AccelConf/ipac2018/papers/thpak082.pdf

[179] G.J. Sussman & J. Wisdom. "Structure and interpretation of classical mechanics: second edition". MIT press (2001). https://mitpress.mit.edu/sites/default/files/titles/content/sicm_edition_2/chapter006.html

[180] Taylor Hobson precision. "A guide to the measurement of roundness". https://pdfs.semanticscholar.org/15d6/fd70a8ba19bebf008bdb33b37c83ccca1b2a.pdf